A MULTISCALE FRAMEWORK FOR THE CHARACTERIZATION OF DAMAGE IN TEXTILE COMPOSITES UNDER THERMOMECHANICAL LOADS

A Dissertation

by

WESLEY ROSS MCLENDON

Submitted to the Office of Graduate and Professional Studies of
Texas A&M University
in partial fulfillment of the requirements for the degree of

DOCTOR OF PHILOSOPHY

Chair of Committee,	John D. Whitcomb
Committee Members,	Dimitris C. Lagoudas
	J.N. Reddy
	Ozden Ochoa
Head of Department,	Rodney D. W. Bowersox

December 2013

Major Subject: Aerospace Engineering

ABSTRACT

This work examines composite failure at multiple scales. The first scale that is examined is the fiber-matrix scale, where fibers and matrix are discretely modeled. A model is developed at this scale which includes randomness in the fiber positions. This randomness is found to significantly influence the stress field and resulting failure that occurs under thermomechanical loads as compared to fiber-matrix microstructures with regular arrays of fibers. The fiber-matrix model is utilized to characterize variability and temperature dependence of the composite strength arising from microstructural randomness and the presence of thermally induced stresses.

The second scale that is examined is that of a textile unit cell. Failure initiation behavior is examined for a variety of thermomechanical loadings at this scale, and it is found that failure tends to initiate in a limited number of ways for a wide variety of loadings. A new progressive failure model is then examined for the textile unit cell. This model utilizes cohesive interface elements in the tows, neat matrix pockets, and tow and matrix interfaces to account for crack opening in the textile, as well as a continuum damage model to account for diffuse damage in the tows. Variability and temperature dependence of the transverse tow strength is introduced by specifying varying cohesive strengths in the intra-tow cohesive zones using a Weibull distribution characterized using the random fiber-matrix model. Progressive failure analyses are then performed for the textile unit cell under a variety of thermomechanical loads, and the resulting behaviors are compared to identify characteristic modes of damage development and their effect on the textile response.

A continuum damage model for the textile material, which can be applied to engineering structures, is developed based on the characteristic damage modes observed in the textile unit cell analyses. This model tracks the evolution of each characteristic mode of damage based on the structural-scale stress and predicts the degradation in the textile response as a result of this damage. The ability of this model to predict the textile's response under various damage-inducing loads is then compared to the response obtained from textile unit cell progressive failure analysis, and both models are found to be in good agreement for most loadings.

For Lucy and Ethan

ACKNOWLEDGEMENTS

The research presented here is by no means an individual effort. I have been helped along the way in many respects by a variety of exceptional individuals. Foremost among these is my advisor, Dr. John D. Whitcomb. None of this work would be possible without his guidance, depth of knowledge, and patience, not to mention the foundation of analysis capabilities he worked to establish before I even became a graduate student. Further, I owe a debt of gratitude to the members of my committee, Dr. Dimitris Lagoudas, Dr. JN Reddy, and Dr. Ozden Ochoa. Beyond providing me with guidance as I conducted the research for this thesis, they have been involved in various aspects of my education and research activities from my time as an undergraduate until now, and in various ways have made investments in me which I carry forward. I am also appreciative of Dr. Mohammad Naraghi, who has provided his expertise while serving as a substitute for committee members who were away on travel. Beyond these, there are other faculty who have been particularly instrumental in my development along the way - Dr. Walter Haisler, Dr. Ramesh Talreja, Dr. Vikram Kinra, and Dr. Darren Hartl in particular.

Beyond the faculty, I have been extremely fortunate to have a number of fellow graduate students whom I have worked alongside, and who have helped me accomplish much more than I could have on my own. Kevin Maxwell, Brian Owens, Keith Ballard, Dr. Kaushik Das, Yellevenkatasunil Jonnalagadda, Dr. Julian Varghese, and Dr. Deepak Goyal within the group of researchers connected to my advisor, as well as many others who have served as collaborators and sounding boards - Brian

Lester, Hieu Truong, Ankush Kothalkar, Robert Brown, Austin Cox, Antonino Parrinello, and Dr. Brent Volk, just to name a few. There have been individuals beyond Texas A&M with whom I have collaborated and who have provided helpful input to my research, including Dr. Tim Breitzman, Dr. David Mollenhauer, and Dr. Endel Iarve at the Air Force Research Lab, and Dr. Jae Noh, formerly at Goodrich. I also am incredibly grateful for the funding that supported this work, the Multidisciplinary University Research Initiative grant FA9550-09-1-0686 from the Air Force Office of Scientific Research to Texas A&M University with Dr. David Stargel as the program manager.

I am ever grateful and indebted to my family who have supported me through these years as a graduate student. Without the support and foundation established by my parents, pursuing graduate school would not have been an option, and without the steadfast, patient, and selfless love and support of my wife, Meredith, I would not have completed it.

Finally, and most importantly, I am thankful to God, who saw fit to make the universe a place of unending complexity, and man a creature of unending curiosity.

TABLE OF CONTENTS

Page

CHAPTER Page

CHAPTER Page

LIST OF FIGURES

FIGURE Page

FIGURE Page

FIGURE Page

FIGURE Page

LIST OF TABLES

TABLE Page

CHAPTER I

INTRODUCTION

Although carbon-fiber composite materials have existed for roughly half of a century, the prediction of failure in composite structures continues to be a challenging problem when compared to the prediction of failure in structures using more traditional materials. This reality was recently manifest by the difficulty that Boeing encountered in passing the static structural safety test for the 787, the first full-scale airliner with composite wings and fuselage. In the first full-scale structural test of the airframe, the aircraft experienced a delamination in the wing box just after reaching limit load, and long before reaching the required ultimate load [1]. This failure was in stark contrast to the test of the 777, an aluminum aircraft whose structure failed at 154% of limit load (just 4% above the required ultimate load) in its first full-scale structural test [2].

That the 777 was able to pass the structural test by such a small margin (indicating that the structure was optimally sized to have the required strength) is a testament to Boeing's thorough understanding of the failure of aluminum structures. The difficulty in accurately predicting failure in composite structures of the 787 lies in the variety of failure mechanisms that exist at multiple scales throughout the structure. These failure modes can result in non-critical degradation of the structure, such as matrix cracking in off-axis plies and textile tows, or can represent more critical events like large-scale delamination, fiber breaking, and kink-band formation. Additionally, the failure modes can interact with one another, such as delamination

onset in adjacent plies due to interaction of matrix cracks. The criticality of a given failure mode is typically dependent on the overall structural configuration. For instance, it is possible for some laminate specimens to completely fail without any fiber breakage through the development of a network of delaminations and matrix cracks that cross the entire specimen. Failure prediction is additionally complicated by the presence of potentially large thermally-induced stresses that exist in the composite due to a mismatch in the thermal expansion coefficients of the constituents.

The current work addresses the problem of predicting damage development and failure in plain-weave textile composite structures undergoing in-plane loading. This is to be accomplished at the scale of engineering structures by characterizing failure behavior at smaller scales. The three scales of interest are illustrated in Fig. I.1.

The ultimate goal of this work is to develop an understanding of damage development in textile composites that facilitates the creation of a continuum damage mechanics model that can be employed at the structural scale, shown in Fig. I.1c. This is the scale that is of greatest utility to engineering design, since analyses at this scale will determine whether an engineering structure is able to effectively (i.e. with an acceptable level of deformation) sustain its limiting load case within the required factor of safety. Elevated stress levels in the textile composite will lead to the development of small cracks, or damage, which will affect the overall response of the textile. This damage will increase in severity as stresses continue to increase, until finally a critical type of failure occurs, such as fiber failure or the collapse of the composite under shear loading. The objective of the continuum damage mechanics model is to predict how the damage state in the textile evolves as the stresses act-

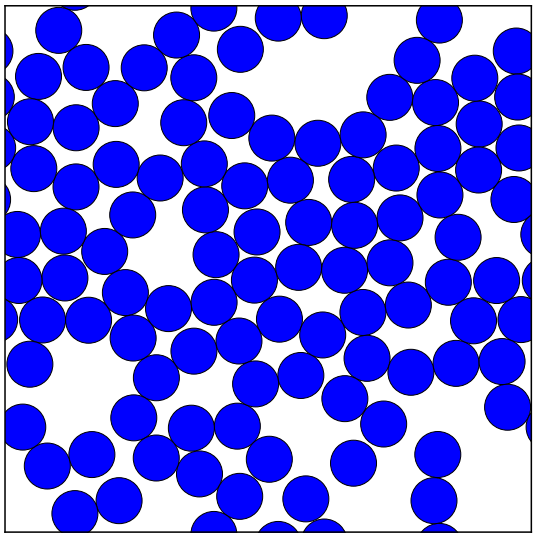

(a) Fiber-matrix scale

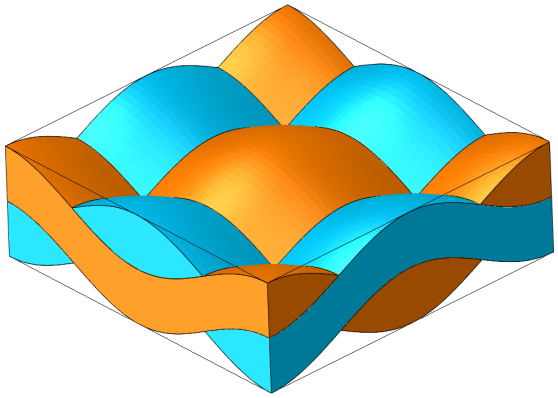

(b) Textile unit-cell scale

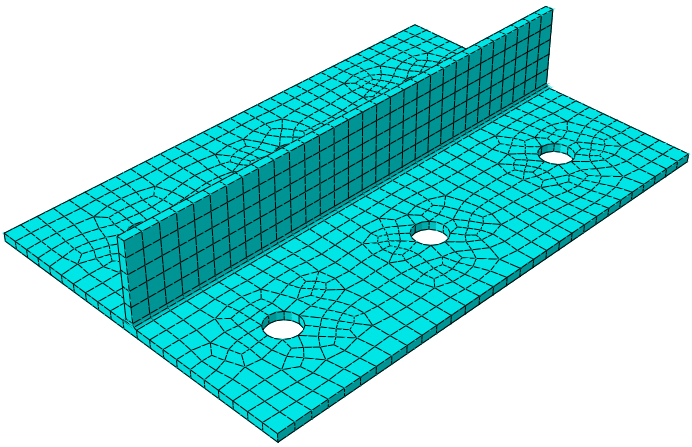

(c) Structural scale

Figure I.1: Composite scales examined in current study.

ing on the textile are increased up until the point that critical failure occurs, and to predict how this damage state modifies the response of the textile. Preferably, this is accomplished by adequately characterizing the behavior of the textile under various stresses a priori, rather than utilizing a plethora of detailed analyses which run concurrently to the structural analysis and track the local evolution of damage at different locations in the structure.

Determining the damage state of the textile for a given load, as well as the effect of the damage on the textile's overall response, requires analysis to be performed at the textile scale, shown in Fig. I.1b. At this scale, tows, or bundles of fibers, are modeled discretely as transversely isotropic continua. The current work accounts for various types of damage which can occur, including matrix cracking (or splitting) of the tows, crack growth through the pockets of neat matrix, failure of the interfaces between adjacent tows and between the tows and the matrix pocket, and shear failure of the tows. Cohesive zones are used to model the opening of cracks, while a continuum damage model is used to account for diffuse microdamage in the tows. Due to the transversely isotropic nature of the tow's thermal expansion coefficients along with the different tow orientations in the textile, temperature changes result in development of stresses in the tows and matrix pocket. These stresses interact with stresses from mechanical loadings to influence damage development in the textile. Damage growth is studied for a variety of different thermomechanical loading cases using periodic unit cell analysis. Based on this study, characteristic damage states are identified and related to the overall response of the textile. This information forms the basis of the structural-scale continuum damage mechanics model for the

textile.

The prediction of failure in the textile's tows is facilitated through analyses conducted at the composite's fiber-matrix scale, shown in Fig. I.1a. At this scale, fibers are accounted for discretely. A periodic, random model of the fiber-matrix microstructure is utilized to accurately capture the effect of interactions between closely-spaced fibers. The analysis at this scale is focused on characterizing the statistical distribution of the tow strength under transverse normal and longitudinal shear loading (the strength will exhibit variability due to the intrinsic randomness of the fiber-matrix microstructure) and determining how the strength distribution varies with temperature. Temperature dependence exists due to thermally induced stresses in the fiber-matrix microstructure that develop because of the thermal coefficient mismatch between fibers and matrix. Just as in the textile unit cell, these stresses interact with the stresses from mechanical loading, changing the applied mechanical load at which failure occurs. One major difficulty which must also be addressed at the fiber-matrix scale is the determination of some of the material properties. Due to the small fiber diameter (roughly 5 μm, or less than $\frac{1}{10}$ the diameter of a typical human hair), the direct measurement of transverse fiber properties presents considerable difficulty. Additionally, it is possible that the polymer matrix in the composite may interact with the fibers in a manner which causes it to exhibit a different strength properties than it would as a neat specimen. This different strength is referred to as the "in situ strength". Due to the difficulty of measuring these properties directly, they will be predicted through the solution of inverse problems using the random fiber-matrix model and known stiffness and strength properties for unidirectional

tape laminates.

Once the distribution of the transverse strength of the textile is characterized for a given temperature, it will be used to seed values for the transverse tow strength in the textile-scale model. This allows for both variability and temperature dependence of the transverse tow strength to be incorporated into the textile scale analysis which is used to develop the structural scale failure model.

This work is divided into four chapters. The first chapter contains a survey of much of the literature that exists regarding failure prediction in composite materials, with an emphasis on configurations that bear resemblance to those being examined here. The second chapter provides a description of various theories that are utilized in the current work. This includes finite element analysis, the formulation of interfacial elements to account for crack opening, and the cohesive zone model which governs the opening behavior of those elements. The third chapter details the analysis conducted at the fiber-matrix scale, including the development of the random periodic fiber-matrix microstructure, the determination of material properties through inverse analysis, an investigation into the effect that the assumed microstructure has on the interaction between thermally and mechanically induced stresses, the development of a progressive failure model, an examination of the sensitivity of strength statistics to different sizes of representative volume element (RVE), and finally the characterization of the strength distribution for the fiber-matrix at different temperatures. The final chapter details the various analyses that were performed at the textile scale. This chapter examines the development of the textile unit cell model, an investigation that was performed into failure initiation in the

textile, and the results of progressive failure analysis of the textile under a variety of loadings. Finally, a structural scale continuum damage mechanics model for the textile composite, which is based on the behavior determined using the textile scale model, is developed. Predictions of the textile's response for various loadings using this model are then compared to predictions made directly using the textile scale model to verify the structural scale model's fitness.

CHAPTER II

SURVEY OF LITERATURE

The body of research into the failure behavior of composite materials is extensive. This chapter attempts to categorize this research. The first category that will be reviewed covers general approaches for modeling different types of damage. These will be examined more from the standpoint of general approaches which can be applied to a variety of materials, including composites. Next, research into the failure of unidirectional composite material will be examined. This includes consideration at both the fiber-matrix scale and at larger scales that consider the behavior of a single lamina. This sort of investigation is useful for predicting failure of a tow in a textile, or an individual ply in a tape laminate. The next category is the failure of multi-layer tape laminates. The final category is the failure of textile composites.

II.A. Approaches for Modeling Failure

A number of different approaches have been put forward to account for the presence of damage in a variety of materials, including composites. This section provides a brief survey of some of these approaches.

II.A.1. Continuum Damage Mechanics

One of the simpler approaches for modeling the presence of damage is continuum damage mechanics (CDM). This approach was first put forward by Kachanov to account for the generation of voids and microcracks in the creep of metals [3].

In Kachanov's approach, the development of damage was accounted for by modifying the properties of the material using a damage scalar. Murakami and Ohno [4] extended this work to account for damage using a tensor representation. Talreja developed a tensor-based continuum damage mechanics model for application to composite materials. [5, 6].

This approach to accounting for failure is most appropriate in situations where damage consists of a large number of small, diffuse cracks relative to the length scale that is being considered in the analysis. This would be the case, for instance, when accounting for the development of matrix cracking in an analysis of a laminated structure. However, if one examines a smaller scale, such as the scale where each individual lamina of the laminate is discretely modeled, it may not be appropriate to apply CDM to account for matrix cracking since matrix cracks are of the same length-scale as the elements in the analysis. In such cases, it may be more appropriate to account for cracks in a more explicit, discrete manner.

II.A.2. Virtual Crack Closure Technique

The virtual crack closure technique (VCCT) is a method for performing fracture mechanics in a finite element framework. Originally presented by Rybicki and Kanninen [7], the method allows the calculation of the stress intensity factor at the crack tip by determining the work required to close the crack along one element length. Through Irwin's contention, it is assumed that this energy is the same as the energy that was consumed in the process of extending the crack this same length. This energy measurement can be accomplished in a finite element analysis framework by

examination of the crack opening displacements immediately behind the crack tip and the nodal forces immediately in front of the crack tip. In this manner, one is able to determine if the energy available to drive crack growth has exceeded the critical strain energy release rate of the crack. This approach does have several limitations, however. First, it is dependent upon the presence of an initial crack, meaning it cannot predict crack nucleation. Additionally, the crack front must correspond to element boundaries in the finite element mesh. Furthermore, modeling progressive crack opening requires the addition of new nodes to the finite element mesh as the crack opens. Despite these limitations and difficulties, VCCT has become a popular method for predicting the growth of fracture in finite element analyses (for example, see [8–12]).

II.A.3. Cohesive Zone Model

Cohesive zone models have become a widely-used tool for modeling the growth of fracture. The concept of the cohesive zone was first put forward by Dugdale [13], Barenblatt [14], and Hillerborg [15]. The idea behind the cohesive zone is based on the premise that in reality, the tractions at the tip of a crack cannot in actuality go to infinity as predicted in linear elastic fracture mechanics, but rather are bounded to not exceed the yield stress of the material undergoing fracture. This leads to the development of a region in front of the crack tip where partial separation of the material takes place. This region is the so-called "cohesive zone". A variety of numerical implementations of cohesive zone models have been put forward by several researchers, including Needleman [16], Jin et al. [17], Park et al. [18], Roy

and Dodds [19], and Turon et al. [20] to name a few.

There are several commonalities between these various models. The first is the definition of a traction-separation relationship, which relates the traction across the cohesive surface to the displacement jump across the cohesive surface. This relationship typically has a very high initial stiffness to resist opening of the cohesive element. In addition, there is a maximum traction which can be transmitted across the surface. Finally, the area under the traction-separation curve corresponds to the energy release rate for fracture growth in the material A variety of forms for this relationship exist, including bilinear, trilinear, polynomial, and potential-based functions. A state variable is typically used to track the evolution of damage and ensure irreversibility of crack opening, and unloading typically follows a linear path back to the origin of the traction-separation plot. There is wide variability in the way that these various models handle mixed-mode opening, both in determining what the critical traction under mixed-mode opening should be and in determining the mixed-mode strain energy release rate.

Typically, cohesive zone models are used to govern the opening behavior of interfacial elements which must be inserted into the finite element model a priori along likely fracture paths. As opposed to the virtual crack closure technique, however, these interfacial elements provide an increased degree of flexibility in how crack fronts are able to evolve. It is also possible, though the use of enrichment methods such as extended finite elements, to arbitrarily insert cohesive zones into continuum elements.

II.A.4. Extended Finite Elements and Partition of Unity

Fairly recently, approaches have been developed for introducing jump discontinuities into finite elements using the partition of unity method put forward by Babuska and Melenk [21]. The application of this approach to modeling fracture was presented by Belytschko and Black [22] as the Extended Finite Element Method, typically referred to as X-FEM. By adding a heaviside function to the displacement field in the element, tracking the location of the crack plane using a level set method, and adding additional degrees of freedom to the element to interpolate the crack opening, a crack can be inserted through a finite element mesh without the need for remeshing. This approach can also be used to account for weak discontinuities (e.g. material interfaces) that are not conformally meshed, as demonstrated by Belytschko et al. [23]. The difficulties associated with the extended finite element method include modifying the integration of an enriched element (typically, each segment of an element containing a crack or weak discontinuity must be integrated separately), the dynamic addition of enriched degrees of freedom to the finite element model as cracks extend into previously unfractured elements, and the description of the fracture surface in the element. X-FEM also presents some limitations. One of these is a general inability to have multiple cracks or crack branching within an element, primarily due to the additional complexity that this would introduce to performing integration and accounting for crack topology.

II.B. Fiber-Matrix Behavior

Much of the early failure prediction methods developed for composites centered around the problem of determining when an individual lamina in a composite would undergo failure. In general, one may divide these approaches into those that are based on the state in the homogenized lamina, and those that are based on the micromechanics of the fibers and matrix.

II.B.1. Lamina-based Failure Models

Numerous approaches of varying complexity have been developed to address the problem of lamina failure prediction. A large number of these were examined in the World-Wide Failure Exercise (WWFE) [24]. The current discussion categorizes these into those which do not account for different modes of failure, and those that do.

II.B.1.a. Polynomial-Fit Failure Criteria

Due to the transverse isotropy (or in more general cases, orthotropy) of composite lamina, failure criteria used for isotropic materials, such as von Mises' criterion or Christensen's criterion [25](which is used in the current study to predict matrix failure) are not appropriate for predicting failure of a composite lamina or tow. Hill [26] developed a yield theory for orthotropic metals (which can come about due to processes such as rolling and drawing) which was adapted by Tsai into the Tsai-Hill criterion [27] and also by Hoffman [28] for application to composite lamina. These criteria are based on strengths of a unidirectional lamina under a various loads. The application of Hill's criterion to composites is a phenomenological convenience

based on the fact that composites are orthotropic; there is no fundamentally physical basis for applying a yield criterion to predict the often brittle failure of composite materials.

Tsai and Wu subsequently developed the Tsai-Wu tensor polynomial failure criterion [29]. This criterion assumes that the failure surface of the composite can be fit by a second-order polynomial of the form of equation 2.1.

$$F_\alpha \sigma_\alpha + F_{\alpha\beta} \sigma_\alpha \sigma_\beta = 1 \tag{2.1}$$

This form for the failure surface allows for first order stress interactions that cannot be accounted for using the Tsai-Hill and Hoffman criteria. The transverse isotropy characterizing composites means that only 7 of the 27 values F_α and $F_{\alpha\beta}$ (which is symmetric) are independent. These values can mostly be determined from uniaxial and shear tests on a unidirectional composite lamina. However, the value F_{12} relates to biaxial strength and is particularly difficult to determine experimentally. As a result, a number of means have been developed for approximating it [30–33]. Liu and Tsai [34] along with Kuraishi [35] utilized an adaptation of the Tsai-Wu criterion coupled with a material degradation law for the WWFE.

II.B.1.b. Mode-Based Failure Criteria

Different types of loads can lead to very different modes of failure in composites. For instance, axial tensile loading in the fiber direction will typically lead to fiber failure, while axial compressive loads will lead to the development of kink bands. Transverse tensile loads lead to brittle matrix fracture, and longitudinal shear loading leads to matrix plasticity. All of these failure behaviors are significantly different from

one another. As a result, a number of researchers have developed failure criteria that move away from fitting the failure envelope to a single polynomial function and use different criteria to predict different modes of failure. This general approach to failure prediction has been well regarded in several reviews of failure behavior [36, 37].

While difficult to attribute to a single researcher, the maximum stress criterion is essentially this type of failure criterion, since different modes of failure correspond strongly with different components of the fiber-aligned stress tensor. Zinoviev et al. [38, 39] utilized an adaptation of the max stress criterion to predict ply failure for the WWFE. Another related criterion which in a sense is mode-based is the max strain criterion. Bogetti et al. [40, 41] utilized this type of failure criterion to predict ply-failure in their submission to the WWFE.

Hashin's criterion [42], a notable absence from the WWFE, is a piecewise criterion formulated in terms of stress invariants that uses different criteria for various possible failure modes - tensile or compressive failure of the fibers or matrix. Fiber direction failure modes in Hashin's failure theory typically assume the same form as the max-stress criterion, but shear interaction can be included. Matrix failure prediction is loosely based on Mohr-Coulomb fracture theory [43], although Hashin avoids the difficulty of identifying the critical fracture plane by using a quadratic approximation.

Christensen [44] put forward a somewhat simpler failure criterion that reduces to two polynomial functions - one for fiber-dominated failure and another for matrix-dominated failure. Like Hashin's criterion, Christensen's criterion is formed in terms of invariant stresses. The coupling that Christensen includes in predicting failure

differs somewhat from Hashin's criterion, largely in that it includes interaction of hydrostatic stress in the prediction of fiber-dominated failure.

Puck and Schurmann [45, 46] proposed a criterion for the WWFE. Like Hashin's criterion, Puck's criterion predicts fiber failure from the axial stress in the composite. Transverse failure prediction is accomplished using the Mohr-Coulomb criterion. For a laminate experiencing a state of plane stress, the critical fracture plane from the Mohr-Coulomb criterion can be directly calculated. However, when considering a fully three dimensional state of stress in the composite (as would exist in a textile tow), determining failure using Mohr-Coulomb's criterion requires a search to determine the critical fracture plane before determining if the traction across that plane is sufficient to cause failure (it is not possible to analytically determine this plane). Furthermore, Puck's criterion involves the use of a variety of traction interaction parameters representing material properties that can be difficult to characterize through experiment [47]. Cuntze and Freund [48, 49] submitted a criterion for the WWFE that was similar in many respects to that of Puck and Schurmann. The primary difference between these methods was the way that properties were degraded after transverse failure was predicted in a ply and the fact that Cuntze's method includes some interaction between failure modes which are excluded by Puck.

More recently, Dávila et al. [50] proposed the LaRC03 failure criterion. This six-part criterion shares many aspects of the previously mentioned criteria. Prediction of matrix failure under transverse loading is accomplished in a manner similar to that of Puck, but with the use of fewer parameters regarding the interaction of different components of traction acting on potential fracture surfaces (values which can be

difficult to determine experimentally). This failure criterion has been utilized in several recent studies into laminate behavior, for instance, in a collection of work from the Air Force Research Laboratory and associated organizations [51–53].

II.B.2. Micromechanics Based Lamina Modeling

Another approach to modeling the behavior of composite lamina and tows is to utilize a micromechanics model. Such models found early utility in the prediction of transverse composite properties, or in the determination of constituent properties (such as transverse fiber moduli) based on bulk lamina properties. With the development of an appropriate micromechanics model, it is possible from the microscale stresses to predict when a given constituent in the composite will experience failure under larger-scale loading.

With regards to the effective response of composites based on micromechanics, Hashin et al. [54] presented an analytical model capable of predicting bounds for the effective properties of a composite microstructure. Sun and Vaidya [55] utilized regular square and hexagonal fiber-matrix unit cells and finite element analysis to predict the effective linear response of composites.

Asp et al. [56] investigated the failure of polymer-matrix composites under transverse load using finite element analysis of a hexagonal fiber-matrix unit cell model. It was found that under transverse tension, strong hydrostatic tensile stresses developed in the regions between fibers. Because the stresses are strongly hydrostatic, the polymer has a fairly linear response, and a dilitational strain energy criterion was used to predict the onset of failure based on previous investigations they made into

polymer failure under triaxial stress states [57].

Mayes and Hansen presented an approach called multicontinuum Theory for failure prediction [58], which originally formed the basis of the analysis package called Firehole Composites™. This approach uses a micromechanics model to determine how the volume averaged stress in a given constituent of the composite varies with the larger-scale stress in addition to determining the overall contribution of each constituent to the overall stiffness of the composite. Failure of the constituents are then predicted based on their volume average stresses using an invariant-based failure criterion. The change in the composite's overall damaged response is approximated by eliminating the failed constituent's stiffness contribution to the composite. This approach has several apparent shortcomings. The first is basing constituent failure on the volume averaged stress in a constituent. In reality, failure is an extrema-driven occurrence. There will be large spatial variation of stresses in the constituents of a composite. Therefore, using the volume averaged stress as the basis for predicting constituent failure leads to a purely empirical failure model. Another issue is that the approach to degradation does not account for the nature of the load path in a composite. For instance, while the both the fibers and matrix contribute to the transverse stiffness of a composite lamina, transverse failures generally do not involve the fibers (instead occurring in the matrix and on the fiber-matrix interface). However, these failures result in a severing of the transverse loading path, resulting in a complete loss of transverse stiffness, not just the stiffness associated with the matrix as predicted using multicontinuum theory.

Ha et al. [59] improve upon the multicontinuum approach by accounting for local

variation of stress in the fiber-matrix. They utilize a hexagonal fiber-matrix unit cell model and calculate the stress intensity factors for a given lamina stress at critical locations in the matrix and fiber. Matrix failure at the micro-scale is accounted for using a criterion put forward by Raghava [60] for polymers. The effective response of the lamina is degraded using an isotropic damage parameter. These responses are utilized in a larger-scale analysis of a tape lamina under a general thermomechanical load.

Stamblewski et al. [61] utilized a hexagonal fiber-matrix unit cell model to predict failure initiation for a variety of applied loadings. Determination of failure initiation for a large number of multiaxial loadings was facilitated using superposition of the stress fields associated with a single large-scale loading component. These failure-initiation stresses were used to fit parameters for the Tsai-Wu tensor polynomial criterion.

II.B.2.a. Random Microstructures

Brennan and Walrath [62] provide a good overview of various approaches that have been utilized to generate random fiber-matrix microstructures, as well as an examination of statistical measures of the fiber-matrix geometry. Wilding and Fullwood [63] additionally have performed work in the field of examining clustering metrics for random fiber-matrix geometries. Bhattacharyya and Lagoudas [64] examined the effect of clustering on effective composite moduli, which were determined using analytical micromechanics approaches. They found that longitudinal shear modulus and the plain strain bulk modulus were sensitive to clustering of fibers.

Adams and Tsai [65] were among the first researchers to examine the issue of randomness in the fiber-matrix microstructure. They developed random microstructures from square and hexagonal grids by randomizing which grid locations contained fibers. They used this model to predict lamina properties and found that a hexagonal grid with randomly positioned fibers provided a more accurate prediction of elastic properties than either a regular hexagonal or square array. Aghdam and Dezhesetan [66] recently undertook a similar study.

Teng [67] utilized microstructure a with a regular grid of fibers, but randomly specified some fibers to be partially debonded from the matrix to determine the effect of fiber debonding. Monte-Carlo simulations using finite element analysis were then performed to obtain effective transverse properties for the composite under tension and compression.

Ghosh et al. [68] utilized Voronoi finite elements to examine the effect of various parameters which can be used to quantify a microstructure, such as local area fraction and nearest neighbor distance, to determine how these parameters effected the predicted response. The Voronoi tessellation provides a convenient approach to discretizing random microstructures.

Bulsara et al. [69] examined the issue of determining an appropriate RVE size for the prediction of failure initiation in a ceramic matrix composite microstructure with randomness, with particular interest regarding the issue of thermal loading.

Recently, there have been a few investigations into the progressive failure of composite materials that utilized random models of the fiber and matrix. Mollenhauer et al. [70] developed a random fiber-matrix RVE model with a variety of approaches

such as element degradation, cohesive zone modeling, and mesh-independent cracks to account for the development of failure in the matrix and failure of the fiber/matrix interface. This model was utilized to predict the Mode I critical strain energy release rate for crack growth associated with transverse failure of the composite.

Totry et al. [71] performed progressive failure analysis at the fiber-matrix scale using a random fiber-matrix model generated using an adaptation of work by Segurado and LLorca [72], which itself is an adaptation of work into random dispersions by Rintoul and Torquato [73]. Damage and nonlinearity in the model is accounted for using cohesive zone elements on the fiber/matrix interface and a Mohr-Coulomb governed plasticity model in the matrix. Gonzalez and LLorca [74] used a similar approach to model failure of a composite under transverse compression, making note of the development of plasticity bands running at an angle of about 50-56° to the normal plane of the applied load. One serious shortcoming of both [71] and [74] is that the carbon fibers are modeled as isotropic, when in reality, carbon fibers have much higher moduli in the longitudinal direction than the transverse directions. O'Dwyer et al. [75] recently improved upon this shortcoming by using transversely isotropic fiber properties. They performed a similar analysis using a periodic random RVE generated using the approach in [76]. Matrix failure was modeled using a Mohr-Coulomb based plasticity model, and failure of the fiber-matrix interface was governed using cohesive zones. This work explored the effect that various cohesive parameters had on the overall response of the composite for several different loadings.

Garnich et al. [77] utilized a random fiber matrix microstructure to investigate the fatigue behavior of composite materials. Their microstructure was generated

using an algorithm developed by Anderson [78]. One of the interesting features of this algorithm is that while it generates periodic unit cells of randomly arranged fibers, the mesh boundaries are defined using a Voronoi tessellation, which ensures that fibers never cross the unit cell boundary.

One problem which is of particular interest in the current work, due to the application of composite materials to structural systems operating at elevated temperature, is the effect that temperature change has on the strength of composite materials. While the current work will focus on the effect of thermally-induced stresses due to thermal expansion coefficient mismatch, the thermal dependence of the matrix properties can also be a factor. There have been a number of papers on both of these aspects of temperature change, and interestingly, many of them come to different conclusions, especially with regards to whether the stresses that result from cooling the composite after cure tend to strengthen or weaken it under transverse loading.

Asp et al. [56] included an investigation of the effect of thermally induced stresses in their studies on failure initiation in various arrayed composite microstructures. They determined that for low volume fractions, thermal cooling led to stresses which reduced transverse strength, while at high volume fractions, the opposite was true - strength tended to increase due to the thermally induced stresses.

Fiedler et al. [79] investigated the effect of thermally induced stresses from cooling on transverse strength at various volume fractions by examining interfacial tractions. They found that higher volume fractions tended to reduce the transverse strength of composites while thermally-induced stresses tended to have the opposite

effect (strengthening). Hobbiebrunken et al. (including Fiedler) [80] showed that stresses from cooling tended to increase the applied stress at which failure occurred (i.e. had a strengthening effect). However, in a later investigation, Fielder et al. [81] concluded that thermally induced stresses tended to reduce the composite's transverse strength while the temperature dependence of the matrix property tended to increase it to a greater degree (resulting in a net increase in transverse strength as the composite is cooled from cure).

Maligno et al. [82] examined the effect of thermally induced stresses on failure initiation in a hexagonal unit cell for a glass-fiber epoxy composite, and concluded that under transverse loads, residual thermal stresses from cooling are generally beneficial to the transverse strength of the composite.

Leong and Sankar [83] used a superposition approach to calculate the failure initiation envelope for a hexagonal fiber-matrix unit cell under a variety of loadings, including thermal loading. Failure initiation was determined using a maximum stress criterion within each of the constituents. Although they did not draw a particular conclusion regarding the influence of temperature change on transverse strength, they did determine that temperature decrease does change the overall failure envelope for a tow or lamina.

Hojo et al. [84] examined the effect of fiber spacing by using a finite element model developed using digital image correlation of actual composite cross-sections. They examined the interactions between thermally-induced stresses from cooling after cure and stresses resulting from transverse normal loads. Their focus was on the normal components of the interfacial tractions between fibers and matrix.

They found that cooling resulted in compressive radial tractions which became quite large in magnitude when fibers were in very close proximity. These compressive normal tractions counter-acted the tensile tractions which arose due to transverse normal loading, thereby delaying the onset of interfacial failure. They also examined hexagonal fiber arrays and found that these arrays were not able to predict the degree to which this interaction occurred in fiber-matrix microstructures with random fiber positions. Based on this finding, they concluded that thermally induced stresses from cooling after cure tend to strengthen composites under transverse shear load.

Vaughan and McCarthy [85] performed a progressive failure analyses on periodic random fiber-matrix arrays and also found that thermally induced stresses from cooling after cure tended to increase the transverse strength of composites. Yang et al. [86] performed progressive failure investigations on random microstructures with varying amounts of fiber spacing and came to a different conclusion - that cooling from thermally induced stresses tends to weaken the composite when experiencing transverse loading.

II.C. Laminate Behavior

There are a very wide variety of failure modeling approaches that have been put forward in the field of modeling failure in textile composites, and since the primary focus of the proposed research is textiles, only a brief summary of prior work will be provided.

The so called shear-lag approach is one of the early models, put forward by Aveston et al. [87, 88], that can be applied to modeling the progressive failure tape

laminates. This theory is based on the principle that when a laminate layer fails, the load it carried is redistributed via shear tractions to adjacent layers. Another approach put forward by Hashin [89,90] is based on an analytical stress analysis that accounts for multiple cracking in the central plies (Hashin's original work only applies to $[0°/90°]_S$ cross-ply tape laminates). Talreja [5, 6] put forward the "continuum damage mechanics" approach, in which damage is treated as an internal state that modifies the stiffness of the damaged ply (and consequently, the laminate). This approach is founded on the work of Kachanov [3] that used a state variable to track the evolution of diffuse defects in metals undergoing creep.

More recent developments have made significant progress in modeling the development and effect of damage in various tape laminate configurations. The previously-mentioned WWFE was primarily performed for the purpose of identifying effective approaches for modeling failure in various tape laminate configurations under a variety of loadings (prediction of failure initiation is only one part of such an effort). As a result, each of the models put forward have some associated degradation algorithm that is applied to a ply when failure occurs. Many of these models follow an approach similar to that of Puck [46], which in the presence stresses that exceed the criteria for a non-critical failure (i.e. matrix cracking) reduces the effective stiffness of damaged material such that the resulting stress state meets but does not exceed the failure initiation criteria. The multi-continuum approach presented by Mayes and Hansen [58] predicts the response of a damaged material by adjusting the overall constitutive response of the composite in response to the loss of a failed constituents stiffness contribution. However, such an approach does not account for the fact that

the failure of a single constituent could affect the loading path in such a way that the unfailed constituent in the composite no longer carries any load.

Ladéveze and Libaneau [91] have put forward a model for tracking the evolution of damage and the resulting response of a single ply in a laminate. This model is based on damage parameters which are related to the development of diffuse damage in a ply (resulting from the development of a very large number of very small cracks and voids evenly spaced throughout the laminate, typically arising due to local shear stresses) and larger-scale matrix microcracking within the ply along with resulting small-scale inter-ply delaminations at the ends of the matrix microcracks. This approach is based on the finding that there is little coupling between these two modes of damage, and that these modes of damage show little dependence on the ply thickness and adjacent ply orientations. This so-called Ladéveze model has recently been well regarded [92–97].

"Damage" in composites refers to the development of cracks. All the models discussed thus far keep track of damage in terms of parameters that can be related to crack density or some other feature that exists globally throughout a single ply, but individual cracks are not accounted for. Discretely accounting for individual cracks in composites is fairly difficult to do in practice due to the fact that a large number of cracks typically develop (among other factors), and it is typically not necessary because the cracks have a distributed effect when observed from larger scales. However, approaches have recently been put forward for discretely modeling fracture within the framework of finite element analysis. The cohesive zone model offers a convenient framework for modeling the initiation and growth of fracture. It

also lends itself nicely to finite element formulations. If the crack path is known a priori, then zero-thickness interfacial decohesion elements can be inserted into the model that open up according to some traction-separation law. This approach works very well for modeling delamination, since the material interface between plies typically corresponds to a mesh interface in meso-scale finite element models.

In the case of multiple matrix cracking within a ply, it is not generally feasible to create a model that has a mesh that will allow for crack propagation along the fiber direction of any ply using interfacial decohesion elements because the crack must exist on an element boundary. However, this approach may be tractable for simple configurations with a limited number of ply orientations where crack paths can be accurately predicted a priori. This approach was reviewed by Wisnom [98] and has been performed by Wisnom et al. [99], Hallett and Wisnom [100], and Jiang et al. [101] for notched laminates, Jalavand et al. [102] for cross-ply laminates, and de Moura and Gonalves [103] for composite specimens undergoing impact. However, for configurations where crack paths cannot be accurately anticipated, the introduction of cracks using interfacial elements requires a tedious remeshing process which will likely become intractable for layups containing may plies of differing orientations and a large number of cracks. However, recent developments in finite element analysis have provided a means of accounting for discontinuities in the displacement fields of elements through the addition of enrichment degrees of freedom, thus avoiding the remeshing problem altogether. This approach, commonly referred to as the extended finite element method or X-FEM, was developed by Möes et al. [104].

While the application of interface elements for modeling delamination and/or

matrix cracking has been done in a number of studies [58-61], [63-66], using X-FEM to model cracking in the fiber-matrix plies of a tape laminate has been implemented in a limited number of applications. One recent application by Mollenhauer et al. [51, 52] uses a cohesive zone model based on work by Turon et al. [20]. Decohesion elements were used on the ply interfaces to model delamination, and a slightly modified X-FEM approach utilizing continuous enrichment functions (which simplify the process of integrating shape functions over an enriched element), developed by Iarve [105], was used to introduce cracks into the fiber-matrix plies. This approach was found to provide very good agreement with the pattern of damage that was found to develop in experimental specimens for several different configurations. Van der Meer and Sluys [94] have also put forward similar work in which both matrix cracks and delaminations are modeled discretely. Matrix cracking within a ply is accounted for using the so-called phantom node method [106] that is largely analogous to the extended finite element method.

While the work of Böhm et al. [97, 107] is applied to textile composites, it is fundamentally based on damage mechanics of individual orthotropic layers which correspond to one layer of textile material, making it more analogous to failure modeling of tape laminates than meso-scale modeling of textiles. The model is rooted in the Failure Mode Concept of Cuntze [108] which identifies failure conditions related to stress invariants. Each textile layer is considered to undergo elastic deformation up to a given loading at which point diffuse and/or discrete (when considered at the scale of an entire layer) damage begins to occur, resulting in a nonlinear response of the layer up until the textile layer undergoes complete failure. The stress-driven

evolution of diffuse damage is determined using an evolution law that gradually increases the internal damage variables as loading increases. The model requires the determination of a large number of parameters through experiment. Furthermore, its reliance on the Failure Mode Concept of Cuntze [108] introduces an assumption that the failure modes in a textile layer are related to the invariants put forward by Cuntze for an orthotropic layer. The accuracy of such an assumption can be examined through characterization of the failure behavior of a textile layer at the meso scale as is being proposed in the current work.

II.D. Textile Behavior

II.D.1. Geometry

Simply predicting or determining the arrangement and shape of tows in textiles is a complex problem, and generating a mesh of the meso-scale architecture once its geometry has been determined can present additional difficulty. Analyses of these complex geometries are typically performed at the unit-cell level and exploit periodicity, meaning that any representation of the geometry disregards small perturbations in tow path and shape that will in reality exist from one unit cell to another. Several approaches have been developed to address the problem of unit cell geometry generation.

In works by Whitcomb et al. [109–112], a sinusoidal form of the tow cross-section and path is assumed that eliminates matrix pockets between tows and provides a geometry which is relatively simple to mesh. This configuration also possesses a large number of symmetries and equivalent coordinate systems which allow for the

reduction of the analysis domain through the use of a clever set of periodic boundary conditions and multi-point constraints [113]. Disadvantages of this approach are that it is limited to 2D textile configurations ("2D textile" in the sense that there are not multiple layers of tows that are interwoven - 3D finite element analysis is used to analyze these architectures), it is not based on any physical principle beyond the fact that interwoven tows are expected to be in direct contact, and it does not capture the variations in cross-section that exist along the tow path in actual textiles.

Another approach for generating textile architectures is TexGen, originally developed by Sherburn [114]. This tool is under active development at the University of Nottingham and allows for textile geometries to be defined with varying (but not completely general) tow cross sections and tow paths that are defined using splines. It also can enforce periodicity in the tows paths and is able to create models of 3D textile architectures. It contains meshing functionality and provides the user with a convenient graphical interface. It has several major detractors, however, including a lack of functionality for handling tow interpenetration for all but the most simple textile configurations as well as a lack of physically based modeling of tow paths. As a result of these factors, tows that should be in direct contact with one another often will have unrealistic matrix pockets located between their surfaces.

Another tool for developing textile geometries is WiseTex, used by Lomov et al. to perform a wide variety of textile analyses [92, 115–118]. WiseTex performs analyses on the textile architecture that seek to minimize strain energy of the textile under the presence of manufacturing loads, and therefore it is more physically based than the previously discussed approaches. It also possesses greater functionality

for handling interpenetrating tows in the form of iterative finite element analyses that insert spring-like elements between adjacent tows. However, the possible tow cross-sections are still limited to variations of a few fundamental shapes (they are not completely general), and like TexGen, WiseTex also leaves pockets of neat resin between tows which should be in direct contact.

Seemingly the most general and possibly best approach for predicting the meso-scale textile architecture is the so-called Digital Fiber approach developed by Wang et al. [119–121]. This approach has developed to its current state in which a tow is modeled as a bundle of about 20 or more chains of rod elements (i.e. "Digital Fibers"). Tension is applied to each tow, and a contact analysis is performed. The tows paths and cross-section shapes are then determined from the rod positions, and the geometry is meshed. This approach is applicable to a wide variety of textile architectures and is extremely general.

II.D.2. Damage

Modeling the progressive growth of damage in a textile presents significant challenges beyond those encountered for tape laminates. These challenges are primarily due to the variations in stress that exist within individual tows. In tape laminates, it can be assumed that before the onset of damage, the state of stress in a single ply away from the free edge is constant or varies in a predictable fashion (linear variation of in-plane stress under bending, parabolic distribution of transverse shear stress, etc.). This is not the case for tows in a textile. Therefore, the typical approach for modeling damage in textiles involve greater consideration of the local stress fields

in tows, since the stress level in a tow may exceed the allowable stress in only a small region.

One of the first examples of modeling failure using 3D finite element analysis for textiles was performed by Blackketter et al. [122]. Their approach, which was applied to failure analysis of a plain weave textile, involved degradation of material properties at quadrature points where the stress exceeded the failure criterion for the material. For the neat matrix pockets, a maximum principle stress criterion was used, and material stiffness and shear modulus were reduced to 1% and 20%, respectively, of their original values. For the homogenized fiber-matrix, the maximum stress criterion was utilized which had the added benefit of giving an indication of what kind of failure occurs. When failure in the fiber matrix was detected, the orthotropic material properties were degraded in a manner depending upon what kind of failure was detected to occur. A plasticity model was used to predict the constitutive behavior of the composite up to failure. It was found that the overall non-linearity in the textile behavior was primarily due to damage and not plasticity. Furthermore, it was observed that ultimate strength was somewhat over-predicted as compared to experiments in addition to over-predicting the effective stiffness loss in the textile due to the onset of matrix cracking in the transverse tows.

Whitcomb and Srirengan [123] performed a failure analysis on a plain weave textile and examined the effect of mesh refinement, degradation scheme, waviness ratio, and integration order on the predicted failure behavior. It was found that the failure behavior was sensitive to all of these parameters, although it appeared that as mesh refinement increased, a converged solution was approached. Choi and Tamma

[124] presented a failure analysis of plain weave textiles that shared a great number of similarities to the work presented by Blackketter et al. [122]. They attempted to improve upon the predictions in [122] by considering post-failure anisotropy of the matrix depending on the failure stress as well as modification of the Poissons ratio of failed material. This work improved upon the ultimate failure stress predictions of Blackketter.

Guagliano and Riva [125] utilized the approach of Blackketter to examine plain weave textiles with various inter-ply stacking patterns. It was found that experiments for textiles with 8 stacked layers tended to match closely with predictions for infinite stacking, either in-phase or symmetric. It was found that if in-phase stacking is assumed, the predicted failure behavior shows significant sensitivity to the number of textile layers when a low number of layers is modeled.

Tang and Whitcomb [110] utilized a failure prediction approach similar to that of Blackketter, but with degradation values based upon investigations of Srirengan and Whitcomb [126] for textiles containing matrix cracks. Additionally, a modification to the degradation algorithm was examined that accounted for the fact that under normal compressive stresses, cracks will close and thus the failed material will retain stiffness to resist normal compressive deformation (although the shear compliance will remain degraded as the crack surfaces can slide relative to one another). They also examined the change in predicted behavior observed when accounting for geometric nonlinearity. Their investigation was performed for a variety of textile architectures (plain weaves, twills, and satins). It was found that the various architectures exhibited significantly different behaviors even though all had the same

fiber volume fraction. However, marked similarities in failure behavior were noted in the locally similar regions of different architectures, such as the undulated region of a satin and a plain weave. This result suggests the existence of characteristic failure behaviors. It was also noted that higher waviness ratio textiles showed greater sensitivity to the selected degradation model, while low waviness ratio textiles showed very little sensitivity. Accounting for geometric nonlinearity was observed to have an effect on the predicted failure behavior of the composite although it had little impact on the material response before damage onset.

Zako et al. [127] modeled failure in plain weave composites using Hoffman's criterion [28] to predict failure initiation and an anisotropic degradation scheme based on Murakami's damage tensor [128] to model the degrading effect of the damage. Upon detection of failure, certain entries in the damage tensor were completely degraded based on what mode of failure occurs. There was no evolution from undamaged to damaged material properties. This approach was found to provide fairly accurate predictions when compared to experiment, both in terms of the failure modes that were observed to occur and the effective stress-strain behavior. Lomov et. al. [116] performed an analysis on a triaxial braided composite utilizing the same method of failure prediction and degradation as Zako [127]. This work was conducted in conjunction with a very thorough set of experimental tests [129] which found that failure developed in several distinct stages. It was noted that although the initiation of failure was accurately predicted, progressive failure prediction was problematic. The primary problem noted was that matrix cracking in tows oriented 45° relative to the applied load was predicted to grow across the tow, whereas in reality failure

propagated in matrix cracks running along the tow direction (along the fibers). This issue was addressed more thoroughly by Gorbatikh et al. [130] and was found to be due to a fundamental shortcoming associated with modeling fracture through the reduction of elastic properties over a finite volume. This work found that for the case of shear load applied to a degraded region, the critical stress location on the boundary of the degraded region does not correspond to the tips of the crack that the degraded region is attempting to account for, leading to an unrealistic prediction for damage zone growth.

Ivanov et al. [92] have since performed failure analyses on triaxial braided textiles, but instead of utilizing the failure modeling approach of [127], failure prediction was performed using Puck's criterion [45]. Degradation is applied globally to straight sections of the tows (as opposed to individual finite elements) according to the degradation scheme put forward by Ládeveze [91]. This is done based on the belief that these straight tow regions behave in a manner similar to plies in tape laminates that are undergoing multiple cracking. This approach was found to provide good agreement with the experimentally observed progressive failure behavior and avoids the fundamental issues that were noted in [130].

Based on the issues that were raised by Lomov [116] and Gorbatikh [130], it seems likely that the optimal approach to modeling progressive failure in textiles at the meso-scale would be something similar to the discrete damage modeling approach used by Mollenhauer et al. [51] for laminates. However, a broad search of the literature did not reveal any study in which such an analysis was applied to textile mesoscale models, likely due to the high level of difficulty associated with implement-

ing discrete damage modeling in a 3D finite element environment in addition to the complexities associated with modeling textile meso-scale architectures.

One of the shortcomings of the previously mentioned analyses is that they describe either a single or a limited number of load cases. While such analyses are useful for gaining understanding about the failure behavior of the textile, they are not sufficient for fully characterizing the failure behavior of the textile for an arbitrary load case. Accomplishing such a characterization (which is the ultimate goal of the proposed research) requires examining the failure behavior for a wide variety of loading cases. Karkkainen and Sankar [131] presented work along this line. Their analyses were based on various combinations of in-plane loading and bending of a plain weave textile composite. They examined failure initiation in the textile (no progressive failure analysis was performed). They utilized the previously described "Direct Micromechanics Method (DMM)" to develop failure initiation envelopes for textiles undergoing various combination of in-plane and bending loads. They then compared these envelopes to envelopes that would be predicted using other functional forms of failure criteria, such as max stress and Tsai-Wu [29], and found that the failure envelope based on DMM analysis detected features that could not be captured using these other theories. Subsequent work by Karkkainen et al. [132, 133] developed a quadratic failure criteria that can be applied to multilayer textile composites under an arbitrary load state based on findings using DMM.

The work by Sankar et al. [61, 131–133] is similar in many respects to the preliminary work into determining textile failure initiation behaviors that is reported in later sections, but there are several major differences. The biggest difference is that

the work of Sankar et al. makes no attempt to identify common modes of failure initiation. The only data provided regarding failure for a particular proportional loading is the magnitude of load at which failure occurs in the model. The idea of failure modes is central to the preliminary and proposed research, and as will be reported, complicated features on the failure initiation envelope of a textile appear to be strongly related to the different modes of failure that occur under different load conditions.

The use of tools like cohesive zones to progressively account for discrete crack opening in textile composites is a fairly new field. Hsu and Cheng [134] recently presented an analysis which used cohesive elements to account for interfacial failure between tows and the tows and neat matrix pocket. However, their model did not include any method for accounting for failures within the tows.

II.D.3. Other Aspects of Textiles

There are a variety of additional aspects of textile composites which may influence failure behavior. One is the presence of free surfaces. Owens et al. [112] performed work examining the stress distribution in textiles with both free surfaces and free edges and found that the stress distribution in surface mats often differ considerably from the stresses in interior mats. Ivanov et al. [117] put forward boundary conditions which can be used to account for the finite thickness of a textile in a unit cell analysis. The effects of free surfaces are incongruous with traditional unit cell analysis which assumes infinite periodicity of the unit cell. Therefore, to fully predict the failure behavior of an actual textile of finite thickness, some consideration should

be made of the effect of the free surface.

In addition to free surface effects, a textile will typically exhibit what is called nesting, a phenomenon in which one mat tends to sit in the matrix pockets of an adjacent mat. Thus, the mats will not be perfectly aligned as is assumed in a typical periodic unit cell analysis. The effect of this phenomena was examined by Ivanov et al. [118]. It was found that two limiting cases exist. In the first case, each mat is arranged symmetrically to the adjacent mats. In the second, each mat is perfectly in phase through the entire thickness of the textile laminate. Ivanov's work suggests that the in-phase mat configuration undergoes earlier initial failure but delays the onset of critical fiber-failure as compared to the configuration with symmetrical adjacent mats.

CHAPTER III

OVERVIEW OF THEORY

This chapter provides a number of details regarding several of the computational tools used to perform the investigations contained in this work.

III.A. 3D Finite Element Formulation

The analyses performed in this work make use of a three-dimensional finite element formulation. This section describes such a formulation. The finite element method consists of the discretization of the physical problem domain into a mesh. Various constitutive properties are then assigned to sub domains within the mesh, generally corresponding to various materials. These constitutive properties are utilized to determine element stiffnesses which are determined from the governing equations of equilibrium. Boundary conditions defining either force or displacement are defined for all surfaces of the mesh. The definition of sufficient boundary conditions leads to the formation of a system of linear equations whose solution is the set of nodal displacements and forces resulting in static equilibrium for the entire problem domain. These displacements can be spatially differentiated to obtain strains through kinematic relationships, which can then be converted into stresses using constitutive relationships. The mathematical details of the finite element method are described in the following subsections.

III.A.1. Kinematic Relationships

The constitutive relationship between strain and stress in a body depends first on how strain is defined for the body. Assume a body is initially in some reference configuration. Two reference frames exist for describing the configuration of the body. The first, the Lagrangian frame, defines the configuration of the body using reference, or material coordinates $X_i(t)$, which are defined at some reference time and track the body as it deforms. The second, Eulerian reference frame, defines the configuration of a deformed body by the spatial coordinates $x_i(t)$ which remain fixed in space as the body deforms. The Eulerian description of the body's configuration can be expressed in terms of the Lagrangian reference frame by a mapping function $\chi(X_i, t)$ such that $x_i = \chi(X_i, t)$. The deformation gradient is then defined as

$$F_{ij} = \frac{\partial x_i}{\partial X_j} = \frac{\partial \chi(X_i, t)}{\partial X_j} \tag{3.1}$$

Also define the displacement of some point on the body as

$$u_i = x_i - X_i \tag{3.2}$$

Next, define B_{ij} and C_{ij} the left and right stretch tensors, respectively.

$$\begin{aligned} B_{ij} &= F_{ik}F_{jk} \\ C_{ij} &= F_{ki}F_{kj} \end{aligned} \tag{3.3}$$

From these stretch tensors, one can derive two strains. First, the Green - St. Venant Strain is defined as

$$\begin{aligned} E_{ij} &= \frac{1}{2}\left(C_{ij} - \delta_{ij}\right) \\ &= \frac{1}{2}\left(F_{ki}F_{kj} - \delta_{ij}\right) \\ &= \frac{1}{2}\left(\frac{\partial u_j}{\partial X_i} + \frac{\partial u_i}{\partial X_j} + \frac{\partial u_k}{\partial X_i}\frac{\partial u_k}{\partial X_j}\right) \end{aligned} \tag{3.4}$$

where δ_{ij} is the Kronecker delta. Second, the Almansi-Hamel Strain is defined as

$$\begin{aligned} e_{ij} &= \frac{1}{2}\left(\delta ij - B_{ij}^{-1}\right) \\ &= \frac{1}{2}\left(\delta ij - \left(F_{ik}F_{jk}\right)^{-1}\right) \\ &= \left(\frac{\partial u_j}{\partial x_i} + \frac{\partial u_i}{\partial x_j} - \frac{\partial u_k}{\partial x_i}\frac{\partial u_k}{\partial x_j}\right) \end{aligned} \tag{3.5}$$

Now, the linearizing assumption will be inserted into the derivation. It will be assumed for all deformations, that the deformation gradient is small. That is

$$\left|\frac{\partial u_i}{\partial X_i}\right| = \mathbf{O}(\delta) \quad \delta \ll 1 \tag{3.6}$$

It follows that

$$\frac{\partial u_i}{\partial X_i} = \frac{\partial u_i}{\partial x_i} + \mathbf{O}(\delta^2) \tag{3.7}$$

Appealing to the assertions in Eq. (3.6) and Eq. (3.7) in the context of the strains of Eq. (3.4) and Eq. (3.5) yields

$$\begin{aligned} E_{ij} &= \varepsilon_{ij} + \mathbf{O}(\delta^2) \\ e_{ij} &= \varepsilon_{ij} + \mathbf{O}(\delta^2) \end{aligned} \tag{3.8}$$

where ε_{ij} is the linearized strain tensor, defined as

$$\begin{aligned} \varepsilon_{ij} &= \frac{1}{2}\left(\frac{\partial u_j}{\partial X_i} + \frac{\partial u_i}{\partial X_j}\right) \\ &\approx \frac{1}{2}\left(\frac{\partial u_j}{\partial x_i} + \frac{\partial u_i}{\partial x_j}\right) \end{aligned} \tag{3.9}$$

It can be seen that the strain tensor will always be symmetric, as the addition of a matrix with its transpose always results in a symmetric matrix. Also, it can be seen that the linearized strain is very nearly equal when taken in either a Eulerian or Lagrangian reference frame. From this point forward in the derivations, the Lagrangian frame will be used, and all spatial coordinates will be given in the form x_i.

III.A.2. Constitutive Relationships

With the linearized strain now defined, it is possible to clearly state the constitutive relationship between stress and strain. The most general relationship between the stress and strain tensors is given by

$$\sigma_{ij} = C_{ijkl}\varepsilon_{kl} \tag{3.10}$$

where C_{ijkl} is a fourth-order tensor, often referred to as the stiffness tensor, containing 81 constants. It is convenient to represent this fourth order tensor as a two-dimensional matrix by expressing the stress and strain tensors as vectors with 6 components by exploiting their symmetry. Like the strain tensor, the stress tensor for a static body is symmetric. The symmetry of the stress tensor is required to maintain equilibrium for angular momentum for all points in the body. Exploiting these symmetries implies that $C_{ijkl} = C_{jikl} = C_{ijlk}$ and reduces the number of constants relating stress and strain from 81 to 36 as can be seen in the following relationship.

$$\begin{pmatrix} \sigma_{11} \\ \sigma_{22} \\ \sigma_{33} \\ \sigma_{23} \\ \sigma_{31} \\ \sigma_{12} \end{pmatrix} = \begin{pmatrix} C_{1111} & C_{1122} & C_{1133} & C_{1123} & C_{1131} & C_{1112} \\ C_{2211} & C_{2222} & C_{2233} & C_{2223} & C_{2231} & C_{2212} \\ C_{3311} & C_{3322} & C_{3333} & C_{3323} & C_{3331} & C_{3312} \\ C_{2311} & C_{2322} & C_{2333} & C_{2323} & C_{2331} & C_{2312} \\ C_{3111} & C_{3122} & C_{3133} & C_{3123} & C_{3131} & C_{3112} \\ C_{1211} & C_{1222} & C_{1233} & C_{1223} & C_{1231} & C_{1212} \end{pmatrix} \begin{pmatrix} \varepsilon_{11} \\ \varepsilon_{22} \\ \varepsilon_{33} \\ 2\varepsilon_{23} \\ 2\varepsilon_{31} \\ 2\varepsilon_{12} \end{pmatrix} \tag{3.11}$$

Table III.1: Orthogonal reflection transformation matrices

Reflection Plane	Transformation Tensor
23	$\boldsymbol{Q} = \begin{pmatrix} -1 & 0 & 0 \\ 0 & 1 & 0 \\ 0 & 0 & 1 \end{pmatrix}$
31	$\boldsymbol{Q} = \begin{pmatrix} 1 & 0 & 0 \\ 0 & -1 & 0 \\ 0 & 0 & 1 \end{pmatrix}$
12	$\boldsymbol{Q} = \begin{pmatrix} 1 & 0 & 0 \\ 0 & 1 & 0 \\ 0 & 0 & -1 \end{pmatrix}$

The overall symmetry of the stiffness tensor is established by relating stress and strain using the strain energy density functional U. This relationship is given as

$$\sigma_{ij} = \frac{\partial U}{\partial \varepsilon_{ij}} = C_{ijkl}\varepsilon_{kl} \quad \Longrightarrow \quad \frac{\partial^2 U}{\partial \varepsilon_{ij}\partial \varepsilon_{kl}} = C_{ijkl} \tag{3.12}$$

which implies that $C_{ijkl} = C_{klij}$ due to the fact that the order of differentiation will not change its result. This reduces the total number of independent constants relating stress and strain to 21.

The number of terms in $\boldsymbol{C}$ can be further reduced by appealing to material symmetries. For the analyses in this work, it will be assumed that materials possess at least orthotropic symmetry. That is, all materials possess, at a minimum, three orthogonal planes of symmetry about which a reflection can take place with no change in the response of the material. It is assumed that the material will be defined such that these planes of symmetry are aligned with the coordinate axes. The orthogonal transformation matrices associated with these reflections are given in table III.1. The

stiffness matrix resulting from such a reflection is given as

$$C'_{ijkl} = Q_{ip}Q_{jq}Q_{kr}Q_{ls}C_{pqrs} \tag{3.13}$$

Provided that Q_{ij} represents a reflection about a plane of material symmetry, it can be stated that

$$C_{ijkl} = C'_{ijkl} \tag{3.14}$$

Applying Eq. (3.13) and Eq. (3.14) to Eq. (3.11), it is found that a number of terms must equal zero to satisfy the material symmetry. The resulting stiffness tensor for orthotropic materials contains 9 independent constants as follows.

$$\boldsymbol{C} = \begin{pmatrix} C_{1111} & C_{1122} & C_{1133} & 0 & 0 & 0 \\ C_{1122} & C_{2222} & C_{2233} & 0 & 0 & 0 \\ C_{1133} & C_{2233} & C_{3333} & 0 & 0 & 0 \\ 0 & 0 & 0 & C_{2323} & 0 & 0 \\ 0 & 0 & 0 & 0 & C_{3131} & 0 \\ 0 & 0 & 0 & 0 & 0 & C_{1212} \end{pmatrix} \tag{3.15}$$

Material properties are given in terms of engineering constants. These constants are most conveniently expressed in the compliance tensor $\boldsymbol{S}$, which is the inverse of the stiffness tensor. The compliance tensor for orthotropic materials relates strain to

stress in the following manner.

$$\begin{pmatrix} \varepsilon_{11} \\ \varepsilon_{22} \\ \varepsilon_{33} \\ 2\varepsilon_{23} \\ 2\varepsilon_{31} \\ 2\varepsilon_{12} \end{pmatrix} = \begin{pmatrix} \frac{1}{E_1} & -\frac{\nu_{12}}{E_1} & -\frac{\nu_{13}}{E_1} & 0 & 0 & 0 \\ -\frac{\nu_{21}}{E_2} & \frac{1}{E_2} & -\frac{\nu_{23}}{E_2} & 0 & 0 & 0 \\ -\frac{\nu_{31}}{E_3} & -\frac{\nu_{32}}{E_3} & \frac{1}{E_3} & 0 & 0 & 0 \\ 0 & 0 & 0 & \frac{1}{G_{23}} & 0 & 0 \\ 0 & 0 & 0 & 0 & \frac{1}{G_{31}} & 0 \\ 0 & 0 & 0 & 0 & 0 & \frac{1}{G_{12}} \end{pmatrix} \begin{pmatrix} \sigma_{11} \\ \sigma_{22} \\ \sigma_{33} \\ \sigma_{23} \\ \sigma_{31} \\ \sigma_{12} \end{pmatrix} \tag{3.16}$$

$$\frac{\nu_{23}}{E_2} = \frac{\nu_{32}}{E_3} \qquad \frac{\nu_{31}}{E_3} = \frac{\nu_{13}}{E_1} \qquad \frac{\nu_{12}}{E_1} = \frac{\nu_{21}}{E_2}$$

III.A.3. Governing Equations of Elasticity and the Weak Form

The primary equation governing the loading of bodies is that of equilibrium. For static bodies, the equilibrium equation takes the following form:

$$\frac{\partial \sigma_{ij}}{\partial x_j} + \rho b_i = 0 \tag{3.17}$$

where ρ is density and b_i is the specific body force. Eq. (3.17) is then multiplied by test functions (often referred to as virtual displacements) δu_i and integrated over the problem domain Ω. The resulting "weak form" of the equation of equilibrium is

$$\int_\Omega \delta u_i \left(\frac{\partial \sigma_{ij}}{\partial x_j} + \rho b_i \right) d\Omega = \int_\Omega \left(\delta u_i \frac{\partial \sigma_{ij}}{\partial x_j} + \delta u_i \rho b_i \right) d\Omega = 0 \tag{3.18}$$

The first term of Eq. (3.18) can be expanded through integration by parts.

$$\int_\Omega \left(\delta u_i \frac{\partial \sigma_{ij}}{\partial x_j} \right) d\Omega = \int_\Omega \frac{\partial \left(\delta u_i \sigma_{ij} \right)}{\partial x_j} d\Omega - \int_\Omega \left(\frac{\partial \delta u_i}{\partial x_j} \sigma_{ij} \right) d\Omega \tag{3.19}$$

Applying the result of Eq. (3.19) into Eq. (3.18) yields the following expression for the weak form.

$$\int_\Omega \frac{\partial \left(\delta u_i \sigma_{ij} \right)}{\partial x_j} d\Omega + \int_\Omega \left(\rho b_i \delta u_i - \frac{\partial \delta u_i}{\partial x_j} \sigma_{ij} \right) d\Omega = 0 \tag{3.20}$$

Applying Gauss's divergence theorem to the first term in Eq. (3.20) yields

$$\int_{\Gamma} (\delta u_i \sigma_{ij} n_j)\, d\Gamma + \int_{\Omega} \left(\rho b_i \delta u_i - \frac{\partial \delta u_i}{\partial x_j} \sigma_{ij} \right) d\Omega = 0 \tag{3.21}$$

Γ is the surface of the domain Ω, and n_i is the normal vector at a point on Γ. Now, Cauchy's stress formula, which relates stress σ_{ji} to the traction T_i on a surface with normal n_j, will be incorporated.

$$T_i = \sigma_{ji} n_j = \sigma_{ij} n_j \tag{3.22}$$

Incorporating Eq. (3.22) into Eq. (3.21) yields

$$\int_{\Gamma} (\delta u_i T_i)\, d\Gamma + \int_{\Omega} \left(\rho b_i \delta u_i - \frac{\partial \delta u_i}{\partial x_j} \sigma_{ij} \right) d\Omega = 0 \tag{3.23}$$

Additionally, The symmetry of the Cauchy stress tensor and Eq. (3.9) allow the following equivalence to be established

$$\frac{\partial \delta u_i}{\partial x_j} \sigma_{ij} = \delta \epsilon_{ij} \sigma_{ij} \tag{3.24}$$

Applying the relationship established in Eq. (3.24) to the last term in the volume integral of Eq. (3.23) yields the following

$$\int_{\Gamma} (\delta u_i T_i)\, d\Gamma + \int_{\Omega} (\rho b_i \delta u_i - \delta \varepsilon_{ij} \sigma_{ij})\, d\Omega = 0 \tag{3.25}$$

Now Galerkin approximations will be used to represent the trial function δu_i. The approximation is based upon the principle that a function can be represented as an infinite sum of smooth basis functions $\psi^{(A)}$. In the finite element analysis, there will be as many basis functions as there are nodes in the element. This results in the trial function taking the following form.

$$\delta u_i = \sum_{A=1}^{n} \delta u_i^{(A)} \psi^{(A)} \tag{3.26}$$

such that A denotes the A^{th} node in the element and n is the total number of nodes in the element. All components of all nodal displacements $u_i^{(A)}$ for an element will be expressed as q_{A_i} for convenience (in essence, a vector of all degrees of freedom for the element), where the capital subscript A denotes the node and the lowercase subscript i denotes the direction. The subscript "A_i" is treated as a single subscript for summation purpose, which permutes through i, and then A, as follows.

$$q_{A_i} = \left(u_{i=1}^{(A=1)}, u_{i=2}^{(A=1)}, u_{i=3}^{(A=1)}, u_{i=1}^{(A=2)}, u_{i=2}^{(A=2)}, u_{i=3}^{(A=2)}, \cdots, u_{i=1}^{(A=n)}, u_{i=2}^{(A=n)}, u_{i=3}^{(A=n)} \right) \tag{3.27}$$

Virtual displacement and strain can now be expressed in the following manner.

$$\delta u_i = \frac{\partial u_i}{\partial q_{A_j}} \delta q_{A_j} \tag{3.28}$$

$$\delta \varepsilon_{ij} = \frac{\partial \varepsilon_{ij}}{\partial q_{A_k}} \delta q_{A_k} \tag{3.29}$$

Substitution of Eq. (3.28) and Eq. (3.29) into Eq. (3.25) and summing over the nodes of an element yields

$$\delta q_{A_k} \left(\int_\Gamma \left(\frac{\partial u_i}{\partial q_{A_k}} T_i \right) d\Gamma + \int_\Omega \left(\rho b_i \frac{\partial u_i}{\partial q_{A_k}} \right) d\Omega - \int_\Omega \left(\frac{\partial \varepsilon_{ij}}{\partial q_{A_k}} \sigma_{ij} \right) d\Omega \right) = 0 \tag{3.30}$$

Since this relationship must hold for any arbitrary non-zero value of the test function δq_{A_k}, it is necessary that for all values of A_k

$$\int_\Gamma \left(\frac{\partial u_i}{\partial q_{A_k}} T_i \right) d\Gamma + \int_\Omega \left(\rho b_i \frac{\partial u_i}{\partial q_{A_k}} \right) d\Omega - \int_\Omega \left(\frac{\partial \varepsilon_{ij}}{\partial q_{A_k}} \sigma_{ij} \right) d\Omega = 0 \tag{3.31}$$

For convenience, Voigt notation will be used from this point forward to represent the

strain and stress tensors as follows

$$\varepsilon_\alpha = \begin{pmatrix} \varepsilon_{11} \\ \varepsilon_{22} \\ \varepsilon_{33} \\ \gamma_{23} = 2\,\varepsilon_{23} \\ \gamma_{31} = 2\,\varepsilon_{31} \\ \gamma_{12} = 2\,\varepsilon_{12} \end{pmatrix}, \qquad \sigma_\alpha = \begin{pmatrix} \sigma_{11} \\ \sigma_{22} \\ \sigma_{33} \\ \sigma_{23} \\ \sigma_{31} \\ \sigma_{12} \end{pmatrix} \tag{3.32}$$

Greek subscripts will be utilized as the indices in matrices and vectors expressed using Voigt notation. This notation simplifies the formation of the strain-displacement matrix, $B_{\alpha A_i}$, which is defined through the kinematic relationship defining strain in Eq. (3.9) in conjunction with the Galerkin approximation for displacement of Eq. (3.26).

$$B_{\alpha A_i} = \frac{\partial \varepsilon_\alpha}{\partial q_{A_i}} = \left(\begin{array}{ccc|c|ccc} \frac{\partial \psi^{(1)}}{\partial x_1} & 0 & 0 & & \frac{\partial \psi^{(n)}}{\partial x_1} & 0 & 0 \\ 0 & \frac{\partial \psi^{(1)}}{\partial x_2} & 0 & & 0 & \frac{\partial \psi^{(n)}}{\partial x_2} & 0 \\ 0 & 0 & \frac{\partial \psi^{(1)}}{\partial x_3} & & 0 & 0 & \frac{\partial \psi^{(n)}}{\partial x_3} \\ 0 & \frac{\partial \psi^{(1)}}{\partial x_2} & \frac{\partial \psi^{(1)}}{\partial x_3} & \cdots & 0 & \frac{\partial \psi^{(n)}}{\partial x_2} & \frac{\partial \psi^{(n)}}{\partial x_3} \\ \frac{\partial \psi^{(1)}}{\partial x_1} & 0 & \frac{\partial \psi^{(1)}}{\partial x_3} & & \frac{\partial \psi^{(n)}}{\partial x_1} & 0 & \frac{\partial \psi^{(n)}}{\partial x_3} \\ \frac{\partial \psi^{(1)}}{\partial x_1} & \frac{\partial \psi^{(1)}}{\partial x_2} & 0 & & \frac{\partial \psi^{(n)}}{\partial x_1} & \frac{\partial \psi^{(n)}}{\partial x_2} & 0 \end{array}\right) \tag{3.33}$$

The strain displacement matrix is used to calculate strains based on the element displacement vector by

$$\varepsilon_\alpha = B_{\alpha A_i} q_{A_i} \tag{3.34}$$

This results in the final term of Eq. (3.31) taking the form

$$\int_\Omega \left(B_{\alpha A_i} \sigma_\alpha\right) d\Omega \tag{3.35}$$

Furthermore, through the constitutive relationship of Eq. (3.10) the stress tensor can be represented in the following manner

$$\sigma_\alpha = C_{\alpha\beta}\varepsilon_\beta = C_{\alpha\beta}B_{\beta A_i}q_{A_i} \tag{3.36}$$

Incorporating Eq. (3.36) into Eq. (3.35) leads to the formation of the familiar element stiffness matrix in the following manner

$$\begin{aligned}\int_{\Omega_e}\left(B_{\alpha A_i}\sigma_\alpha\right)d\Omega_e &= \int_{\Omega_e}\left(B_{\alpha A_i}C_{\beta\alpha}B_{\beta B_j}q_{B_j}\right)d\Omega_e \\ &= \int_{\Omega_e}\left(B_{\alpha A_i}C_{\beta\alpha}B_{\beta B_j}\right)d\Omega_e\, q_{B_j} \\ &= K_{A_iB_j}q_{B_j}\end{aligned} \tag{3.37}$$

or, in matrix form (with boldface representing a matrix or vector),

$$\int_{\Omega_e}\left(\boldsymbol{B}^{\mathrm{T}}\sigma\right)d\Omega_e = \int_{\Omega_e}\left(\boldsymbol{B}^{\mathrm{T}}\boldsymbol{C}\boldsymbol{B}\mathbf{q}\right)d\Omega_e = \int_{\Omega_e}\left(\boldsymbol{B}^{\mathrm{T}}\boldsymbol{C}\boldsymbol{B}\right)d\Omega_e\,\mathbf{q} = \boldsymbol{K}\mathbf{q} \tag{3.38}$$

The subscript e signifies that the integral is taken over the domain of a single element. The partial derivative of the displacement field with respect to the nodal displacements which appears in the remaining terms of Eq. (3.31) can be expressed using a method similar to Eq. (3.33).

$$\frac{\partial u_k}{\partial q_{A_i}} = \left(\begin{array}{ccc|c|ccc|c|ccc} \psi^{(1)} & 0 & 0 & & \psi^{(A)} & 0 & 0 & & \psi^{(n)} & 0 & 0 \\ 0 & \psi^{(1)} & 0 & \cdots & 0 & \psi^{(A)} & 0 & \cdots & 0 & \psi^{(n)} & 0 \\ 0 & 0 & \psi^{(1)} & & 0 & 0 & \psi^{(A)} & & 0 & 0 & \psi^{(n)} \end{array}\right) \tag{3.39}$$

This leads to the creation of the element force vector as follows

$$
\begin{aligned}
f_{A_i} &= \int_{\Gamma_e} \left(T_k \frac{\partial u_k}{\partial q_{A_i}} \right) d\Gamma_e + \int_{\Omega_e} \left(\rho b_k \frac{\partial u_k}{\partial q_{A_i}} \right) d\Omega_e \\
&= \begin{pmatrix}
\int_{\Gamma_e} \left(T_1 \psi^{(1)} \right) d\Gamma_e + \int_{\Omega_e} \left(\rho b_1 \psi^{(1)} \right) d\Omega_e \\
\int_{\Gamma_e} \left(T_2 \psi^{(1)} \right) d\Gamma_e + \int_{\Omega_e} \left(\rho b_2 \psi^{(1)} \right) d\Omega_e \\
\int_{\Gamma_e} \left(T_3 \psi^{(1)} \right) d\Gamma_e + \int_{\Omega_e} \left(\rho b_3 \psi^{(1)} \right) d\Omega_e \\
\vdots \\
\int_{\Gamma_e} \left(T_1 \psi^{(A)} \right) d\Gamma_e + \int_{\Omega_e} \left(\rho b_1 \psi^{(A)} \right) d\Omega_e \\
\int_{\Gamma_e} \left(T_2 \psi^{(A)} \right) d\Gamma_e + \int_{\Omega_e} \left(\rho b_2 \psi^{(A)} \right) d\Omega_e \\
\int_{\Gamma_e} \left(T_3 \psi^{(A)} \right) d\Gamma_e + \int_{\Omega_e} \left(\rho b_3 \psi^{(A)} \right) d\Omega_e \\
\vdots \\
\int_{\Gamma_e} \left(T_1 \psi^{(n)} \right) d\Gamma_e + \int_{\Omega_e} \left(\rho b_1 \psi^{(n)} \right) d\Omega_e \\
\int_{\Gamma_e} \left(T_2 \psi^{(n)} \right) d\Gamma_e + \int_{\Omega_e} \left(\rho b_2 \psi^{(n)} \right) d\Omega_e \\
\int_{\Gamma_e} \left(T_3 \psi^{(n)} \right) d\Gamma_e + \int_{\Omega_e} \left(\rho b_3 \psi^{(n)} \right) d\Omega_e
\end{pmatrix}
\end{aligned}
\tag{3.40}
$$

Eq. (3.37) and Eq. (3.40) allow the weak formulation of Eq. (3.31) to be expressed for an element in the familiar form of a linear system of equations

$$
\boldsymbol{K}\mathbf{q} = \mathbf{f} \tag{3.41}
$$

III.A.4. Element Formulations

III.A.4.a. Basis Functions

Recall from Eq. (3.26) that the displacement throughout an element is determined by summing the products of the nodal displacements and their corresponding basis functions. The formation of basis functions for an element is critical to its computation. Generally, a basis function for a node is formed such that it possesses

a value of unity at that node and a value of zero at all other nodes. For these elements, the basis functions will be in the form of polynomials. This will allow their integration using quadrature rules described in later subsections.

Although elements can assume non-regular shapes in the problem domain described in the global coordinates (x_1, x_2, x_3), the shape function formulations will be calculated in the master element coordinate system defined by (ξ_1, ξ_2, ξ_3), in which the element assumes a structured shape and extends across a pre-determined domain (e.g., from -1 to 1 in all coordinate directions for a hexahedron). The various analyses in this work utilize 20 node hexahedral, 15 node wedge, 8 node qudrilateral, and 6 node triangular element formulations. The topologies of these elements are shown in Fig. III.1. These elements are referred to as serendipity elements because they are quadratic elements in which all the nodes exist on edges (as opposed to the Lagrange family of elements which possess internal and mid-face nodes). Being quadratic, the basis functions are 2nd order polynomials of the spatial coordinates. The approach for developing the basis functions for the 20 node element are now described. For the first node, which possesses coordinates $(-1, -1, -1)$, it is desired to construct a basis function with a value of unity at node 1 and a value of zero at all other nodes. Therefore, the basis function for node 1 should vanish on the planes defined by the following functions.

$$\begin{aligned}
\xi_1 - 1 &= 0 \quad \text{(nodes 13, 14, 15, 16, 17, 18, 19, and 20)} \\
\xi_2 - 1 &= 0 \quad \text{(nodes 3, 4, 5, 10, 11, 15, 16, and 17)} \\
\xi_3 - 1 &= 0 \quad \text{(nodes 5, 6, 7, 11, 12, 17, 18, and 19)} \\
\xi_1 + \xi_2 + \xi_3 + 2 &= 0 \quad \text{(nodes 2, 8, and 9)}
\end{aligned} \tag{3.42}$$

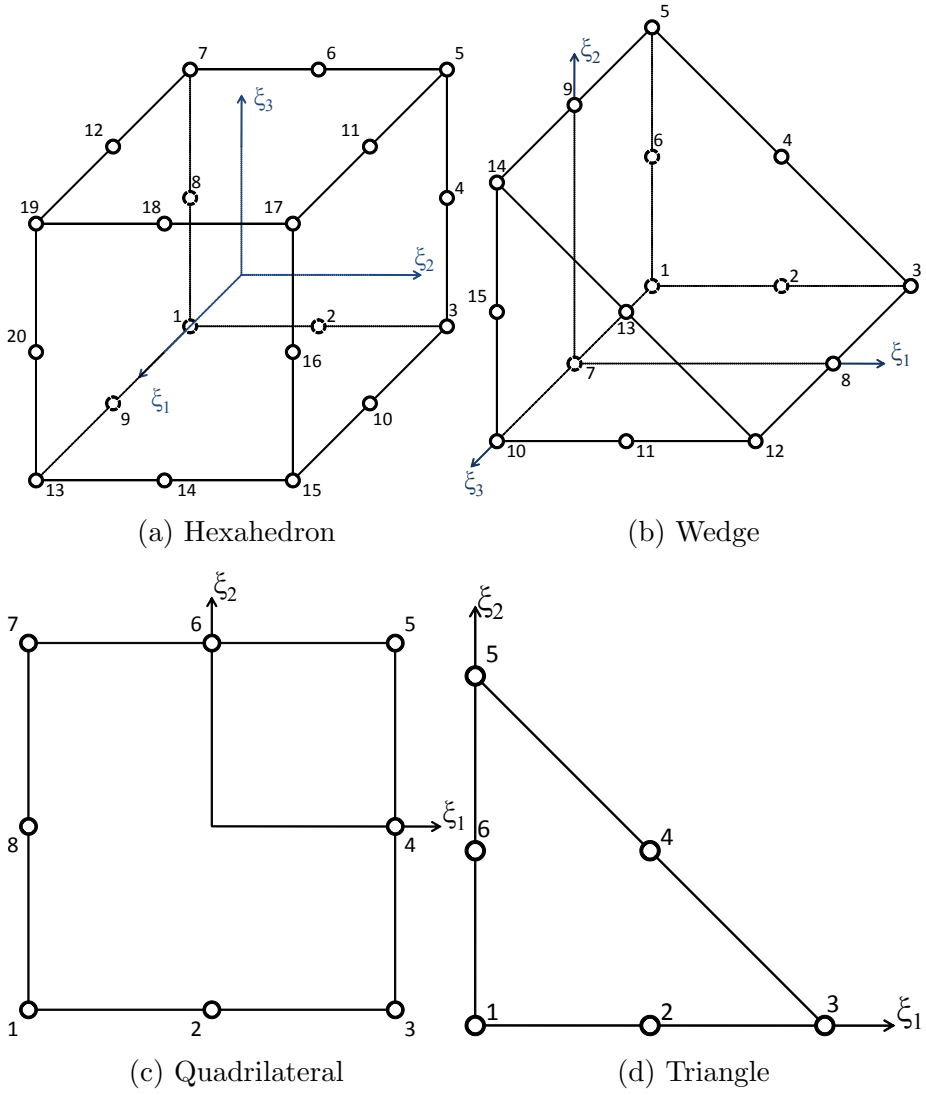

Figure III.1: Various element topologies.

This yields a function of the following form

$$\psi^{(1)}(\xi_1,\xi_2,\xi_3) = C(\xi_1-1)(\xi_2-1)(\xi_3-1)(\xi_1+\xi_2+\xi_3+2) \tag{3.43}$$

It is desired that $\psi^{(1)}$ have a value of unity at node 1, resulting in

$$\psi^{(1)}(\xi_1,\xi_2,\xi_3) = \frac{1}{8}(\xi_1-1)(\xi_2-1)(\xi_3-1)(\xi_1+\xi_2+\xi_3+2) \tag{3.44}$$

This convention can be followed for the remainder of the nodes, yielding the following set of basis functions for the master hexahedral quadratic serendipity element.

$$\begin{aligned}
\psi^{(1)} &= \tfrac{1}{8}(\xi_1-1)(\xi_2-1)(\xi_3-1)(\xi_1+\xi_2+\xi_3+2)\\
\psi^{(2)} &= -\tfrac{1}{4}(\xi_1-1)\left(\xi_2^2-1\right)(\xi_3-1)\\
\psi^{(3)} &= \tfrac{1}{8}(\xi_1-1)(\xi_2+1)(\xi_3-1)(-\xi_1+\xi_2-\xi_3-2)\\
\psi^{(4)} &= \tfrac{1}{4}(\xi_1-1)(\xi_2+1)\left(\xi_3^2-1\right)\\
\psi^{(5)} &= \tfrac{1}{8}(\xi_1-1)(\xi_2+1)(\xi_3+1)(\xi_1-\xi_2-\xi_3+2)\\
\psi^{(6)} &= \tfrac{1}{4}(\xi_1-1)\left(\xi_2^2-1\right)(\xi_3+1)\\
\psi^{(7)} &= \tfrac{1}{8}(\xi_1-1)(\xi_2-1)(\xi_3+1)(-\xi_1-\xi_2+\xi_3-2)\\
\psi^{(8)} &= -\tfrac{1}{4}(\xi_1-1)(\xi_2-1)\left(\xi_3^2-1\right)\\
\psi^{(9)} &= -\tfrac{1}{4}\left(\xi_1^2-1\right)(\xi_2-1)(\xi_3-1)\\
\psi^{(10)} &= \tfrac{1}{4}\left(\xi_1^2-1\right)(\xi_2+1)(\xi_3-1)\\
\psi^{(11)} &= -\tfrac{1}{4}\left(\xi_1^2-1\right)(\xi_2+1)(\xi_3+1)\\
\psi^{(12)} &= \tfrac{1}{4}\left(\xi_1^2-1\right)(\xi_2-1)(\xi_3+1)\\
\psi^{(13)} &= \tfrac{1}{8}(\xi_1+1)(\xi_2-1)(\xi_3-1)(\xi_1-\xi_2-\xi_3-2)\\
\psi^{(14)} &= \tfrac{1}{4}(\xi_1+1)\left(\xi_2^2-1\right)(\xi_3-1)\\
\psi^{(15)} &= \tfrac{1}{8}(\xi_1+1)(\xi_2+1)(\xi_3-1)(-\xi_1-\xi_2+\xi_3+2)\\
\psi^{(16)} &= -\tfrac{1}{4}(\xi_1+1)(\xi_2+1)\left(\xi_3^2-1\right)\\
\psi^{(17)} &= \tfrac{1}{8}(\xi_1+1)(\xi_2+1)(\xi_3+1)(\xi_1+\xi_2+\xi_3-2)\\
\psi^{(18)} &= -\tfrac{1}{4}(\xi_1+1)\left(\xi_2^2-1\right)(\xi_3+1)\\
\psi^{(19)} &= \tfrac{1}{8}(\xi_1+1)(\xi_2-1)(\xi_3+1)(-\xi_1+\xi_2-\xi_3+2)\\
\psi^{(20)} &= \tfrac{1}{4}(\xi_1+1)(\xi_2-1)\left(\xi_3^2-1\right)
\end{aligned} \tag{3.45}$$

The basis functions for the serendipity wedge element are given by

$$\begin{aligned}
\psi^{(1)} &= -\tfrac{1}{2}\,(\xi_3-1)\,(\xi_1+\xi_2-1)\,(2\,\xi_1+2\,\xi_2+\xi_3)\\
\psi^{(2)} &= 2\,\xi_1\,(\xi_3-1)\,(\xi_1+\xi_2-1)\\
\psi^{(3)} &= -\tfrac{1}{2}\,\xi_1\,(\xi_3-1)\,(2\,\xi_1-\xi_3-2)\\
\psi^{(4)} &= -2\,\xi_1\,\xi_2\,(\xi_3-1)\\
\psi^{(5)} &= -\tfrac{1}{2}\,\xi_2\,(\xi_3-1)\,(2\,\xi_2-\xi_3-2)\\
\psi^{(6)} &= 2\,\xi_2\,(\xi_3-1)\,(\xi_1+\xi_2-1)\\
\psi^{(7)} &= (\xi_3-1)\,(\xi_3+1)\,(\xi_1+\xi_2-1)\\
\psi^{(8)} &= -\xi_1\,(\xi_3-1)\,(\xi_3+1)\\
\psi^{(9)} &= -\xi_2\,(\xi_3-1)\,(\xi_3+1)\\
\psi^{(10)} &= \tfrac{1}{2}\,(\xi_3+1)\,(\xi_1+\xi_2-1)\,(2\,\xi_1+2\,\xi_2-\xi_3)\\
\psi^{(11)} &= -2\,\xi_1\,(\xi_3+1)\,(\xi_1+\xi_2-1)\\
\psi^{(12)} &= \tfrac{1}{2}\xi_1\,(\xi_3+1)\,(2\xi_1+\xi_3-2)\\
\psi^{(13)} &= 2\,\xi_1\,\xi_2\,(\xi_3+1)\\
\psi^{(14)} &= \tfrac{1}{2}\,\xi_2\,(\xi_3+1)\,(2\,\xi_2+\xi_3-2)\\
\psi^{(15)} &= -2\,\xi_2\,(\xi_3+1)\,(\xi_1+\xi_2-1)
\end{aligned} \tag{3.46}$$

III.A.4.b. Spatial Mapping

The integrations of Eq. (3.37) are performed using Gaussian Quadrature. To simplify the procedure by which the quadrature will be applied, it will be applied over the master element's domain, rather than the domain of the element in actual physical space. This master domain is mapped to an element's physical domain by the following formula

$$x_i\,(\xi_j) = \sum_{A=1}^{n} x_i^{(A)} \psi^{(A)}\,(\xi_j) \tag{3.47}$$

$x_i^{(A)}$ represents the physical coordinate of the A^{th} node of the element, and $x_i\,(\xi_j)$ is the coordinate in physical space that maps to the master coordinate ξ_j. Note that

this formulation is isoparametric, that is to say the spatial approximation over the element matches the approximation of the displacement over the element.

Because of this coordinate transformation, it will be necessary to obtain the jacobian matrix $\boldsymbol{J}$ for the coordinate transformation between the physical coordinate system x_i and the master coordinate system ξ_i. The jacobian is defined by the equation

$$\boldsymbol{J} = \frac{\partial x_i}{\partial \xi_j} \tag{3.48}$$

The derivatives which form the Jacobian can be calculated using the basis functions and nodal coordinates from Eq. 3.47 through

$$\frac{\partial x_i}{\partial \xi_j} = \sum_{A=1}^{n} x_i^{(A)} \frac{\partial \psi^{(A)}}{\partial \xi_j} \tag{3.49}$$

The transformation of a differential volume dV in the physical element domain Ω_e to the master element domain $\hat{\Omega}_e$ is accomplished through the use of the Jacobian's determinant as follows

$$dV = dx_1 dx_2 dx_3 = |\boldsymbol{J}| \, d\xi_1 d\xi_2 d\xi_3 \tag{3.50}$$

It can be noted from Eq. (3.33) and Eq. (3.37) that the calculation of the element stiffness matrix requires evaluating the partial derivatives of the basis functions with respect to the physical coordinate system over the volume of the element. This presents a difficulty due to the fact that the basis functions are defined in terms of the element's master coordinate system. Through the chain rule, the derivatives of the basis functions in the physical coordinates system can be expressed in terms of the derivatives in the master coordinate system.

$$\frac{\partial \psi^{(A)}}{\partial x_i} = \frac{\partial \xi_j}{\partial x_i} \frac{\partial \psi^{(A)}}{\partial \xi_j} \tag{3.51}$$

Unfortunately, it is not generally possible to develop a closed form expression for $\frac{\partial \xi_j}{\partial x_i}$, the partial derivatives of the master coordinates with respect to the physical coordinates. However, this relationship can be obtained by inverting the jacobian matrix to obtain $\boldsymbol{J^{-1}}$.

$$\frac{\partial \xi_j}{\partial x_i} = \left(\frac{\partial x_i}{\partial \xi_j} \right)^{-1} \tag{3.52}$$

Note that for the inversion of the Jacobian to be possible, its determinant must not be zero at any point in the element.

III.A.4.c. Numerical Integration

With a method for obtaining the derivatives of the basis functions with respect to physical coordinates, it is now possible to perform the stiffness matrix integration of Eq. (3.37) over the master domain using Gaussian Quadrature. Gaussian quadrature is based on the principle that the following relationship is exact for polynomials $f(\eta)$ of degree $2n-1$ or less, provided an appropriate selection of points η_i and weights w_i.

$$\int_{-1}^{1} f(\eta)\, dx \approx \sum_{i=1}^{n} w_i f(\eta_i) \tag{3.53}$$

The selection of points η_i and weights w_i is conducted using Legendre polynomials $P_n(\eta)$. These polynomials are given by the following equation

$$P_n(\eta) = \frac{1}{2^n n!} \frac{d^n}{d\eta^n} \left(\left(\eta^2 - 1 \right)^n \right) \tag{3.54}$$

To start, $P_n(\eta)$ is normalized to give $P_n(1) = 1$. Point η_i is the i^{th} root of $P_n(\eta)$. The weight is given by the following relation.

$$w_i = \frac{2}{\left(1 - \eta_i^2\right) \left(P_n'(\eta_i) \right)^2} \tag{3.55}$$

Table III.2: Points η_i and weights w_i for various orders of Gaussian quadrature

n	η_i	w_i
1	0	2
2	$\pm\sqrt{1/3}$	1
3	0	$\frac{8}{9}$
	$\pm\sqrt{3/5}$	$\frac{5}{9}$
4	$\pm\sqrt{\left(3-2\sqrt{6/5}\right)/7}$	$\frac{18+\sqrt{30}}{36}$
	$\pm\sqrt{\left(3+2\sqrt{6/5}\right)/7}$	$\frac{18-\sqrt{30}}{36}$

Table III.2 gives the points and weights for a number for different quadrature schemes. Integration over three dimensions is simply the result of multiple one dimensional integrations, where the points are simply tensor-products of the one dimensional formulation. The integral of Eq. (3.37) is transformed to the master domain for evaluation, resulting in

$$\begin{aligned}\boldsymbol{K} &= \int_{\Omega_e} \left(\boldsymbol{B}^{\mathrm{T}}\boldsymbol{C}\boldsymbol{B}\right) dV \\ &= \int_{\hat{\Omega}_e} \left(\boldsymbol{B}^{\mathrm{T}}\boldsymbol{C}\boldsymbol{B}\right) dV \\ &= \int_{-1}^{1}\int_{-1}^{1}\int_{-1}^{1} \left(\boldsymbol{B}^{\mathrm{T}}\boldsymbol{C}\boldsymbol{B}\right) |\boldsymbol{J}|\, d\xi_1\, d\xi_2\, d\xi_3\end{aligned} \tag{3.56}$$

where $\hat{\Omega}_e$ is the master domain of the element and $|\boldsymbol{J}|$ is the determinant of the Jacobian matrix. One final step remains to permit the integration of the element stiffness matrix. The strain-displacement matrix $\boldsymbol{B}$ of Eq. (3.33) contains the spatial

derivative of the basis functions $\psi^{(A)}$ with respect to the physical coordinates, but the basis functions are defined in terms of the master coordinates. Therefore, the elements of $\boldsymbol{B}$ must undergo the following transformation outlined in Eq. (3.51), that is

$$\frac{\partial \psi^{(A)}}{\partial x_i} = J_{ij}^{-1} \frac{\partial \psi^{(A)}}{\partial \xi_j} \tag{3.57}$$

where ξ_i is the master coordinate system.

Finally , the element force vector is calculated by transforming the integration of Eq. (3.40) to the master domain as follows

$$\begin{aligned} f_{A_i} &= \int_{\Gamma_e} \left(T_k \frac{\partial u_k}{\partial q_{A_i}} \right) d\Gamma_e + \int_{\Omega_e} \left(\rho b_k \frac{\partial u_k}{\partial q_{A_i}} \right) d\Omega_e \\ &= \int_{\hat{\Gamma}_e} \left(T_k \frac{\partial u_k}{\partial q_{A_i}} \right) |\boldsymbol{J}| d\hat{\Gamma}_e + \int_{\hat{\Omega}_e} \left(\rho b_k \frac{\partial u_k}{\partial q_{A_i}} \right) |\boldsymbol{J}| d\hat{\Omega}_e \end{aligned} \tag{3.58}$$

The element stiffness matrices and force vectors for all elements of the model are then combined through the process of assembly into a global system which is solved for nodal displacements using any number of schemes for solving symmetric-positive-definite linear systems.

III.A.5. Post-processing

Once nodal displacements are determined, the displacement at any location in an element can be calculated from the nodal displacements for that element via the Galerkin approximation by

$$u_i = \sum_{A=1}^{n} u_i^{(A)} \psi^{(A)} \tag{3.59}$$

These displacements can now be used to calculate strain by the relationship specified in Eq. (3.34). It ends up that the error reaches a minimum at the points used for Gaussian quadrature, so strain is calculated at these locations. Once strain has

been calculated at a point, the stress at that point can be determined using the constitutive relationship of Eq. (3.10). These quadrature point stresses are used to examine failure criteria at the quadrature points. For plotting field data which is calculated at quadrature points, the field values are extrapolated to the nodes of the element. Then, nodal averages are taken between adjacent elements with the same material. Discontinuities are generally permitted across material interfaces, meaning that nodes on interfaces generally possess one value of the field variable for each material type with a boundary at that node. These nodal averaged field values are then used to generate a contour plot visualizing the field.

III.B. 3D Interfacial Element Formulation

The following sections describe the formulation of the interfacial element. The formulation is split into three parts. The first outlines the procedure for determining the orientation of the interface. The second describes the development of the element stiffness matrix. The third describes the procedure for performing integration over the element's domain.

III.B.1. Determination of Interfacial Orientation

An interfacial element is an element with zero thickness initially that interpolates a jump in the solution field. In the current studies, this is the displacement field. Since this field has direction, it will be necessary to distinguish between the normal and tangential components of the displacement jump across the interface. This requires the determination of unit vectors which are normal and tangential to the

interface, illustrated in Fig. III.2. This determination is complicated by the lower dimensionality of the interfacial element (2D) as compared to the solution space of the finite element problem (3D) in the sense that the local element directions expressed in the global coordinates cannot be simply found by inverting the jacobian matrix for the element. Instead, the following procedure is used.

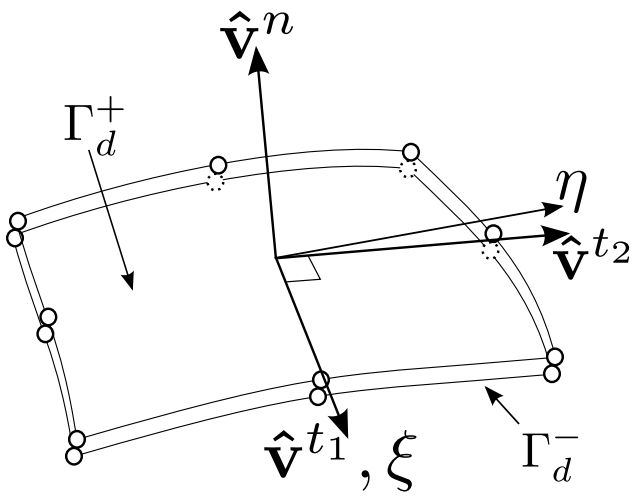

Figure III.2: Interfacial element.

The two local element coordinate directions, expressed in the three global coordinate directions, can be expressed in the manner of Eq. 3.60, where x_i are the global coordinates and ξ and η are the the local element coordinates.

$$v_i^{\xi} = \frac{\partial x_i}{\partial \xi} \qquad v_i^{\eta} = \frac{\partial x_i}{\partial \eta} \tag{3.60}$$

The derivatives of the global coordinates with respect to the local element coordinates at a point on the element can be determined from the interpolation functions using

Eq. 3.61, where $\psi^{(A)}$ is the shape function for node A and X_{A_i} is the global coordinate of node A (summation over A is implied).

$$\frac{\partial x_i}{\partial \xi} \approx X_{A_i} \frac{\partial \psi^{(A)}}{\partial \xi} \tag{3.61}$$

While v_i^{ξ} and v_i^{η} are not generally orthogonal to one another, they will not be parallel unless the element is ill-shaped. They both possess the quality of being tangential to the interface. Therefore, the local unit normal vector to the interface is obtained from the cross-product of these tangential vectors as given in Eq. 3.62.

$$\hat{\mathbf{v}}^n = \frac{\mathbf{v}^{\xi} \times \mathbf{v}^{\eta}}{\|\mathbf{v}^{\xi} \times \mathbf{v}^{\eta}\|} \tag{3.62}$$

Unit vectors which are mutually orthogonal and tangential to the interface are determined from the local ξ direction and a vector which is orthogonal to both the local ξ direction and $\hat{\mathbf{v}}^n$ as shown in Eqs. 3.63 and 3.64.

$$\hat{\mathbf{v}}^{t_1} = \frac{\mathbf{v}^{\xi}}{\|\mathbf{v}^{\xi}\|} \tag{3.63}$$

$$\hat{\mathbf{v}}^{t_2} = \hat{\mathbf{v}}^n \times \hat{\mathbf{v}}^{t_1} \tag{3.64}$$

The three unit vectors $\hat{\mathbf{v}}^n$, $\hat{\mathbf{v}}^{t_1}$, and $\hat{\mathbf{v}}^{t_2}$ form the direction cosine matrix given in Eq. 3.65. This direction cosine matrix will transform the displacement jump vector (as well as tractions) expressed in the global coordinate system so that they are expressed in an interface-aligned frame, with the first component being normal to the interface and the second and third components being tangential.

$$Q_{ij} = \begin{bmatrix} \hat{v}_1^n & \hat{v}_2^n & \hat{v}_3^n \\ \hat{v}_1^{t_1} & \hat{v}_2^{t_1} & \hat{v}_3^{t_1} \\ \hat{v}_1^{t_2} & \hat{v}_2^{t_2} & \hat{v}_3^{t_2} \end{bmatrix} \tag{3.65}$$

III.B.2. Calculation of the Element Stiffness Matrix

The calculation of the element stiffness matrix for interfacial elements is analogous in many ways to the process of defining the stiffness matrix for a fully 3D element. First, a "B" matrix is developed which transforms nodal displacements into values at points in the element that are compatible with the constitutive law. For interfacial elements, this is a traction-separation relationship, and so nodal displacements must be transformed into opening displacements resolved into the interfacial coordinate system. the "B" matrix for an interfacial element is therefore defined according to Eq. 3.66.

$$\bar{B}_{iA_j} = Q_{ij}\bar{\psi}_A \tag{3.66}$$

The value $\bar{\psi}_A$ is a shape function defined especially for interfacial elements depending on what face of the element the node is on (see Fig. III.2) according to Eq. 3.67.

$$\bar{\psi}_A = \begin{cases} \psi_A & A \in \Gamma_d^+ \\ -\psi_A & A \in \Gamma_d^- \end{cases} \tag{3.67}$$

The element stiffness matrix is subsequently defined in terms of the interfacial stiffness as in Eq. 3.68, where D_{mn} relates the interfacial opening displacement to the traction.

$$K_{A_iB_j} = \int_{\Gamma_d} \bar{B}_{mA_i} D_{mn} \bar{B}_{nB_j} dA \tag{3.68}$$

III.B.3. Numerical Integration

The integration for the stiffness matrix is one dimension less than the domain of the finite element model. This means that the traditional approach for numerical integration of using the determinant of the jacobian to perform the integration in

the element domain is not applicable to cohesive elements. Instead, the following approach is used. A differential area on an element in the model space is obtained by taking the cross-product of two differential vectors aligned with the element coordinates given in Eq. 3.69.

$$dA = \left\| d\mathbf{S}^1 \times d\mathbf{S}^2 \right\| \tag{3.69}$$

The variables $d\mathbf{S}^1$ and $d\mathbf{S}^2$ are aligned with the element's ξ and η coordinates, respectively, and are both expressed in the global coordinate system. In a similar fashion to equation 3.60, these can be expressed in terms of partial derivatives of the global coordinates with respect to the local coordinates. Thus, equation 3.69 can be expressed as Eq. 3.70, using the permutation tensor ϵ_{ijk} to represent the cross product.

$$dA = \left\| \epsilon_{ijk} \frac{\partial x_i}{\partial \xi} d\xi \frac{\partial x_j}{\partial \eta} d\eta \right\| \tag{3.70}$$

Expanding Eq. 3.70 yields the following differential area to be substituted in for the differential area in the integral of Eq. 3.68.

$$dA = \left(\sqrt{\begin{array}{l} \left(\dfrac{\partial x_2}{\partial \xi}\dfrac{\partial x_3}{\partial \eta} - \dfrac{\partial x_3}{\partial \xi}\dfrac{\partial x_2}{\partial \eta} \right)^2 + \\ \left(\dfrac{\partial x_3}{\partial \xi}\dfrac{\partial x_1}{\partial \eta} - \dfrac{\partial x_1}{\partial \xi}\dfrac{\partial x_3}{\partial \eta} \right)^2 + \\ \left(\dfrac{\partial x_1}{\partial \xi}\dfrac{\partial x_2}{\partial \eta} - \dfrac{\partial x_2}{\partial \xi}\dfrac{\partial x_1}{\partial \eta} \right)^2 \end{array}} \right) d\xi \, d\eta \tag{3.71}$$

The partial derivatives in Eq. 3.71 can be evaluated using the element shape functions and nodal coordinates with Eq. 3.61. The integration of Eq. 3.68 can then be simply performed in the local element coordinates using an appropriate quadrature scheme. In the current work, the interfacial elements are integrated using a Newton-Cotes quadrature rule based on the recommendation of Turon et al. [135].

III.C. Cohesive Zone Formulation

The following sections describe the cohesive zone formulation used to govern opening of interfacial elements, as well as investigations that were made into the behavior of the cohesive zone model.

III.C.1. Adaptation of Turon's Cohesive Zone Model

The current work utilizes an adaptation of the cohesive zone formulation of Turon et al. [20]. Turon's formulation is for mixed-mode opening in three dimensions. It makes no distinction between modes II and III, and is based on a bilinear traction-separation law. Irreversibility is ensured through the use of a damage scalar d that increases monotonically from zero to one. This constitutive law relates the traction across the interface, τ, to the displacement jump across the interface $\boldsymbol{\Delta}$. For a given value of the damage scalar, the traction and displacement jump are related by Eq. 3.72.

$$\begin{Bmatrix} \tau_n \\ \tau_{t_1} \\ \tau_{t_2} \end{Bmatrix} = (1-d)\,K \begin{Bmatrix} \Delta_n \\ \Delta_{t_1} \\ \Delta_{t_2} \end{Bmatrix} - dK \begin{Bmatrix} M\left(-\Delta_n\right) \\ 0 \\ 0 \end{Bmatrix} \tag{3.72}$$

When no damage exists, the penalty stiffness K defines the traction-separation relationship. This parameter needs to be set high enough that no discernible opening occurs before the interface starts to degrade. In cases where the normal opening is negative (representing crack closure) crack closure is resisted through the use of the MacAulay operator $M\left(\bullet\right)$ which returns zero if an input value is negative. This

operator is defined in Eq. 3.73.

$$M(x) = \frac{1}{2}(x + |x|) \tag{3.73}$$

The evolution of the damage parameter is related to the maximum effective opening that the cohesive element has experienced. The effective opening λ is defined in Eq. 3.74

$$\lambda = \sqrt{(M(\Delta_n))^2 + (\Delta_s)^2} \tag{3.74}$$

Δ_s is the magnitude of the opening that is tangential to the interface, defined in Eq. 3.75.

$$\Delta_s = \sqrt{(\Delta_{t_1})^2 + (\Delta_{t_2})^2} \tag{3.75}$$

For opening displacements that are between the opening at which damage initiates (Δ^0), and the opening at which the interface has completely failed (Δ^f), the damage parameter is determined from the the monotonically increasing Eq. 3.76.

$$d(\lambda) = \frac{\Delta^f(\lambda - \Delta^0)}{\lambda(\Delta^f - \Delta^0)} \tag{3.76}$$

The damage parameter must be always increasing, so if Eq. 3.76 yields a value that is less than the current value of d at a given point of the cohesive surface (which could occur due to crack closure or a change in mode mix), then the larger value of d is used to calculate the traction. For effective openings less than the minimum opening for damage ($\lambda < \Delta^0$), the damage parameter is zero (unless the damage parameter previously had a value greater than zero). For effective openings in excess of the final effective opening ($\lambda > \Delta^f$), the damage parameter is 1.0 (i.e. the interface is completely failed). The resulting traction-separation relationship assumes a bi-linear form shown in Fig. III.3.

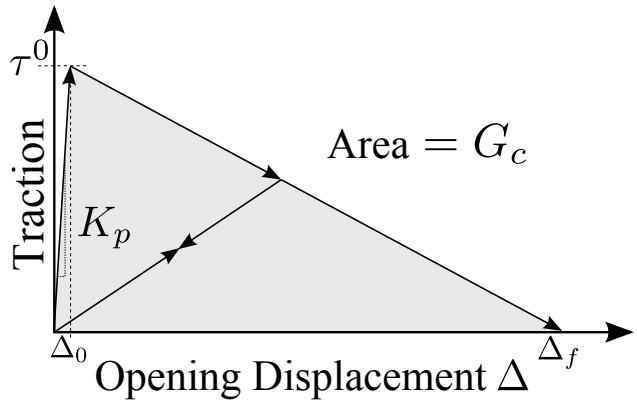

Figure III.3: Traction separation curve.

All that remains of the formulation is the determination of Δ^0 and Δ^f. These values depend on the material properties and the current mode ratio β for the opening displacement. The mode ratio is defined by Eq. 3.77.

$$\beta = \frac{\Delta_s}{\Delta_s + M\left(\Delta_n\right)} \tag{3.77}$$

The critical strain energy release rate under mixed-mode loading according to Turon is given by Eq. 3.78

$$G_c = G_{Ic} + \left(G_{IIc} - G_{Ic}\right)\left(\frac{G_s}{G_T}\right)^{\eta} \tag{3.78}$$

G_{Ic} and G_{IIc} are the critical strain energy release rates under pure mode I and mode II opening, respectively. η is a material parameter that is used to fit data from mixed-mode fracture testing. G_T is the total strain energy release rate, and G_s is the strain energy release rate associated with only mode II and mode III opening, as

shown in Eq. 3.79

$$\begin{aligned} G_T &= G_I + G_s \\ &= G_I + G_{II} + G_{III} \end{aligned} \tag{3.79}$$

It will be convenient to define the ratio between the shear strain energy release rate and the total strain energy release rate as B, defined in Eq. 3.80.

$$B = \frac{G_s}{G_T} \tag{3.80}$$

For a given mode mix, the area under the force-displacement curve is equal to the critical strain energy release rate for that mode mix, as given by Eq. 3.81

$$G_c = \frac{1}{2} K \Delta^0 \Delta^f \tag{3.81}$$

Combining Eqs. 3.81 and 3.78 gives an expression for the final crack opening Δ^f for a given mode mix, given in Eq. 3.82.

$$\Delta^f = \frac{\Delta_n^0 \Delta_n^f + \left(\Delta_s^0 \Delta_s^f - \Delta_n^0 \Delta_n^f\right) B^\eta}{\Delta^0} \tag{3.82}$$

Δ_n^0 and Δ_n^f are the initial and final crack openings associated with pure mode I loading, and Δ_s^0 and Δ_s^f are for pure mode II or III loading. The final opening displacements can be found using Eq. 3.83. The initial opening displacements are determined from K and the critical traction using based on the traction-separation curve (Fig. III.3).

$$\begin{aligned} \Delta_n^f &= \frac{2G_{Ic}}{K\Delta_n^0} \\ \Delta_s^f &= \frac{2G_{IIc}}{K\Delta_s^0} \end{aligned} \tag{3.83}$$

For a given mixed-mode ratio β, the normal and shear energy release rates are given

by the Eq. 3.84.

$$\begin{aligned} G_I &= \frac{1}{2} K \left(\Delta_n^0 (\beta) \, \Delta_n^f (\beta) - \Delta_n \Delta_n^f (\beta) \right) \\ G_s &= \frac{1}{2} K \left(\Delta_s^0 (\beta) \, \Delta_s^f (\beta) - \Delta_s \Delta_s^f (\beta) \right) \end{aligned} \tag{3.84}$$

$\Delta_n^0 (\beta)$ and $\Delta_s^0 (\beta)$ are the normal and shear displacement jumps, respectively, corresponding to decohesion onset for the given mixed-mode ratio β. Similarly, $\Delta_n^f (\beta)$ and $\Delta_s^f (\beta)$ correspond to displacement jumps at complete decohesion. From Eq. 3.77, the relations of Eq. 3.85.

$$\begin{aligned} \Delta_s &= \Delta_n \frac{\beta}{1-\beta} \\ \Delta_s^0 (\beta) &= \Delta_n^0 (\beta) \frac{\beta}{1-\beta} \\ \Delta_s^f (\beta) &= \Delta_n^f (\beta) \frac{\beta}{1-\beta} \end{aligned} \tag{3.85}$$

Combining Eqs. 3.79, 3.84, and 3.85 permits the ratio of strain energy release B to be expressed in terms of β as given in Eq. 3.86.

$$B = \frac{G_s}{G_T} = \frac{\beta^2}{1 + 2\beta^2 - 2\beta} \tag{3.86}$$

Next, the critical effective traction τ^0 (and consequently, the critical effective crack opening Δ^0) for a given mode mix must be determined. The critical effective traction is determined using the quadratic criterion of Eq. 3.87

$$\begin{aligned} \left(\tau^0\right)^2 &= \left(\tau_n\right)^2 + \left(\tau_{t_1}\right)^2 + \left(\tau_{t_2}\right)^2 \\ &= \left(\tau_n^0\right)^2 + \left(\left(\tau_s^0\right)^2 - \left(\tau_n^0\right)^2 \right) B^\eta \end{aligned} \tag{3.87}$$

τ_n^0 and τ_s^0 are the critical tractions under pure mode I or mode II/III opening, respectively. The critical effective crack opening is therefore given by Eq. 3.88.

$$\Delta^0 = \sqrt{\left(\Delta_n^0\right)^2 + \left(\left(\Delta_s^0\right)^2 - \left(\Delta_n^0\right)^2 \right) B^\eta} \tag{3.88}$$

The critical opening displacement under single-mode loading is given by Eq. 3.89.

$$\begin{aligned} \Delta_n^0 &= \frac{\tau_n^0}{K} \\ \Delta_s^0 &= \frac{\tau_s^0}{K} \end{aligned} \tag{3.89}$$

III.C.1.a. Cohesive Stiffness

For the purpose of determining the formation of the tangent modulus, indicial notation will be used. The 1 component will correspond to the direction normal to the fracture plane, and 2 and 3 will correspond to the tangential directions. The secant equation for calculating traction can be expressed as in Eq. 3.90.

$$\tau_i = D_{ij}\Delta_j \tag{3.90}$$

The secant modulus D_{ij} is defined in Eq. 3.91.

$$D_{ij} = \delta_{ij}K\left[1 - d\left(1 + \delta_{1j}\frac{\langle -\Delta_j \rangle}{\Delta_j}\right)\right] \tag{3.91}$$

Differentiation of Eq. 3.90 with respect to the opening displacement yields the tangent stiffness relationship given in Eq. 3.92. This is useful when calculating the incremental displacement for Newton-Raphson iterations.

$$\dot{\tau}_i = D_{ij}^{\tan}\dot{\Delta}_j$$

$$D_{ij}^{\tan} = \begin{cases} \left\{D_{ij} - K\left(1 + \delta_{1j}\frac{\langle -\Delta_j \rangle}{\Delta_j}\right)\left(1 + \delta_{i1}\frac{\langle -\Delta_i \rangle}{\Delta_i}\right)\frac{\Delta^f\Delta^0}{\Delta^f - \Delta^0}\frac{1}{\lambda^3}\Delta_i\Delta_j\right\}, \\ \qquad r < \lambda < \Delta^f \\ D_{ij}, \quad r > \lambda \text{ or } \Delta^f < \lambda \end{cases} \tag{3.92}$$

r is the effective opening displacement that when exceeded will result in additional damage according to Eq. 3.76.

III.C.2. Study of Cohesive Zone Behavior

The behavior of the cohesive zones were examined in several different contexts. The observed behaviors, and the adjustments that were made to the cohesive zone formulation due to the observed behaviors, are detailed in the following sections.

III.C.2.a. Double-Cantilevered Beam

The cohesive zone behavior was validated through the use of a model of a double cantilevered beam undergoing mode I opening, shown in Fig. III.4. The model was implemented in a Newton-Raphson type nonlinear finite element analysis. The model was found to exhibit good convergence behavior provided that the active cohesive process zone (i.e. the part of the cohesive zone in front of the crack tip which is undergoing partial opening) was adequately refined, meaning that the active zone was resolved by at least two elements. In Fig. III.4, the refinement is considerably greater than this. In cases where the mesh refinement was reduced, it was possible to obtain good convergence behavior by reducing the maximum traction for the cohesive zone as recommended by Turon et al. [135]. This resulted in an increase in the size of the active cohesive zone, resulting in its being adequately resolved by meshes with lower refinements.

While this approach works well for problems involving crack propagation, it introduces problems for the prediction of crack nucleation. Reducing the maximum traction reduces the stress at at which cracks will be predicted to nucleate. Since crack nucleation in composites exhibits a high sensitivity to stress, this approach will not be appropriate for predicting the initiation of failure in composites. There-

fore, a modification was made to the overall analysis executive. Instead of utilizing Newton-Raphson along with the tangent modulus to predict the increment in the solution, an alternative progressive failure approach was taken. The solution for the current loading and damage state was obtained using a full linear solve. The tractions in the cohesive elements were checked to determine if they exceeded the traction-separation curve shown in Fig. III.3. If the curve was exceeded, then the cohesive damage parameter at that location was increased. This "solve-check tractions-apply degradation" process was repeated iteratively for a given loading until no new degradation occurred, at which point the solution was considered to have converged for that loading.

One difficulty associated with this approach is that the degradation at a given location tends to approach its final value asymptotically. Therefore, determining the final degradation state in the model for a given loading requires a very large number of iterations. This difficulty is addressed by limiting the total number of possible values for the damage parameter to 500. Because the damage parameter's relationship to the effective opening is nonlinear (Eq. 3.76), the these 500 values are associated with 500 effective opening displacements equally spaced between Δ_0 and Δ_f (rather than 500 values of d equally spaced between 0 and 1).

The force-displacement behavior associated with crack opening for several different refinements (given as number of elements along the length x number of elements though half of the thickness) for both the Newton-Raphson approach and the alternative progressive failure approach are shown in Fig. III.5. In addition to this comparison between the force-displacement behavior, the strain energy release rates

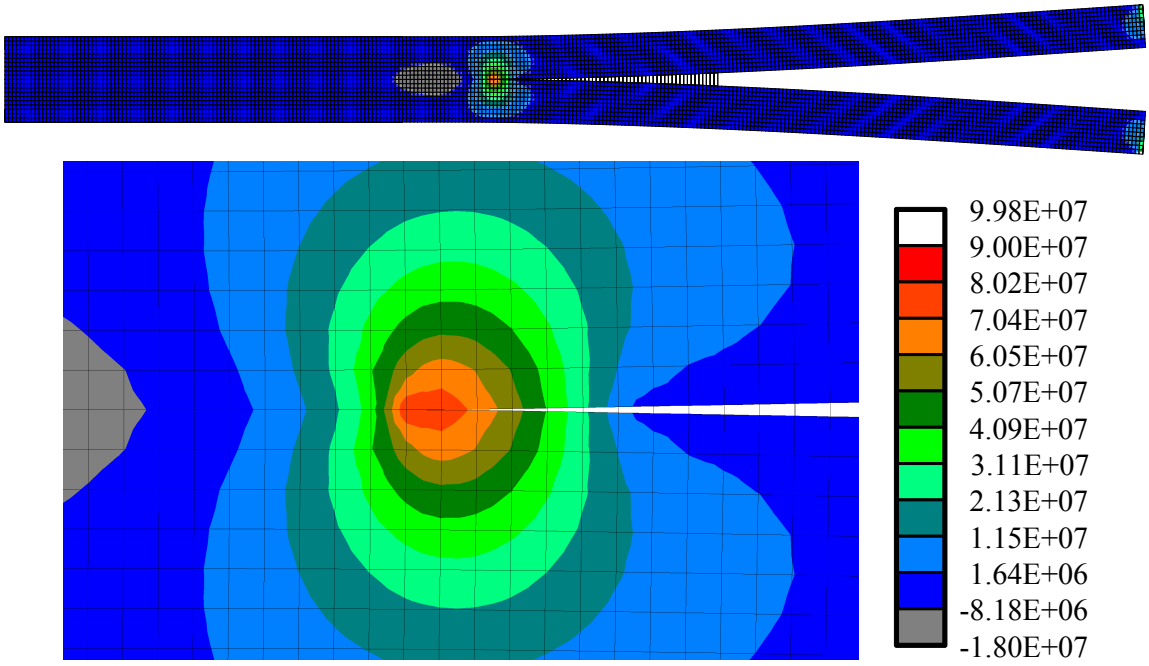

Figure III.4: Double cantilevered beam modeled using cohesive elements, with detail of cohesive process zone under opening.

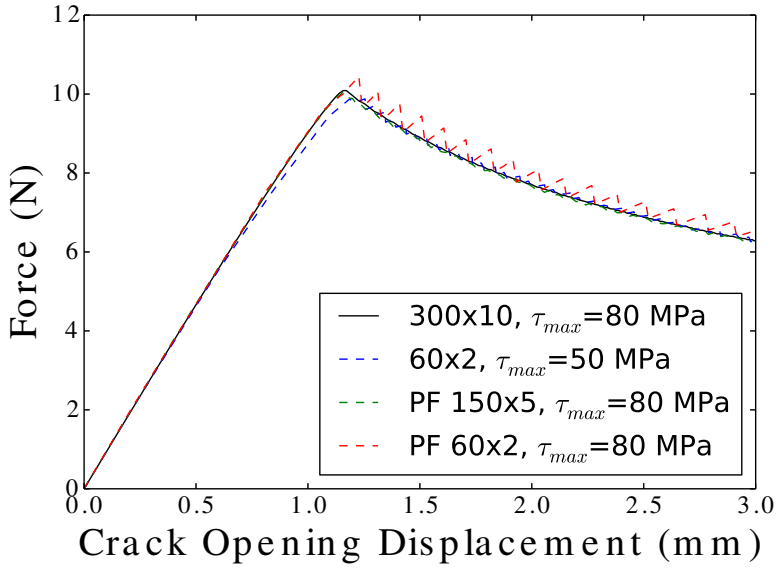

Figure III.5: Comparison of force-displacement for various refinements of double-cantilevered beam.

for crack growth in both models are in good agreement with the critical strain energy release rate input to the model as a parameter of the cohesive zones. One concern associated with specifying a finite number of values for the damage parameter is that this may reduce the strain energy associated with crack opening (since a cohesive element will not exactly follow the softening path given in Fig. III.3). However, this investigation into the behavior indicated that 500 different values are sufficient to prevent a reduction in the strain energy released under cohesive opening. Further study indicated that decreasing the number of possible values for the damage parameter (to 100 or less) did result in a reduction of the energy released by crack opening (as well as a modification in the force-displacement behavior).

III.C.2.b. Progressive Damage of a $[0/90]_s$ Tape Laminate

The next configuration which was examined was a $[0°/90°]_s$ laminate under uniaxial loading along the 0° direction. The expected behavior for this configuration is the occurrence of brittle matrix cracking in the 90° ply, with an increasing number of cracks as the load progressively increases. New crack development should favor regions that are far away from existing cracks, since the development of ply cracks will unload the ply in the regions immediately adjacent to the crack. This configuration is modeled by placing cohesive zone elements on the interface between plies to permit delamination and within the 90° ply to permit ply cracking. Cohesive elements were inserted between every other column of continuum elements in the ply. Each "column" of cohesive elements was assigned a maximum strength value from a Weibull distribution to promote localization of failure. This analysis utilized the progressive-failure type of model described previously.

The first configuration that was examined utilized cohesive parameters that had been determined from a double-cantilevered beam test of the composite which are given in [20]. The resulting response for crack opening is shown in Fig. III.6. As shown, this configuration resulted in partial opening of many of the cohesive zones in the 90° ply. The expected localization of failure was not obtained. The reason for this is that as the cohesive zones opened, the traction across them decreased more quickly than the maximum traction that they were able to support. As the cohesive zones open, they unload the surrounding material, reducing the stresses and tractions acting across the zones. However, cohesive opening also results in a reduction of the maximum traction that the cohesive zone can support, which is

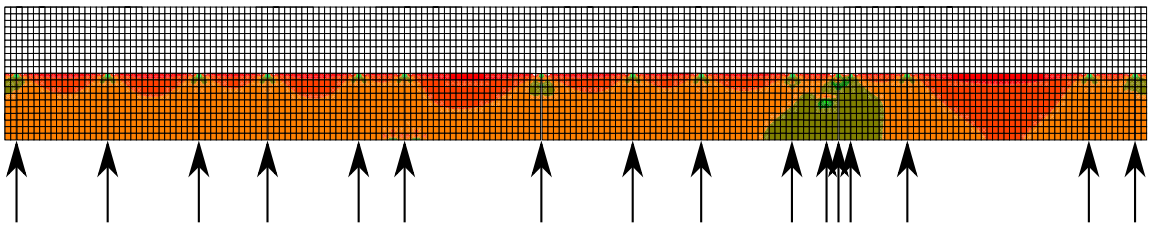

Figure III.6: Crack opening in cross-ply laminate with G_{Ic} from DCB data.

apparent in the traction-opening relationship shown in Fig. III.3. Since the traction across the zones decreases faster than the traction that they are able to support, they reach an equilibrium state at partial opening.

This gradual opening was not deemed to be particularly realistic. It has been widely observed (and will be further shown in later sections about the micromechanical failure behavior of composites) that matrix cracking in composites tends to be brittle in nature, which is quite different than the ductile opening shown in Fig. III.6. As discussed, this ductile behavior is the result of the value of the softening slope in the traction-separation relationship for the cohesive zone in the context of the current model configuration. This slope is primarily determined by two parameters - the maximum traction (which determines the height of the triangle for the traction-separation relation) and the critical strain energy release rate for the cohesive zone (which determines the area beneath the triangle). The maximum traction is not a good candidate for modification, since crack opening in the 90° ply is going to be largely driven by the stress in the ply. This leaves reduction of the critical strain energy release rate as the most appropriate way to increase the rate at which the cohesive zone's strength decreases as it opens. The value of G_{Ic} which was applied to

the composite was obtained from a double-cantilevered beam test in which the crack grew along the fiber direction. Investigations into crack growth, for instance, those by Czabaj and Ratcliffe [136], have shown that for cracks running along the fiber direction, delamination and intra-ply cracking have similar critical fracture energies. However, in the current configuration, although the crack crack plane has a similar orientation in relation to the fiber direction (running along the fiber direction), the crack is growing in a direction perpendicular to the fibers. Therefore, it is entirely possible that the energy associated with crack opening will be completely different for this case than for the double cantilevered beam case. As a result of this, the value of G_{Ic} was reduced by an order of magnitude, and the analysis was re-run. The resulting behavior as loading increases is shown in Fig. III.7

As shown in the figure, matrix cracks in the 90° ply showed a strong tendency to localize and open completely. This resulted in a complete unloading of the surrounding material in the 90° ply. As loading increased, additional cracks developed in regions far away from existing cracks, leading to a progressive increase in crack density. This behavior is in very good agreement with observed behavior for cross-ply laminates. For this reason, in cases where cohesive zones are used to account for the opening of matrix cracks in tows of textiles, values of G_{Ic} will be employed which result in brittle behavior.

One concern associated with the use of a much lower value of G_{Ic} than G_{IIc} is that for the given values of η used in Eq. 3.78, the power law that defines the mixed-mode critical strain energy release rate, the mode I component of the critical strain energy release rate under mixed-mode loading can exceed G_{Ic}. As a result,

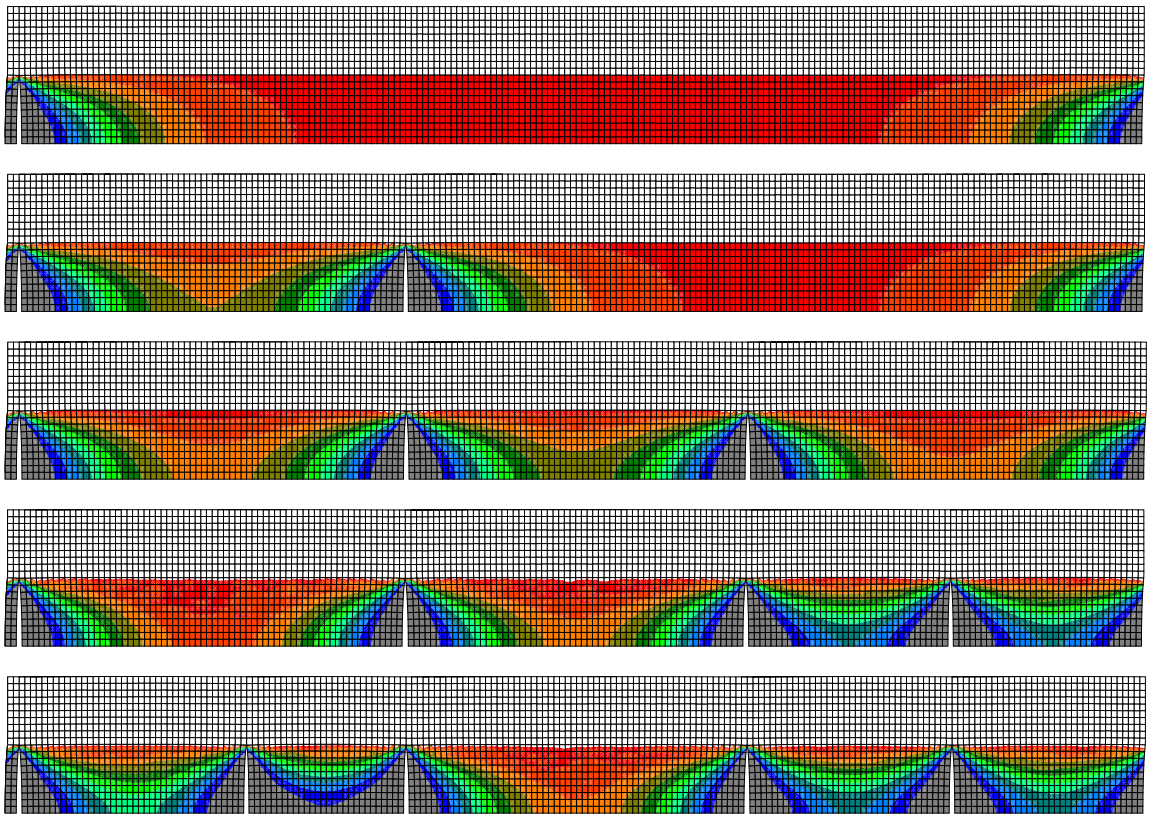

Figure III.7: Crack opening in cross-ply laminate with reduced G_{Ic}.

a different mixed mode critical strain energy criterion will be assumed for cohesive zone models where G_{IIc} is much larger than G_{Ic}. This criterion is given in Eq. 3.93.

$$\frac{G_I}{G_{Ic}} + \frac{G_s}{G_{IIc}} = 1 \tag{3.93}$$

This results in several changes to the cohesive zone formulation. From Eq. 3.80, the G_c for a given ratio can be defined by Eq. 3.94.

$$G_c = \frac{G_{Ic}}{1 + B\left(\frac{G_{Ic}}{G_{IIc}} - 1\right)} \tag{3.94}$$

This causes Eq. 3.82 to be modified to Eq. 3.95.

$$\Delta^f = \frac{\Delta_n^0 \Delta_n^f}{\Delta^0\left(1 + B\left(\frac{\Delta_n^0 \Delta_n^f}{\Delta_s^0 \Delta_s^f} - 1\right)\right)} \tag{3.95}$$

Eq. 3.87 then becomes Eq. 3.96.

$$\left(\tau^0\right)^2 = \frac{\left(\tau_n^0\right)^2}{1 + B\left(\frac{\left(\tau_n^0\right)^2}{\left(\tau_s^0\right)^2} - 1\right)} \tag{3.96}$$

Additionally, Eq. 3.88 becomes Eq. 3.97.

$$\Delta^0 = \sqrt{\frac{\left(\Delta_n^0\right)^2}{1 + B\left(\frac{\left(\Delta_n^0\right)^2}{\left(\Delta_s^0\right)^2} - 1\right)}} \tag{3.97}$$

These modification ensure that under no circumstance does the mode I component of the critical strain energy release rate under mixed-mode opening exceed the critical strain energy release rate under pure mode I loading.

CHAPTER IV

FIBER-MATRIX MICROSCALE MODEL

Developing composite models at the scale of discrete fibers and matrix allows a variety of investigations to be performed. One of the simplest is the determination of effective properties of the homogenized fibers and matrix (i.e. lamina or tow properties). Related to this is the determination of fiber properties that cannot be directly measured. Graphite fibers are generally thought to be transversely isotropic, but their small transverse dimension means that the accurate measurement of any elastic modulus other than the longitudinal Young's modulus E_1^f is extremely difficult. A micromechanics model allows these moduli to be estimated from unidirectional lamina properties through the use of inverse methods.

Once the elastic properties for the constituents are determined, the micromechanics model can be utilized to model a variety of behaviors at the fiber-matrix level. One of these is the determination of thermally-induced stresses which result from cooling after cure. These stresses can interact with the stresses that result from mechanical loading to alter the apparent strength of composite tows or lamina. This effect can be modeled by incorporating the thermally-induced stresses into a progressive failure analysis of the fiber-matrix.

One important feature of the fiber-matrix scale is the random positioning of fibers in the plane transverse to the fiber direction. This randomness leads to a large number of fibers that are in very close proximity to one another. Strong stress concentrations can arise in the matrix regions between these adjacent fibers, both

under thermal and mechanical load. Since failure is an extreme-driven process, these stress concentrations can potentially have a major impact on the larger-scale failure behavior of a lamina or tow.

The following sections describe the development of a random fiber-matrix model, its application to the determination of fiber properties, and various aspects of its use in predicting the failure behavior of unidirectional composite material under thermal loading combined with longitudinal shear and normal transverse mechanical loads.

IV.A. Random Model Generation

An algorithm was developed to generate microstructures which possess the following salient characteristics:

- Randomly positioned fibers
- Fibers in very close proximity (touching)
- Periodic microstructure

Several different approaches to generating random fiber matrices have been used previously. One of these approaches used in a number of studies into composite microstructures [137–140] begins by randomly selecting a location in the RVE and placing a fiber with its center at that location. Then, another location is selected at random for the next fiber from the remaining region of the RVE that will not cause spatial interference with the first fiber. Another random location is then selected for the next fiber from the region that will not interfere with either previously placed fiber. The process is repeated until the desired volume fraction is obtained. One

major issue with this approach is that it results in RVEs that have an unrealistic amount of spacing between adjacent fibers. An additional problem that can be encountered is that of "jamming," discussed at length by Widom [141] for spheres in three dimensions. Essentially, this approach is unable to reach high volume fractions due to the fact that although there will be a large volume of empty space in the RVE, the fiber spacing will be such that there are no regions available which are able to accommodate an additional fiber.

As a result of these shortcomings, several other approaches have been developed for generating random fiber RVEs. One of these, referred to as the "random inclusion displacement" approach by Brennan and Walrath [62], is attributable to Metropolis et al. [142] and is used in a number of different studies on composite microstructures [77, 143–145]. In this approach, fibers are initially placed in a structured grid, such as a hexagonal array. They are then subjected to small random perturbations in their locations such that they do not overlap adjacent fibers. Because this approach can start with hexagonal packing, it is capable of reaching the theoretical maximum volume fraction associated with close-packing of circles (90.7%).

In reality, arrangement of the fibers is the result of manufacturing processes which apply loads to the uncured lamina or textile. This suggests that a contact analysis approach, such as the one utilized by Mollenhauer et al. [70], is perhaps the most appropriate means for developing a realistic fiber-matrix microstructure. This approach yields a microstructure with adjacent fibers that are essentially in direct contact with one another and can result in reasonably high volume fractions without relying on an assumption of a particular initial configuration as in the aforementioned

"random inclusion method".

While the approach utilized in the current study, given in Fig. IV.1, is not a classical contact analysis per se, it includes a pseudo-relaxation iterative step to resolve interference between overlapping fibers that closely mimics the relaxation procedure that would be used in a contact analysis. One very important detail to note in the provided algorithm is in the steps when overlapping fibers are moved away from one another. Each fiber is moved by one-half the total overlap distance *plus 1/1000th the average fiber diameter*. This small additional distance is required for the algorithm to converge. A smaller (non-zero) distance could be chosen with the consequence of increasing the number of iterations required for the algorithm to converge to a geometry with no overlap.

An additional feature of the fiber-matrix microstructural RVE used in the current work is that it is periodic. When a fiber is cut by the boundary, it continues on the opposite boundary of the RVE. This allows periodic unit cell analyses to be utilized. This eliminates difficulties associated with the application of uniform traction or displacement boundary conditions for finite RVEs, which lead to inaccuracies in the solution near the boundary. Periodic boundary conditions have been used in several previous studies into random fiber-matrix microstructures [71, 77, 143, 146].

The geometry definition process is implemented efficiently in a Python module that utilizes a k-d tree implementation [147] from the SciPy package to quickly perform neighbor searches, allowing the algorithm to scale up to tens or hundreds of thousands of fibers (Fig. IV.2) on a single workstation (although meshing and solving a mechanics analysis for such a large geometry is currently intractable). The

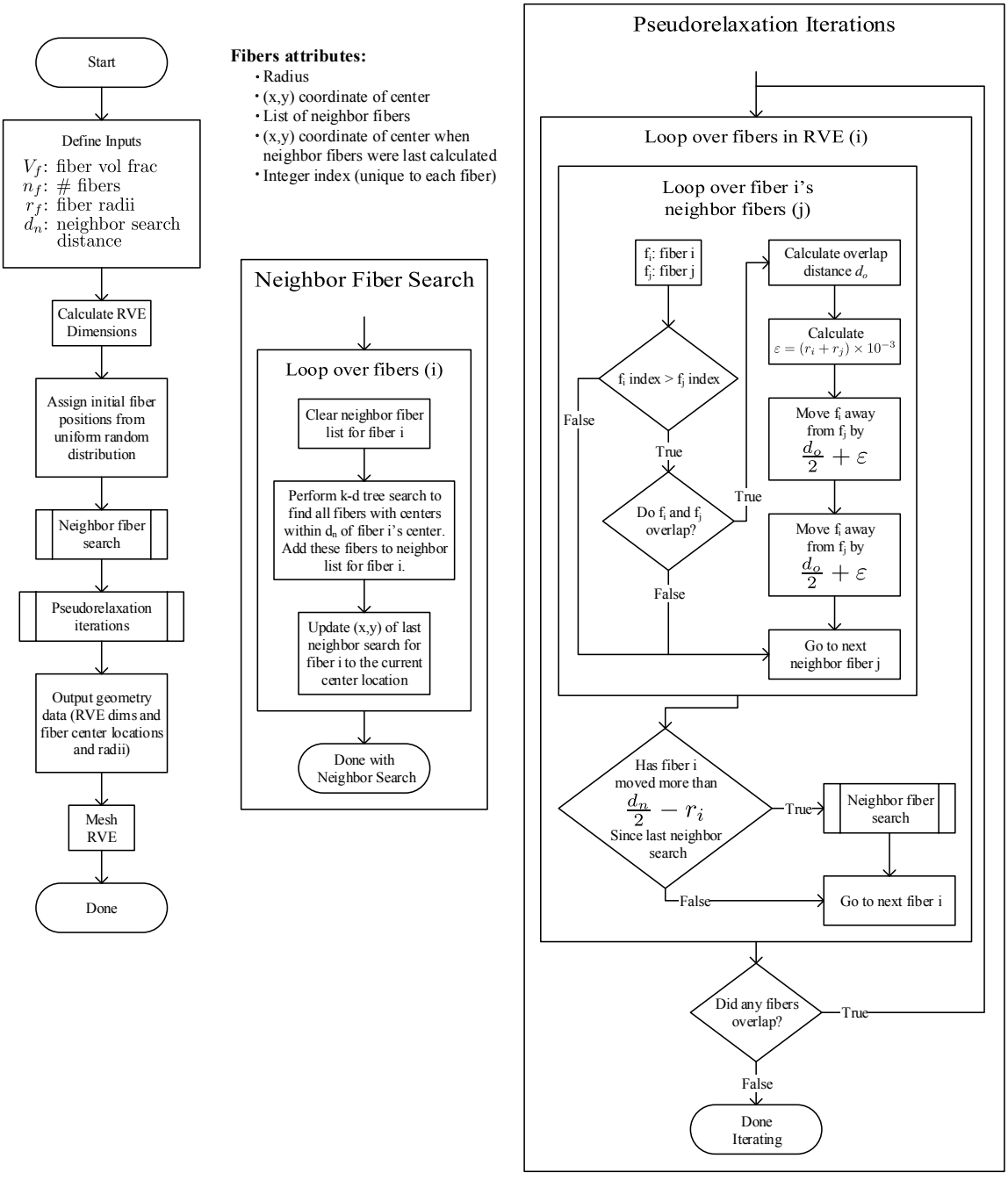

Figure IV.1: RVE generation process.

module makes use of a fiber class that contains information about the fiber location and neighbor fibers, as well as methods to move fibers and determine if one fiber overlaps another. So-called "phantom fibers" are used to account for the periodic positioning of fibers to maintain periodicity of the geometry. The module can be found in its entirety in Appendix A.

Meshing is accomplished using a custom meshing utility written in C++. This tool defines boundary node locations on the fibers and RVE boundaries and utilizes Johnathan Shewchuk's Delaunay meshing library "Triangle" [148] to generate a mesh of 6-node quadratic triangles. Triangle does not generate elements with curved sides, so after the mesh is generated, a post-processing step is performed to position all fiber-matrix interface nodes on the actual geometry of the interface. Although the mesh generator is capable of generating touching fibers (i.e. fibers that share a node), all RVEs in this work leave an extremely thin strip of matrix between adjacent fibers, shown in the detail of Fig. IV.3. This allows for damage paths to develop between fibers in the failure analyses which are described in subsequent sections.

The resulting geometry is modeled in a two-dimensional domain by assuming that the displacement field is quasi3D. This assumption, described by Pipes and Pagano [149], is that the displacement field has the form of Eq. 4.1.

$$\begin{aligned} u_1 &= \varepsilon_{11} x_1 + U(x_2, x_3) \\ u_2 &= V(x_2, x_3) \\ u_3 &= W(x_2, x_3) \end{aligned} \tag{4.1}$$

This assumption is completely valid for the fiber-matrix configuration. Therefore, the reduction in dimensionality greatly reduces the complexity of the numerical problem

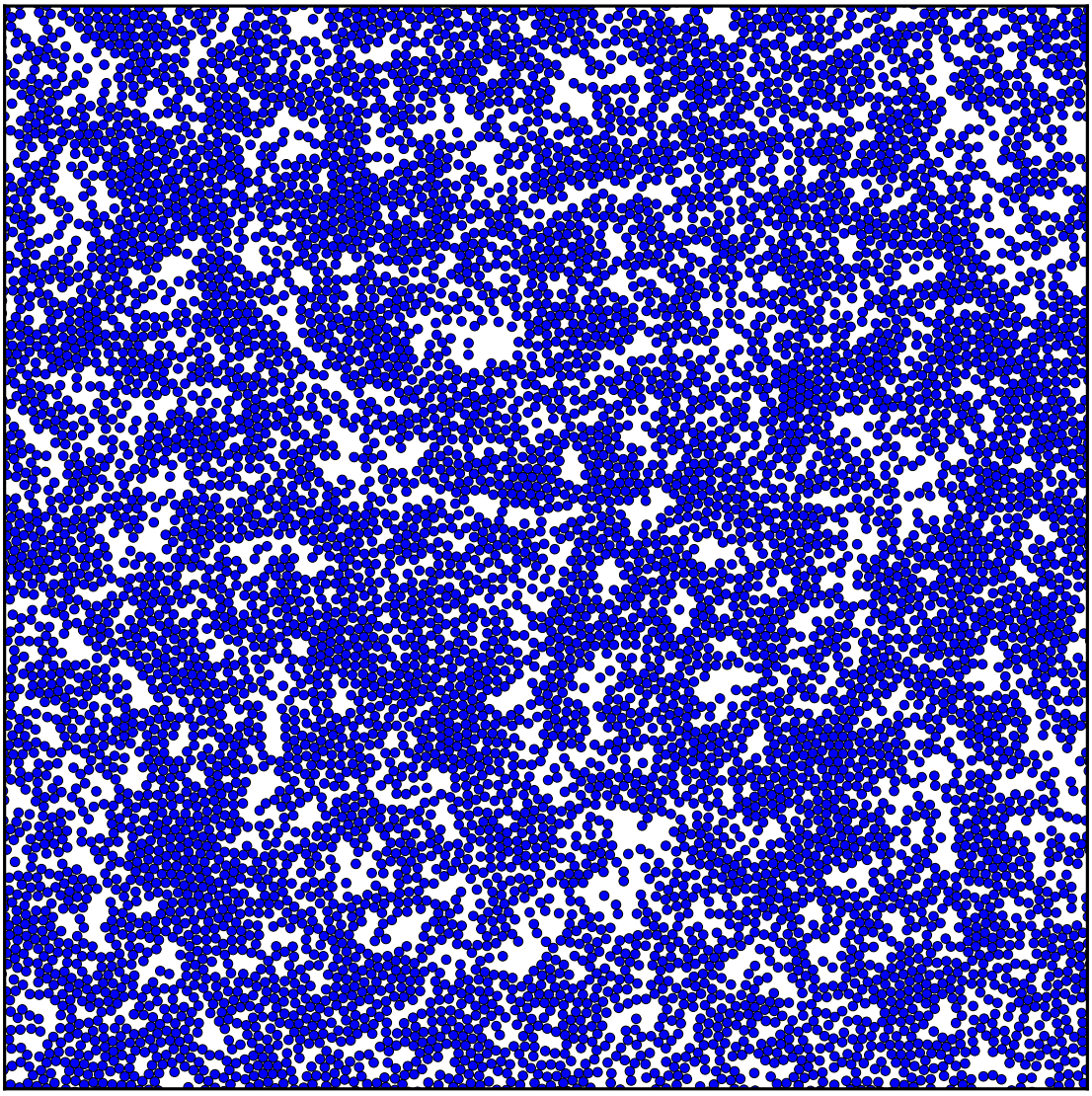

Figure IV.2: 10,000 fiber RVE, generated in 150 seconds.

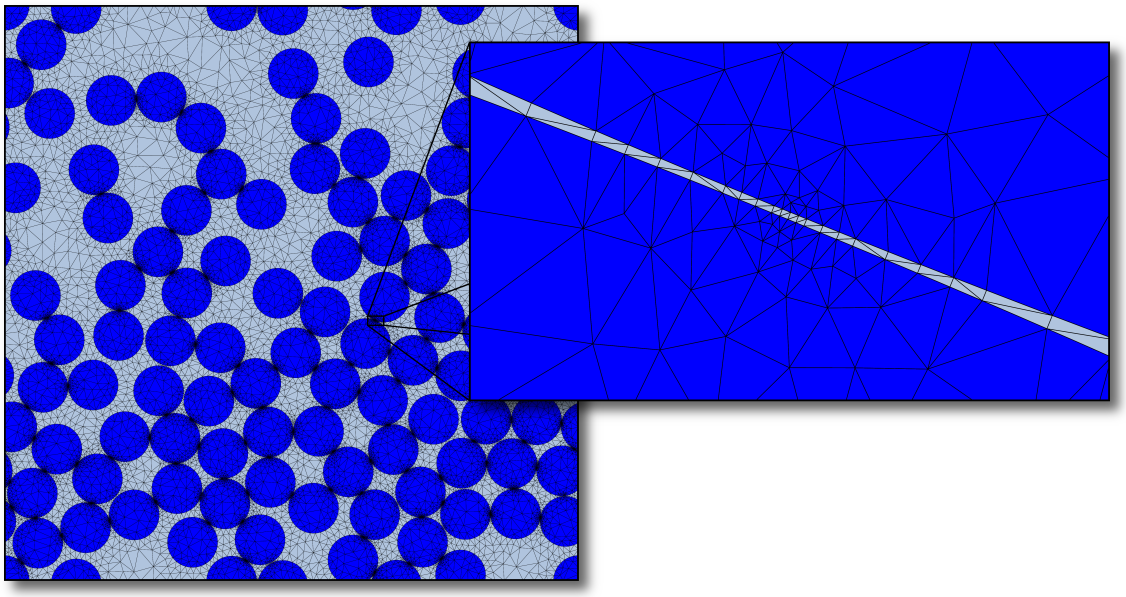

Figure IV.3: Example mesh with detail of inter-fiber region.

without introducing any additional error to the analysis.

IV.B. Constituent Property Determination

The use of a micromechanics model to analyze composites depends upon knowledge of the properties of each constituent. Determining these properties for carbon fibers presents a number of challenges. It is possible to directly measure a fiber's longitudinal modulus E_1^f, but measuring the other engineering properties presents difficulty due to the fact that typical carbon fibers have diameters on the order of 5-10µm. Therefore, it is not generally tractable to directly measure the other transversely isotropic engineering properties G_{12}^f, G_{23}^f, E_2^f, and ν_{12}^f.

Since these properties cannot be measured, but the transversely isotropic prop-

erties of a unidirectional lamina can (although G_{23}^L/ν_{23}^L still presents some difficulty), it is possible to inversely estimate fiber properties using an appropriate micromechanics model. In a review of the literature, it was interesting to note that even recent investigations into composite behavior using random microstructural models largely used fiber properties which had been determined using micromechanics models that did not include randomness. While these studies investigated the effect of randomness on the effective properties of the lamina (either elastic, thermomechanical, or strength), they did not re-examine the problem of fiber property determination using a random microstructure. Therefore, the current random microstructural model was utilized to perform an investigation into fiber property determination. The initial results of this investigation are reported in a proceedings paper by Ballard et al. [150].

This section outlines the approach used to predict the properties of IM7 fibers, as well as the results of the fiber property investigation. The material system investigated in this work consists of IM7 fibers and 8552 epoxy matrix. The properties of unidirectional IM7/8552 composite and neat 8552 matrix used to inversely determine the fiber properties are from Huang et al. [151]. They are given in table IV.1. Superscripts on material properties in this section represent the constituent that they characterize. Fiber properties are denoted by ^{f}, matrix by ^{m}, and unidirectional lamina properties by ^{L}. Based on the axial stiffness for IM7 fibers provided by the manufacturer [152] as 276 GPa, the V_f of the lamina (which is not provided in [151]) was estimated to be 59.1%. This was determined using rule of mixtures, which is widely regarded to be a very accurate approach for predicting axial properties of

Table IV.1: Unidirectional IM7/8552 lamina and neat 8552 properties from literature.

Property	Value
E_1^L	165 GPa
E_2^L	11.38 GPa
G_{12}^L	5.120 GPa
ν_{12}^L	0.30
ν_{23}^L	0.487
E^m	4.67 GPa
ν^m	0.35

unidirectional lamina.

As previously mentioned, the procedure for determining the fiber properties involves the solution of an inverse problem. This is because the fiber properties, which are unknown, are inputs to the micromechanics model, and the lamina properties, which are known, are the outputs. For finite element based micromechanics models, it is not possible to invert this input-output relationship. The problem is solved by iteratively identifying fiber properties which cause the model to yield lamina properties that match the expected values. Both the lamina and fiber are assumed to be transversely isotropic, meaning that each have five independent engineering constants. For convenience, these are expressed as vectors given in Eq. 4.2.

$$\begin{aligned} \Gamma^L &= \left[E_1^L, E_2^L, G_{12}^L, G_{23}^L, \nu_{12}^L\right] \\ \Gamma^f &= \left[E_1^f, E_2^f, G_{12}^f, G_{23}^f, \nu_{12}^f\right] \end{aligned} \tag{4.2}$$

The micromechanics model serves as a function which operates in the manner given in Eq. 4.3.

$$\Gamma^L = f\left(\Gamma^f\right) \tag{4.3}$$

In the case an analytical model such as Mori-Tanaka, this function assumes an analytical form, and in that case may be invertible as was done by Rupnowski et al. [153–155]. For a hexagonal unit cell, this function represents the effective, or volume-averaged response of a single finite element model. For the random RVE, this function represents the mean effective response of 50 different realizations of the random microstructure. Each realization in this study contains 100 fibers. It was found that RVEs with 100 fibers are more than large enough to ensure that the RVE size doesn't influence the mean effective response of the realizations. Further increases of the RVE size do have the effect of decreasing the variance in the distribution of effective responses for a collection of realizations, but since this study is only concerned with the mean effective elastic response, 50 realizations of 100-fiber RVEs were found to be more than adequate.

The overall objective is to find a collection of fiber properties such that the residual of the lamina properties, given in Eq. 4.4, goes to zero within a given tolerance. This allows the problem of fiber property determination to be cast as a root-finding problem in 5 dimensions.

$$\psi_i = \Gamma_i^L - \bar{\Gamma}_i^L \cong 0 \tag{4.4}$$

The overbar signifies the lamina properties from experiments. Due to the large differences in the magnitudes of the various moduli, calculations are performed on a residual vector normalized by the initial fiber guess as shown in Eq. 4.5.

$$\hat{\psi}_i = \frac{\psi_i}{\Gamma_i^{f^0}} = \frac{\Gamma_i^L - \bar{\Gamma}_i^L}{\Gamma_i^{f^0}} \text{ (no summation on } i) \tag{4.5}$$

Similarly, the fiber properties are normalized by the initial fiber guess as in Eq. 4.6.

$$\hat{\Gamma}_i^f = \frac{\Gamma_i^f}{\Gamma_i^{f^0}} \text{ (no summation on } i) \tag{4.6}$$

The Newton-Raphson method is used to find the value of the fiber properties that result in the correct lamina properties. To avoid numerical problems, the Jacobian matrix, given in Eq. 4.7 is formed using changes in the normalized fiber and lamina properties.

$$J_{ij} = \frac{\partial \hat{\psi}_i}{\partial \hat{\Gamma}_j^f} \cong \frac{\Delta \hat{\psi}_i}{\Delta \hat{\Gamma}_j^f} \tag{4.7}$$

The initial guess for the fiber properties is obtained from the literature for similar material systems. It is only necessary that each engineering constant in the guess have a realistic order of magnitude for the purpose of normalization, but more accurate guesses can reduce the number of iterations required for convergence. For each Newton-Raphson iteration, a new guess for the fiber properties is obtained by calculating the correction given in Eq. 4.8.

$$\Delta \hat{\Gamma}_i^f = -\left(\frac{\partial \hat{\psi}_i}{\partial \hat{\Gamma}_j^f} \right)^{-1} \hat{\psi}_j \tag{4.8}$$

Iteration on the fiber properties continues until the L_2 norm of the normalized residual decreases to a value of 10^{-6} or less, at which point the fiber properties have been determined.

The calculation of the gradient matrix is computationally expensive, requiring lamina properties to be determined for six different sets of fiber properties. One set corresponds to the current guess of the fiber properties, while the other five sets of properties perturb one of the fiber properties by 1% to obtain gradients. Due to this high cost, the gradient matrix is only recalculated after an iteration results in

Table IV.2: Transversely isotropic properties for IM7 fibers determined from micromechanics.

Property	Random RVE	Pagano et al.
E_1^f	276 GPa	276 GPa
E_2^f	22.4 GPa	27.6 GPa
G_{12}^f	12.0 GPa	138 GPa
G_{23}^f	7.53 GPa	7.67 GPa
ν_{12}^f	0.274	0.3

less than a 50% decrease in the normalized residual. Additionally, it was found that some iterations would result in unrealistic guesses for the fiber properties. When this occurred, the problematic property was truncated to a realistic value (positive values for moduli and values between 0.01 and 1.0 for Poisson ratios).

Following this procedure, fiber properties were determined from the lamina and matrix properties given in table IV.1. The determined properties are given in table IV.2 along with values reported by Pagano et al. [156] using a micromechanics approach outlined by Pagano and Tandon [157] to back out the fiber properties for a IM7/5250-4 composite system.

One immediately noted difference between the two sets of properties is the *very* large (1 order of magnitude) difference between the longitudinal shear moduli G_{12}^f. It is believed that this is due to the low stiffness of 5250-4 matrix ($E^m = 3.45$ GPa, $\nu^m = 0.35$) used in [156] along with the fact that the micromechanics model described in [157] does not account for the high degree of interaction that will occur between fibers that have randomness in their transverse locations. In fact, many other micromechanics models such as Mori-Tanaka will fail to yield a fiber longitudinal shear

modulus for the material system examined in [156] due to the fact that when interactions between fibers are not adequately accounted for, even rigid fibers do not have sufficient stiffness to yield an appropriate effective shear modulus. This study is therefore an excellent example of the importance of having a realistic microstructural model when determining fiber properties based on lamina properties.

IV.C. Elastic Behavior and Investigation of Stresses

This section describes findings that were made regarding the microstructural stress field in the composite due to thermomechanical loading, with an emphasis on the effects of the random microstructure and how the microstructural stresses arising due to various combinations of mechanical and thermal loads may influence failure of the composite.

IV.C.1. Failure Criterion for Neat Matrix

Failure in the matrix of the microstructure is predicted to occur according to Christensen's criterion for isotropic materials [25]. This multi-part criterion is given in Eqs. 4.9 and 4.10.

$$\sigma_{kk}\left(\frac{1}{T}-\frac{1}{C}\right)+\frac{\sigma_{VM}^2}{CT}=1 \tag{4.9}$$

$$\sigma_I = T \text{ if } T \leq \frac{C}{2} \tag{4.10}$$

T and C are the tensile and compressive strengths of the material under uniaxial loading, respectively. σ_{kk} is the trace of the stress tensor, σ_{VM} is the scalar Von Mises stress, and σ_I is the largest tensile principle stress. The second part of the criterion, given by Eq. 4.10, is only applicable when the included relationship between

T and C is satisfied. Christensen bills this criterion as being applicable to a variety of isotropic materials which undergo both ductile and brittle failure. Raghava et al. [60] put forward a criterion equivalent to Eq. 4.9 for predicting yield of polymers, which was used by Ha et al. [59] to predict the failure of hexagonal fiber-matrix unit cells. For the compressive and tensile matrix strengths utilized in the current study, the inequality of 4.10 is not satisfied, leading to a failure criterion which is equivalent to that Raghava et al.

In addition to predicting when brittle or ductile failure begins, Christensen's criterion also provides a means to ascertain whether a stress which causes failure will result in brittle or ductile behavior. When Eq. 4.10 predicts that failure occurs, the failure will be brittle. The criterion of Eq. 4.9, however, predicts both brittle and ductile failure. The nature of the failure can be ascertained from the magnitude of the hydrostatic stress according to Eq. 4.11.

$$\begin{aligned} \frac{\sigma_{kk}}{3} &< T - \frac{C}{3} \qquad \text{Ductile} \\ \frac{\sigma_{kk}}{3} &> T - \frac{C}{3} \qquad \text{Brittle} \end{aligned} \tag{4.11}$$

Christensen notes that the ductile/brittle delineation of Eq. 4.11 should not be thought of as a hard boundary - the transition from ductile to brittle failure will tend to be more gradual for states of stress which are close to the boundary defined by the inequality.

For the investigations of this section, matrix strength values of $T = 128$ MPa and $C = 204$ MPa will be utilized. These values were found to be the matrix strengths that yielded the appropriate overall lamina strength. The process of determining these values is described in much greater detail in section IV.F.

The following subsections describe the stresses that arise in the composite microstructure under various loadings. Particular attention will be paid to phenomena that depend upon a random microstructure with fibers that are in close proximity. Except where specifically noted, the investigations are performed on a single 100-fiber realization of the random periodic unit cell with V_f =55.6%. The goal of these investigations is to develop a qualitative understanding of how the microstructure and close proximity of fibers can effect the development of failure in the composite under thermomechanical loads.

IV.C.2. Micromechanical Stresses Under Thermal Loading

Polymer matrix carbon fiber composite fabrication typically includes a cure process that occurs at high temperature. This process facilitates cross-linking and solidification of the polymer matrix once it has infused the carbon fibers. Once cure is completed, the composite is allowed to cool. Because the solidification of the polymer occurs at an elevated temperature, the cooling process results in the development of thermal strains in the fibers and matrix. The thermal expansion coefficients of fibers and matrix differ considerably, which leads to the development of stresses. The transversely isotropic thermal expansion coefficients for IM7 fibers were investigated experimentally by Kulkarni and Ochoa [158] and are used in the current analyses. The thermal expansion coefficient of the 8552 matrix is a manufacturer value given in [159]. These values are listed in table IV.3.

The after-cure temperature drop of -160 °C used by Hallett et al. [11] for IM7/8552 laminates is adopted in the current study. This temperature change was

Table IV.3: Constituent thermal expansion coefficients.

Property	Value
α_1^f	-4.0×10^{-7} ($^\circ C^{-1}$)
α_2^f	6.94×10^{-6} ($^\circ C^{-1}$)
α^m	4.335×10^{-5} ($^\circ C^{-1}$)

applied uniformly across the RVE. The volume average strains of the RVE were left unconstrained, but the RVE was constrained to deform in a periodic manner through the use of multi-point constraints. This simulates the application of a temperature change to an unconstrained specimen (the volume average stress is zero). The resulting hydrostatic stress contours are shown in Fig. IV.4, and the Von Mises stress contours in the matrix are shown in Fig. IV.5.

It is observed that the matrix region is predominantly under hydrostatic tension, while the fibers are under hydrostatic compression. However, careful examination of the matrix regions between adjacent fibers shows local zones of compressive hydrostatic stress. The hydrostatic stress goes compressive in these regions because of compressive radial stresses around the fibers. Because the matrix is in effect "squeezing" the fiber, the radial component of the matrix stress in the vicinity of the fiber must be compressive, while the hoop and longitudinal components are tensile. When two fibers come into close proximity, this radial compressive stress between them becomes much larger in magnitude than the other tensile stress components, leading to a hydrostatic stress which is compressive in nature. The Von Mises stress in the matrix goes to a maximum in the inter-fiber regions. Examining the failure criterion of Eq. 4.9 shows that for the current values of T and C, compressive hydrostatic stresses

have a deletory effect on Christensen's failure index, increasing the Von Mises stress required to cause failure. For the current model, the value of Christensen's failure criterion given by the left-hand side of Eq. 4.9 (referred to as the Christensen factor), has lower values in the inter-fiber regions and higher values in matrix pockets which are located in fiber clusters but away from the zones where fibers get extremely close to one another, as seen in Fig. IV.6. One other important fact to note from Fig. IV.6 is that for this microstructure, Christensen's criterion does not predict failure at any location in the matrix for the thermally-induced stresses associated with cooling after cure. This is only applicable to *unconstrained* composite materials. The deformation of tows and plies in larger-scale laminated or textile structures are often constrained by adjacent tows and plies with different orientations. These constraints result in thermally induced stresses at the scale of textiles and laminates which are, in effect, mechanically-induced stresses at the fiber-matrix scale (i.e. stresses with a non-zero volume average) which act in addition to the thermally induced stresses arising from the thermal expansion coefficient mismatch between the fibers and matrix.

Unlike the regions between fibers in very close proximity, the hydrostatic stress does not go compressive in matrix regions between fibers that are separated by a moderate distance. To examine the effect of fiber spacing, another RVE was generated, but additional space was artificially introduced between the fibers by initially specifying a higher volume fraction and fiber diameter for the geometry generation step of the RVE creation process, and then reducing the fiber diameters to recover V_f =55.6% before performing the meshing step. The resulting mesh, along with the hydrostatic stress contours, is shown in Fig. IV.7. Although the magnitude of the

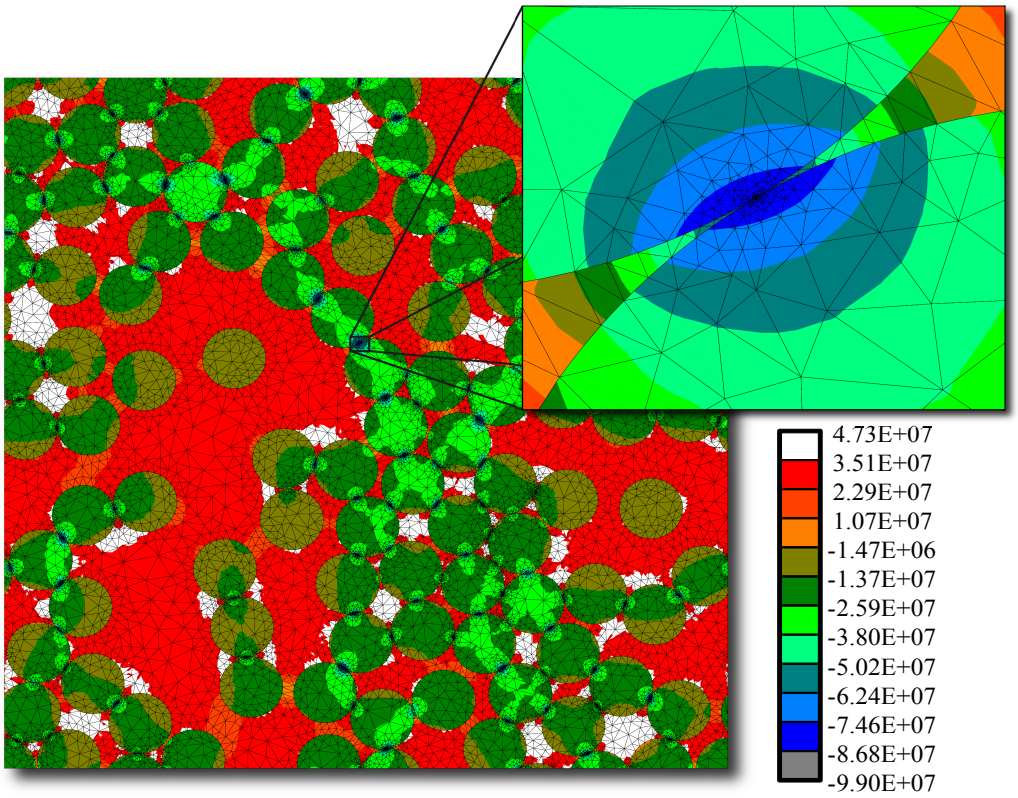

Figure IV.4: Hydrostatic stress in fibers and matrix for temperature change of $\Delta T = -160$ °C (contours are in Pa).

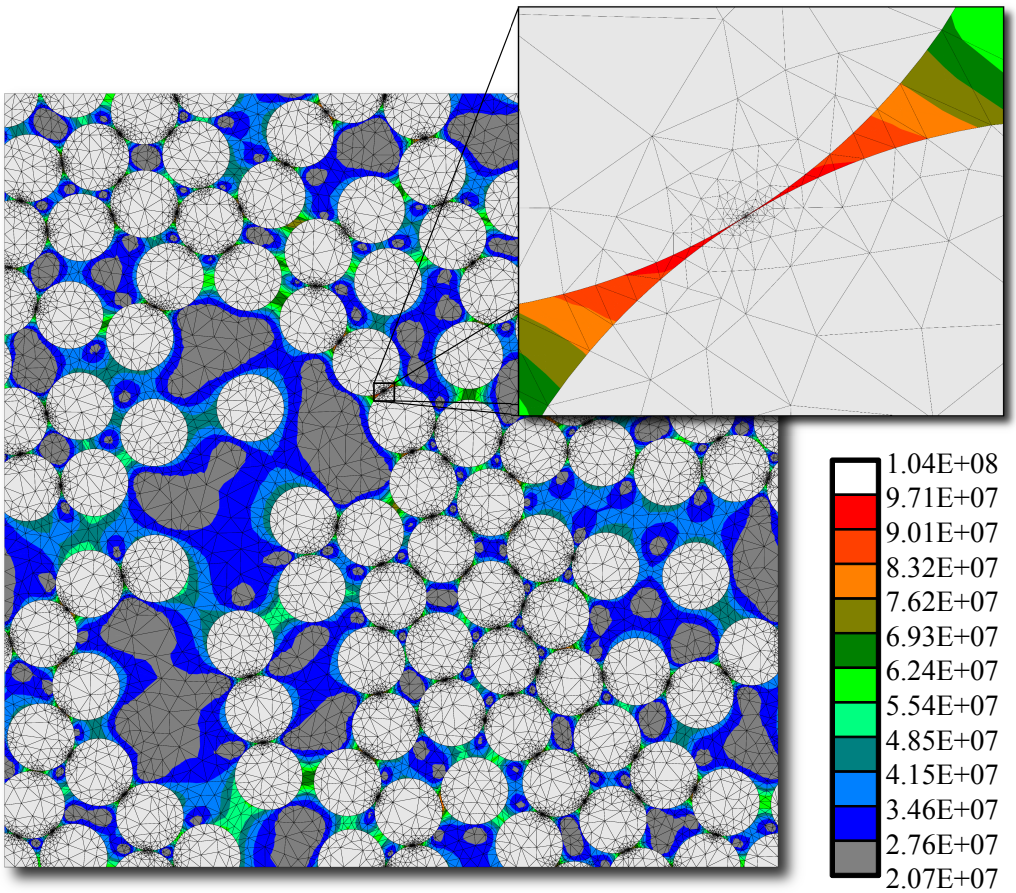

Figure IV.5: Von Mises stress in matrix for temperature change of $\Delta T = -160$ °C (contours are in Pa).

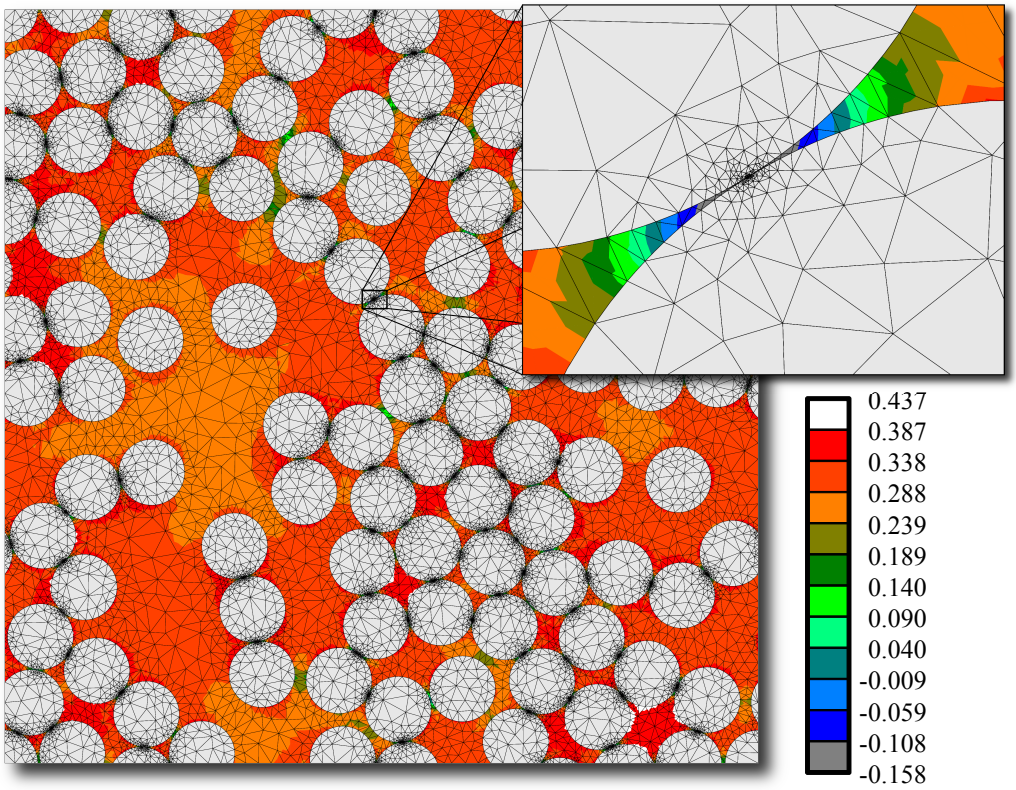

Figure IV.6: Christensen factor contours in matrix for temperature change of $\Delta T = -160$ °C.

hydrostatic stress in the matrix is reduced in the interfiber regions, it is tensile everywhere for this RVE. This is because when fibers are not in close proximity to one another, the tensile hoop and longitudinal stresses in the matrix will be larger than the radial compressive stress component. The fibers in this microstructure are not in close enough proximity to cause the radial compressive stress around the fibers to grow large enough to make the overall hydrostatic stress compressive. This suggests that if these regions end up being important to the development of failure, then microstructures without proper interfiber spacing are unlikely to accurately capture the effect that thermally-induced stresses have on the failure of the fiber matrix.

One other interesting characteristic of the stress-state which was noted was that the longitudinal microstructural shear stresses σ_{12} and σ_{13} were identically zero everywhere in the microstructure, indicating that the irregular spacing between fibers does not lead to the development of this type of local stress under thermal loads.

IV.C.3. Micromechanical Stresses Under Transverse Normal Loading

Transverse normal loading is the first type of mechanical loading that is examined. Under this loading, the y-direction normal volume averaged stress component is prescribed to be 50 MPa, with all other components set equal to zero. This loading corresponds to normal x_2 or x_3 loading applied to a unidirectional composite with fibers running in the x_1 direction. 50 MPa is chosen due to the fact that it is slightly below the transverse normal strength of a unidirectional lamina at room temperature. The resulting hydrostatic stresses are given in Fig. IV.8.

It is immediately noted that the hydrostatic stress in the matrix experiences

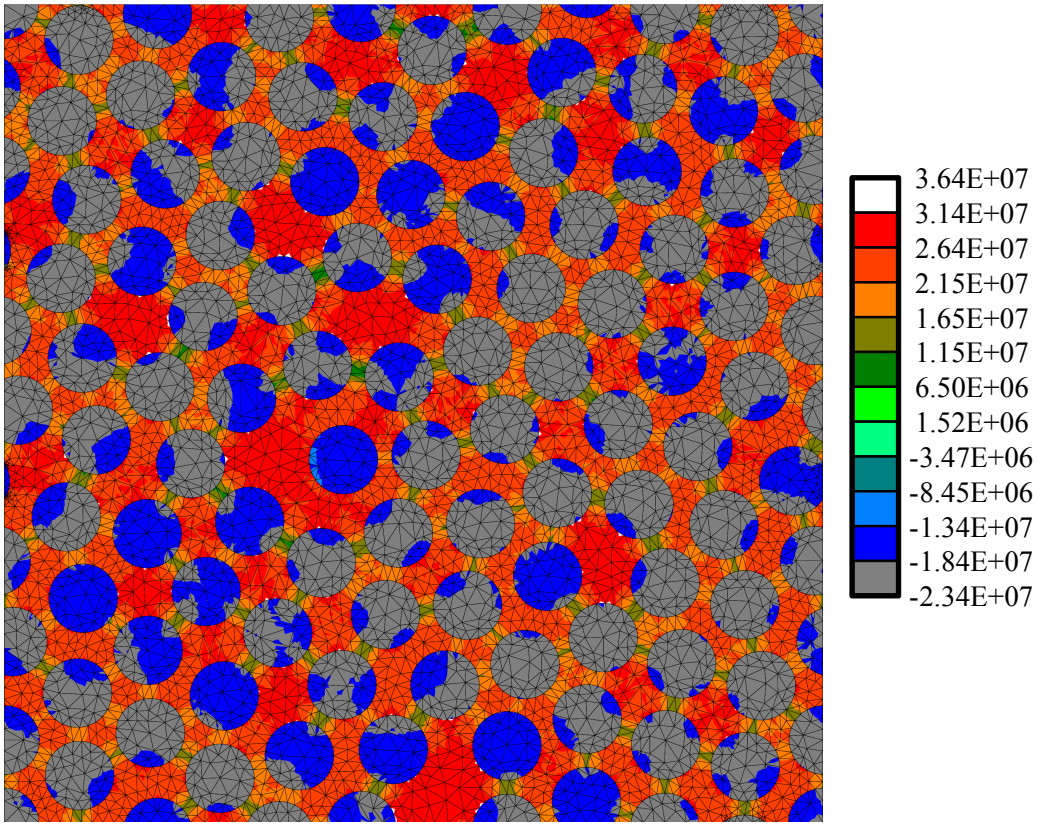

Figure IV.7: Hydrostatic stress in fibers and matrix with artificially high fiber-spacing for temperature change of $\Delta T = -160$ °C (contours are in Pa).

strong tensile concentrations in the regions immediately between fibers which are in close proximity and predominantly aligned in the x_2 direction. These concentrations go to a maximum in the regions where fibers are closest to one another. It has been suggested by Asp et al. [56] that these hydrostatic stresses play the predominant role in the failure of composites under transverse normal loading. For the RVE with artificially spaced fibers, the hydrostatic stress distribution had the same characteristics, but with lower stress concentrations.

The Von Mises stresses in the matrix, shown in Fig. IV.9, experience local maximums in locations between fibers that are aligned with planes oriented $\pm 45^\circ$ to the applied load direction (in this case, x_2), as these are regions of high shear stress in the model. The combination of the hydrostatic and Von Mises stresses yields values for Christensen's criterion which are contoured in Fig. IV.10. The locations for the maximum values of Christensen's failure criterion generally correlate better with the locations of the maximum hydrostatic stresses than the Von Mises stresses, indicating that the hydrostatic stress plays a greater role in the critical stress states that exist at the microscale under normal transverse loads (a result which agrees with that of Asp et al.).

IV.C.4. Micromechanical Stresses Under Longitudinal Shear

The second mechanical loading which is examined is longitudinal shear stress. A volume-averaged shear stress of 40 MPa was applied in the 1-2 plane. This stress was chosen due to the fact that although the ultimate strength of the composite under this loading is around 90 MPa, nonlinear behavior begins at much lower shear stresses.

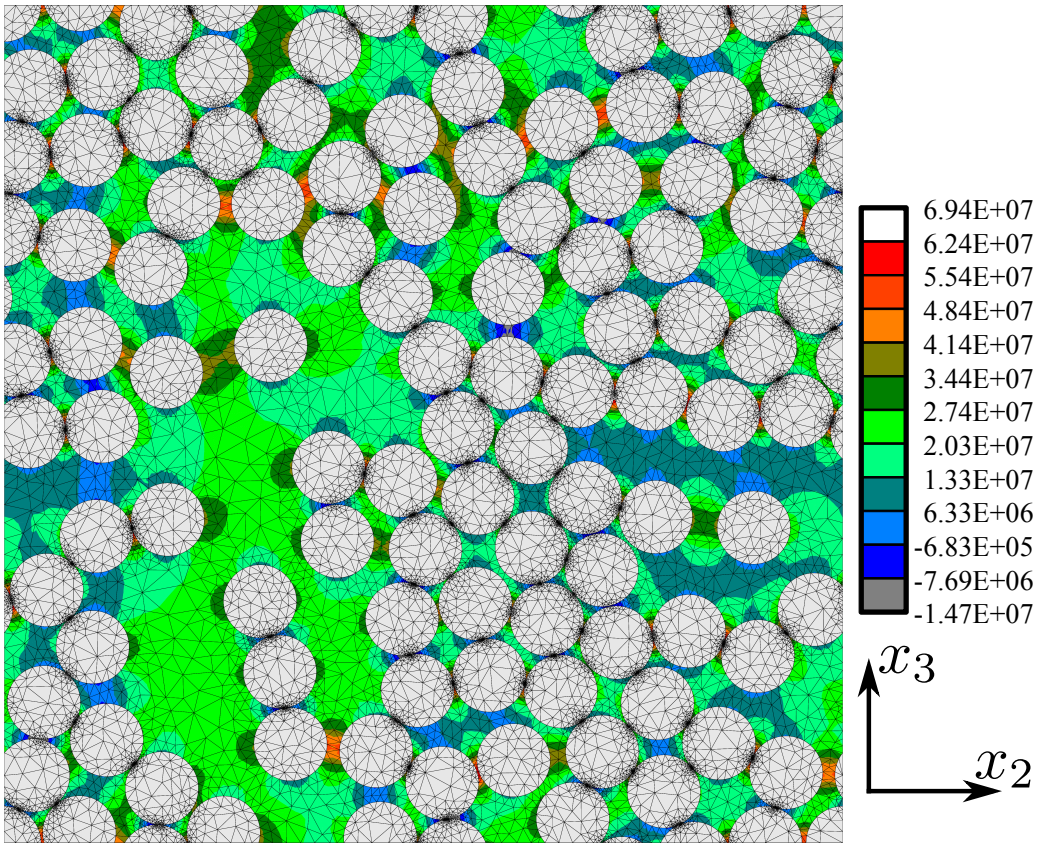

Figure IV.8: Hydrostatic stress in matrix for normal transverse tensile load of 50 MPa (contours are in Pa).

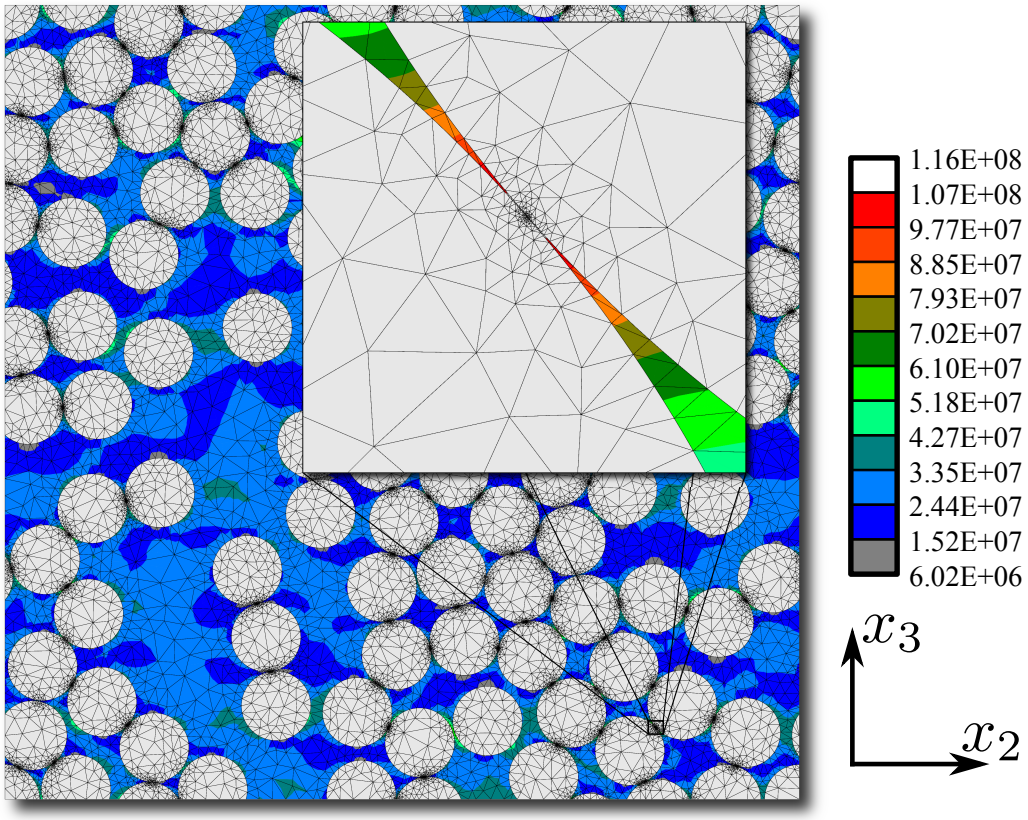

Figure IV.9: Von Mises stress in matrix for normal transverse tensile load of 50 MPa (contours are in Pa).

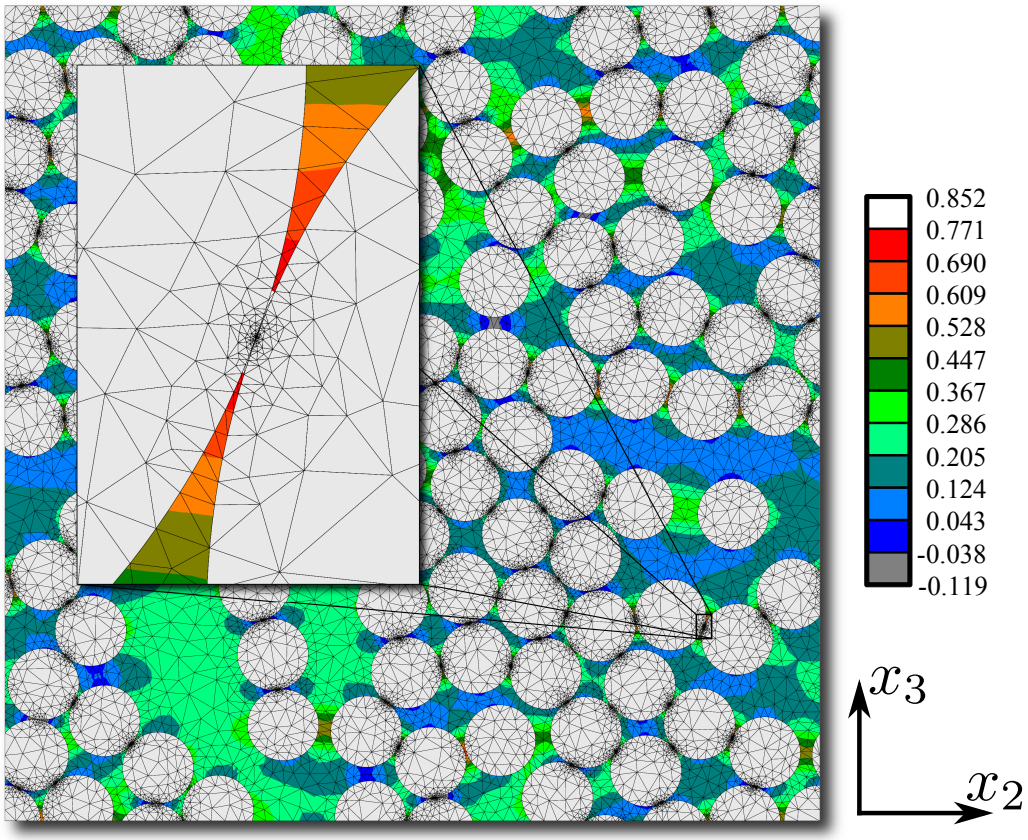

Figure IV.10: Christensen factor contours in matrix for normal transverse tensile load of 50 MPa.

Just as normal and thermal loadings yielded zero longitudinal shear (σ_{12}, σ_{13}) stress components in the microstructure, longitudinal shear loading yields zero normal (σ_{11}, σ_{22}, σ_{33}) or transverse shear (σ_{23}) stress components in the microstructure. Therefore, the hydrostatic stress is identically zero everywhere. The Von Mises stress contours are shown in Fig. IV.11. These stresses experience very strong and highly localized concentrations (more so than microscale stresses under thermal or transverse normal loading) in regions between adjacent fibers. This stress state leads to ductile failure of the matrix according to Christensen's criterion (Eq. 4.11). These stress concentrations are more pronounced in fibers which are aligned in the x_2 direction, and there is greater variation in the maximum stresses between fibers than under normal or thermal loading. Also, it was noted that artificially introducing space between the fibers resulted in a very large decrease in the maximum Von Mises stress that existed in the matrix.

IV.C.5. Interaction of Thermally and Mechanically Induced Stresses

One of the major points of interest in the current study is how thermally induced stresses in the microstructure interact with stresses from mechanical loading to change the mechanical load at which failure occurs. An examination of stress contours for various combinations of mechanical and thermal loads revealed that in all cases, the most critical stress states occur in the regions between adjacent fibers. To examine the interactions in this region in a more systematic manner, a two-fiber RVE model, shown in Fig. IV.12 was developed in which the fiber spacing was varied. The Christensen factor will be plotted along a line running between the two

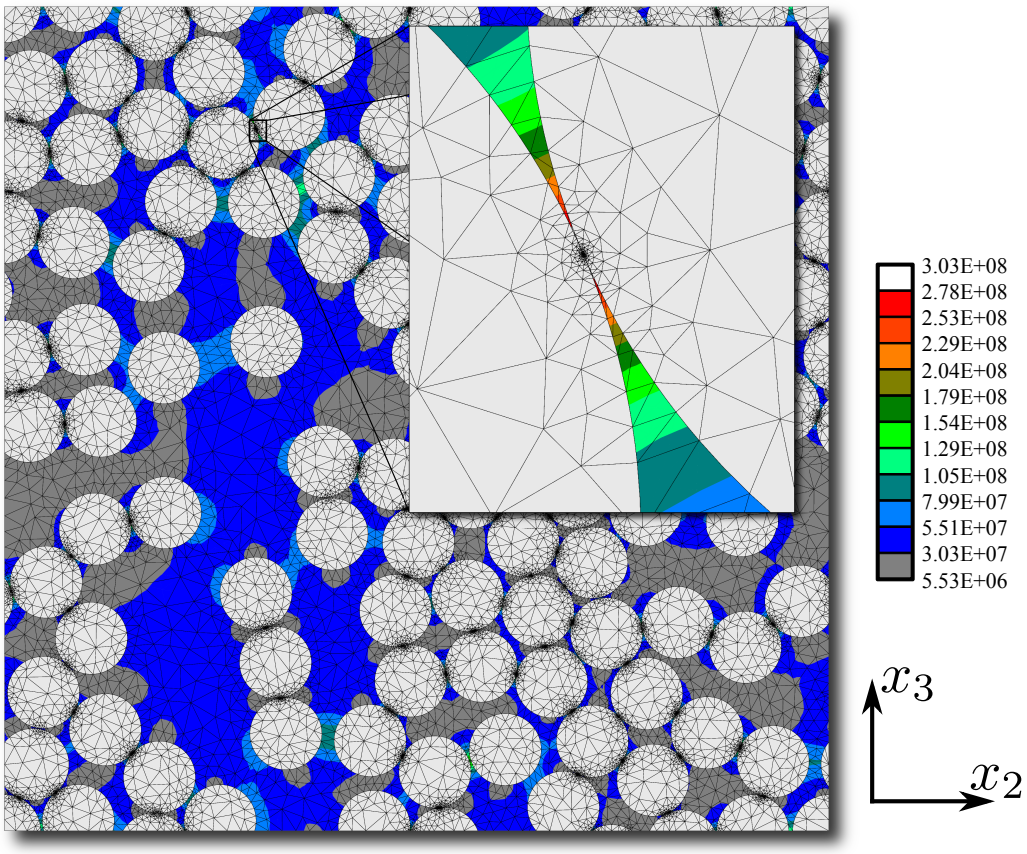

Figure IV.11: Von Mises stress in matrix for longitudinal shear load of 40 MPa (contours are in Pa).

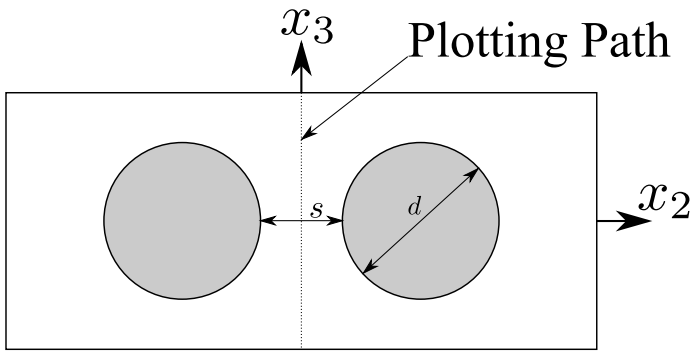

Figure IV.12: Two fiber model.

fibers.

The Christensen factor between two fibers under a normal transverse load of 50 MPa is shown for two different fiber spacings and a variety of temperatures (relative to the stress-free cure temperature) in Fig. IV.13. It is immediately apparent for close fiber spacing (Fig. IV.13a) that the temperature drop following cure has the effect of reducing the severity of the stress in the region where the fibers come closest together. This effect is due to the compressive hydrostatic stresses which develop in the matrix between fibers under pure thermal loading. Under combined loading, these compressive stresses offset the tensile hydrostatic stresses that arise due to mechanical loading. This finding suggests thermally induced stresses from cooling after cure are likely to increase the strength of the composite.

The inter-fiber Christensen factor was also examined for a two-fiber model with more space between fibers, given in Fig. IV.13b. This configuration yields very different behavior than was observed for fibers with very little spacing. When space is introduced between fibers, temperature decrease results in a monotonic increase

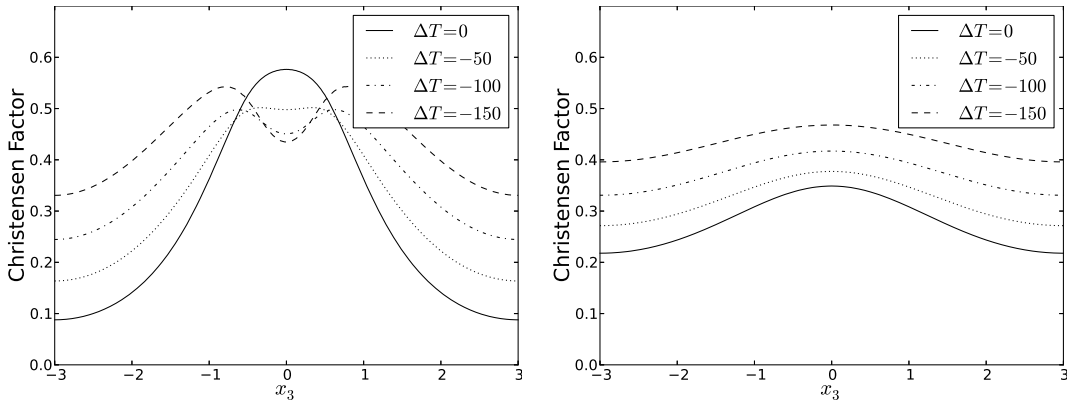

(a) $s = d \times 10^{-3}$ (b) $s = d \times 1/2$

Figure IV.13: Christensen factor along line between fibers under nominal 50 MPa transverse normal load $\langle \sigma_{22} \rangle$ for two fiber spacings at various temperatures.

in the Christensen factor at every location between the fibers. This is likely to result in a completely different relationship between thermal loads and the overall fiber-matrix strength than what is predicted for microstructures in which fibers come very close to one another.

The Christensen factors resulting from interaction between thermally induced stresses and stresses from a longitudinal shear stress of $\langle \sigma_{12} \rangle$ =40 MPa is shown in Fig. IV.14. For both spacings, the maximum Christensen's factor always occurs at the location where the fibers are closest to one another. The maximum factor is more severe when the fibers are closer to one another, indicating that nonlinear behavior will occur in the matrix earlier for microstructures with less space between fibers. The maximum value for the Christensen factor shows very little dependence on temperature when the fibers are close to one another, suggesting that the overall

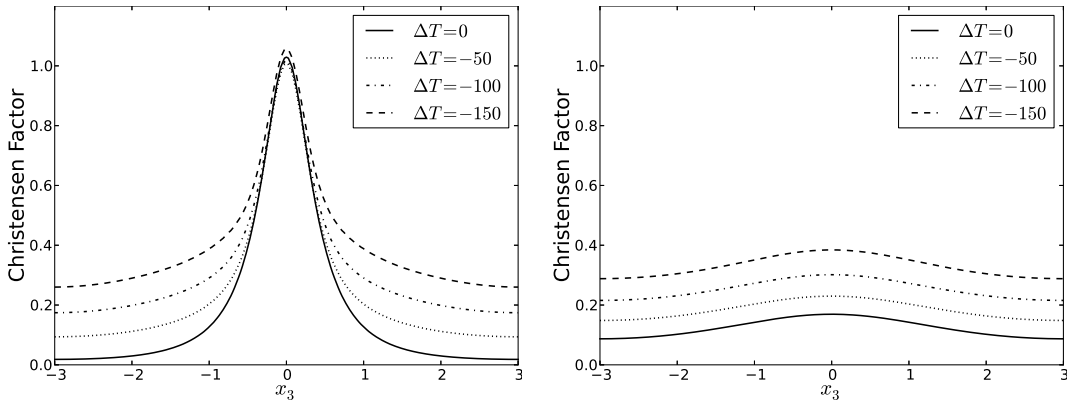

(a) $s = d \times 10^{-3}$ (b) $s = d \times 1/2$

Figure IV.14: Christensen factor along line between fibers under nominal 40 MPa longitudinal shear load $\langle \sigma_{12} \rangle$ for two fiber spacings at various temperatures.

fiber-matrix shear strength for this microstructure may not exhibit a strong dependence on the temperature. The maximum Christensen factor for the model with greater fiber spacing shows a much larger dependence on temperature, indicating that microstructures with different inter-fiber spacing are likely to result in different predictions when determining the dependence of the overall fiber-matrix shear strength on temperature.

IV.D. Failure Model

This section describes the progressive failure model that is used to predict the non-linear failure response of the fiber-matrix RVE. This model is centered around prediction of failure in the matrix regions of the composite. The model assumes perfect bonding between the fibers and matrix. The calculation of failure in the

matrix and the subsequent application of material degradation to failed locations is performed at the quadrature points of the matrix elements. The following sections describe the progressive failure executive, the two different damage laws that are examined, and the approach for determining an apparent tow strength from an ensemble of fiber-matrix realizations.

IV.D.1. Progressive Failure Executive

A flowchart of the general progressive failure executive is given in Fig. IV.15. An analysis proceeds by incrementally increasing the load and then performing damage iterations on that load. At the beginning of each damage iteration, the equilibrium solution is obtained for the current damage state. For each quadrature point which is subject to being damaged, the stress state is examined and the damage state at that location is updated if new failure occurs. If the damage state increases at any location in the model (such that the equilibrium solution would change), then a new damage iteration begins. If no new damage is determined to occur, then the damage state has converged. In that case, the load is increased and damage iterations begin for the new load. This process is repeated until the maximum specified load is reached or some other stopping criteria (e.g. a large drop in strain energy from damage iterations) is met.

IV.D.2. Damage Laws

Two different damage laws were examined for the fiber-matrix model. A damage-law defines how material properties are modified in the presence of a stress which

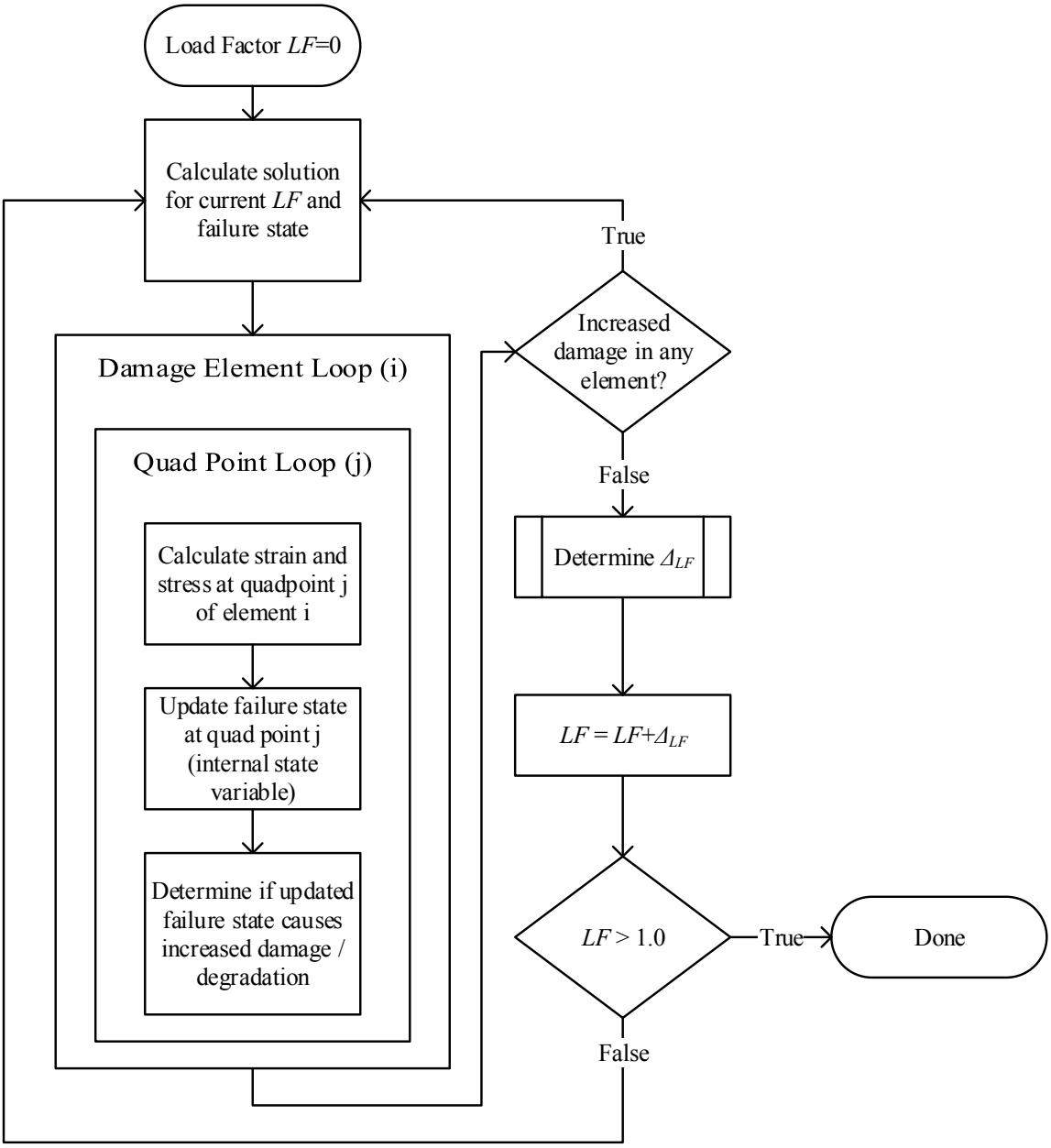

Figure IV.15: Flowchart of damage executive.

exceeds the failure criterion for the material. Both damage laws center around the modification of a damage parameter d for the quad point. This parameter has an initial value of 0.0 and monotonically increases to 1.0 as a quadrature point experiences failure. The stiffness of each quadrature point is scaled by the value $(1.0 - d)$.

IV.D.2.a. Stiffness Deletion

The first damage law examined is referred to as the stiffness deletion damage law. In this damage law, whenever failure is predicted to occur according to Christensen's criterion (Eq. 4.9), the value of d is set to $1.0 - 10^{-6}$. This effectively reduces the stiffness of the quadrature point by a factor of 10^6. The stiffness is not set to zero in ordered to avoid numerical difficulties.

This damage law was found to result in brittle behavior of the composite under both transverse tension (Fig. IV.16) and longitudinal shear (Fig. IV.17). While brittle behavior is expected under transverse tensile loading, longitudinal shear loading of unidirectional composites normally results in lots of nonlinearity in the effective stress-strain response. Additionally, this damage law resulted in failure of the composite at very low volume average longitudinal shear stresses for realistic values of matrix strength. This suggests that under shear loading, the sudden local stiffness loss that occurs in the regions of large Von Mises stress between fibers (see Fig. IV.11) tends to cause unstable damage growth throughout the fiber-matrix. This unrealistic behavior under shear loading casts doubt on the applicability of this damage law to the current problem.

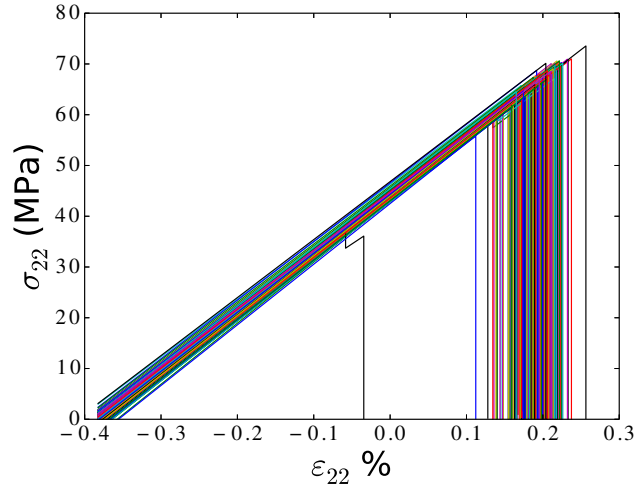

Figure IV.16: Stress-strain behavior under transverse tension using stiffness deletion damage law.

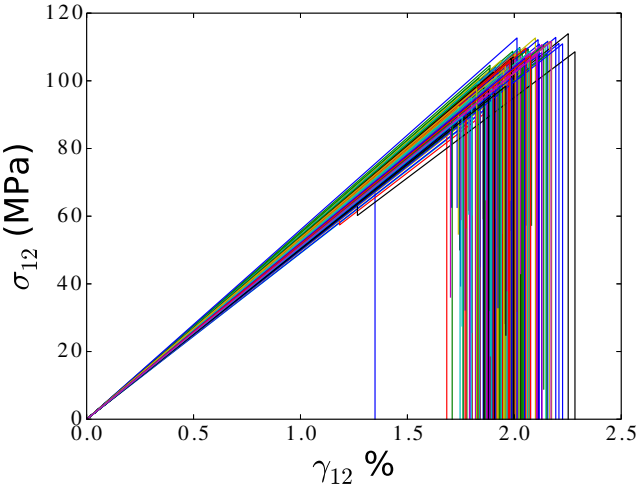

Figure IV.17: Stress-strain behavior under longitudinal shear using stiffness deletion damage law.

IV.D.2.b. Brittle/Ductile

The second damage law is referred to as the brittle/ductile damage law. In this damage law, the increase in d that occurs when failure is predicted by Eq. 4.9 depends upon Christensen's ductile/brittle criterion given in Eq. 4.11. When brittle failure is predicted to occur, d is set to $1.0 - 10^{-6}$, just as in the stiffness deletion damage law. However, when ductile failure is predicted, d is increased by a value of 10^{-3}. This has the effect of gradually reducing the stiffness of material that undergoes ductile failure, which it is hoped will more accurately represent the gradual redistribution of loads that occurs around regions that fail in a ductile manner. The disadvantage of this second damage law is that it requires considerably more damage iterations to reach a converged damage state due to the fact that the d only increases by a small amount at each iteration. This results in longer run-times for progressive failure models using this damage law. However, as seen in Figs. IV.18 and IV.19, while this damage law results in brittle behavior under transverse tension, it predicts the type of nonlinear behavior under longitudinal shear that is expected for a composite material. It also leads to a more realistic maximum volume-averaged shear stress for realistic values of matrix strength. This indicates that gradually degrading regions that fail due to strongly deviatoric stresses under shear prevents the unstable damage growth that was observed for the stiffness deletion damage law.

Further investigations indicated that ultimately, the nature of damage growth in the fiber-matrix model depends primarily on the way that degradation is applied rather than the applied loading. An additional brief study was performed in which the stiffness of the matrix was decreased gradually for all matrix failures (brittle or

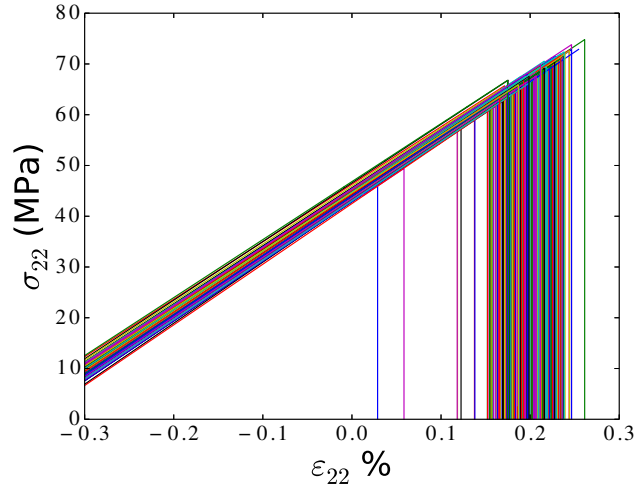

Figure IV.18: Stress-strain behavior under transverse tension using brittle/ductile damage law.

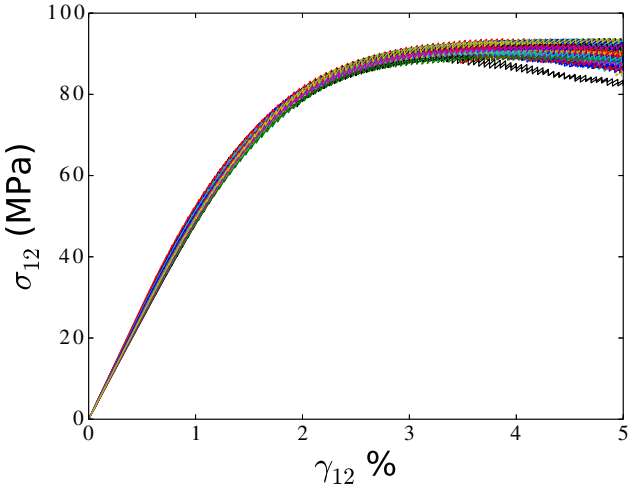

Figure IV.19: Stress-strain behavior under longitudinal shear using brittle/ductile damage law.

ductile). This resulted in transverse normal loading leading to an overall ductile response rather than a brittle one. In short, gradual degradation tends to result in self-arresting failures that yield gradual nonlinear behavior, while complete deletion of the stiffness of a failed element results in unstable growth of the damage and overall brittle behavior. In essence, the "brittle/ductile" damage law correctly predicts the nonlinear response of the composite for longitudinal shear loading because this type of load leads to ductile failure locally and thus gradual degradation. Similarly, transverse tension leads to local brittle failure, and thus complete deletion of the local stiffness, leading to unstable damage growth and brittle behavior overall.

IV.D.3. Typical Progressive Failure Behaviors

The fiber-matrix model experiences distinctly different behaviors under transverse normal loading and longitudinal shear loading when using the ductile-brittle damage law. This section describes typical behaviors observed for the two different loadings.

The failure evolution under transverse normal loading is shown in Fig. IV.20, the initial failure that occurs in the fiber-matrix is ductile failure due to σ_{23} between adjacent fibers which are positioned with centers on a line that makes a roughly 45° angle with the applied load. These ductile failures are self-arresting, tend to occur over extremely small regions, and have a nearly imperceptible effect on the overall stress-strain response of the fiber-matrix unit cell. As the load continues to increase, a brittle failure occurs at a single location between two fibers which are in close proximity and have centers that are aligned with the load direction. Typically, this

brittle failure will proceed to grow in an unstable manner (even for displacement-controlled loading) and propagate into a localized band of damage which completely severs the load path through the unit cell. Therefore, the overall failure behavior under transverse normal loading tends to be brittle and highly dependent on the initial occurrence of brittle failure at a single location in the unit cell. Furthermore, failure tends to evolve into a highly localized feature running through the unit cell, indicating the development of a discrete crack through the composite.

The failure evolution under longitudinal shear loading, shown in Fig. IV.21, represents a significantly different behavior. At very low loadings, ductile failure begins to occur in multiple locations between adjacent fibers whose centers are aligned with the plane in which the shear load is applied. As the load is increased, the regions of damaged matrix gradually increase in size, and the severity of the damage in each region gradually increases. This process results in a gradual reduction of the overall stiffness of the fiber-matrix unit cell, leading to nonlinear stress-strain behavior which is typically seen in longitudinal shear tests of unidirectional composites. As the load is increased further, this diffuse damage continues to increase in magnitude until it finally begins to coalesce into a larger-scale damage feature that crosses the unit cell. The development of this feature, which indicates the formation of a discrete crack, tends to correspond to the unit cell reaching its maximum effective shear stress. Therefore, the overall failure behavior under longitudinal shear tends to be ductile, with stiffness reduction starting at a fairly low load. The damage is initially very diffuse throughout the unit cell, and finally starts to coalesce into a larger-scale fracture as the effective stress reaches its maximum level.

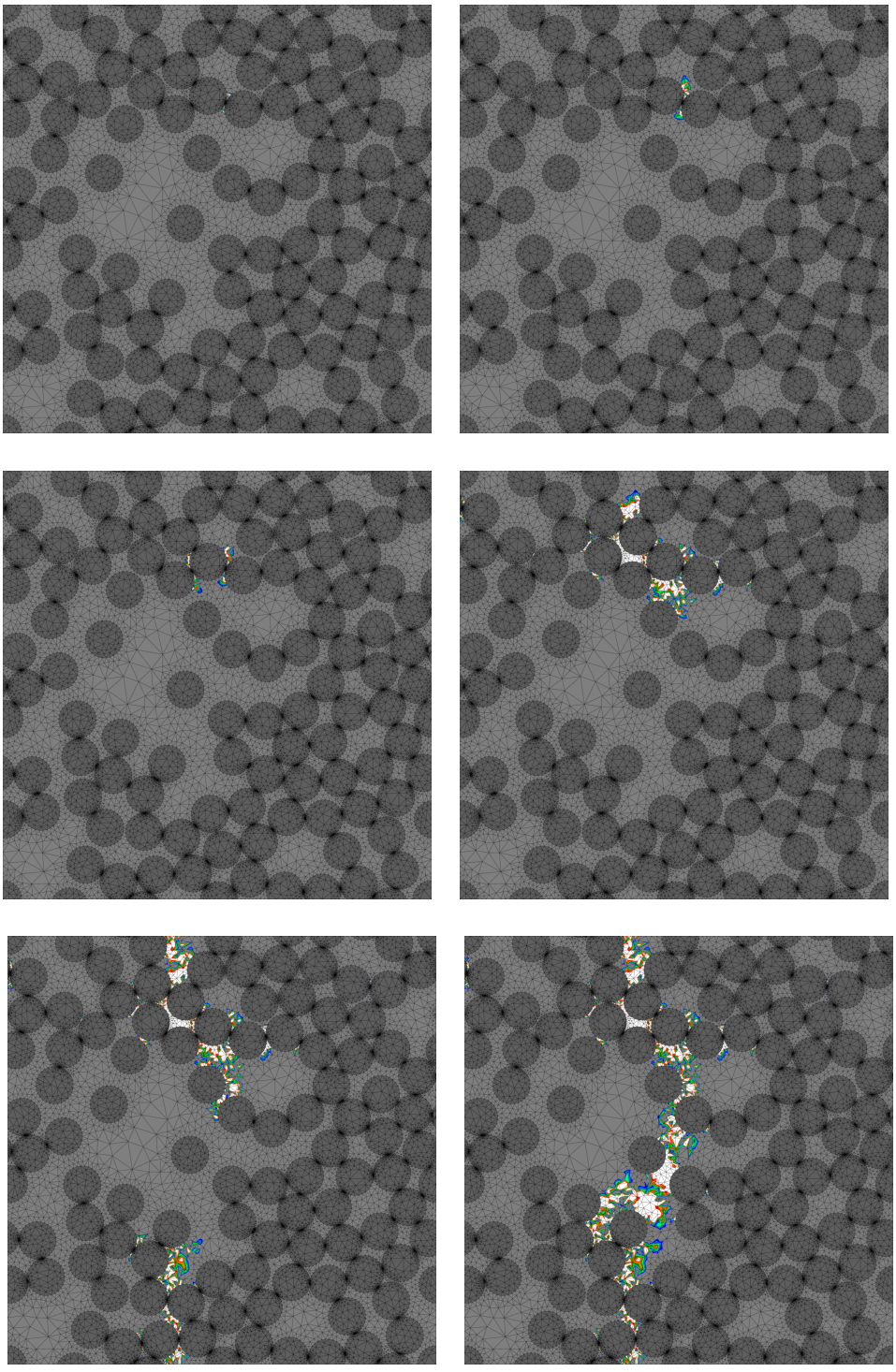

Figure IV.20: Damage scalar evolution under transverse tension.

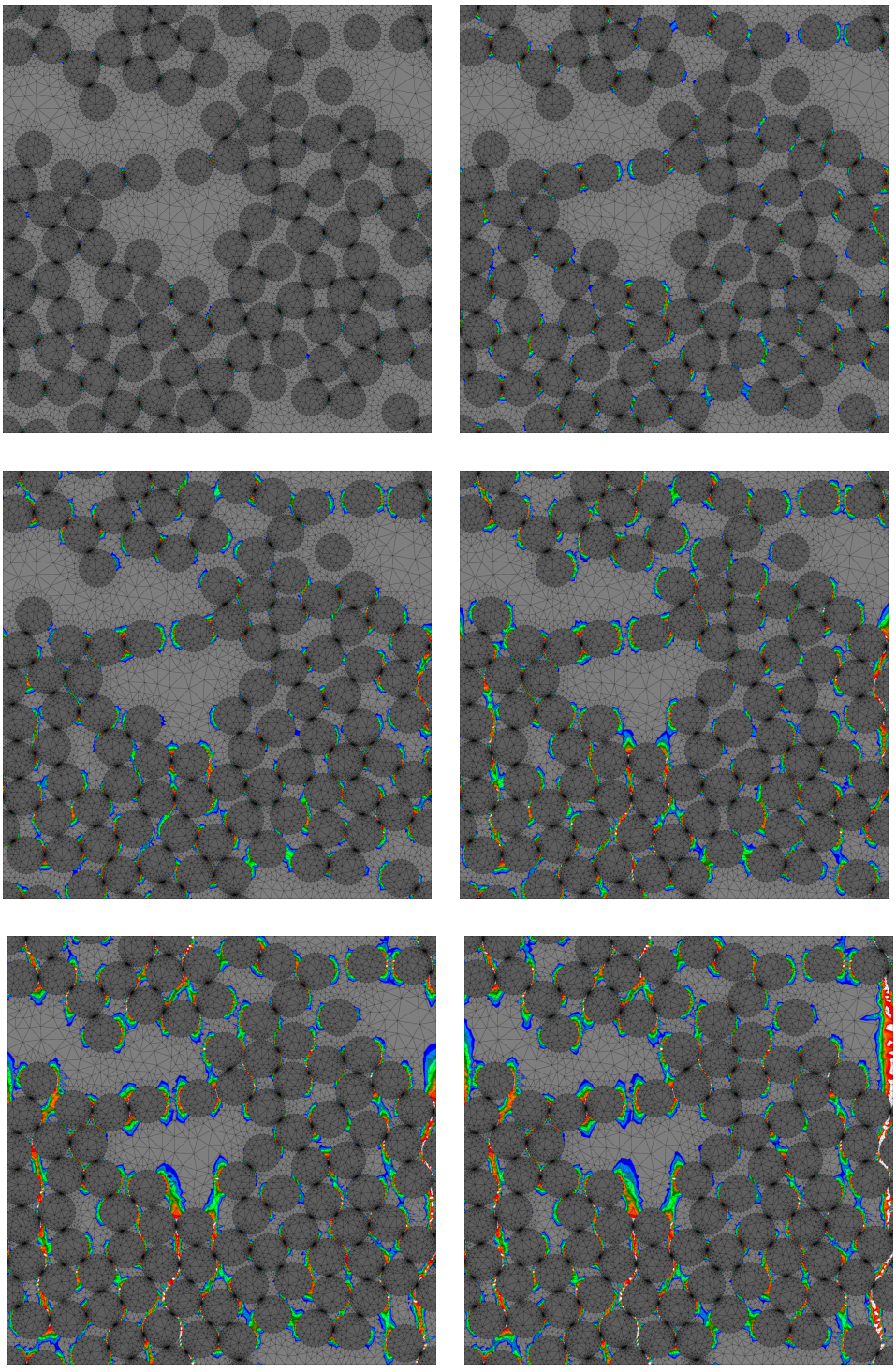

Figure IV.21: Damage scalar evolution under longitudinal shear.

IV.D.4. Tow Strength Determination from Realization Ensemble

Due to the randomness that exists in the fiber-matrix microstructure, an ensemble of fiber-matrix realizations are run for each configuration that is examined. In most cases, this ensemble consists of a little over 200 different realizations. The previously described progressive failure executive is performed for each realization. For each realization, the volume-averaged stresses and strains are tracked as the model undergoes failure. These volume-averaged stresses and strains correspond to the stress and strain that would be observed from a larger scale where fibers and matrix are homogenized in a lamina or tow. Therefore, the maximum volume average stress that is experienced by a realization can be thought of as the strength in some region of a tow or lamina. By obtaining the strengths from a large number of realizations, a distribution can be fit which characterizes the likelihood that a given location in a tow or lamina will have a particular strength. For the current study, the a Weibull distribution, which has a probability density function given by Eq. 4.12, is fit to the realization strengths.

$$f(x) = \begin{cases} \frac{k}{\lambda}\left(\frac{x}{\lambda}\right)^{k-1} e^{-(x/\lambda)^k} & \text{if } x \geq 0 \\ 0 & \text{if } x < 0 \end{cases} \tag{4.12}$$

The Weibull distribution is fully characterized by the scale parameter k and the strength parameter λ. This distribution was chosen due to the fact that it has a lower bound at zero (i.e. it does not admit the possibility of there being a "negative" strength) and because it is commonly used throughout mechanics to characterize strength uncertainty.

IV.E. RVE Size Effects

It was observed in previous sections that failure under transverse tension was found to be quite sensitive to the occurrence of brittle failure at a single location in the unit cell. This finding suggests that failure of a given fiber-matrix unit cell realization will be particularly sensitive to the most critical feature in the microstructure. The larger a given RVE is, the more likely it is to contain a more critical microstructural feature. Additionally, the assumption of periodicity means that when damage occurs at a given location of the unit cell, that same damage exists in every other unit cell. It is important to ensure that the assumption of periodicity does not unduly influence the manner in which damage grows, especially in its early stages. This will be the case if the RVE is large enough so that a damage feature in one unit cell has a negligible effect on the stress state around the same damage feature in an adjacent unit cell.

These aspects of the RVE size were examined by running analyses for a variety of RVE sizes, ranging from just a few fibers up to 400 fibers. Only the behavior under transverse tension was examined, since this failure tends to be very sensitive to the first occurrence of brittle failure at any location in the unit cell. The response under longitudinal shear loading is not sensitive to the first failure, and is the result of a large number of small damage features distributed throughout the RVE, which should make this behavior fairly insensitive to RVE size. For each RVE size examined, about 800 realizations were examined to fully characterize the predicted distribution of strengths.

As shown in Fig. IV.22, it was found that as the RVE size was increased, the

width of the strength distribution decreased. There was a fairly rapid drop in the top-end of the distribution while the lower end of the distribution remained more consistent. The mode of the distribution, (the most likely value of the strength, or the value with the highest probability density) also decreased towards the minimum value. This supports the idea that failure depends on a critical feature, and that it is more likely that more severe features will exist in larger RVEs. The lower end of the distribution is determined by the behavior associated with the most critical microstructure possible, and therefore this lower limit doesn't experience large changes as the RVE size is increased since some of the smaller RVE realizations will contain severe microstructural features which result in lower strength values. However, larger RVE sizes tend to have more critical features, meaning that the maximum strength value larger RVEs yield is less than the maximum strength for smaller RVE sizes.

Beyond reinforcing the conclusion that the strength of a unit cell under transverse tension is heavily dependent on the most critical feature that exists in the unit cell, this study also provides some guidance when it comes to matching the strength distribution to experimentally obtained data. The next section describes the process of inversely determining the in-situ matrix strength that causes the fiber-matrix model to predict the same strength that is obtained from testing of a unidirectional composite specimen. This requires comparing a distribution of strengths from many realizations of the microstructure to a single value from experiments. However, one may consider a unidirectional composite specimen to be a very, very large RVE. Therefore, based on the findings of this section, one can make the argument that the strength obtained from a unidirectional composite can be related to the bottom

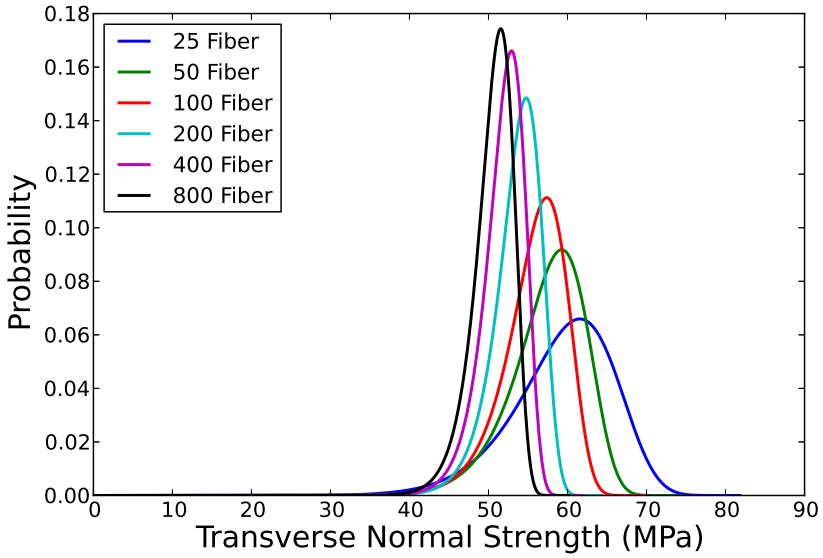

Figure IV.22: Transverse normal strength dependence on RVE size

end of the strength distributions for smaller RVE sizes since the bottom end of the distribution stays fairly consistent across different RVE sizes, and larger RVEs tend to yield strengths which are closer to this minimum threshold for the strength.

In addition to examining the resulting strength distributions for different RVE sizes, the applied stress associated with failure initiation and the subsequent ultimate strength were examined for the realizations to determine if a correlation existed between the two values. No meaningful relationship was observed from this investigation. This result was somewhat expected since it was observed that failure initiation tended to be related to limited ductile failure between fibers and ultimate failure tended to be associated with the onset of brittle failure in the composite which grew in an unstable manner.

IV.F. Determination of In-Situ Matrix Strength

Once an adequate RVE size has been determined for progressive failure analysis of the microstructure, the final step in developing a micromechanics model is the determination of the appropriate matrix strength values. These values were determined in an inverse fashion from experimentally determined lamina strengths due to the fact that the behavior of the matrix within a composite may change when compared to the behavior of neat matrix specimens. This is due in large part to the highly constrained nature of the stresses in the matrix due to the proximity of the much stiffer fibers. Additionally, there is a possibility of chemical interaction between the fibers and matrix which could alter the matrix properties. Therefore, the micromechanics model will be utilized to determine what values of T and C in the matrix result in lamina strengths that match experiments. Since the lamina strengths are obtained at room temperature, a temperature change of $\Delta T = -160^{\circ}$ is applied to the composite to account for the presence of thermally induced stresses and strains from cooling after cure. This temperature change was also utilized by Hallett et al. [11] to account for the thermally induced stresses in IM7/8552 laminates. The process for inversely determining the in-situ strength is outlined in Fig. IV.23. To start the process, the lamina strength distributions under transverse tension and longitudinal shear are determined for three different combinations of T and C in the matrix. These are obtained using at least 200 realizations of RVEs containing 100 fibers. Based on these predictions, the gradients of the 5th percentile of the lamina strength distributions with respect to the in-situ matrix strengths T and C are estimated by assuming that the resulting lamina strengths vary linearly with T and C. These gradients are used

to predict the T and C values which will yield 5th percentile lamina strengths which match the experimental lamina strengths under transverse tension and longitudinal shear. The lamina strength distributions for the new guess of T and C are obtained, and new gradients are calculated using the improved prediction along with the two best previous predictions of T and C. This process is repeated iteratively until a T and C value are identified which yield strength distributions with 5th percentile values that match the experimental strengths within 1%.

The first attempt at determining in-situ matrix strength values was made using the quadrature point deletion approach to material degradation. As described in previous sections, in this approach, the stiffness contribution of a quadrature point is completely deleted when the stress at that quadrature point reaches a level sufficient to cause failure. As was previously described, while this approach yielded the expected brittle behavior under transverse tension, it also yielded brittle behavior under longitudinal shear. That behavior is not in agreement with general observations of composite material behavior. Also, it was noted that the shear stresses in the fiber-matrix unit cell under longitudinal shear loading tended to give rise to failure at very low loadings. Since the subsequent behavior was brittle, this initial failure subsequently led to low strengths in the composite under shear loading. In ordered to obtain a shear strength that matched the experimentally observed value for a unidirectional laminate, it was necessary to delay the onset of shear failure by increasing the compressive strength of the matrix to an unrealistically large value (about 2.6 GPa) and increasing the tensile strength of the matrix to a fairly large value of 239 MPa. These large values were completely driven by the shear response

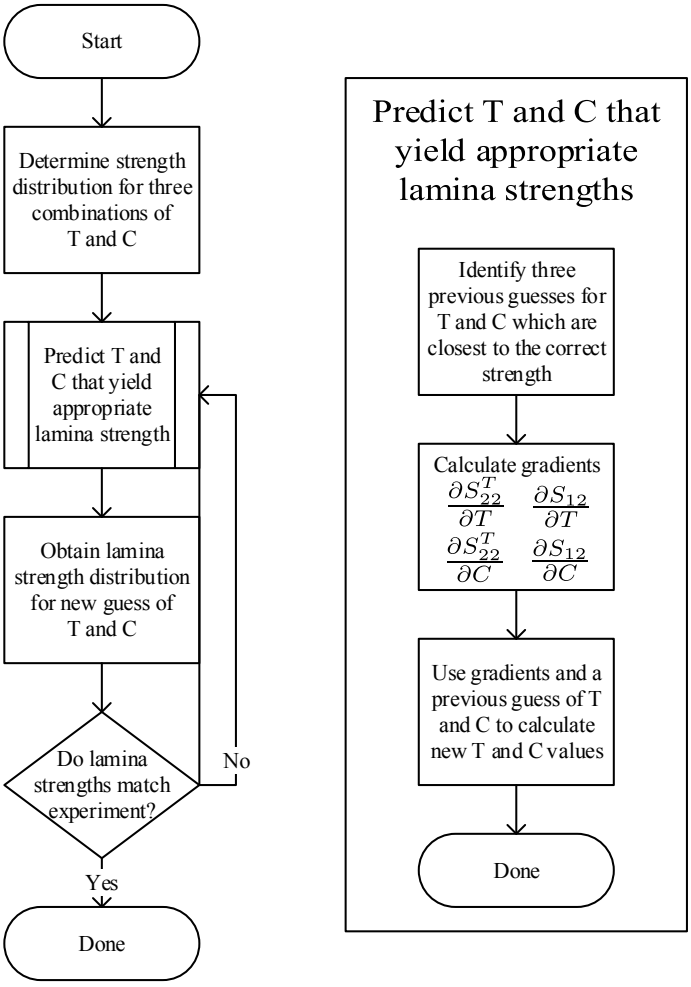

Figure IV.23: Approach for determining in-situ matrix strength

of the composite; if only transverse normal loading was considered, there were more realistic combinations of T and C which yielded the appropriate lamina strength (although it is not possible to determine a unique combination of T and C using a single lamina strength).

These results were not deemed to be satisfactory for simulation of failure in the fiber-matrix. The particularly problematic aspect about them was the fact that under shear, the onset of failure led to unstable growth of damage in a similar manner to transverse tension. After some investigation, it appeared that this was likely due to the fact that the stress state experienced by the matrix under shear would tend to cause local ductile failure of the matrix rather than a brittle failure. As a result, it was decided to utilize the ductile-brittle aspect of Christensen's failure criterion along with the previously described ductile/brittle damage law. In this way, the more gradual redistribution of stresses that occurs under ductile failure and plastic flow could be more closely approximated by gradually degrading material which is experiencing stresses which cause ductile failure and yielding. While plasticity is not directly modeled in the sense that there is no accounting for the existence or flow of plastic strain, the local stress-strain response of the material as it undergoes failure bears strong similarity to an elastic-plastic response so long as significant unloading doesn't occur (which was observed to be the case for these configurations).

When this modification was applied to the fiber-matrix analysis, the behavior under shear loading completely changed. As described in previous sections, the brittle/ductile damage law resulted in a brittle response under transverse tension and a ductile response under longitudinal shear. Since the initiation of shear failure

no longer resulted in unstable failure of the fiber-matrix unit cell, it was no longer necessary to artificially increase the matrix strength to delay failure onset. The appropriate lamina strengths were obtained using matrix strengths of much more reasonable values - a tensile strength of 128 MPa and a compressive strength of 204 MPa. Although the objective of this investigation is not to match the neat matrix strength values exactly, it is expected that the in-situ strength should be at least somewhat similar. These values compare well to the manufacturer listed [160] room-temperature tensile strength for 8552 epoxy of 121 MPa as well as the tensile and compressive strengths of 95 MPa and 180 MPa for a somewhat similar Epon 862 neat resin determined in experiments by Littell et al. [161] (neat resin compressive strengths for 8552 epoxy could not be located in the literature).

IV.G. Thermal Stress Effects

Once the in-situ matrix strengths were determined, it was possible to determine the effect that thermally induced stresses have on the apparent strength of a tow or lamina. To accomplish this, the fiber-matrix microstructural realizations were analyzed for a series of thermal loadings that represented various increases above room temperature. Weibull distributions were fit to the strength distributions obtained at each temperature for transverse tensile and longitudinal shear loading. These distributions, along with the 5th percentile strength from the distribution are listed in table IV.4. The 5th percentile strengths for transverse tensile load are plotted in Fig. IV.24. For the random microstructure, it was found that the overall tow strength under transverse tension tended to decrease as the temperature was increased above

Table IV.4: Weibull parameters for fiber-matrix strength at various temperatures. K is the shape parameter and λ is the scale parameter.

	Normal			Shear		
ΔT	K	λ (MPa)	5th % (MPa)	K	λ (MPa)	5th % (MPa)
-160	23.96	68.38	60.40	134.73	92.52	90.50
-135	25.99	67.80	60.48	143.40	92.97	91.06
-110	24.24	66.41	58.76	102.38	93.24	90.58
-85	24.13	64.17	56.74	135.35	93.70	91.66
-60	22.45	61.17	53.59	111.09	94.01	91.53
-35	21.08	57.47	49.92	140.82	94.50	92.53
-10	17.24	53.61	45.12	141.10	94.82	92.84

room temperature, while the strength under longitudinal shear load was fairly insensitive to temperature. This result is in good agreement with the conclusions which were drawn from the linear analysis into the microstructural stresses under thermomechanical loads.

As part of this investigation, a brief side-study was also conducted on a hexagonal unit cell. The unit cell orientation associated with the closest fiber spacing in the load direction, which results in the highest stresses between fibers, was chosen. A calibration of the in-situ strengths was performed for this configuration by maintaining the $T : C$ ratio determined from the random microstructure and identifying the strengths that caused the hexagonal unit cell to result in a strength of 60 MPa under transverse tension at room temperature. Once appropriate matrix strengths were determined for the hexagonal unit cell, its overall strength under transverse normal loading was determined for a variety of temperatures. The resulting strengths are also provided in Fig. IV.24. This investigation demonstrates that the two different

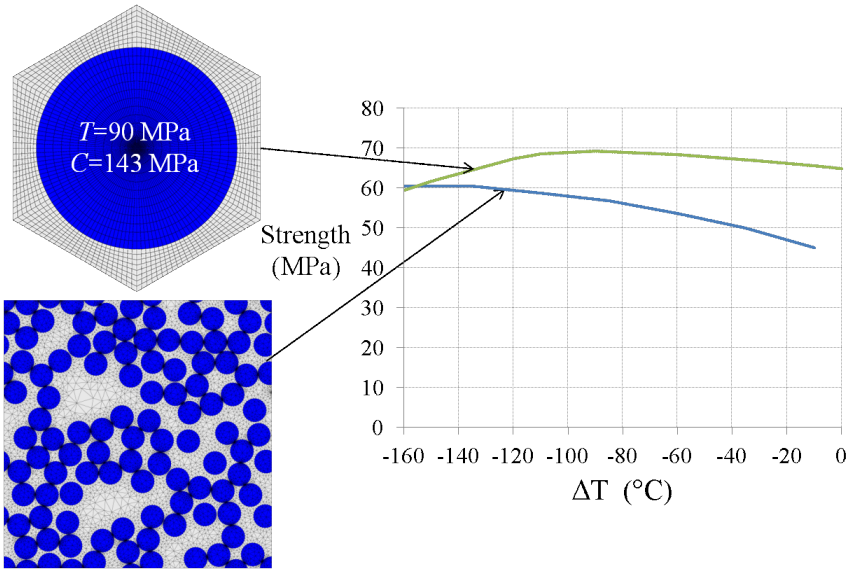

Figure IV.24: Variation of 5th % transverse normal tensile strength with ΔT from cure.

microstructures predict significantly different thermal dependence for tow or lamina strength. The hexagonal unit cell predicts an initial increase in the tow strength as temperature is increased above room temperature, which is in agreement with the predictions from the linear investigations for fibers which are not in very close proximity.

The conclusion drawn from the random microstructure model that thermally induced stress from temperature increases (relative to room temperature) decrease the tow and lamina strength (or conversely, that thermally induced stresses from cooling after the curing process tend to strengthen the composite) differs from the conclusions stated in a number of previous works that examined the effect of thermally-induced stresses on failure. The overall tendency of a composite's transverse strength to

decrease under increasing load has been generally observed, but often times, it has been supposed that this decrease is purely the result of the thermal dependence of the constituent properties (e.g. a decrease in the matrix strength with increasing temperature), and that the thermally induced stresses tend to counter-act this effect (for instance, this was the conclusion of Miyano et al. [162]). The majority of these studies, however, did not account for the close proximity of the fibers. As shown by the investigation into the hexagonal unit cell, microstructures with fibers that have more spacing tend to predict a different thermal dependence than more realistic random microstructures. While some recent work has demonstrated that thermally induced stresses from cooling after cure can counter-act the effect of transverse tensile loads in the context of fiber-matrix debonding (Hojo et al. [84]), to the author's knowledge this is the first work to demonstrate that the temperature drop after cure increases the mechanical load required to cause matrix failure in the composite under transverse tension.

CHAPTER V

TEXTILE UNIT-CELL MODEL

In addition to the characterization of damage and failure carried out at the microstructure, the behavior of the textile was investigated. The following sections detail the development of the textile-scale model as well as investigations that were carried out regarding failure initiation behavior and progressive failure behavior. The final section describes the development of a continuum damage model for textile materials that can be applied to structural level analyses.

V.A. Textile Unit-cell Model Development

V.A.1. Geometry

The textile unit cell analysis is performed on an idealized textile geometry shown in Fig. V.1. This geometry has been utilized in a number of investigations into textile composite behavior by Whitcomb et al. [10, 109–113, 123, 126, 163]. Ultimately, the geometry of this textile is defined by the waviness ratio WR, defined in Eq. 5.1.

$$WR = \frac{t}{w} \tag{5.1}$$

This fiber-matrix unit cell consists of tows which have a sinusoidal path as well as sinusoidal cross-sections with boundaries which follow different phases of equations of the form given in Eq. 5.2.

$$z = \pm\frac{t}{4}\sin\left(\left(2\pi\right)\left(WR\right)x\right) \tag{5.2}$$

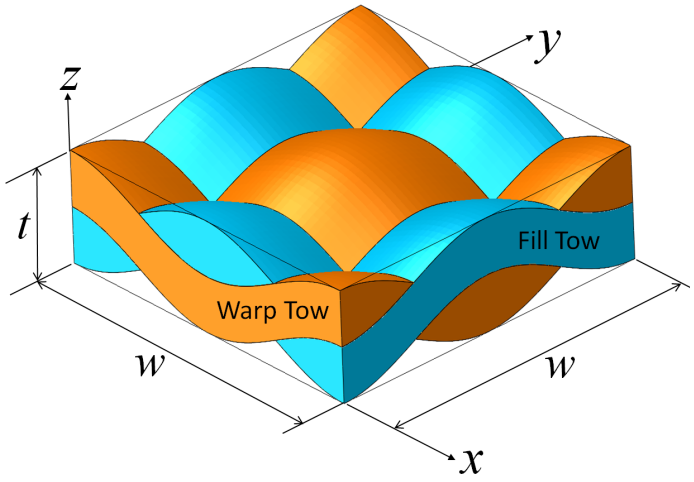

Figure V.1: Dimensions of textile unit cell

This results in a unit cell with no gap between the tows.

V.A.2. Insertion of Cohesive Zones

Due to the tendency of failure in the textile to localize into discrete cracks for a variety of loadings, most damage in the textile is modeled discretely using interfacial elements with opening governed by a cohesive zone formulation. Interfacial elements are inserted along the tows to model matrix cracking within the tows, within the neat matrix pockets to model fracture within the matrix, on the interfaces between adjacent tows to model "delamination" between tows, and on the interface between the tow and neat matrix pockets to model fracture growth along the tow surface. The development of this model presented several difficulties. The first is the insertion of cohesive elements into the model. This was accomplished by developing a meshing utility that inserts cohesive elements between any two adjacent elements that are in different element groups. Each tow was assigned two different alternating element

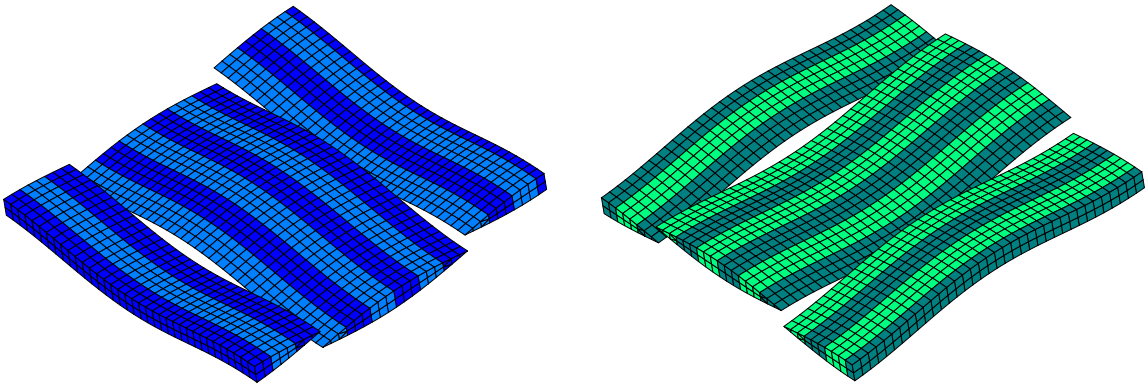

Figure V.2: Element group definition in tows.

groups as shown in Fig. V.2. The matrix was then assigned four different element groups in a checkerboard type of pattern, as shown in Fig. V.3. Once these element group assignments were completed, cohesive interface elements were inserted between the different groups as shown in Fig. V.4. In practice within the script used to generate the meshes, as well as in the analyses themselves, an "element group" was defined using a unique material identifier, with multiple material identifiers referring to the same set of material properties.

The second significant challenge associated with developing models using cohesive zones was the definition of periodic boundary conditions. In the FEA analysis code, collections of nodes are defined for the prescription of boundary conditions by defining the geometry of the node collection. For example, the collection of nodes on the negative x face of the unit cell are defined using the coordinates A, B, and C given in Fig. V.5, and the collection of nodes on the positive x face are defined using coordinates A', B', and C'. The nodes in each collection are sorted according to their location relative to the coordinates used to define the collection. This ensures that

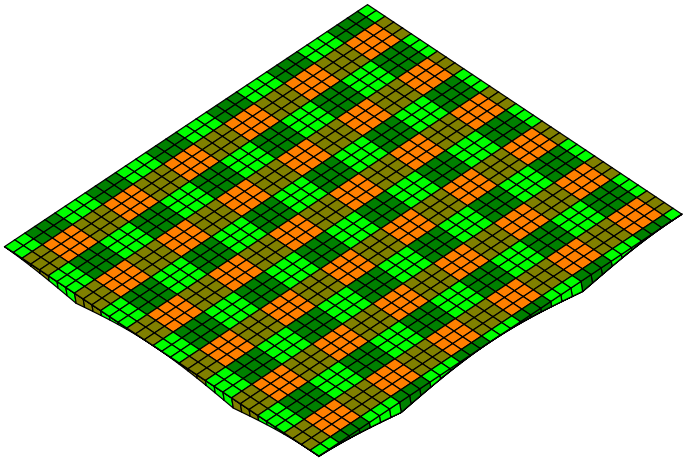

Figure V.3: Element group definition in matrix pockets.

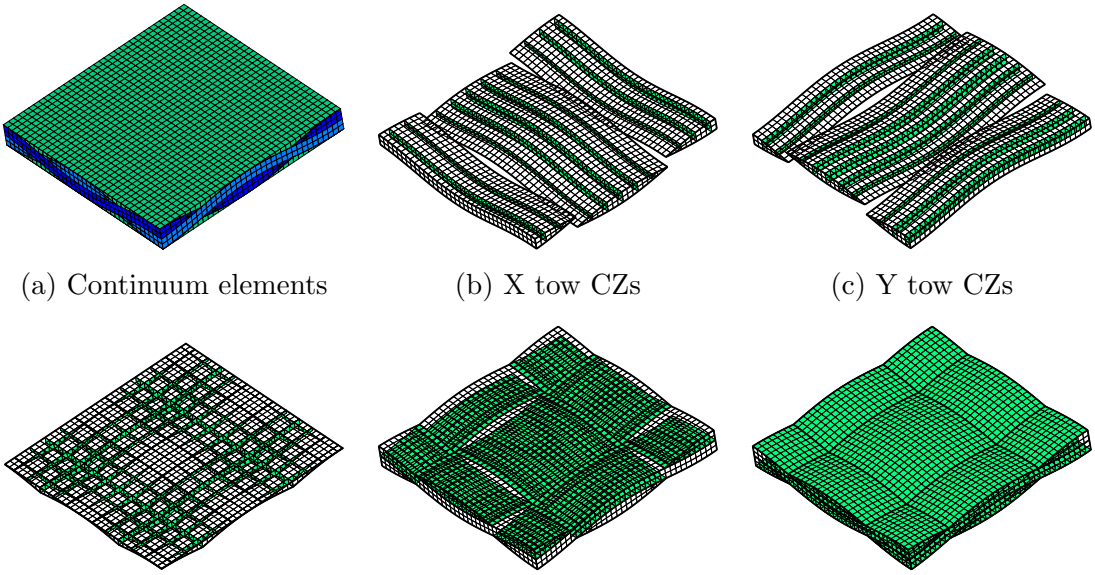

(a) Continuum elements (b) X tow CZs (c) Y tow CZs

(d) Matrix pocket CZs (e) Inter-tow CZs (f) Inter-tow-matrix CZs

Figure V.4: Textile unit cell with cohesive zones (CZs).

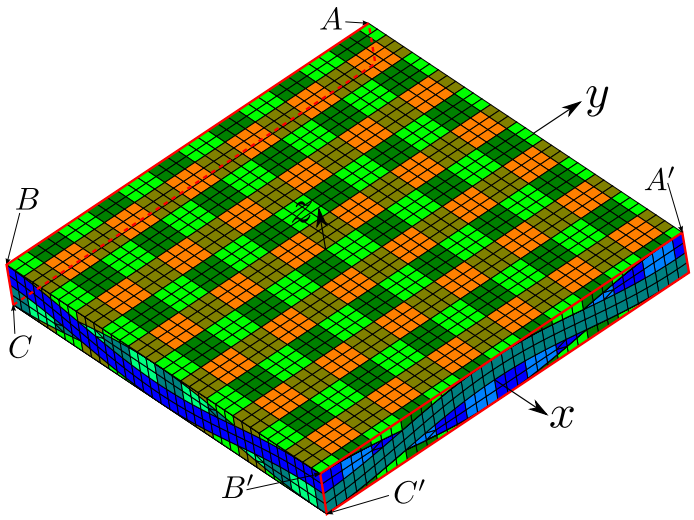

Figure V.5: Planes for x-direction periodic boundary conditions.

the appropriate nodes are constrained to one another using multi-point constraints.

The introduction of cohesive elements to the model presents a problem with this approach. Because the interfacial elements have zero thickness, there are locations on the unit cell boundary that contain multiple coincident nodes. This means that appropriate pairing of nodes cannot be accomplished by sorting the nodes based on their position relative to a set of coordinates, because the ordering of coincident nodes will not be well defined using such an approach. This will almost assuredly lead some pairs of nodes being constrained across interfaces when they should not be. This problem was addressed by adding functionality to the FEA code to remove nodes from a collection based on whether or not they are connected to a given element group. This enabled the creation of multiple node collections for each of the unit-cell surfaces where for each node collection, there are not any nodes that share the same coordinate. Node ordering in these collections is well defined, and so multi-point

constraints can be applied to these collections without fear of tying nodes across cohesive interfaces.

One other challenge that was encountered was the presence of cohesive elements running along the unit-cell boundary. This was addressed by shifting the unit-cell boundaries by one element width in the x and y directions. This shift can be noted in Fig. V.4 in that the unit cell boundary does not lie on the center of the tows, but rather is offset one element away from the center. This shift foils the symmetry of the unit cell which can allows analysis of a reduced domain (as in [113]), but such reductions are not possible in cases where combined normal and shear loads are being considered.

V.B. Failure Initiation Prediction

Before undertaking the task of identifying characteristic progressive failures in a composite material, an investigation was made into failure initiation behavior. The primary goal of this work was to determine if failure initiation in a composite could be reduced down to a few characteristic behaviors, even for a broad variety of applied loadings. This was accomplished by developing a tool which superposed linear stress solutions and interrogated the stress field to determine where failure initiated in the textile unit cell. This approach, as well as the findings obtained using it, are described in the following sections.

V.B.1. Theory for Predicting Failure Initiation Under Various Loadings

The following sections describe the approaches used to determine the stress state in the textile for an arbitrary thermomechanical loading, determine where failure initiates in the textile for a given loading, and group failure initiation behaviors for a large number of loads into characteristic behaviors.

V.B.1.a. Stress Superposition Method

This study involves examining the stress field in a textile unit cell for thousands of different stress states. Obtaining this many stress fields directly using finite element analysis presents several challenges. The application of mixed normal and shear loading precludes the use of reduced analysis domains described in [113] (the failure initiation investigation does not include the use of interfacial elements and shifting of the unit cell boundaries, and therefore, the geometric symmetries required for a reduced-domain analysis are preserved in this investigation), and the finite element analysis for a full textile unit cell would take on the order of a few minutes for each load case examined. However, this investigation only focuses on failure initiation. By assuming that the response of the textile is linear up to failure initiation, it becomes possible to utilize superposition to expedite the process of obtaining a stress field for a given multiaxial loading. This process is accomplished in the following manner.

Finite elements is utilized to obtain stress field for a single component of loading. The loads that are considered in the current study include volume average stresses $\langle \sigma_{ij} \rangle$ that correspond to the stress observed at larger scales as well as a uniform temperature change ΔT. Finite element analysis is used to obtain the stress field

for an individual loading component with unit magnitude. These stress fields are denoted as $\sigma_{ij}^{\langle\hat{\sigma}_{kl}\rangle}(x,y,z)$ and $\sigma_{ij}^{\Delta\hat{T}}(x,y,z)$, where the superscript indicates the unit loading that was applied to obtain the stress field. Because the stress fields correspond to the application of a unit load, the stress field for a particular multiaxial thermomechanical loading can be obtained through superposition according to 5.3 in a fraction of the time required for a full finite element analysis of the unit cell under a the same thermomechanical load state.

$$\sigma_{ij} = \Delta T\sigma_{ij}^{\Delta\hat{T}} + \langle\sigma_{11}\rangle\sigma_{ij}^{\langle\hat{\sigma}_{11}\rangle} + \langle\sigma_{22}\rangle\sigma_{ij}^{\langle\hat{\sigma}_{22}\rangle} + \langle\sigma_{33}\rangle\sigma_{ij}^{\langle\hat{\sigma}_{33}\rangle} + \langle\sigma_{23}\rangle\sigma_{ij}^{\langle\hat{\sigma}_{23}\rangle} + \langle\sigma_{13}\rangle\sigma_{ij}^{\langle\hat{\sigma}_{13}\rangle} + \langle\sigma_{12}\rangle\sigma_{ij}^{\langle\hat{\sigma}_{12}\rangle} \tag{5.3}$$

By examining the stress fields for a large number of different combinations of thermomechanical loading components and predicting the failure initiation behavior for each, characteristic behaviors can be identified. The approach to accomplishing this is outlined in the following sections.

V.B.1.b. Determination of Failure Initiation Load

Determining where failure will initiate in the textile for a given applied loading is in most cases more complicated than simply determining where a failure criterion goes to a maximum value. This is because, for most criteria, failure does not occur until the criterion reaches a critical value, which is coupled with the fact that most failure criteria are nonlinear in terms of stress. Therefore, the problem that must be solved is that of determining where in the textile the failure criterion will first reach a critical value as the magnitude of a given proportional load applied to the textile is increased. A further complication is that for thermomechanical loading, it

is likely that one will want to determine failure initiation under a given proportional mechanical loading for a fixed thermal state.

The following approach is adopted to solve these challenges. First, the failure criterion is expressed in the manner of Eq. 5.4.

$$f\left(\sigma_{ij}^{crit}, F_{\alpha}\right) = 0 \tag{5.4}$$

That is, the criterion f yields zero when a critical stress state σ_{ij}^{crit} is reached for some set of material strength parameters F_{α}. Take for example the Tsai-Wu criterion, given in Eq. 2.1. Expressing this equation in the form given by Eq. 5.4 yields Eq. 5.5.

$$F_{\alpha}\sigma_{\alpha}^{crit} + F_{\alpha\beta}\sigma_{\alpha}^{crit}\sigma_{\beta}^{crit} - 1 = 0 \tag{5.5}$$

Next, the critical stress is divided into a fixed component σ_{ij}^{fixed} and a component that scales with the applied proportional loading $\sigma_{ij}^{scalable}$, given in Eq. 5.6.

$$\sigma_{ij}^{crit} = \sigma_{ij}^{fixed} + \lambda^{crit}\sigma_{ij}^{scalable} \tag{5.6}$$

λ^{crit} is the scaling factor that results in a critical stress. Determining the applied loading that will cause failure at a given location then becomes a matter of solving Eq. 5.4 for λ^{crit}. In many cases, such as for the Tsai-Wu criterion and any other criterion that is quadratic in terms of stress, this will require the solution of the quadratic equation. Typically only the positive root from the equation is of interest, since the negative root would indicate load reversal. For some other criteria, however, such as those related to Mohr-Coulomb (i.e. Puck's criterion) or principle stresses, it is not tractable to analytically solve for λ^{crit}. Such cases will generally depend on numerical root-finding algorithms. For multi-part criteria, such as that put forward

by Puck or Hashin, λ^{crit} must be determined for each part of the criterion, and the minimum value of λ^{crit} for any part of the criterion determined. The part of the criterion which yields the minimum value for λ^{crit} indicates which aspect of the criterion will be exceeded first (i.e. it indicates what mode of failure will occur). The determination of failure initiation in the entire textile is accomplished by identifying the minimum value of λ^{crit} at any location in the textile. This global minimum value represents the scaling that must be applied to the loading to cause failure initiation in the textile, and the location of this global minimum value of λ^{crit} is the location of failure initiation.

V.B.1.c. Identification of Characteristic Failure Initiation Behaviors

Two aspects form the basis for reducing all of the failure initiation behaviors predicted for a given set of loadings down to a collection of a few characteristic behaviors. The first is failure location, and the second is the nature of the local failure at that location. If multiple loads result in failure in the same location of the textile, and the nature of the failure there is the same (e.g. transverse tensile failure as predicted by Hashin's criterion), then those loads are said to result in the same characteristic failure initiation behavior.

Failure prediction in the textile was accomplished by using either the Tsai-Wu tensor polynomial failure criterion or Hashin's criterion to predict failure within the tows, and Christensen's criterion, described in section IV.C.1, to predict failure in the pockets of neat matrix. Hashin's criterion, described in detail in [42], is a multi-part criterion which predicts one of four modes of failure - longitudinal tension and

compression, and transverse tension and compression. The implementation utilized in the current work predicts longitudinal failure using max-stress criteria of the form given in Eq. 5.7 (expressed in the form of 5.4).

$$\begin{cases} \dfrac{\sigma_{11}^{crit}}{S_L^T} - 1 = 0 & \sigma_{11}^{crit} > 0 \\ \dfrac{\sigma_{11}^{crit}}{S_L^C} - 1 = 0 & \sigma_{11}^{crit} < 0 \end{cases} \tag{5.7}$$

S_L^T and S_L^C are the strengths of the composite under longitudinal tension and compression, respectively. Transverse failure under tension or compression is predicted using the quadratic criteria given in Eq. 5.8

$$\begin{cases} \dfrac{1}{\left(S_T^T\right)^2}\left(\sigma_{22}^{crit}+\sigma_{33}^{crit}\right)^2 + \\ \dfrac{1}{\left(S_{TT}\right)^2}\left(\left(\sigma_{23}^{crit}\right)^2+\sigma_{22}^{crit}\sigma_{33}^{crit}\right) + & \left(\sigma_{22}^{crit}+\sigma_{33}^{crit}\right) > 0 \\ \dfrac{1}{\left(S_{LT}\right)^2}\left(\left(\sigma_{12}^{crit}\right)^2+\left(\sigma_{13}^{crit}\right)^2\right) - 1 = 0 \\ \\ \dfrac{1}{S_T^C}\left[\left(\dfrac{S_T^C}{2S_{TT}}\right)^2 - 1\right]\left(\sigma_{22}^{crit}+\sigma_{33}^{crit}\right) + \\ \dfrac{1}{4\left(S_{TT}\right)^2}\left(\sigma_{22}^{crit}+\sigma_{33}^{crit}\right)^2 + & \left(\sigma_{22}^{crit}+\sigma_{33}^{crit}\right) < 0 \\ \dfrac{1}{\left(S_{TT}\right)^2}\left(\left(\sigma_{23}^{crit}\right)^2+\sigma_{22}^{crit}\sigma_{33}^{crit}\right) + \\ \dfrac{1}{\left(S_{LT}\right)^2}\left(\left(\sigma_{12}^{crit}\right)^2+\left(\sigma_{13}^{crit}\right)^2\right) - 1 = 0 \end{cases} \tag{5.8}$$

S_T^T and S_T^C are the transverse composite strengths under uniaxial transverse tension and compression, respectively. S_{TT} and S_{LT} are the composite shear strengths in the plane perpendicular to the fibers and in a plane that is aligned with the fibers, respectively. These criteria are used to predict the load-scaling to failure at a location

as well as what mode of failure will occur at that location. When the Tsai-Wu tensor polynomial criterion is utilized to predict failure, the local failure mode was ascertained by identifying the stress component at the failure initiation location which had the greatest value relative to its respective strength.

A broad array of multiaxial loadings were prescribed for the textile unit cell. For each loading, the location of failure initiation and the mode of failure that occurs at that location were determined and stored in a database along with the critical loading value to cause that failure initiation. Once the failure initiation behaviors for each load were determined, they were processed into "bins". Each "bin" contains failure initiation behaviors for different loadings which share similar location and local failure mode. The following approach was used to process each load case's failure initiation behavior in to the bins:

1. Examine each "bin" of characteristic failure behaviors to see if the current failure initiation behavior can be put into that bin, based on whether both of the following criteria are true:

    - The location of the current failure initiation is within a given proximity of at least one failure initiation behavior in the bin
    - The local mode of failure for this behavior is the same as the mode for the initiation behaviors in the bin

2. If the current failure initiation behavior can be placed into multiple bins, then all of the bins it can be placed into are combined and it is placed into the combined bin

3. If the current failure initiation behavior cannot be placed into any bin, then it represents a new characteristic behavior and is placed into a new bin

Once the failure initiation behaviors for all loadings have processed in this manner, the bins represent the total number of characteristic failure initiation behaviors that can occur for the textile under the examined loadings.

V.B.2. Characteristic Failure Initiation Locations in Plain Weave Textile Composites

A study was undertaken into the failure initiation behaviors for several different textile composite configurations for a broad variety of loadings. The results of this study were presented in [164] and are summarized in the following subsections.

V.B.2.a. Configurations

This study investigates the response of textiles with waviness ratios of 1/3, 1/6, and 1/9. The meshes for these investigations are shown in Fig. V.6. 1/16th of the unit cell is analyzed by exploiting reflective and rotational symmetries as described in [113]. The material properties utilized for this investigation are outlined in tables V.1, V.2, and V.3. These values were taken from [151, 160, 165], and are different properties than were used in other textile analyses due to the fact that work on the micromechanics model had not been completed at the point that the investigation into failure initiation in the textile was undertaken.

Load cases to be examined were defined by identifying a broad variety of ratios of stress components in the following manner. Normal components of stress were per-

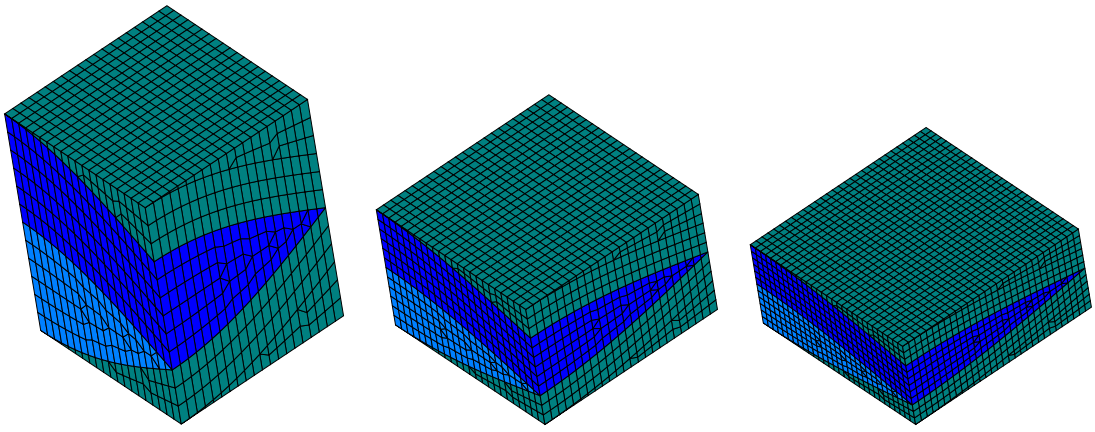

(a) WR=$\frac{1}{3}$ (b) WR=$\frac{1}{6}$ (c) WR=$\frac{1}{9}$

Figure V.6: Textile 1/16th unit cell meshes for failure initiation analysis.

Table V.1: IM7/8552 moduli for failure initiation prediction.

Modulus	Value
E_{11}	165 GPa
E_{22}, E_{33}	11.83 GPa
ν_{12}, ν_{13}	0.30
ν_{23}	0.487
G_{12}, G_{13}	5.12 GPa
G_{23}	3.92 GPa

Table V.2: IM7/8552 strengths for failure initiation prediction.

Strength	Value
S_{11}^T	2600 MPa
S_{11}^C	1500 MPa
S_{22}^T, S_{33}^T	60 MPa
S_{22}^C, S_{33}^C	290 MPa
S_{12}, S_{13}	90 MPa
S_{23}	60 MPa

Table V.3: Neat 8552 properties for failure initiation prediction.

Property	Value
E	4.67 GPa
G	1.73 GPa
T	121 MPa
C	135 MPa

mitted to have values from the set $\left\{0, \frac{1}{3}, \frac{2}{3}, 1\right\}$ (only tensile values were examined). Shear components take any value from the set $\left\{0, \pm\frac{1}{3}, \pm\frac{2}{3}, \pm 1\right\}$. All unique permutations of stress ratios are taken from these sets, yielding 21,521 different load cases to be examined. Failure initiation was determined for each of these load cases, and the characteristic behaviors were identified using the approach described previously.

One issue that was noted for this lenticular tow cross section was that for some load cases, there were strong, highly localized stress concentrations (Fig. V.7) that occurred where all four tow edges come together at a single point (Fig. V.8), a location that will be referred to as the "tow edge crossover". This feature is purely a result of the geometric idealization used to represent the textile, and will not exist in real world textile composites. It was believed that these stress concentrations would result in an artificially low prediction of the load magnitude that would cause failure initiation, and possibly bias the predicted failure initiation locations. Therefore, a strategy was developed to filter out the influence of these strong but spatially small stress concentrations. Because the volume of material with elevated stress is small, it was decided to exclude a small volume of the model around the idealized regions from consideration when searching for the failure initiation site. Two other features of the

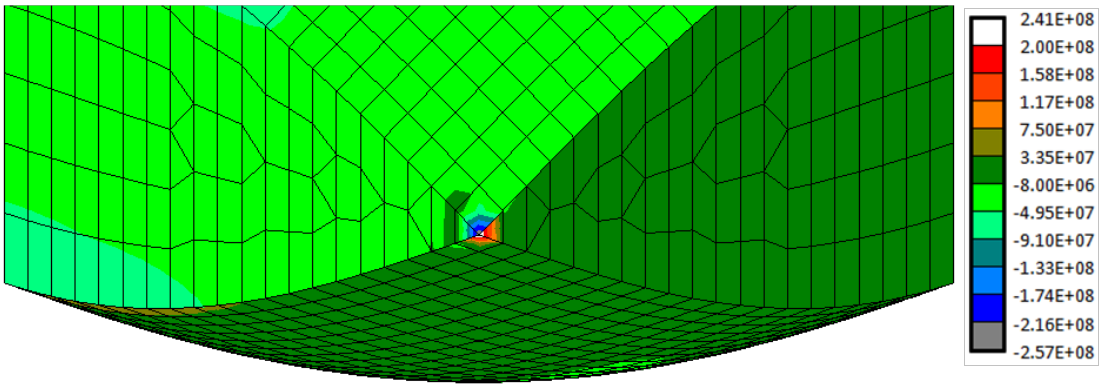

Figure V.7: Local σ_{12} under global $\langle \sigma_{yz} \rangle$ loading, $WR = \frac{1}{3}$.

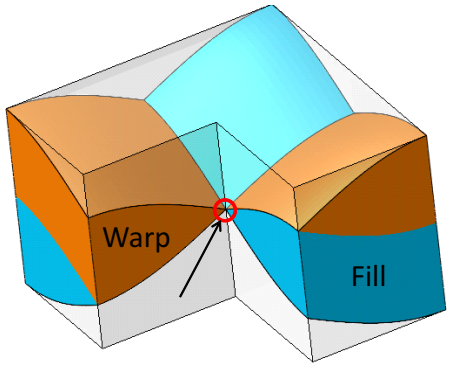

Figure V.8: Cutaway for 1/4 of unit cell showing tow edge crossover.

assumed textile architecture were considered "idealized". One was the minimum and maximum z coordinates of the tows. At these locations, due to the assumed in-phase periodic stacking of the textile, the tow of one mat touches the tow of the adjacent mat at exactly one point. The other "idealized" feature is the tow edge. It is assumed to be sharp, when in reality its "sharpness" is limited by the diameter of the fibers, and more practically by the fact that the tow doesnt generally assume a perfectly lenticular shape.

After trying several different dimensions, it was determined that excluding the regions within $0.025w$ of the tow edge crossover (refer to Fig. V.1 for the textile dimensions) and minimum and maximum z coordinates of tows, and the region within $0.0125w$ of the sharp tow edge appropriately filtered out the effect of any suspect stress concentration without overly biasing the failure initiation predictions. These dimensions are adequate to omit the elevated stresses from very small but strong stress concentrations such as that in Fig. V.7, but are not so large that they significantly effect the prediction of failure initiation in stress concentrations which exist over larger dimensions that aren't purely the result of geometric idealizations in the textile.

V.B.2.b. Characteristic Locations

Failure initiation was determined for each load case using the Tsai-Wu criterion, given in Eq. 2.1 for failure in the tows and Christensen's criterion, given in Eqs. 4.9 for failure in the matrix. The mode of failure in the tow was determined by identifying the local stress component in the tow at the location of failure initiation

which had the largest value relative to the corresponding tow strength. No distinct failure mode was determined for failure initiation in the neat matrix pocket. For the application of the Tsai-Wu criterion, the biaxial strength term F_{12} was predicted using the approach put forward by Tsai and Hahn [33], given in Eq. 5.9.

$$F_{12} = -\frac{1}{2}\sqrt{F_{11}F_{22}} \tag{5.9}$$

The failure initiation locations for lenticular tows are presented in Figs. V.9, V.10, and V.11. For each waviness ratio, two figures are provided that show the locations in the textile where failure initiation is predicted for the 21,521 sampled load cases. Each dot in the plot represents a location where at least one load case was predicted to result in failure initiation (multiple load cases could be associated with a single location). It was observed that the locations tend to occur in clusters, which are denoted with letters. There is also a rotational symmetry to these cluster locations, so an overbar is utilized to denote clusters that exhibit this symmetry. For each waviness ratio, two figures are presented. The first shows the failure initiation locations when the entire model volume is considered, and the second shows the predicted initiation locations when the previously described problematic regions of the assumed textile geometry are removed from consideration. Tables V.4, V.5, and V.6 are provided for each waviness ratio and show how many of the load cases resulted in failure at a particular location. These tables also indicate which local stress component caused the local failure (i.e. what the most critical stress component is at the failure initiation location).

There are several trends that may be observed from the results for all waviness ratios. The most apparent is that the 21,521 sampled load cases led to failure initia-

tion in just a few different regions of the textile. This finding supports the idea that there are a limited number of ways that failure will occur in textile composites even for a wide variety of loading cases. It was also observed that the number of load cases that resulted in failure initiation at the tow edge crossover decreased dramatically when the small region around the node at location A at the tow edge crossover was removed from consideration. This indicates that the stress concentration that exists at location A (Fig. V.7) in some cases biased the failure location prediction. However, removing this region from consideration did not introduce a large number of additional zones where failure initiation was predicted to occur, indicating that that the clustering of failure initiation locations in the textile is not simply due to idealizations in the textile geometry, but more generally due to the overall distribution of stresses that exist in the textile.

One interesting result to note is that for the various waviness ratios, the relative locations of the sites that favored failure initiation were approximately the same, although there were a few sites that existed in the WR=1/6 and WR=1/9 which did not exist in the WR=1/3 case, (for instance, the region labeled E). This supports the idea that the locations which favor failure initiation in textiles exhibit low sensitivity to variations in the textile geometry.

V.B.3. Failure Initiation Envelope Under In-Plane Loading

The tools developed for this investigation permit the numerical development of a failure initiation envelope in stress space. This was undertaken for a textile with $WR = \frac{1}{6}$ containing the material system described in tables V.1, V.1, and V.3.

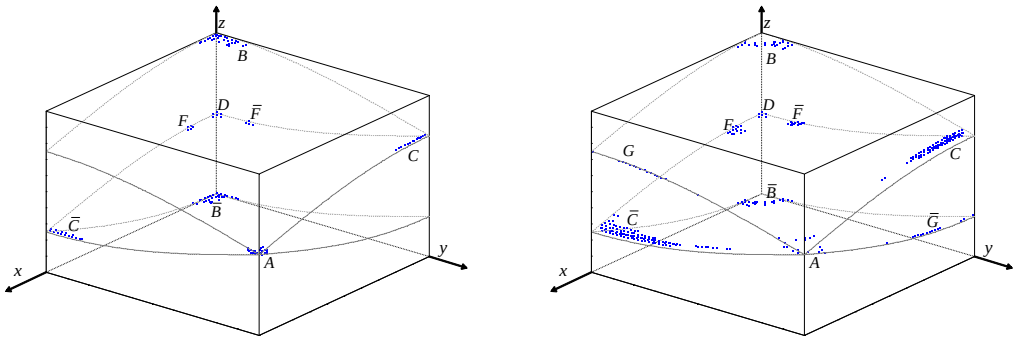

(a) Entire Model (b) Excluding problem geometries

Figure V.9: Failure initation locations in $WR = \frac{1}{3}$ specimen.

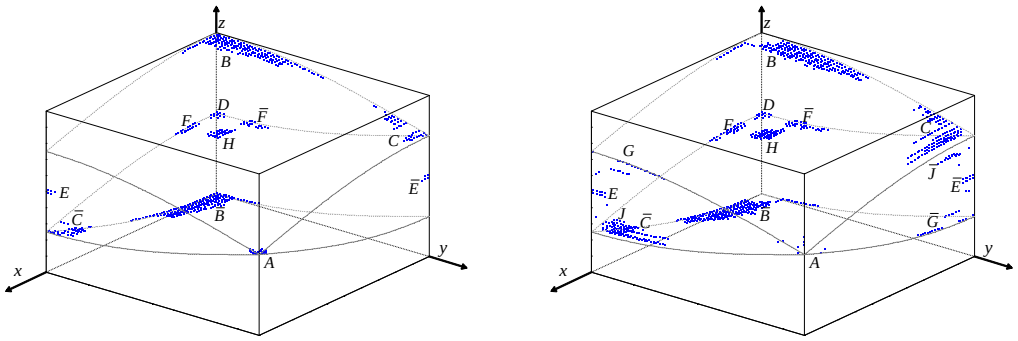

(a) Entire Model (b) Excluding problem geometries

Figure V.10: Failure initation locations in $WR = \frac{1}{6}$ specimen.

Table V.4: Number of load cases resulting in failure at each cluster for $WR = \frac{1}{3}$ due to a particular local stress component (parentheses denote cases in which idealized geometries are excluded).

Location	Failure Mode					
	σ_{22}	σ_{33}	σ_{12}	σ_{23}	σ_{13}	Matrix
A	6,851 (638)		5,894 (1,865)			
B	336 (1,533)	1,342 (1,933)		852 (2,913)	464 (1,058)	611 (124)
$\overline{B}$	339 (1,598)	1,431 (2,135)		940 (3,213)	463 (1,056)	735 (115)
C	908 (1,498)	0 (4)				
$\overline{C}$	907 (1,493)	0 (4)				
D		16 (34)				
F		7 (11)				
$\overline{F}$		5 (7)				
G	0 (17)	0 (156)	0 (312)			
$\overline{G}$	0 (16)	0 (155)	0 (302)			

Table V.5: Number of load cases resulting in failure at each cluster for $WR = \frac{1}{6}$ due to a particular local stress component (parentheses denote cases in which idealized geometries are excluded).

Location	Failure Mode					
	σ_{22}	σ_{33}	σ_{12}	σ_{23}	σ_{13}	Matrix
A	8,922 (2,394)		8,407 (4,869)			
B	654 (2,497)	644 (1,376)		125 (557)	99 (385)	3 (5)
$\overline{B}$	693 (2,607)	684 (1,461)		162 (634)	99 (387)	3 (10)
C	689 (2,362)					
$\overline{C}$	695 (2,268)					
D		24 (42)				
E	0 (12)	4 (12)			19 (95)	
$\overline{E}$	0 (12)	4 (13)			20 (96)	
F		7 (16)				
$\overline{F}$		7 (14)				
G	0 (1)		0 (20)		0 (1)	
$\overline{G}$	0 (1)		0 (20)		0 (1)	
H		4 (10)				
J	0 (1)	0 (4)	0 (4)		0 (5)	
$\overline{J}$	0 (4)	0 (4)	0 (3)		0 (5)	

Table V.6: Number of load cases resulting in failure at each cluster for $WR = \frac{1}{9}$ due to a particular local stress component (parentheses denote cases in which idealized geometries are excluded).

Location	Failure Mode					
	σ_{22}	σ_{33}	σ_{12}	σ_{23}	σ_{13}	Matrix
A	10,393 (4,485)		8,034 (3,891)			
B	938 (3,544)	451 (1,215)		59 (301)	30 (162)	0 (2)
$\overline{B}$	941 (3,625)	456 (1,266)		59 (310)	30 (165)	0 (6)
C	167 (1,445)	0 (1)	0 (2)			
$\overline{C}$	166 (1,537)		0 (1)			
D		26 (50)				
E	5 (129)	0 (18)	0 (5)		36 (222)	
$\overline{E}$	5 (135)	0 (18)	0 (13)		36 (225)	
F		7 (14)				
$\overline{F}$		7 (14)				
G			0 (6)			
$\overline{G}$			0 (6)			
H		4 (10)				

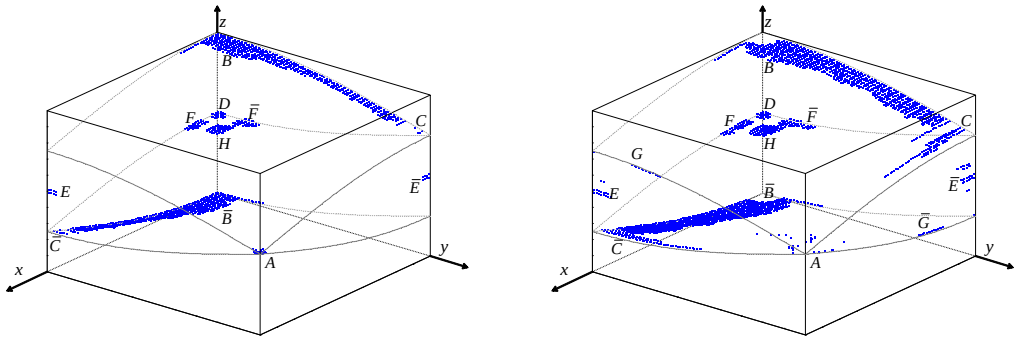

(a) Entire Model (b) Excluding problem geometries

Figure V.11: Failure initation locations in $WR = \frac{1}{9}$ specimen.

For the development of the failure initiation surface, Hashin's criterion (described in section V.B.1.c) was used for the tows and Christensen's criterion for the neat matrix pockets. Since textile composites are typically subjected to in-plane loadings, and because it is difficult to visualize failure envelopes in more than three dimensions, the failure envelope for in-plane normal and shear loading was developed. The reduction in parameter space allows the surface of the failure envelope to be sampled with much higher resolution than was possible when examining all six components of loading. Furthermore, for this study, both tensile and compressive normal loadings were examined.

The load component ratios which were examined were defined in the following manner, illustrated in Fig. V.12:

1. Determine the failure initiation load associated with each component (both tension and compression)

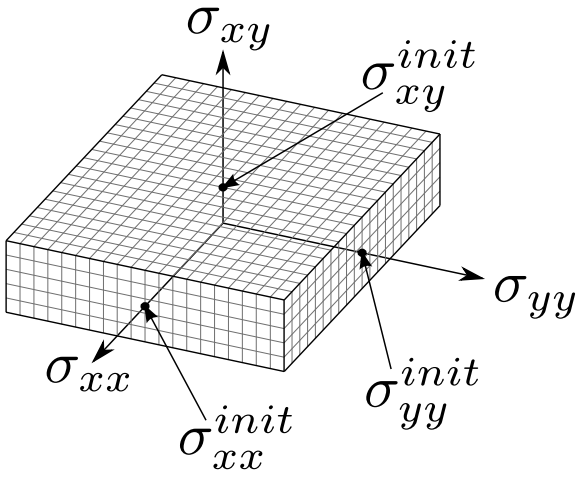

Figure V.12: Load case development for in-plane loading failure envelope.

2. Define a bounding box in stress-space from the failure initiation loads

3. Define a grid on each face of the bounding box such that each grid element has an aspect ratio close to 1

4. Define the loading ratios to examine from the gridpoints on the box in stress space.

Once the loading ratios were determined, the failure initiation location, local failure mode, and globally applied loading at failure initiation was determined for each of them. The failure initiation behaviors were organized into characteristic behaviors using the same approach described in previous sections. A surface triangulation of the failure stresses in stress space was then performed. The color of each triangular facet was determined from the characteristic failure behavior of the loads representing each vertex (each characteristic behavior was assigned a unique color). Triangular facets which connected loading states with different characteristic behaviors were

colored black. This process was repeated for several different temperatures to see how the failure initiation envelope changed with different thermal stress states. These envelopes are shown in Fig. V.13

Several interesting features can be noted from the series of failure envelopes. The first is that for the most part, each characteristic failure behavior forms a contiguous sub-region of the failure envelope. This somewhat expected result indicates that away from "boundaries," similar load states tend to result in similar characteristic behaviors. Additionally, there are a limited number of different characteristic behaviors present on the envelopes, and these failure modes stay fairly consistent across various temperatures. As expected, there is some variation in the failure initiation envelope as the temperature is changed. For instance, as temperature is increased, there is an initial increase in the load to failure initiation for stress states that consist of in-plane tension and shear, while there is a decrease in the failure loads for stress states which consist of biaxial in-plane compression. At $\Delta T = 25^\circ$ C, there is the introduction of new characteristic failure modes associated with biaxial tension. As the temperature increases further, the same noted trends continue. However, the initiation load for biaxial tension associated with the newly introduced failure modes exhibit a different temperature dependence, decreasing as the temperature increases. At $\Delta T = 50^\circ$ C, new failure modes are noted for loads which are predominantly shear with moderate biaxial tension. As the temperature continues to increase to 100° C, the envelope continues to change shape, and the arrangement of the failure modes in the envelope continues to undergo moderate changes.

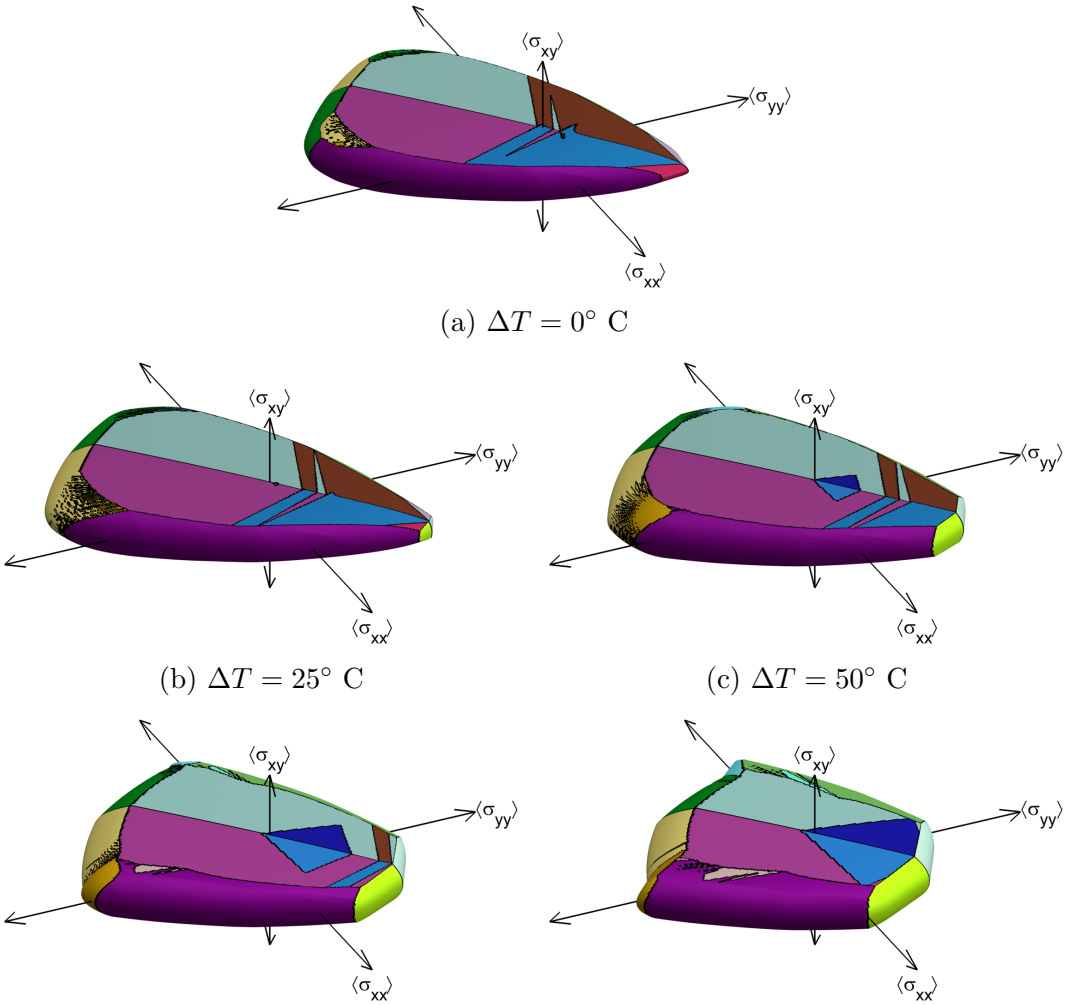

(a) $\Delta T = 0°$ C

(b) $\Delta T = 25°$ C

(c) $\Delta T = 50°$ C

(d) $\Delta T = 75°$ C

(e) $\Delta T = 100°$ C

Figure V.13: Failure initiation envelopes for in-plane loading of $WR = \frac{1}{6}$ at various temperatures.

V.B.4. Discussion of Failure Initiation Results

While a detailed study of each failure mode may be warranted for applications in which failure initiation is a critical issue, such as in composite pressure vessels (which may leak if small cracks open up in the composite), the particulars of failure initiation are not a matter of great interest in the current study. The main research question that the failure initiation investigation was intended to answer is "Does failure initiation in composites occur in a limited number of characteristic ways for a broad variety of thermal and mechanical loads?" This investigation strongly indicates an affirmative answer to this question. While this finding cannot be directly applied to progressive failure, it indicates that progressive failure may evolve in characteristic ways for various thermomechanical loadings.

V.C. Progressive Failure of Textile

This section describes the progressive failure model for the textile unit cell and the progressive failure behaviors that were observed for various thermomechanical loads.

V.C.1. Elastic Tow Properties

The transversely isotropic tow properties for the progressive failure textile model were obtained using the random fiber-matrix model assuming a fiber volume fraction v_f (within a tow) of 60%. These properties are given in table V.7.

Table V.7: Predicted IM7/8552 properties for $v_f = 60\%$, used in tows for progressive failure of textile.

Modulus	Value
E_{11}	167 GPa
E_{22}, E_{33}	11.6 GPa
ν_{12}, ν_{13}	0.30
G_{12}, G_{13}	5.23 GPa
G_{23}	3.87 GPa

V.C.2. Damage Models

Damage within the textile unit cell is accounted for in primarily one of two ways. Larger-scale discrete failures, such as cracking in the neat matrix pockets and interfacial failure between adjacent tows and between tows and the neat matrix pocket, are accounted for through the use of interfacial elements with opening governed by a cohesive zone model. Failure of the tows is accounted for in different ways depending on the nature of the failure. As was noted from the micromechanics model, under transverse normal loading the fiber-matrix material undergoes brittle behavior with damage localization into a single band representative of a crack. Therefore, cohesive elements will be used to account for matrix cracking under transverse normal load. The strength of these cohesive elements will be determined from a distribution of strengths obtained using many realizations of the random fiber-matrix microstructure. Under shear load, however, the fiber matrix unit cell experienced the development of a diffuse field of ductile matrix failure in the regions between fibers which eventually began to coalesce into a single larger damage feature at the maximum shear stress. These initial damage features under shear, like the fibers themselves,

are small on the scale of the textile unit cell. Therefore, their homogenized effect at the textile scale will be accounted for using continuum damage mechanics. The stress-strain behavior for this continuum damage mechanics model will be defined in such a manner that the tangential traction across cohesive elements in the tows will eventually exceed the allowable values, leading to cohesive opening once the shear stresses in the tows reach the maximum shear stress predicted from the fiber-matrix analyses. This is used to account for the eventual coalescence of microstructural damage features into matrix cracks in the tows. The details of these damage models are described in the following subsections.

V.C.2.a. Continuum Damage Model for Shear Damage in the Tows

This section describes the continuum damage model that is applied to the tows to account for diffuse shear damage. As was noted in previous sections regarding progressive failure simulation of the fiber-matrix model, the progression of damage development under longitudinal shear loading is as follows. Ductile failure initiates in the matrix between fibers aligned with the loading direction at a low shear stress level (relative to the maximum shear stress). As longitudinal shear loading is increased, the composite material experiences a gradual increase of this distributed damage around fibers. This leads to a gradual reduction in the effective stiffness of the composite. Eventually, the effective stress in the composite reaches a plateau as additional damage development begins to localize along a single band running through the microstructure which is roughly perpendicular to the plane of the applied shear.

Accounting for the distributed damage in the tows and the subsequent gradual reduction in the material stiffness will be accomplished through the use of a continuum damage mechanics model. The continuum damage mechanics approach is very well suited for this type of failure; its original conception by Kachanov [3] is based on the premise that a reduction in the materials modulus is caused by the formation of a large number of very small defects in the material, which is the case for the initial stage of damage development under longitudinal shear. In the current continuum damage model, the degraded shear moduli G_{12}^{dam} and G_{13}^{dam} at a given location in the tows are obtained from the original shear moduli using Eq. 5.10.

$$\begin{aligned} G_{12}^{dam} &= (1 - d_{12})\, G_{12} \\ G_{13}^{dam} &= (1 - d_{13})\, G_{13} \end{aligned} \tag{5.10}$$

d_{12} and d_{13} are damage parameters which increase monotonically from zero to a maximum value of one. Their evolution ensures that under monotonically increasing load, the the stress-strain relationship for longitudinal shear in the tows follows the path shown by the dashed line in Fig. V.14, which is based on the shear stress-strain behavior observed from the fiber-matrix microscale analyses. Unloading follows a linear path back to the origin. This stress-strain relationship is a piecewise function with three segments. The first segment, which accounts for linear elastic deformation is simply linear with no evolution of shear damage.

The intermediate stage, labeled the damaging stage, has a stress-strain relationship following a cubic polynomial $\sigma_{12}(\gamma_{12})$ given in Eq. 5.11 with coefficient values that are defined based on the conditions of Eq. 5.12, which ensure value and slope

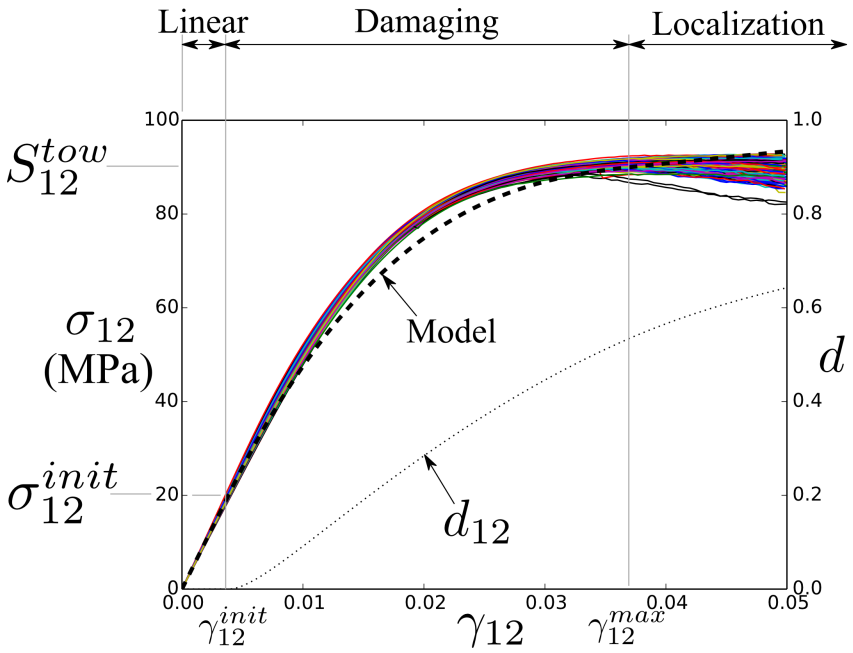

Figure V.14: Shear response and damage evolution compared to micromechanics results.

continuity of the stress under increasing load.

$$\sigma_{12}\left(\gamma_{12}\right) = A\gamma_{12}^{3} + B\gamma_{12}^{2} + C\gamma_{12} + D \tag{5.11}$$

$$\begin{aligned} \sigma_{12}\left(\gamma_{12}^{init}\right) &= G_{12}\gamma_{12}^{init} \\ \sigma_{12}\left(\gamma_{12}^{max}\right) &= S_{12}^{tow} \\ \left.\frac{\partial\sigma_{12}}{\partial\gamma_{12}}\right|_{\gamma_{12}^{init}} &= G_{12} \\ \left.\frac{\partial\sigma_{12}}{\partial\gamma_{12}}\right|_{\gamma_{12}^{max}} &= G_{12}^{\mathrm{loc}} \end{aligned} \tag{5.12}$$

This stage captures the gradual loss of stiffness in the material as damage grows in the tows, but before localization of failure starts to occur. A cubic polynomial was chosen due to the relative ease of calculating the polynomial coefficients as compared to other nonlinear functions that were considered.

The last stage is the localization stage, which begins once the maximum stress observed from the micromechanics models has been reached. In this stage, the stress in the tows continues to gradually increase with shear strain based on a linear tangent modulus G_{12}^{loc} that is some small proportion of the initial shear modulus. This proportion is an input to the model. This continuing increase in the stress ensures that as loading increases, the tangential tractions in adjacent cohesive elements will increase to a level sufficient to cause cohesive opening. It was noted in the micromechanics model that once the maximum stress was reached, localization of the damage began to occur. Continuum damage mechanics is not well suited for accounting for this localization (see the investigation by Gorbatikh et al. [130] regarding problems associated with the use of continuum damage to account for the presence of discrete cracks under shear loading). Therefore, it is desirable that the cohesive zones begin

Table V.8: Parameters for shear damage model in tows.

Property	Value
$G_{12} = G_{13}$	5.23 GPa
$S_{12}^{t}ow$	90 MPa
σ_{12}^{init}	20 MPa
γ_{12}^{max}	0.037
$G_{12}^{\mathrm{loc}}/G_{12}$	0.05

to open to account for this localization, since the localization of failure ultimately represents the formation of a discrete crack running along a tow. The opening of cohesive elements in and around the tows will prevent the shear stresses in the tow from becoming unrealistically large. This damage model is applied to both longitudinal shear moduli in the tows, although for in-plane loading, most damage occurs for the 1-2 component. The parameters used to define the model used in the current study are provided in table V.8.

V.C.2.b. Cohesive Opening Model for Tows

Discrete crack opening in the tows is accounted for through the use of interfacial elements inserted along the tow length (Figs. V.4b and V.4c) with opening governed by a cohesive zone formulation. Two distinct types of discrete crack opening were noted for the tows based on the micromechanics analysis. The first, associated with transverse tension, is brittle crack opening resulting from the onset and unstable growth of brittle failure in the matrix. The second, associated with longitudinal shear, is the gradual localization of ductile shear damage (which is initially diffusely

distributed within the microstructure) into a band of failed material. The onset of both of these behaviors occurs when the stress in the tow reaches some critical value.

As discussed in section III.C.2.b, obtaining brittle behavior in a cross-ply laminate (resulting in transverse normal loading in the 90° ply) requires the specification of a low mode I strain energy release rate to the cohesive zone model. The 90° ply in the cross-ply laminate example is analogous in many ways to a tow running perpendicular to a uniaxial load applied to a plain weave composite. Like the cross-ply laminate, it was noted that the brittle or ductile nature of crack opening was governed by the strain energy release rate used in the cohesive zone model. Therefore, a very low strain energy release rate is used for the intra-tow cohesive zone model under mode I opening to ensure brittle behavior under transverse tensile failure.

The critical strain energy release rate for mode II opening of the cohesive zone (under longitudinal shear) is set to the same value as that obtained from Mode II delamination testing of IM7/8552 laminates [20]. Delamination growth between between two 0° plies bears a strong similarity to the the failure of a tow under longitudinal shear in terms of the stresses at the crack tip/delamination front and the direction of crack growth.

As discussed in section III.C, the large disparity between the critical strain energy release rates means that the power-law mixed-mode criterion for crack growth used by Turon is not appropriate since no fitting parameter exponent η has been experimentally determined for this configuration and because most values for η determined for other configurations would permit the mode I component of strain energy under mixed-mode opening to exceed G_{Ic} from pure mode I loading. There-

fore, the critical strain energy release rate under mixed-mode loading will be defined using the alternative form given in Eq. 3.93, and the formulation will be modified from that of Turon according in the manner described in section III.C.2.b.

The final aspect of the cohesive zone to be defined is the maximum traction. Typically, these values would be obtained from experiments on unidirectional laminates under transverse normal and shear load. However, it can be expected that within a tow, this cohesive strength will be subject to variability because of the randomness which exists in the smaller-scale microstructure. Also, as was demonstrated in the micromechanics analysis, this strength exhibits temperature dependence due to the thermally-induced stresses which exist in the fiber-matrix microstructure, particularly for failure under transverse normal loading. The strength variability and temperature dependence from the fiber-matrix scale analysis are incorporated into the textile-scale analysis by specifying a different strength at each quadrature point in the intra-tow cohesive elements at the textile scale. These strengths are specified at the beginning of the progressive failure analysis and stay constant throughout the analysis. Each strength value is obtained at random using a Weibull distribution that is characterized by fitting the strengths from progressive failure analyses performed on hundreds of fiber-matrix microstructural realizations at the same temperature as the tow.

The cohesive zone properties that are applied to the intra-tow cohesive zones are given in table V.9. The Weibull distribution parameters for the cohesive strength under transverse tension and shear loading for various temperatures were reported with the fiber-matrix analysis results in table IV.4. An investigation was performed

Table V.9: Intra-tow cohesive zone properties

Property	Value
K	10^{17} N/m
G_{Ic}	20.94 N/m
G_{IIc}	1047 N/m

into the effect of using a variable strength value rather than a uniform strength value in the textile by examining the evolution of tow cracking under uniaxial loading when using a uniform strength (which represented the 5th percentile strength from the distribution) as well as four different seedings of the random strength. In all cases for a given temperature, the different seedings of random strength values all provided extremely similar predictions for the overall evolution of tow cracking, although the particular locations of cohesive zone opening varied somewhat. When the temperature of the composite was close to cure temperature (i.e. when thermally-induced stresses were low) the random strength distribution and uniform strength models predicted fairly similar behaviors in terms of the extent of tow cracking at a given mechanical load. However, when the temperature was reduced to room temperature, the cases which were seeded with random strength values from the Weibull distribution predicted the onset of tow cracking at lower loads than the uniform strength case.

V.C.2.c. Cohesive Opening Model for Interfaces and the Neat Matrix Pocket

Interfacial elements are also utilized to model failure of the interfaces between the tows (Fig. V.4e) and between the tows and the neat matrix pocket (Fig. V.4f),

Table V.10: Properties for inter-tow, inter-tow-matrix, and intra-matrix cohesive zones.

	G_{Ic} (N/m)	G_{IIc} (N/m)	η	τ_n^0 (MPa)	τ_t^0 (MPa)
Inter-tow	200	1000	1.45	60	90
Inter-tow-matrix	200	1000	1.45	60	90
Intra-matrix	680	1000	1.45	120	180

as well as cracking within neat matrix pocket (Fig. V.4d). The opening of these elements are governed by the cohesive zone law of Turon et al. [20] with the modifications given in section III.C.2.a. The values utilized for the cohesive zone models are provided in table V.10. The inter-tow properties were selected based on mixed-mode delamination testing of IM7/8552 material used by Hallett et al. [11]. It is thought that the interface between tows will be reasonably similar to the interface between two adjacent lamina. There was no experimental data available that seemed appropriate for modeling the interface between a tow and the neat matrix pocket, so for the current set of analyses, this interface was modeled using the same properties as the inter-tow interfaces. Tensile strength data as well as G_{Ic} are provided by the manufacturer for 8552 epoxy [160], but shear failure strength and G_{IIc} are not. Values for mode II were chosen to be higher than for mode I by a proportion which is similar to other epoxy resin systems that have been experimentally characterized [166].

V.C.3. Failure Under In-Plane Loadings

The next three sections examine the behavior of the textile under various types of in-plane loading. For each loading, the damage is presented in figures such as Fig.

V.15. In these figures, cohesive elements with quadrature points that have undergone partial degradation but not complete opening are shaded green. Cohesive elements which contain quadrature points that have experienced complete opening are shaded red. Cohesive elements that have not experienced any opening are left transparent. Each of these analyses was stress controlled. Loading was increased until (1) the model reached an instability under load-controlled loading (i.e. the effective stress in the model reached its maximum) or (2) until the onset of fiber failure was predicted, as this is considered a critical type of failure. Fiber failure onset is predicted to occur when more than 0.5% of the tow volume in the textile exceeds 2.6 GPa, which is the axial stress associated with fiber failure in a unidirectional IM7/8552 laminate. This value is not considered to be temperature dependent, although in reality, cooling a unidirectional lamina will tend to place the fibers into a mildly compressive state (the IM7 fibers will want to increase slightly in length due to their slightly negative longitudinal coefficient of thermal expansion, but the surrounding matrix will want to contract), causing the overall tensile strength of the lamina to increase. Since the current study is more focused on the behavior of the textile before fiber failure occurs, accounting for this temperature dependence was not deemed to be highly important.

V.C.3.a. Failure Under Uniaxial Load

The first loading case that was examined was x-direction uniaxial loading. The predicted progressive failure behaviors for loading at room temperature (with $\Delta T = -160°\text{C}$ applied to account for the temperature differential from cure) and at near-

cure temperature ($\Delta T = -10°\text{C}$) are now described.

At room temperature, as uniaxial loading was applied to the textile, the first type of damage which was predicted to occur was crack opening in the y-direction tows. The damage in the y-direction tows is shown in Fig. V.15. These tows run perpendicular to the applied load, and therefore they experienced large transverse normal stress. The onset of opening began at an applied σ_{xx} of 90 MPa (Fig. V.15b). The tow cracks started to completely open at about $\sigma_{xx} = 100$ MPa (Fig. V.16c). As seen in Fig. V.15a, the fraction of the y-tow cohesive zones which experienced complete opening continued to increase until all y-tow cohesive zones were opened at an applied load of $\sigma_{xx} = 400$ MPa.

In addition to failure in the y-direction tows, the x-direction tows were also predicted to undergo cracking as shown in Fig. V.16. Although these tows are aligned with the applied loading, they experience transverse tensile stress due to the thermal load and Poisson contraction as mechanical loading is applied. Under pure thermal loading, the tows have a tendency to contract more in the transverse direction than in the axial direction. However, because the tows are interwoven and are much stiffer in the axial direction, they are restricted from contracting transversely to the extent they would if unconstrained. This places them under transverse tension. Additionally, under uniaxial load, the transverse tows are restrained by the interwoven transverse tows and are therefore unable to undergo the Poisson contraction they would if unconstrained, leading to additional transverse tensile stress. As shown in Fig. V.16c, this stress becomes sufficient to cause complete opening in limited regions of the axial tows at an applied load of $\sigma_{xx} = 391.5$ MPa. When fiber failure begins

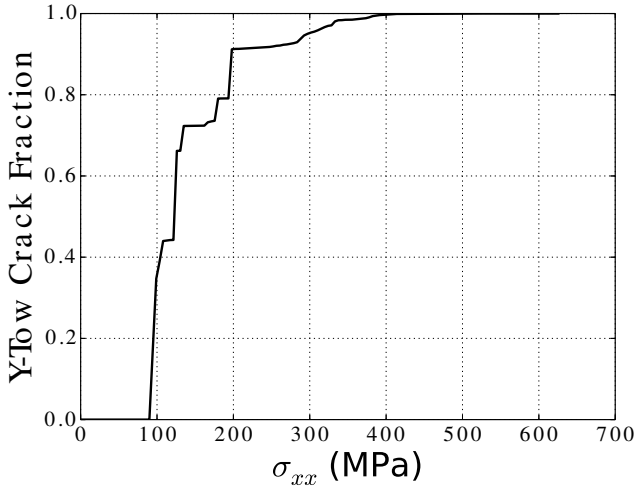

(a) Cracking Extent

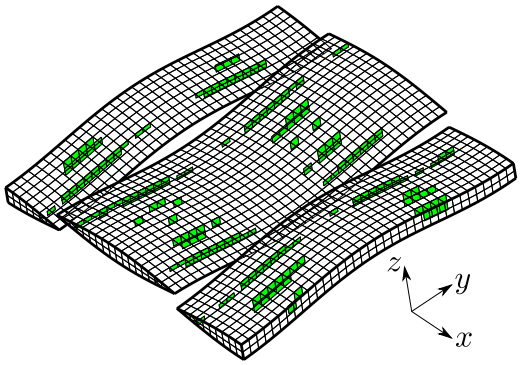

(b) $\sigma_{xx} = 90$ MPa

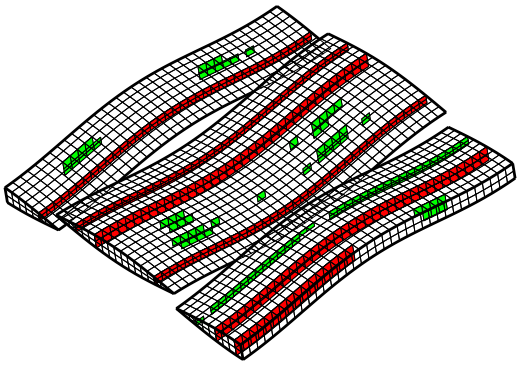

(c) $\sigma_{xx} = 121.5$ MPa

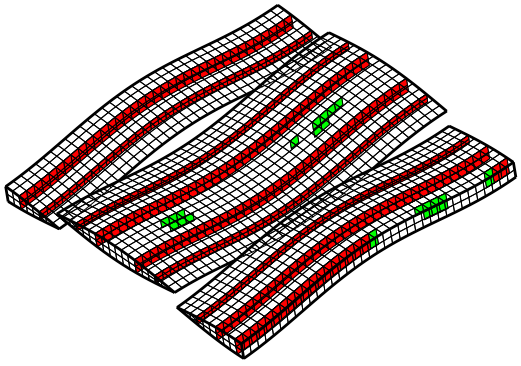

(d) $\sigma_{xx} = 171$ MPa

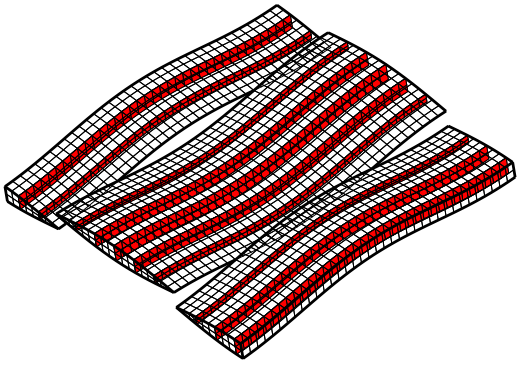

(e) $\sigma_{xx} = 198$ MPa

Figure V.15: Damage growth in y-tows under uniaxial σ_{xx}, $\Delta T = -160°$C.

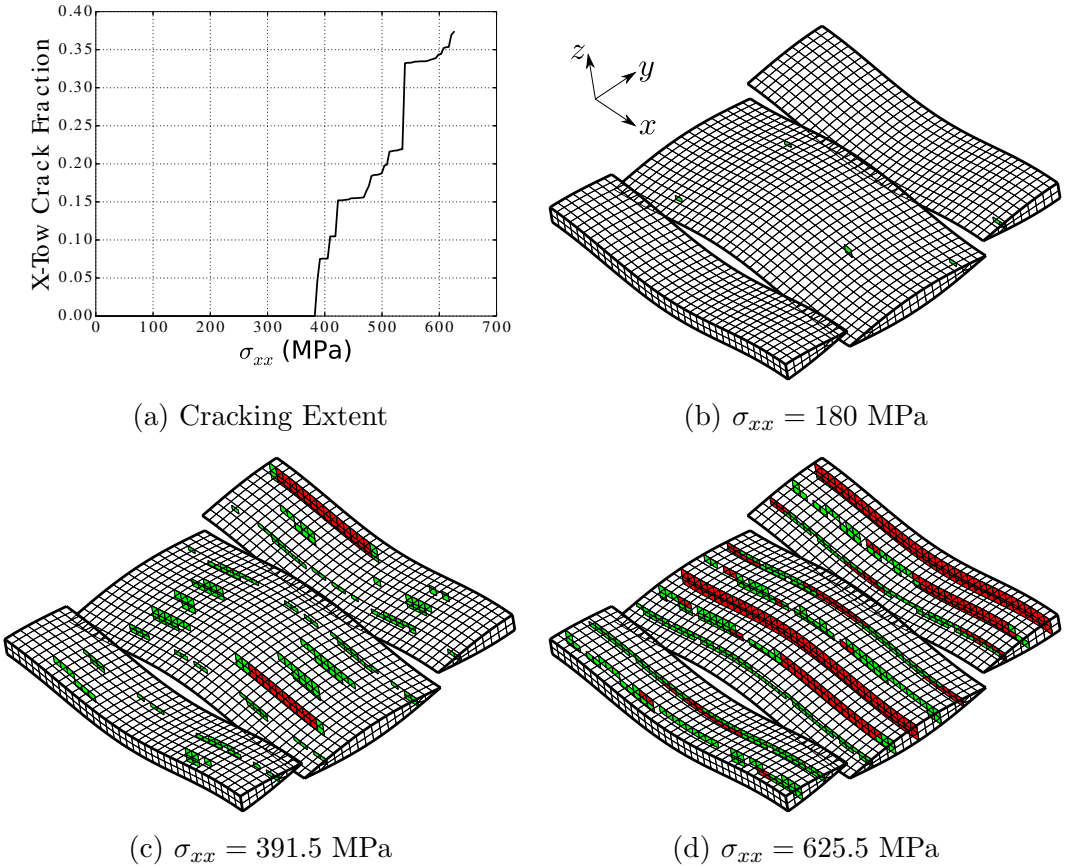

(a) Cracking Extent

(b) $\sigma_{xx} = 180$ MPa

(c) $\sigma_{xx} = 391.5$ MPa

(d) $\sigma_{xx} = 625.5$ MPa

Figure V.16: Damage growth in x-tows under uniaxial σ_{xx}, $\Delta T = -160°$C.

to initiate in the axial tows at an applied uniaxial stress of $\sigma_{xx} = 625.5$ MPa, a little more than 35% of the cohesive zones in the axial tows have experienced complete opening, as shown in Fig. V.16d.

As the tows undergo matrix cracking, the cohesive elements between the tows (Fig. V.17) begin to undergo degradation. The degradation in these regions tends to coincide with the edges of opened cracks in the tows as seen clearly in Fig. V.17b. This is expected for the inter-tow interfaces, as this interface forms a barrier to further extension of matrix cracks in the tows. As a result, these cracks will tend to

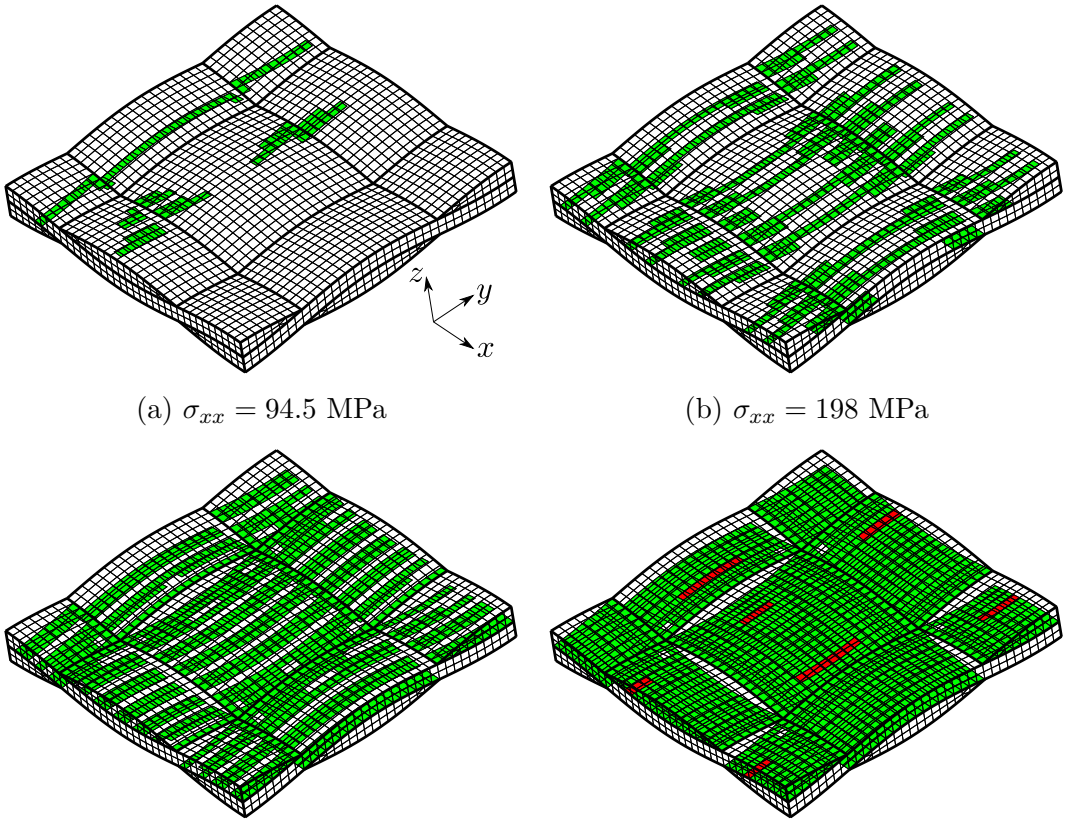

(a) $\sigma_{xx} = 94.5$ MPa

(b) $\sigma_{xx} = 198$ MPa

(c) $\sigma_{xx} = 360$ MPa

(d) $\sigma_{xx} = 625.5$ MPa

Figure V.17: Inter-tow damage under uniaxial σ_{xx}, $\Delta T = -160°$C.

turn and run along interfaces between tows, as observed for 2x2 carbon-fiber twills by Karahan [167]. Similar behavior has been widely observed in tape laminates, where delaminations tend to initiate where matrix cracks interact with inter-ply interfaces. The area of the interface that has experienced degradation increases with increasing load. By the onset of fiber failure, some regions of the interface have experienced complete opening in some of the regions where matrix cracks in the x and y direction tows interact as shown in Fig. V.17d.

Crack opening also occurs in the neat matrix pocket (Fig. V.18) shortly after

tow cracks start to open. As seen in Fig. V.18b, the cohesive zones which open are predominantly adjacent to cracks running in the y-direction tows (Fig. V.15d). This is because when a matrix crack running through a tow encounters the neat matrix pocket, the matrix pocket does not pose a barrier to continued crack growth (as opposed to a perpendicular tow). However, the strain energy required to open cracks in the more ductile neat matrix pocket is considerably higher than that needed to open cracks in the brittle fibers. Therefore, decohesion in the matrix region is not as brittle as it is in the tows. This pattern of intra-tow matrix cracks extending into the matrix pocket is in good agreement with the microscopic observations of Karahan [167]. Once sufficient load has been applied to cause the onset of fiber failure, complete crack opening has occurred in several regions of the neat matrix pocket as seen in Fig. V.18d.

Failure of the interface between the tows and the neat matrix pocket (Fig. V.19) begins to occur at higher load levels than for other cohesive interfaces. Degradation tends to occur in regions where partially opened cracks in the matrix pocket encounter tows which run perpendicular to the crack direction (Figs. V.19b and V.19c). This is expected to occur for a similar reason that cracking is expected to occur between adjacent tows. When the crack running through the matrix pocket encounters a perpendicular tow, it cannot grow into the tow, and therefore it is likely to turn and follow the tow/matrix pocket interface. Once loading is increased to a level sufficient to cause fiber failure, a large region of this interface has experienced partial degradation, and limited regions have experienced complete failure (Fig. V.19d). These regions coincide with cracks that have completely opened in the

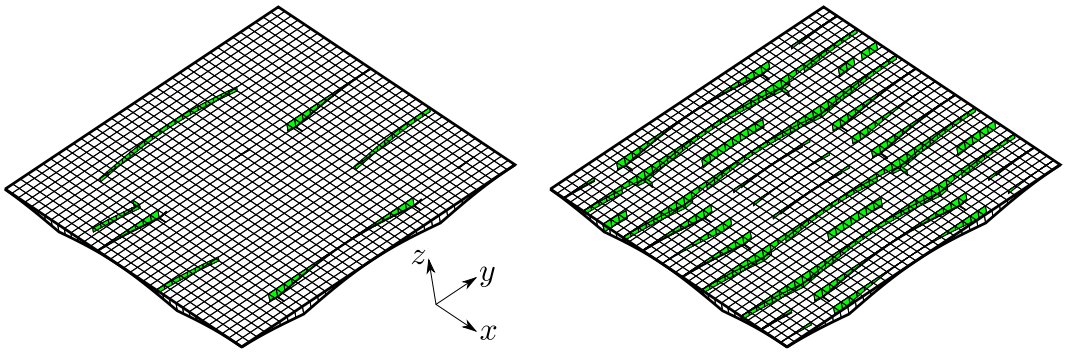

(a) $\sigma_{xx} = 99$ MPa

(b) $\sigma_{xx} = 310.5$ MPa

(c) $\sigma_{xx} = 540$ MPa

(d) $\sigma_{xx} = 625.5$ MPa

Figure V.18: Matrix pocket damage under uniaxial σ_{xx}, $\Delta T = -160°$C (top half only).

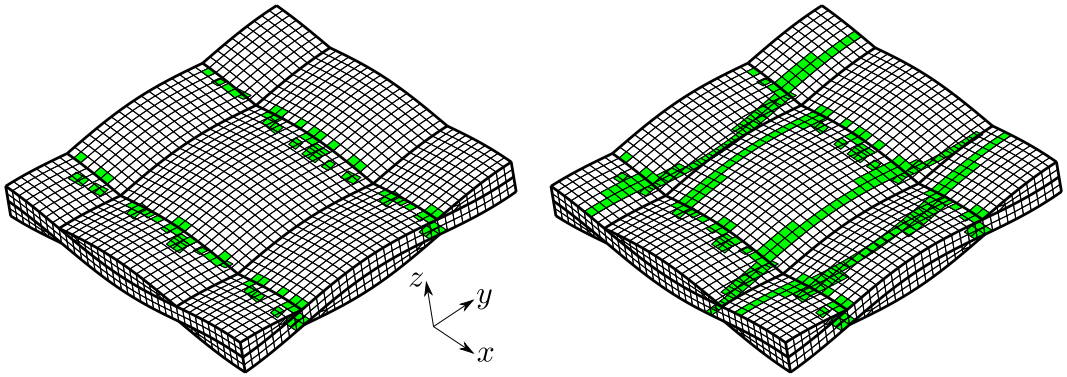

(a) $\sigma_{xx} = 270$ MPa (b) $\sigma_{xx} = 283.5$ MPa

(c) $\sigma_{xx} = 432$ MPa (d) $\sigma_{xx} = 625.5$ MPa

Figure V.19: Inter-tow-matrix damage under uniaxial σ_{xx}, $\Delta T = -160°$C.

neat matrix pocket.

In addition to cohesive zone opening, the accumulation of shear damage was tracked. Due to the low waviness ratio for the textile and the fact that the tows are aligned orthogonally with the applied uniaxial loads, shear stresses remained low, and only a very small amount of shear damage occurs.

As damage evolved in in the textile, the effective compliance of the textile was also tracked. This was accomplished by performing six different "virtual" uniaxial stress-strain tests on the unit cell at each load step. A unit-stress was applied for

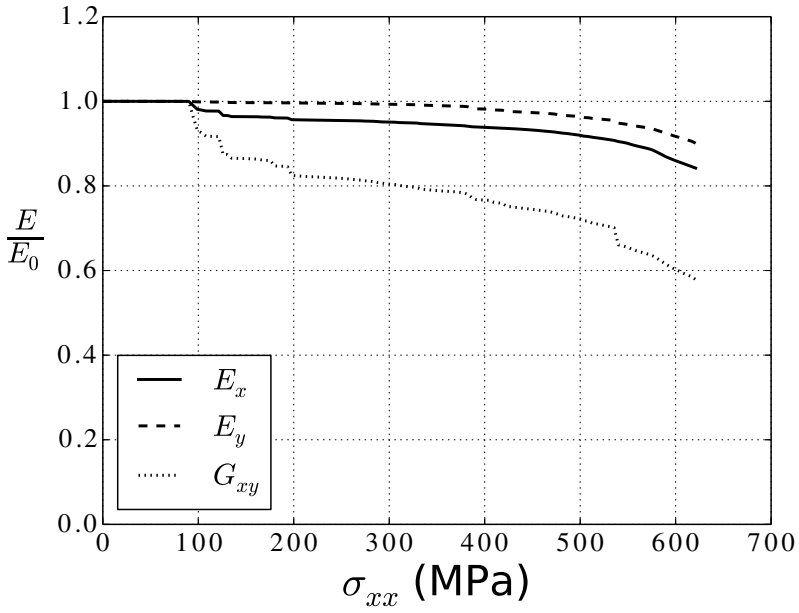

Figure V.20: In-plane property evolution under uniaxial σ_{xx}, $\Delta T = -160°$C.

each test, meaning that the resulting volume average strains made up the rows of the effective compliance matrix for the textile. Effective orthotropic engineering moduli were obtained from the compliance matrix. The evolution of the in-plane moduli is given in Fig. V.20. An examination of these moduli reveals that there is a drop of roughly 5% in E_{xx} and nearly 20% in G_{xy} associated with the saturation of cracking in the y-direction tows, although E_{yy} remains relatively unchanged (as expected, since cracks running along the y direction do not sever the the load path of y-direction normal loading). As the applied stress is further increased, there is a gradual reduction in all three moduli as degradation increases in the matrix pocket as well as on the interfaces. Crack opening in the x-direction tows slightly before the critical failure leads to an additional drop in G_xy.

Progressive failure under uniaxial loading was also examined near cure temperature, with an applied temperature change of $\Delta T = -10°\text{C}$. At this temperature, the thermally induced stresses in the textile (and within the tow microstructure) are much lower than for the room temperature case. The overall behavior for this temperature was similar to that at room temperature, so instead of providing a detailed description of the damage evolution, only the differences noted for this temperature will be highlighted. The initiation of critical fiber failure at this temperature was predicted to occur at an applied stress of $\sigma_{xx} = 688.5$ MPa, a 10% increase relative to the room-temperature case. Like the room-temperature model, y-tow cracking was the predominant failure mechanism under this load, but complete crack opening began at an applied load of about $\sigma_{xx} = 220$ MPa (as opposed to $\sigma_{xx} = 100$ MPa for the room-temperature case). This was primarily due to the reduction in thermally-induced transverse tension in the tows as the temperature increases towards cure. While the reduction in thermally induced stresses in the tows at the textile scale increases the loading required to cause failure, the strength of the tows themselves is significantly lower at this temperature due to the effects of thermally-induced stresses at the microstructure. At higher temperatures, more loading is required to fail the weaker tows. This indicates that the thermally-induced stresses at the textile scale play a larger role than the thermally induced stresses at the fiber-matrix level with regards to the temperature sensitivity of damage development in the textile.

Cracking in the x-direction tow occurred at this temperature as well, although the extent of cracking was much lower at fiber failure than it was for the room-temperature case. A lesser extent of x tow cracking was expected, since thermally

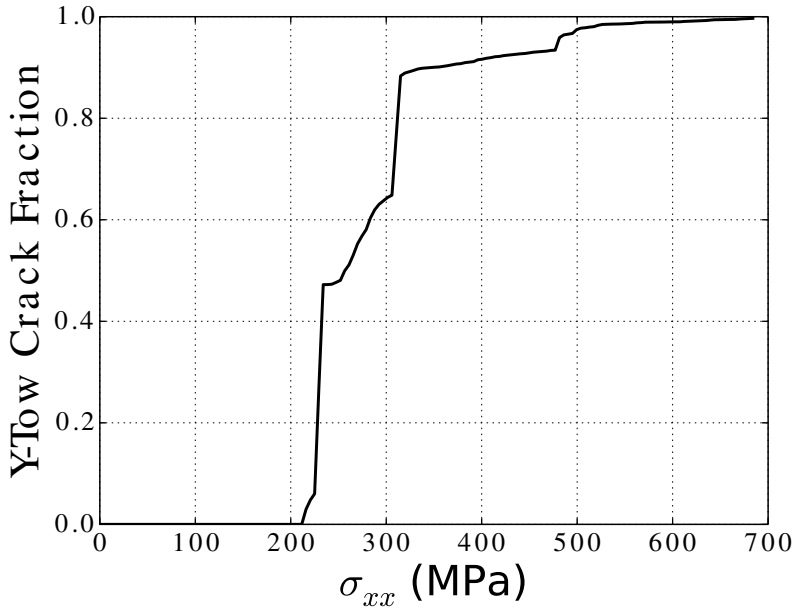

Figure V.21: Damage growth in y-tows under uniaxial σ_{xx}, $\Delta T = -10°$C.

induced stresses contribute significantly to this type of failure. Degradation of the inter-tow interface and within the neat matrix pocket followed the same trend as was seen at room temperature. These forms of damage occurred only after y-tow cracking had initiated, meaning that they began to evolve at higher loadings than were observed at room temperature. Interestingly, the failure of the tow-matrix interface followed a somewhat different trend than was observed at room temperature. For the near-cure loading, degradation of the tow-matrix interface tended to coincide with locations where tow cracks met the matrix pocket (as seen in Fig. V.22), rather than coinciding with locations where crack running through the matrix pocket met perpendicular tows (Fig. V.19c). A definitive reason for this difference was not clear from an investigation of the stresses in the textile unit cell, but these

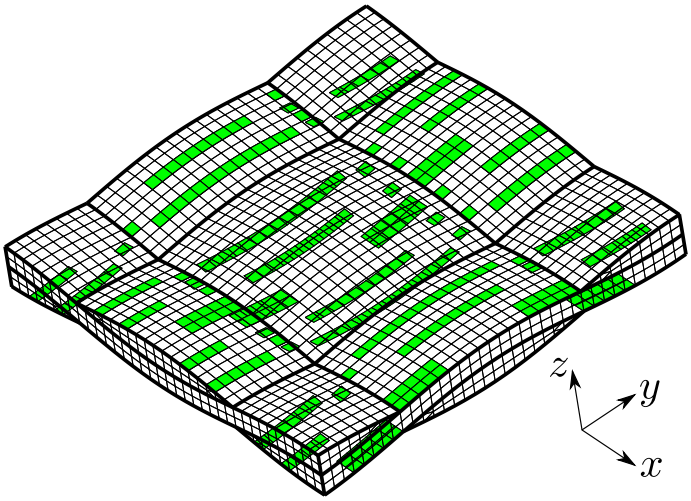

Figure V.22: Inter-tow-matrix damage under uniaxial $\sigma_{xx} = 337.5$ MPa, $\Delta T = -10°$C.

investigations did suggest that temperature reduction leads to primarily compressive tractions on this interface which will tend to prevent failure of the interface for the room temperature case.

The evolution of the in-plane moduli for uniaxial loading near cure temperature, shown in Fig. V.23, bore a strong resemblance to that seen at room temperature (Fig. V.20) in terms of the stiffness degradation associated with different types of damage. The overall level of property degradation was somewhat less than for the room temperature case, particularly for G_{12}, but this is to be expected due to the fact that there was less damage in the near-cure model at fiber failure as compared to the room-temperature model.

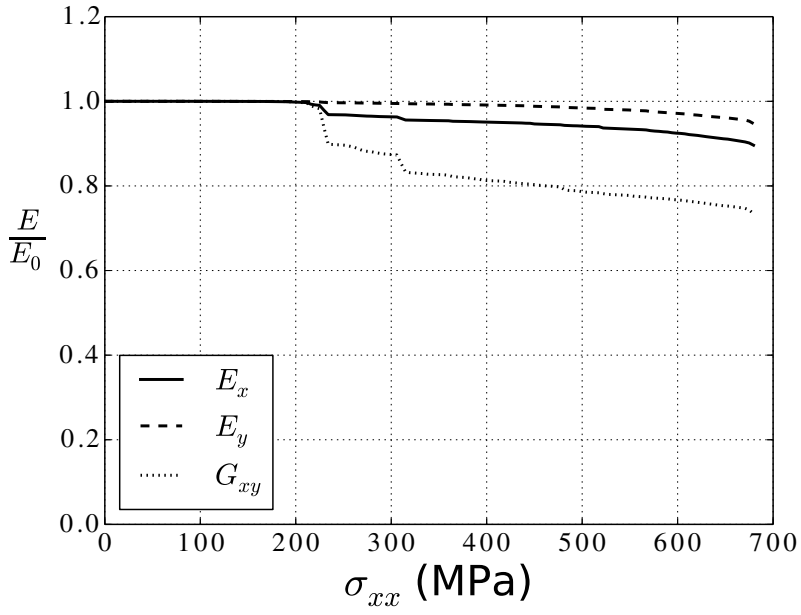

Figure V.23: In-plane property evolution under uniaxial σ_{xx}, $\Delta T = -10°\text{C}$.

V.C.3.b. Failure Under Equal Biaxial Load

Progressive failure under in-plane equal biaxial tension shares many characteristics with unidirectional loading. As shown in Fig. V.24, for textiles at room temperature and near cure temperature, cracking was predicted to initiate in both tows at nearly the same load. The onset of cracking occurred at a considerably lower stress for the room temperature model (Fig. V.24a) than for the model near cure temperature (Fig. V.24b). For both temperatures, cohesive element degradation occurred on the inter-tow interface, in the neat matrix pocket, and on the inter-tow-matrix interface immediately after crack opening began in the tows. The models at both temperatures predicted the onset of fiber failure at nearly the same applied loading: $\sigma_{xx} = \sigma_{yy} = 733.5$ MPa for room temperature and $\sigma_{xx} = \sigma_{yy} = 742.5$ MPa

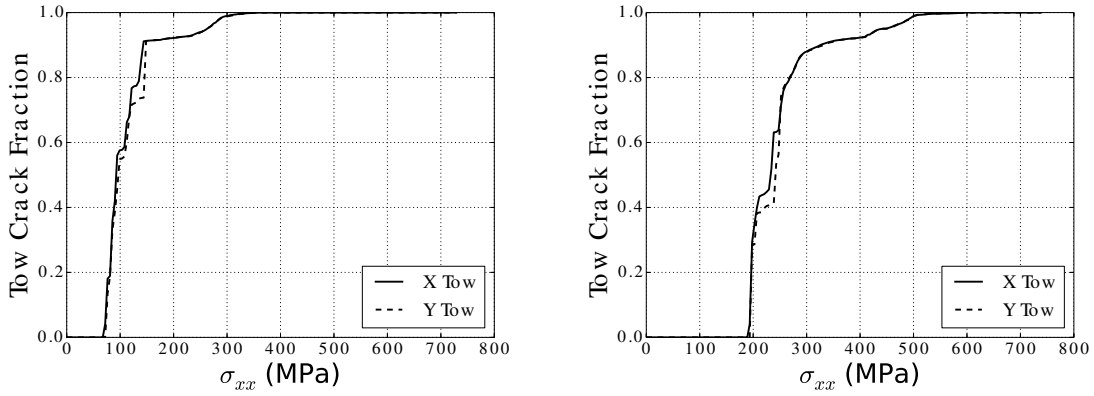

(a) $\Delta T = -160°\text{C}$ (b) $\Delta T = -10°\text{C}$

Figure V.24: Tow crack opening under biaxial tension $\sigma_{xx} = \sigma_{yy}$.

near cure temperature. Like uniaxial loading, biaxial loading resulted in essentially no shear damage in the tows.

The evolution of in-plane properties, shown in Fig. V.25, provides further insight into how different damage mechanisms affect the resulting stiffness of the textile unit cell. Both E_{xx} and E_{yy} experience a 5-6% drop when tow cracking occurs. Furthermore, the total drop in G_{xy} is approximately 35%, which suggests that the effect of tow cracking on the shear modulus is cumulative (that is, the reduction in G_{xy} resulting from cracks in both tow directions is roughly twice the reduction for tow cracking in just one direction).

V.C.3.c. Failure Under In-Plane Shear Load

Under in-plane shear loading, damage evolves in a characteristically different way than under in-plane normal loading. While shear damage was not a major occurrence under in-plane normal loading, it dominates the behavior under in-plane shear. Fig.

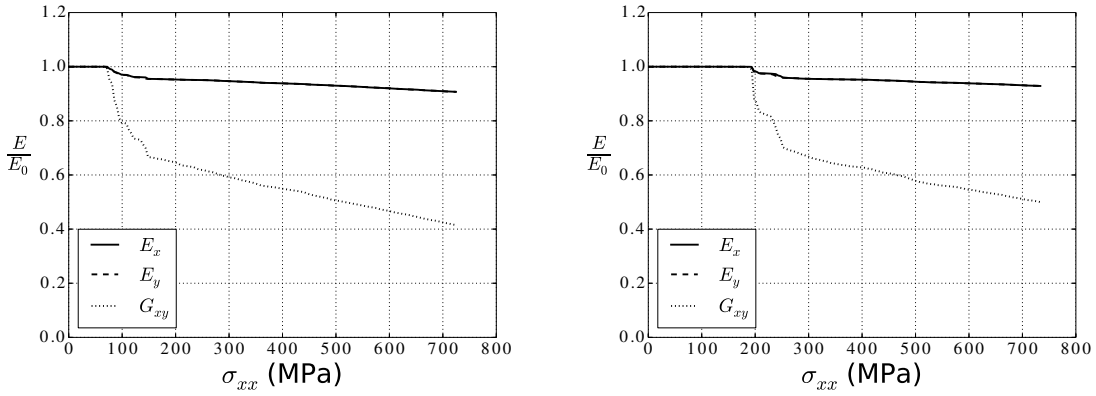

(a) $\Delta T = -160°\text{C}$ (b) $\Delta T = -10°\text{C}$

Figure V.25: In-plane property evolution under biaxial tension $\sigma_{xx} = \sigma_{yy}$.

V.26 shows the evolution of shear damage and tow cracking. Fig. V.26a shows the evolution of the volume average of d_{12} taken over the volume of the tows. For this loading, the value of d_{13} in the tows remains negligible compared to d_{12}. As shear loading is initially applied, shear damage starts to develop at the tow edge crossover (Fig. V.8), along the edges of the tow, and in regions in close proximity to the edges of crossing tows. Continued loading leads to an increase in shear damage as well as the onset of degradation in the intra-tow cohesive zones in regions of elevated shear damage (and elevated shear stress). With further increases in loading, cohesive zone degradation becomes more widespread, and complete decohesion occurs in a limited number of locations. Additionally, at elevated loads, the shear damage in the tows continues to increase, particular in regions where it was originally lower. In Fig. V.26e, bands of tow material with lower shear damage are apparent where tow crack opening and interfacial failure have shielded regions of the tow from elevated shear

stresses.

As was observed under normal in-plane loads, degradation of the cohesive zones on the interfaces and in the neat matrix pocket started as a result of the development of adjacent tow cracks. This degradation appeared to play less of a role in the overall response of the unit cell under shear as compared to uniaxial and biaxial loadings. A metric was developed which tracks the amount of strain energy that has been dissipated in these cohesive zones normalized by the total amount of strain energy that they would be dissipated by the complete failure of all of the cohesive elements. At the maximum shear stress, this metric was 1/7th as large as it was at failure under uniaxial normal load.

Final failure under shear loading came as the result of the onset of a softening response which led to an instability under stress-controlled loading. The overall stress-strain response of the textile is shown in Fig. V.27. It can be noted from the overall response that the gradual development of shear failure in the tows leads to a nonlinear shear response of the textile under shear loading. This is also seen in the evolution of the effective in-plane moduli, shown in Fig. V.28. There is a large decrease in the in-plane shear modulus associated with the development of shear damage in the tows. There is a slight decrease in the normal moduli resulting from partial crack opening in the tows as well as the opening of cohesive zones elsewhere in the unit-cell.

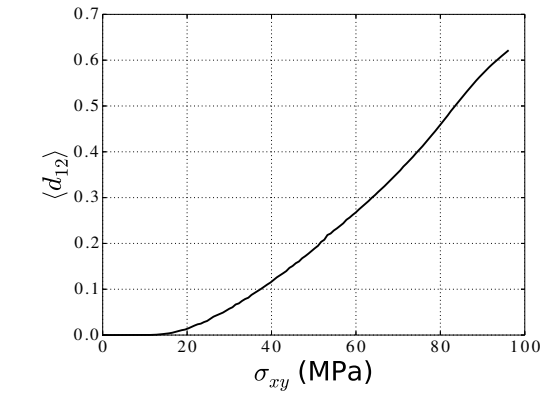

(a) Evolution of d_{12}

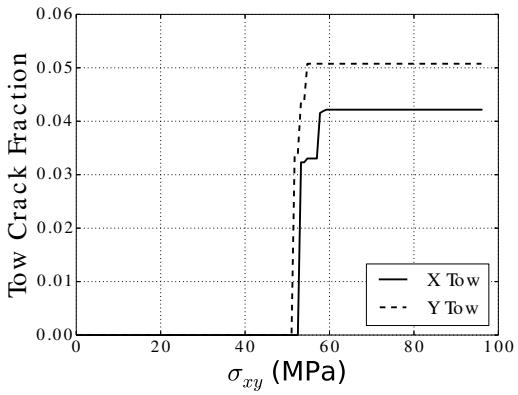

(b) Evolution of tow cracking

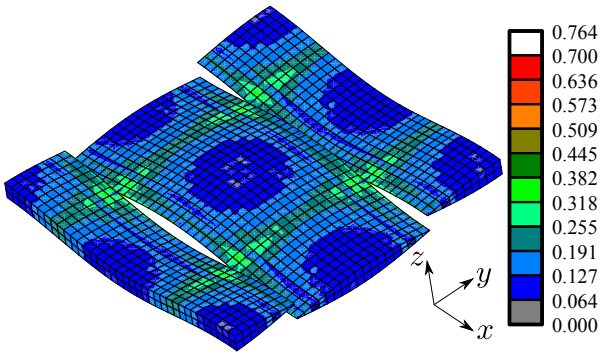

(c) d_{12} contour, $\sigma_{12} = 45$ MPa

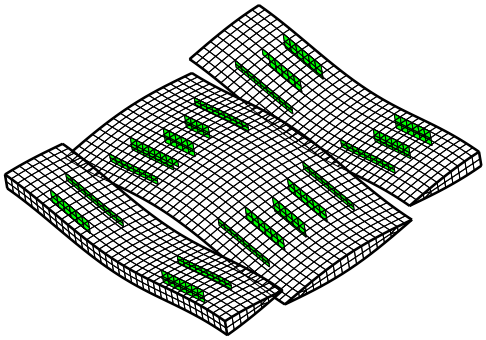

(d) X tow cracking, $\sigma_{12} = 45$ MPa

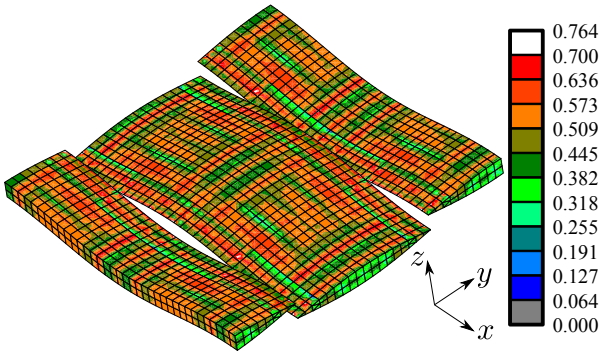

(e) d_{12} contour, $\sigma_{12} = 82.5$ MPa

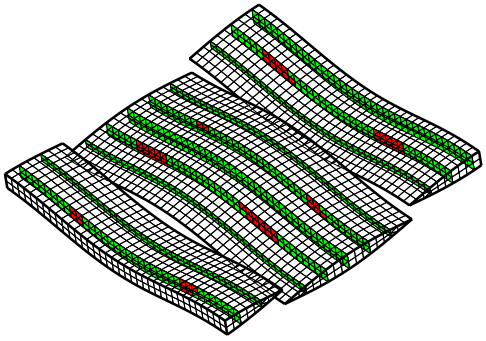

(f) X tow cracking, $\sigma_{12} = 82.5$ MPa

Figure V.26: Shear damage and tow cracking under in-plane σ_{xy}, $\Delta T = -160°$C.

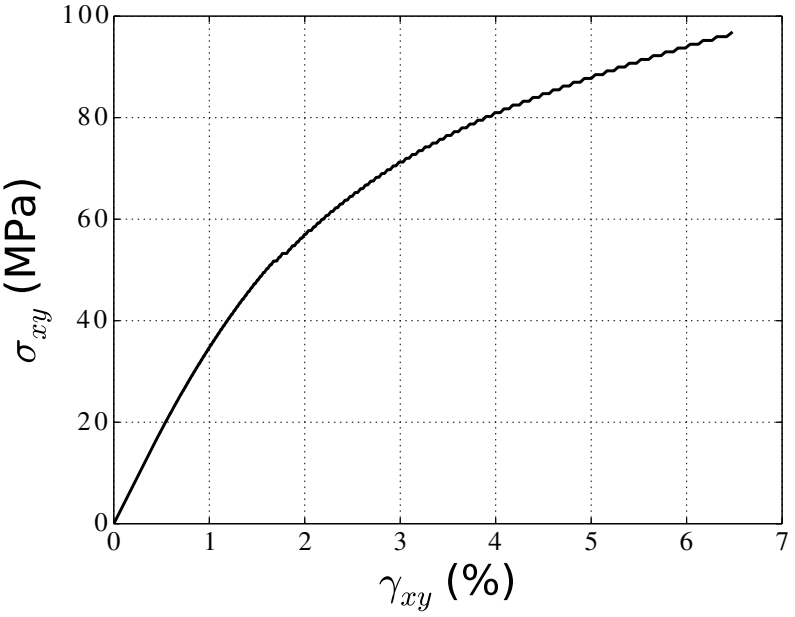

Figure V.27: Stress-strain response under σ_{xy}, $\Delta T = -160°\text{C}$.

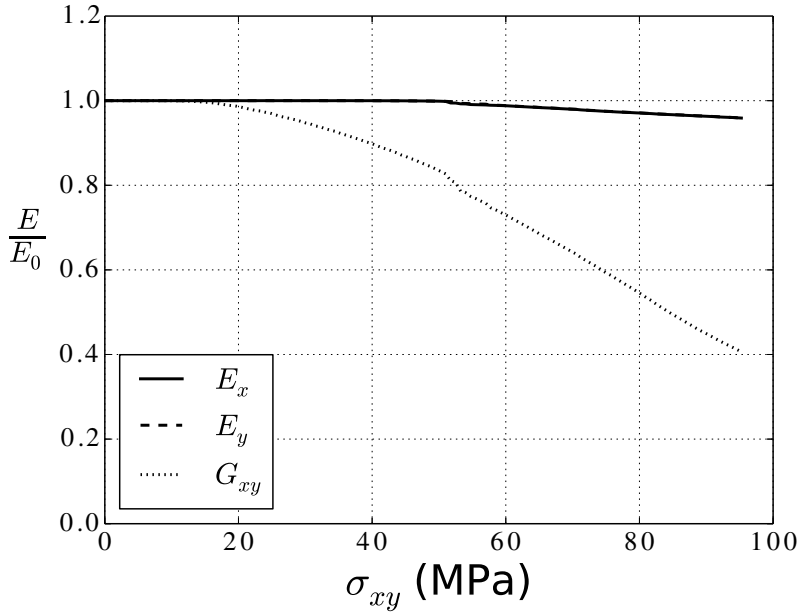

Figure V.28: In-plane property evolution under under σ_{xy}, $\Delta T = -160°\text{C}$.

V.C.4. Characteristic Progressive Failure Behaviors

Based on observations of the behaviors under a variety of loadings, several different characteristic behaviors were noted in the evolution of damage and the resulting material degradation. These behaviors are discussed in the following sections.

V.C.4.a. Tow Cracking

In-plane normal loading was always observed to cause the development of brittle cracking in the tows running transverse to the applied load. This tow cracking typically developed fairly rapidly within the tow at significantly lower loading than that required to cause fiber failure in the axial tows. It was observed that multiaxial normal loads tended to reduce the stress to cause this failure even further. Additionally, thermally induced stresses from cure tend to cause a much earlier onset of tow cracking under tensile loading. Tow cracking also occurred under shear loading after the tows had experienced considerable shear degradation. Crack opening under shear was much more gradual than under normal load, with lots of partial opening. There was a characteristic reduction in the Young's modulus for the direction perpendicular to the cracked tow of about 5%. Also, cracking in one tow direction resulted in a drop in the in-plane shear modulus G_{xy} of almost 20%, while cracking in both tows caused a drop of approximately 35%. A convenient way of tracking the evolution of this failure mode was to track the total area of opened (completely failed) cohesive elements in a tow and normalize it by the total area of cohesive elements in a tow.

V.C.4.b. Shear Damage

Under shear loading, the predominant mode of damage was the development of distributed shear damage within the tows . Shear damage primarily consisted of d_{12}; d_{13} was not observed to have a major effect on the response of the textile. The onset of d_{12} shear damage occurred at fairly low shear stresses relative to the maximum shear stress that is reached. Worsening shear damage led to a steady reduction in G_{xy} for the textile as loading was increased. A convenient way of tracking the evolution of the shear damage parameter d_{12} in the tows was to take the volume average of the damage parameter over the tow volumes. Examining a large number of multiaxial loadings showed that this metric correlates very strongly with the applied shear stress component, regardless of other stress components applied to the textile, as shown in Fig. V.29.

V.C.4.c. Degradation in Interfacial and Matrix Cohesive Zones

The final characteristic type of failure that was observed to occur was the degradation and occasional failure of cohesive zones in the neat matrix pocket and on the interfaces between tows and between the tows and neat matrix pocket. This failure was strongly linked to the development of tow cracks, and almost always developed as an extension of those cracks into adjacent parts of the textile unit cell. This type of failure can be characterized for the composite by taking the total amount of strain energy that has been dissipated over all the cohesive elements in these regions of the textile and normalizing that value by the total critical strain energy for those cohesive elements (i.e., the total amount of energy that would be required to com-

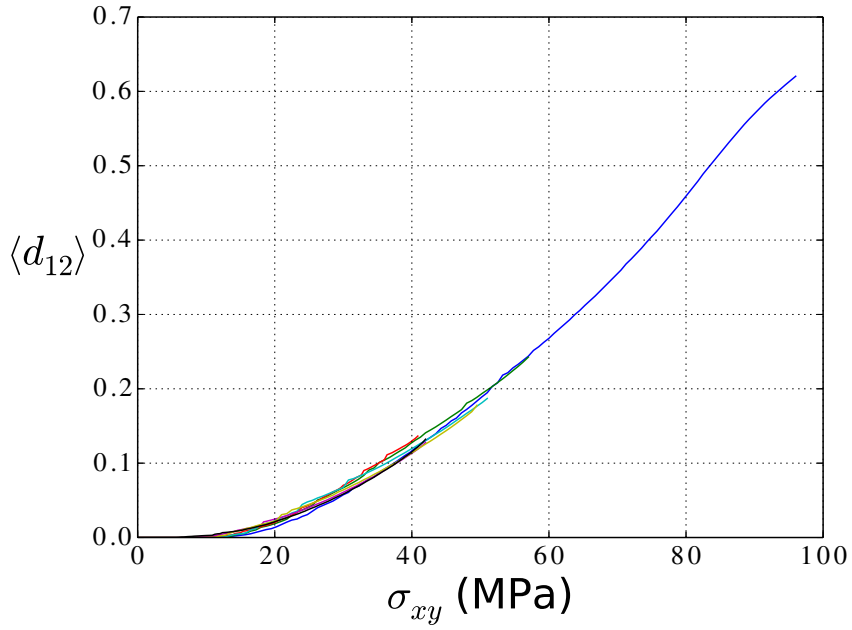

Figure V.29: Evolution of $\langle d_{12} \rangle$ vs. σ_{xy} for various multiaxial loadings, $\Delta T = -160°\text{C}$.

pletely fail all of these cohesive zones from their virgin state). This type of failure was observed to result in a gradual reduction in both in-plane Young's moduli as well as the in-plane shear modulus.

V.D. Towards a Reduced-Order Structural-Scale Continuum Damage Model for Textile Composites

The characterization of failure behaviors at the textile scale permits the development of a continuum damage mechanics model that can be applied to engineering structures made from textile composites. Such a model is used to accomplish the following:

- Determine the overall response of the textile for a given damage state.
- Predict the evolution of the damage state based on the load history.
- Predict the onset of critical failure in the textile.

The following sections describe the development of a continuum damage mechanics model that can be used to accomplish these tasks, as well as a comparison of response predictions made using the continuum damage mechanics model and directly using textile unit-cell analysis.

V.D.1. Determination of Effective Textile Response from Characteristic Damage Parameters

The first aspect of the model that is addressed is determining how the evolution of the damage state in the textile affects its overall response. At the structural

scale, details of the textile architecture are not modeled, and therefore the evolution of damage in the textile cannot be directly modeled. Therefore, damage at the structural scale is accounted for through the use of state variables which represent characteristic damage behaviors that occur at smaller scales in the textile. As described in section V.C.4 there are four primary modes of damage which were observed to develop in textile composites for the range of loadings that were examined:

- Tow cracking in the x-tows
- Tow cracking in the y-tows
- Diffuse damage growth in the tows due to shear
- Cohesive zone opening on the interfaces and within the neat matrix pocket

Approaches were described for each of these modes to represent the overall evolution of the mode in a textile unit cell using a single value. In the continuum damage model applied at the structural scale, these four damage modes will be represented using four different damage state variables, d_x, d_y, d_I, and d_s, which are to be tracked locally in the structure. These damage state variables are described in table V.11. It is important to clearly point out that each state variable corresponds directly to a metric which can be measured using the damage state in a textile unit cell.

These damage state variables will be utilized to predict degradation of the effective in-plane moduli for the textile. The moduli are determined from the following equations.

$$E_x = \left(1 - \left(m_{d_x}^{E_x} d_x + m_{d_y}^{E_x} d_y + m_{d_I}^{E_x} d_I + m_{d_s}^{E_x} d_s\right)\right) E_x^0 \tag{5.13}$$

$$E_y = \left(1 - \left(m_{d_x}^{E_y} d_x + m_{d_y}^{E_y} d_y + m_{d_I}^{E_y} d_I + m_{d_s}^{E_y} d_s\right)\right) E_y^0 \tag{5.14}$$

Table V.11: Damage state variables for textile continuum damage model.

Variable	Description	Formulation from textile UC
d_x	Fraction of crack opening in X tow	$\frac{\text{Area of CZs in tow with } d\text{=1}}{\text{Area of all CZs in tow}}$
d_y	Fraction of crack opening in Y tow	
d_I	Interface and matrix pocket degradation	$\frac{\text{Total } U_{dissipated}}{\text{Total critical strain energy}}$
d_s	Volume averaged shear damage parameter	$\frac{1}{V_{tows}} \int_{\text{tows}} d_{12}\, dV$

$$G_{xy} = \left(1 - \left(m_{d_x}^{G_{xy}} d_x + m_{d_y}^{G_{xy}} d_y + m_{d_I}^{G_{xy}} d_I + m_{d_s}^{G_{xy}} d_s\right)\right) G_{xy}^0 \tag{5.15}$$

In these equations, the variables of the form $m_{d_y}^{E_x}$ are influence parameters which are the partial derivatives of a given normalized modulus with respect to a damage state variable. They are assumed to be constant, and define (for the case of $m_{d_y}^{E_x}$) what proportion of the x-direction Young's modulus E_x is lost due to a change in the y-tow cracking state variable d_y. These parameters, given in table V.12, were determined by examining the change in effective response as damage evolved using the textile unit cell analyses for uniaxial and shear loading cases at room temperature ($\Delta T = -160°C$). For each load case, the damage state variables d_x, d_y, d_I, and d_s were calculated from the damage state in the textile unit cell. Then, the influence parameters were modified so that Eqs. 5.13, 5.14, and 5.15 predicted an effective response as close as possible to the response obtained from the textile unit cell analysis for these two load cases. The uniaxial and shear loading cases were chosen to perform this calibration because of their simplicity, because between the

Table V.12: Damage influence parameters.

	E_x	E_y	G_{xy}
d_x	0	0.05	0.19
d_y	0.05	0	0.19
d_I	1.2	1.2	2.3
d_s	0.04	0.04	0.92

two of them, they exhibited all four of the different types of characteristic damage, and because both of these load cases experience extended ranges of loading where the evolution of one characteristic damage state dominates all the others, which simplifies the process of isolating that damage state's effect on the textile response. All of the influence parameters related to the tow cracking state variables (d_x and d_y) were determined from the stiffness degradation associated with y-tow cracking in the uniaxial loading case. The degradation parameters associated with matrix pocket and interface failure (d_I) were determined from the property degradation that occurred in the uniaxial loading case after the y-direction tows experienced crack opening. The influence parameters associated with diffuse shear damage in the tows (d_s) were determined from the property degradation observed for the shear loading case as the tows experienced diffuse shear damage. It would likely be possible to improve upon the prediction of these influence parameters through the use of optimization methods applied to a broader variety of applied loadings, but as will be shown in later sections, the results obtained using this simpler approach were found to be satisfactory.

Some discussion of these parameters is warranted. Values of zero for $m_{d_x}^{E_x}$ and $m_{d_y}^{E_y}$ indicate that matrix cracks in a tow do not affect the Young's modulus in the direction of that tow. Values of 0.05 for $m_{d_y}^{E_x}$ and $m_{d_x}^{E_y}$ signify that matrix cracks in a

tow do cause a small reduction in the Young's modulus for the direction normal to the crack planes. This effect is limited due to the fact that most of the normal stiffness in a given direction for the textile comes from the tows running in that direction. Therefore, cracking in transverse tows has only a small effect on the Young's modulus. Tow cracking has a larger effect on the shear modulus as evidenced by values of 0.19 for $m_{d_x}^{G_{xy}}$ and $m_{d_y}^{G_{xy}}$. This is because the tows carry most of the in-plane shear loading in the textile, and cracking in the tows severely disrupts the load path for in-plane shear. For this same reason, diffuse shear damage d_s also has a large effect on the overall shear stiffness of the textile as seen from $m_{d_s}^{G_{xy}} = 0.92$. Values of 0.04 for $m_{d_s}^{E_x}$ and $m_{d_s}^{E_y}$ indicate that diffuse shear damage only has a small effect on the transverse moduli, which is expected since the development of diffuse shear damage in the tows of the textile unit cell only changes the local shear modulus of the tow according to Eq. 5.10, and not the tow's local transverse Young's modulus. Finally, the opening of cohesive zones on the interfaces and within the matrix pocket has a moderate effect on all of the in-plane moduli as seen from the values for $m_{d_I}^{E_x}$ and $m_{d_I}^{E_y}$ (1.2) and $m_{d_I}^{G_{xy}}$ (2.3). These values are considerably larger than the other influence parameters because the observed values for d_I in practice are quite low (less than 0.1). The state variable d_I is perhaps the least precise of the four damage measures in terms of it's effect on the overall textile response because it encompasses damage across such a broad part of the textile unit cell, but based on the predictive capability of the current model (which will be examined in later sections), it appears to be adequate to predict the continued evolution of the in-plane properties with fairly good accuracy after a tow has experienced cracking.

V.D.2. Prediction of Damage State for Arbitrary Loadings

With the definition of damage state variables and a determination of how the evolution of those state variables affects the overall response of the textile, the final major aspect of the textile continuum damage model which must be developed is determining the evolution of the damage state variables for an arbitrary in-plane loading. Although it may be possible through a protracted study of the damage evolution in the textile unit cell under various loadings to develop functional relationships between applied loading, temperature, and the damage state variables, a much simpler approach will be taken. Since only tensile and shear in-plane thermomechanical loadings are being considered currently, it is feasible to sample the parameter space of possible applied loads with a high density. This allows the damage state for an arbitrary loading to be interpolated through a table-lookup of damage state evolution for similar loadings whose damage evolution has been determined a priori through textile unit cell analysis. The high-level approach for this is as follows:

1. Calculate the evolution of d_x, d_y, d_I, and d_s and the onset of critical failure for a number of different reference load cases using textile unit cell progressive failure analysis.

2. Organize the damage evolution and critical failure data for each reference load case into a database organized by the ratio of the applied loading components.

3. For a new in-plane load, search the database for the reference load cases which are most similar to the new load case.

4. Interpolate the critical failure load for the new load case from the similar ref-

erence load cases in the database.

5. Interpolate the damage state variable evolution for the new load case from the similar reference load cases in the database.

6. Predict the effective response for the new load case using the interpolated damage states variables and Eqs. 5.13, 5.14, and 5.15.

This approach is carried out on load cases for the same temperature. If the behavior is needed for a temperature that is different from the temperatures used to generate databases of reference behaviors, the databases for the two nearest temperatures will be used to determine the damage state variable evolutions for the loading. These two behavior predictions will then be used to interpolate the damage state variable evolution at the temperature of interest.

The analyses for reference load cases described in step 1 were performed for the stress ratios $\sigma_{xx} : \sigma_{yy} : \sigma_{xy}$ given in table V.13. No cases were examined in which $\sigma_{yy} > \sigma_{xx}$. Due to the symmetry of the unit cell, the behavior from these cases can be obtained from the load cases in table V.13 by swapping d_x and d_y. For instance, the loading ratio $1\sigma_{xx} : 2\sigma_{yy} : 0\sigma_{xy}$ is effectively the same as $2\sigma_{xx} : 1\sigma_{yy} : 0\sigma_{xy}$. The only difference is that the x and y directions for one case are switched in the other. Therefore, d_x for $1\sigma_{xx} : 2\sigma_{yy} : 0\sigma_{xy}$ evolves in an identical manner to d_y for $2\sigma_{xx} : 1\sigma_{yy} : 0\sigma_{xy}$.

Once the damage state variable evolution and final failure loads are determined for the reference load cases using textile unit cell analysis, they are stored in a database as specified in step 2. The different behaviors are organized using a triangulation performed in a normalized loading space. This will facilitate the process

Table V.13: Stress ratios defining reference load cases for development of textile continuum damage model.

σ_{xx}	σ_{yy}	σ_{xy}
1	0	0
2	1	0
1	1	0
12	0	1
12	6	1
12	12	1
6	0	1
6	3	1
6	6	1
0	0	1

of determining which reference load cases in the database are most similar to a new load case. First, the stress components for each reference load case are normalized by the failure stress for that load component. For instance, suppose that under pure shear loading, the textile has a strength of $S_{xy} = 80$ MPa. In that case, the shear component of loading for every reference load case is divided by 80 MPa. This is done for all three components of mechanical loading. Then, these normalized loads are projected onto a unit sphere in the normalized loading space. A Delaunay triangulation is then carried out for the loads on this unit sphere. The resulting triangulation is shown in Fig. V.30.

Identifying the reference load cases that are most similar to a new load (step 3) is accomplished as follows. First, the load components for the new load case are normalized in the same manner as for the reference load cases (as described for step 2) and are then projected onto the triangulation. The reference load cases which

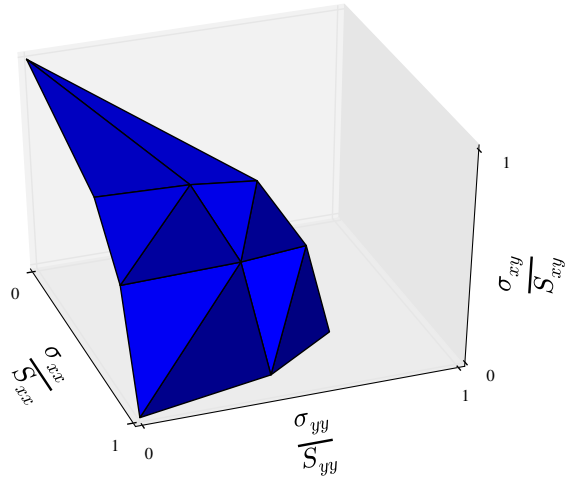

Figure V.30: Triangulation of load cases in normalized stress space.

form the vertices of the triangle that the new load case projects onto are the similar reference load cases that will be used for the interpolation. Area coordinates on the triangle are utilized to determine how much each similar reference load case contributes to the interpolated behavior for the new load case.

The first value that is interpolated for a new load case is the load at which critical failure occurs (step 4). This is determined by interpolating the Euclidean norm (the L^2 norm, given in Eq. 5.16) of the critical failure stress for the similar reference load cases.

$$\left\|\sigma^{crit}\right\| = \sqrt{\left(\sigma_{xx}^{crit}\right)^2 + \left(\sigma_{yy}^{crit}\right)^2 + \left(\sigma_{xy}^{crit}\right)^2} \tag{5.16}$$

It is assumed that the interpolated value will be the Euclidean norm of the critical failure stress for the new load case. The stresses at failure can then be backed out

for the new load case.

Next, the damage states are interpolated for the new load case (step 5). There is some difference in the way that the different damage state variables are interpolated. Interpolation of tow cracking d_x and d_y, as well as interfacial damage d_I, is performed using a load scaling parameter λ which starts at zero when the applied mechanical load is zero and increases to one when the critical failure load is reached. This facilitates a direct comparison between the different load cases. Rather than interpolating the value of the damage state variables at a given value of λ, interpolation will be performed to determine the value of λ at which the damage state variable reaches a given level of severity. This is done because these modes of damage, particularly tow cracking, tend to evolve suddenly. Fig. V.31 provides an illustration of this. Assume that the new load case being interpolated lies halfway between "Load 1" and "Load 2" (the similar reference load cases). One would expect that under this loading, the actual behavior would be a sudden increase in d that occurs halfway between the λ values when the similar reference load cases experience increases in d. However, if one simply interpolates the value of d at a given value of λ, the incorrect behavior will be obtained, with d increasing suddenly to a value of 0.5 when "Load 1" experiences an increase in d, and then increasing to 1 after "Load 2" experiences an increase in d. Instead, it is necessary to interpolate the value of λ at which d reaches a given value for the new load case, which yields the desired result. One challenge that is associated with this approach is that all of the similar reference load cases may not reach the same maximum value of d. This is handled in the following manner. The maximum value of d attained by any similar reference load case is determined first.

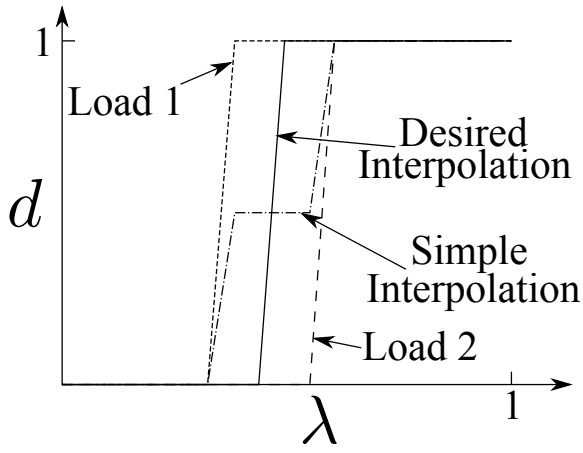

Figure V.31: Example of damage state interpolation between behaviors for two loadings.

Then, when the interpolation is being performed, it is assumed for similar reference load cases that do not reach this maximum d that they *would* reach that value at some $\lambda > 1$ (i.e. if λ were to continue increasing without the occurrence of some critical failure). The current implementation assumes that this value is $\lambda = 1.1$. This approximation works well provided that the similar reference load cases are sufficiently close to the new load case whose behavior is being interpolated.

The interpolation of the diffuse shear damage state variable d_s is handled differently than the other damage state variables. As shown in Fig. V.29, the evolution of diffuse shear damage correlates strongly with the applied σ_{xy} regardless of the multiaxiality of the applied load. Therefore, the evolution of d_s for the new load case is determined using the relationship between d_s and σ_{xy} for the similar reference load case with the largest component of shear loading.

V.D.3. Validation of Model

Several different trial cases were examined to determine the fitness of the currently described continuum damage model for several different cases.

V.D.3.a. Response Prediction Using Damage Parameters.

The first aspect of the model that was examined was the use of the four damage state variables to predict the effective response of the textile. A great deal of information regarding the distribution of crack opening and damage is lost when the damage state in the textile is reduced to just four parameters, so it is important to examine the effect this reduction in information has on the overall response prediction. Figs. V.32 and V.33 show the predicted response at room temperature and near cure temperature using Eqs. 5.13, 5.14, and 5.15 along with the influence parameters given in table V.12. The responses from the continuum damage mechanics model (lines) are compared to the responses determined directly from the textile unit-cell model (dots) for a variety of different loads. The damage state variables for these loadings are computed directly from the actual damage state in the textile unit cell models (they are not interpolated) Therefore, these plots show the effect of using Eqs. 5.13, 5.14, and 5.15 to predict the response with a reduced-order representation of the damage state in the textile. Recall that the determination of the influence parameters in the degradation equations was accomplished by identifying values which caused the predicted response under uniaxial load (Fig. V.32a) and shear load (Fig. V.32j) to match as closely as possible to the response obtained from the textile unit cell model. Therefore, these two load cases, and only these two load cases, should

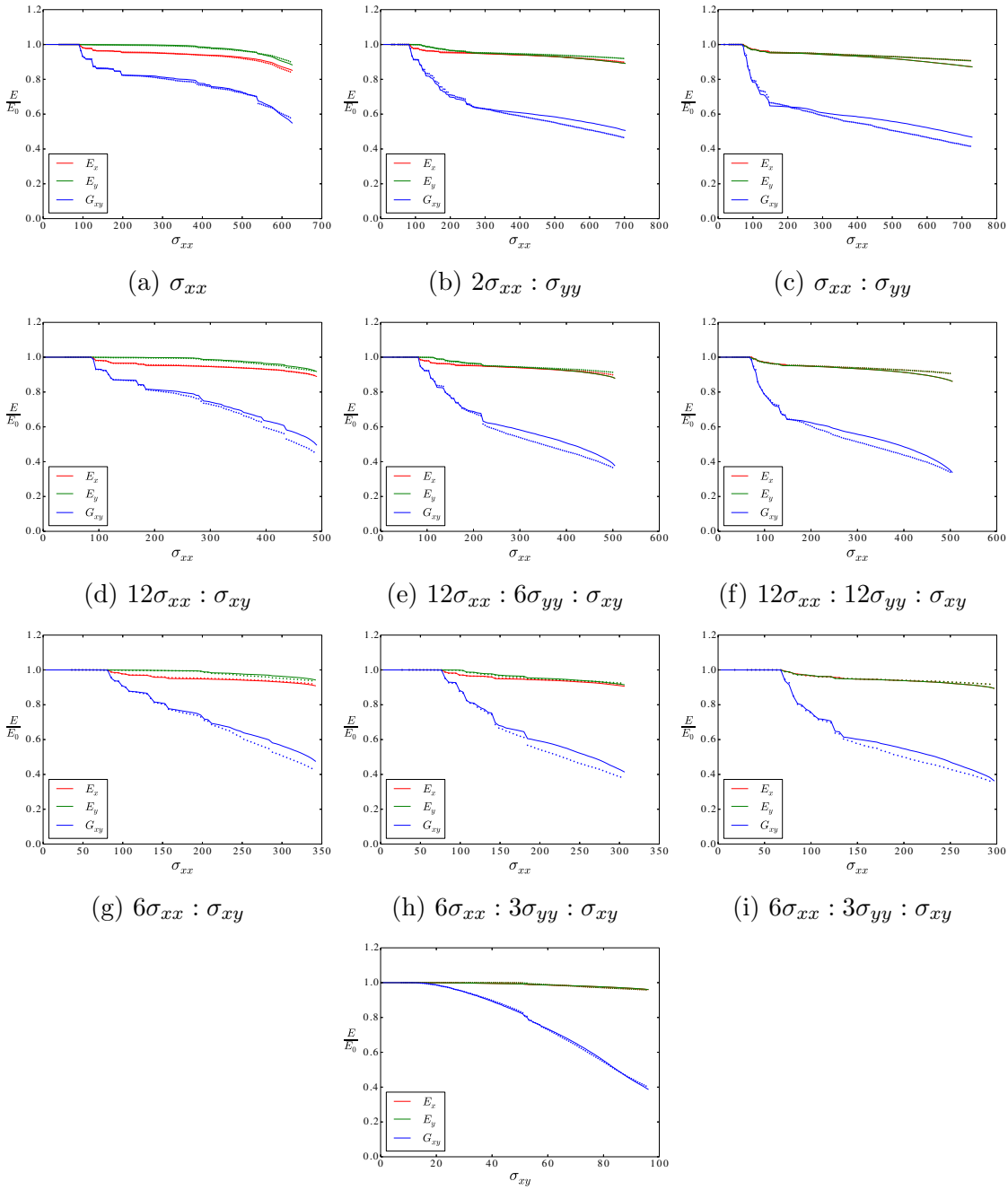

(a) σ_{xx} (b) $2\sigma_{xx} : \sigma_{yy}$ (c) $\sigma_{xx} : \sigma_{yy}$

(d) $12\sigma_{xx} : \sigma_{xy}$ (e) $12\sigma_{xx} : 6\sigma_{yy} : \sigma_{xy}$ (f) $12\sigma_{xx} : 12\sigma_{yy} : \sigma_{xy}$

(g) $6\sigma_{xx} : \sigma_{xy}$ (h) $6\sigma_{xx} : 3\sigma_{yy} : \sigma_{xy}$ (i) $6\sigma_{xx} : 3\sigma_{yy} : \sigma_{xy}$

(j) σ_{xy}

Figure V.32: Comparison of predicted effective response evolution (lines) to textile unit cell analysis (dots) for various ratios of stress loading $\Delta T = -160$

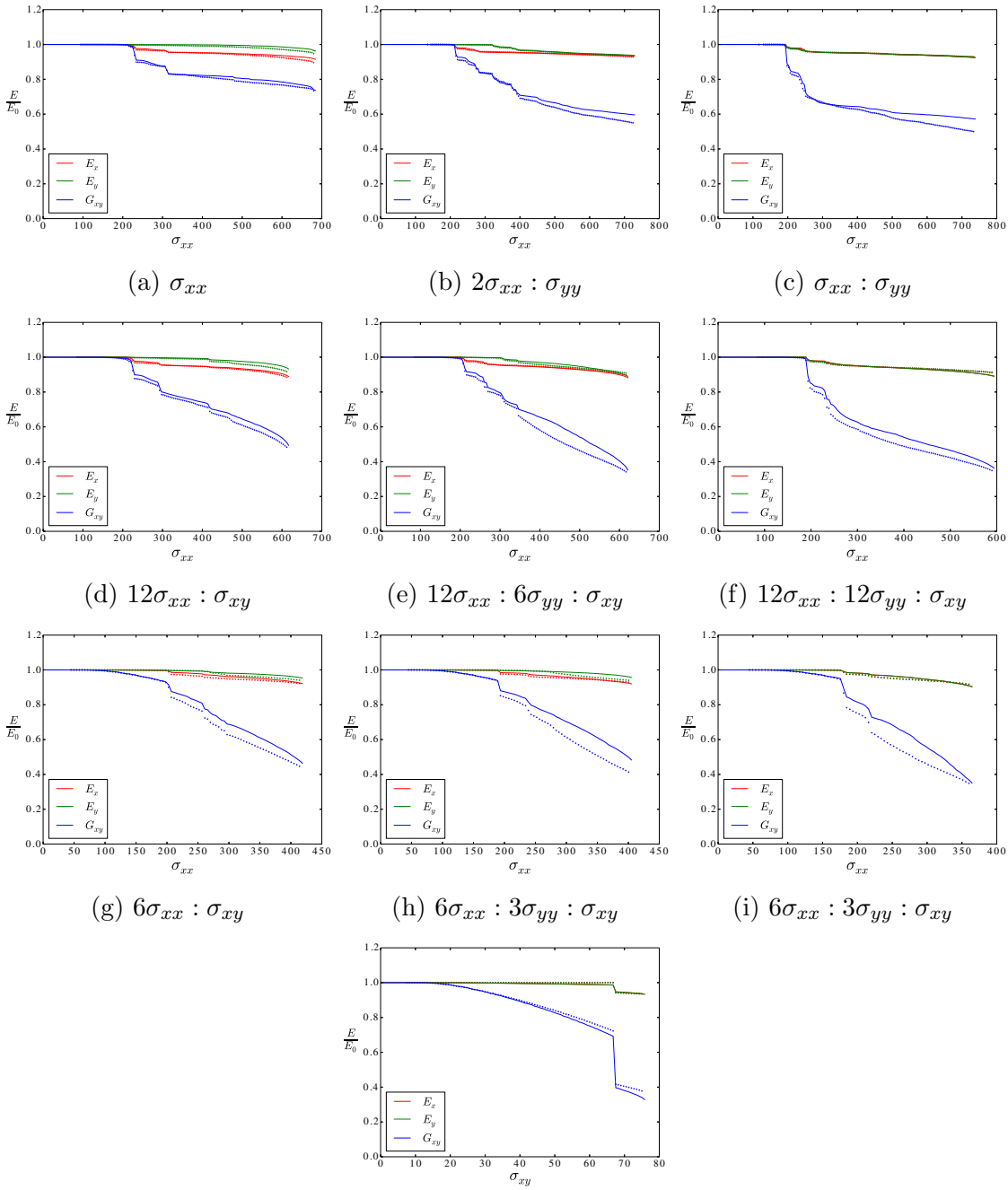

(a) σ_{xx} (b) $2\sigma_{xx} : \sigma_{yy}$ (c) $\sigma_{xx} : \sigma_{yy}$

(d) $12\sigma_{xx} : \sigma_{xy}$ (e) $12\sigma_{xx} : 6\sigma_{yy} : \sigma_{xy}$ (f) $12\sigma_{xx} : 12\sigma_{yy} : \sigma_{xy}$

(g) $6\sigma_{xx} : \sigma_{xy}$ (h) $6\sigma_{xx} : 3\sigma_{yy} : \sigma_{xy}$ (i) $6\sigma_{xx} : 3\sigma_{yy} : \sigma_{xy}$

(j) σ_{xy}

Figure V.33: Comparison of predicted effective response evolution (lines) to textile unit cell analysis (dots) for various ratios of stress loading $\Delta T = -10$

be considered "calibration" cases. The remainder of the loads constitute validation cases, since they were not considered when calibrating the influence parameters. The plots show that for all of the load cases examined, the predicted response evolution compares very well with the response evolution determined directly from the textile unit cell analyses. This indicates that the four damage state variables selected for the textile continuum damage mechanics model characterize the damage state in the textile unit cell in a manner that enables accurate prediction of the textile's response.

V.D.3.b. Predicted Response from interpolated damage state.

The next aspect of the model that was examined is the accuracy of the table-lookup approach for interpolating the damage state evolution of a load case that was not examined through textile unit cell analysis a priori. This was done by choosing a load state which differed from the reference load states used to populate the database of behaviors for the textile. The load state chosen for this investigation was a stress ratio of $90\sigma_{xx} : 10\sigma_{yy} : 3\sigma_{xy}$. The damage evolution and response for this load case were interpolated from similar reference load cases in the database. The load case was also run directly using textile unit cell analysis. The interpolated damage state variable evolution (lines) are compared to the damage state variable evolution calculated directly from the textile unit cell model (dots) in Fig. V.34, and the predicted response is compared to the interpolated response in Fig. V.35. These analyses were performed with a temperature change from cure of $\Delta T = 60°\text{C}$.

The interpolated damage state variable evolution compared reasonably well with the damage state evolution predicted from the textile unit cell analysis. The evolu-

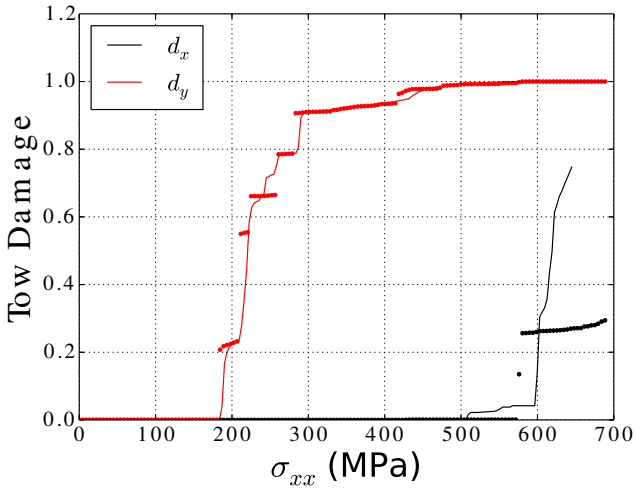

(a) Tow cracking

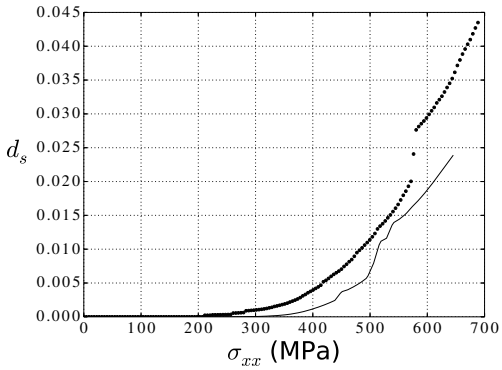

(b) Diffuse tow shear damage

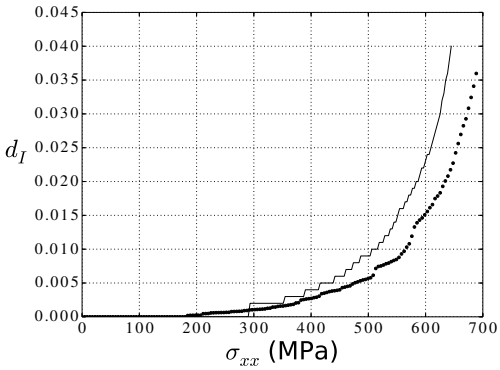

(c) Interface and matrix cracking

Figure V.34: Comparison of interpolated damage state variables (lines) with those calculated from a textile unit-cell analysis (dots).

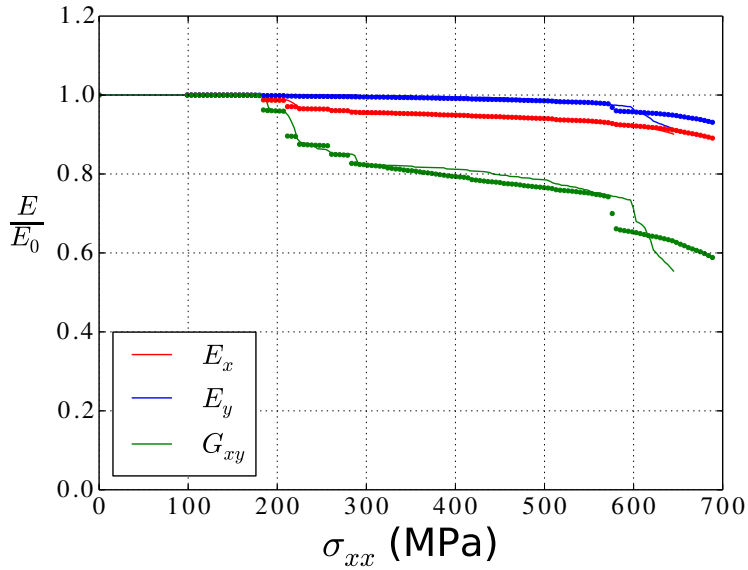

Figure V.35: Comparison of predicted response using interpolated damage state variables (lines) with response from a textile unit-cell analysis (dots).

tion of y tow cracking (d_y) was predicted very well. The evolution of x tow cracking (d_x) was not predicted with as much accuracy. However, this damage state variable suffered from the challenge previously described regarding interpolation of a damage state that doesn't occur in all of the similar reference load cases. Despite this difficulty, the interpolation procedure did correctly predict that d_x occurred for this load case, although its extent was somewhat over-predicted. Shear damage in the tows (d_s) was predicted with fairly good accuracy considering that it stayed at a fairly low level, and interface and matrix crack opening was also predicted with a reasonable degree of accuracy. The critical failure stress for the textile was underestimated by a little less than 10%. The response evolution predicted using the interpolated damage state variables compared quite well with the prediction made directly using textile

unit cell analysis. The inaccuracies related to interpolating the damage parameters could be reduced by using more reference load states to build the database of damage evolution behaviors.

V.D.3.c. Predicted Response for Nonproportional Loading

The final validation case which was examined presents considerably more difficulty. The behavior under a damage-inducing non-proportional load was examined. The stress history applied to the model is shown in Fig. V.36, and was applied with a temperature change from cure of $\Delta T = -60°\text{C}$. The applied stress was tracked by the scaling parameter λ, which increased from 0 to 1. For the first half of the loading, a biaxial load state was applied up to a value of $\sigma_{xx} = \sigma_{yy} = 300$ MPa. As noted from investigating the damage evolution under biaxial loading, 300 MPa of biaxial stress is sufficient to cause extensive tow cracking in both tow directions as well as accompanying damage in the interfaces and neat matrix pocket, but is not sufficient to cause critical failure. When λ reached a value of $\frac{1}{2}$, the biaxial load was removed and in-plane shear stress σ_{xy} was applied. The in-plane shear stress σ_{xy} increased from a value of 0 at $\lambda = \frac{1}{2}$ to a maximum value of $\sigma_{xy} = 150$ MPa at $\lambda = 1$. Complete failure of the textile occurred before the shear stress reached its maximum value.

The predicted behavior was obtained by first tracking the evolution of the damage state variables using the biaxial reference load case. For $0 < \lambda < \frac{1}{2}$, the response was predicted with a high degree of accuracy since the load histories are essentially the same between the reference load case in the database and the validation model.

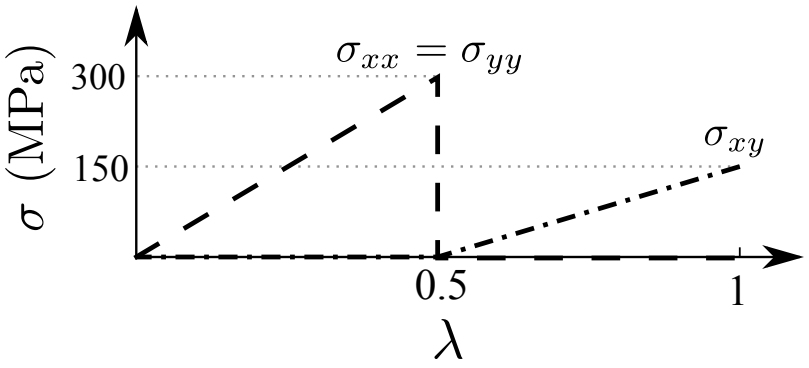

Figure V.36: Non-proportional load.

The slight differences may be attributed to different seedings of the strength values in the tows of the textile unit cell models as well as the fact that the stress increase for each load increment in the validation model is smaller than for the biaxial reference load case in the database. Once the biaxial load is removed and the shear load is applied, the value of a given damage state variable d in the textile was taken as the maximum of either the value of d that was attained during the biaxial loading phase or the value of d associated with the current shear load determined from the shear reference load case. This value of d was then used to predict the effective response of the textile. The resulting prediction and comparison to the response obtained from a textile unit cell model subjected to the non-proportional loading are shown in Fig. V.37. As seen in the figure, the evolution of the response during the second half of the loading history was predicted with good accuracy up to the point of critical failure. However, the critical failure stress was over-predicted considerably by the continuum damage mechanics model when compared to the textile unit cell analysis. The reason for this can be discerned by comparing the predicted evolution of the damage state

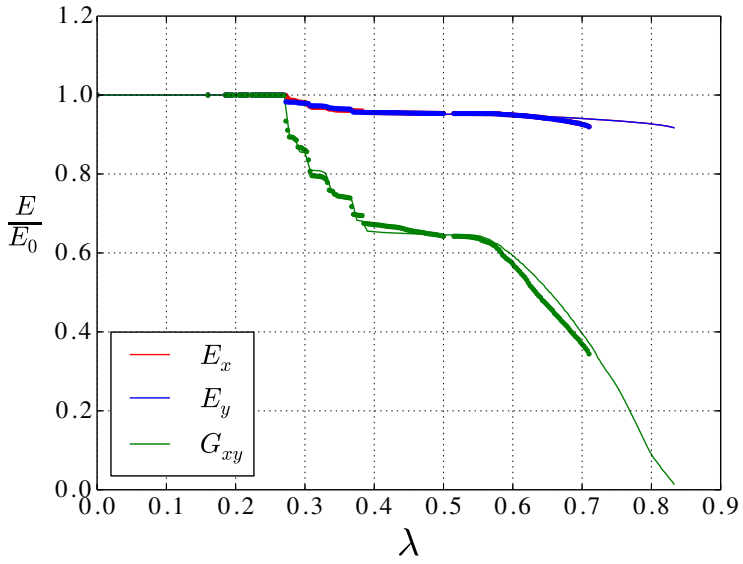

Figure V.37: Predicted response for non-proportional loading (lines) compared to micromechanics (dots).

variables to the damage state variables directly measured from the textile unit cell analysis that was run for validation. This comparison is given in Fig. V.38. While tow cracking (d_x and d_y) and shear damage (d_s) compared favorably, there were very large differences in the evolution of failure in the interfaces and neat matrix pockets (d_I) during the shear loading portion of the non-proportional loading (Fig. V.38c). For this non-proportional loading case, the biaxial loading caused matrix cracks to open, which in turn led to the development of crack opening on the interfaces and in the neat matrix pockets. When shear loading was applied, these interfaces began to fail at very low applied shear loads. This only happened because the tows had already undergone cracking during the biaxial load phase. Furthermore, because the tows were cracked, the interfaces and matrix pocket were part of the critical

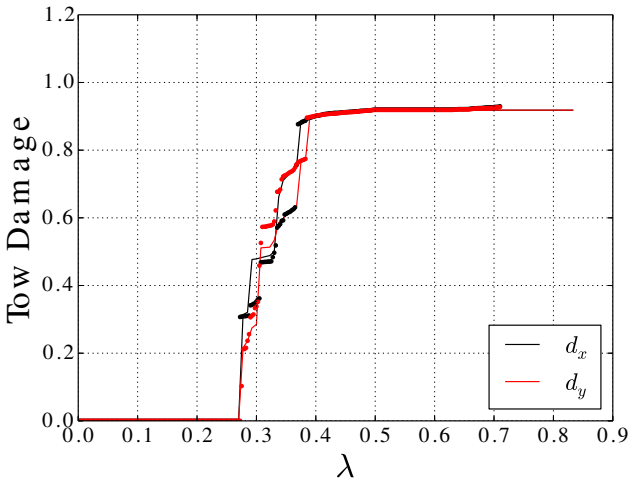

(a) Tow cracking

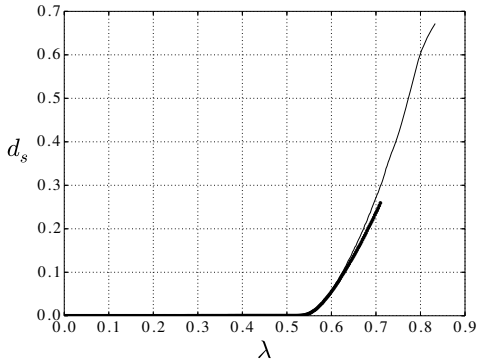

(b) Diffuse tow shear damage

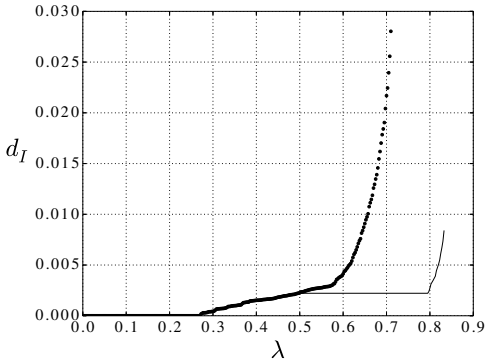

(c) Interface and matrix cracking

Figure V.38: Comparison of predicted damage state variable evolution (lines) to damage parameter evolution from micromechanics (dots) for non-proportional loading.

load path under shear. Essentially, these structures in the textile held together the cracked pieces of tow. Once the cohesive zones in these critical regions failed, the textile was no longer capable of carrying shear load.

The predictive model did not pick up this behavior because the state variable evolution for the shear reference load case is for a textile that does not contain initially opened tow cracks. In an initially undamaged textile, interface and matrix pocket failure does not occur under shear loading until the stress level in the tows is high enough to cause the onset of tow cracking. Therefore, this non-proportional load case provides an example of an interaction between failure modes that does not make itself apparent under proportional loading (i.e., using a virgin textile unit cell loaded under shear, one cannot observe the noted dependence of interfacial and matrix failure on the pre-existence of tow cracks). Modifications would need to be made to the described damage model to account for such interactions before it could be accurately applied to structures which are subject to damage-inducing stress states that experience large changes in proportionality. However, it should be pointed out that when the textile unit cell analysis predicted final failure, the effective shear modulus of the textile had degraded to less than 40% of its original value (which the continuum damage model also predicted). If one were to use a criterion for critical failure that was based on modulus degradation rather than the occurrence of an instability under stress-controlled loading, then the continuum damage model would likely provide an accurate prediction of critical failure (since critical failure would likely be considered to have occurred some time before reaching a 60% loss of shear stiffness).

CHAPTER VI

CONCLUSION

A variety of aspects of composite behavior were investigated at both the fiber-matrix scale and the textile unit cell scale. At the fiber-matrix scale, a method was developed for the generation of random periodic microstructures. This microstructural model was utilized to determine the elastic properties of the fibers from unidirectional lamina and neat matrix properties through the use of an inverse analysis. This investigation showed that the predicted longitudinal shear modulus G_{12} of the fiber exhibits a very strong dependence on the assumed micromechanics model, with the random model yielding much lower values for G_{12} than analytical micromechanics models. The other transverse properties, E_2, G_{23}, and ν_{12}, exhibited lower sensitivities to the micromechanics model.

An investigation into the stress fields in the matrix under thermal loading showed that the nature of the stresses changed considerably in the inter-fiber regions for microstructures with fibers that were very close to one another and microstructures with more uniformly spaced fibers that were not in such close proximity. As a result of these differences, it was noted that the two different microstructures will predict different interactions between thermally-induced stresses and stresses from transverse normal loading, with closely spaced fibers predicting that thermal cooling will increase the load to failure initiation while microstructures with more space between fibers tend to predict that cooling decreases the applied load required to cause failure initiation.

A progressive failure model was developed for the microstructure which accounted for failure in the matrix through a quad-point property reduction scheme. The in-situ matrix strength for the fiber-matrix model was then determined from unidirectional lamina strengths using an inverse analysis. It was found that realistic properties of matrix strength and realistic responses under both transverse tension and longitudinal shear were obtained when the the local material properties were decreased gradually for stresses which caused local ductile failure, and decreased suddenly and completely for stresses which caused local brittle failure. The overall progressive failure behavior under transverse normal load was found to be brittle, with brittle failure occurring at one location in the microstructure and then growing unstably until the failed region completely crossed the RVE. On the other hand, failure under longitudinal shear occurred gradually, with ductile failure occurring in many locations between fibers. This diffuse failure increased gradually until it started to localize when the volume average shear stress acting on the fiber-matrix RVE reached its maximum value.

A study of the effect of RVE size was undertaken for transverse normal loading, since this loading tended to be highly sensitive to the onset of brittle failure at any point in the microstructure. It was found that the lower-end of the strength distributions obtained from a large number of realizations tended to remain fairly consistent across a variety of RVE sizes, while the maximum value of the distribution fell considerably as the RVE size was increased, indicating that larger RVEs predict more consistently lower strengths due to the fact that they are more likely to contain a microstructural feature that causes the onset of brittle failure at a lower applied

loading.

Finally, a parametric study was conducted using the progressive failure fiber-matrix model to determine how the predicted strength distribution changes with temperature. It was found that as the temperature is decreased from the cure temperature, the strength distribution tends to increase, further suggesting that thermally-induced stresses from cooling after cure tend to increase the strength of the composite. The thermal dependence of strength for a hexagonal array was found to predict a considerably different trend, with the thermally induced stresses tending to cause a strength reduction near room temperature, indicating that the predicted thermal dependence varies for different microstructural assumptions.

Next, a study of the behavior at the textile scale was undertaken. The first investigation that was performed examined the failure initiation behavior in the textile for a variety of multiaxial loadings. An analysis tool was developed which utilized superposition of stresses to rapidly determine the location of failure initiation for a given loading as well as what type of failure occurred at the initiation location. The initiation behaviors for different loads were then processed into categories based on location and local failure mode. It was determined that under a broad variety of multiaxial loads, textiles tend to experience just a few characteristic types of failure initiation.

This superposition tool was also utilized to calculate the failure initiation envelope for the textile under in-plane loads. The envelope was calculated for a variety of different temperatures. It was found that different failure modes tended to be distributed in contiguous regions across the failure envelope, meaning that similar

loads tended to result in the same type of failure. While temperature changes gave rise to several new modes of failure, the distribution of modes on the envelope stayed fairly consistent across the range of temperatures examined. It was also found that temperature changes tended to cause failure initiation to happen earlier for some kinds of loads and later for others.

Finally, progressive failure was investigated in the textile. A new progressive failure model was developed which utilized cohesive elements to account for cracking within the tows and matrix pocket as well as on the interfaces between tows and on the interface between the tows and matrix pocket. Furthermore, a continuum damage model was developed to account for the diffuse damage which was observed to occur under longitudinal shear loading of the tows. The behavior of this continuum damage model was calibrated from the response observed in the fiber-matrix analyses. Also, the maximum tractions under normal and shear opening for the cohesive elements in the tows were defined using the strength distributions from the fiber-matrix model at a given temperature. Strength variability was introduced to the textile unit cell model by assigning random strengths to the cohesive zone quadrature points at the beginning of the analysis using these distributions.

The progressive failure of the textile unit cell was examined for a variety of in-plane loadings comprised of tensile values of normal stress as well as shear. From these analyses, four distinct modes of damage development were identified. These modes were cracking of the x tows, cracking of the y tows, opening of the cohesive zones in the matrix pocket and on the interfaces, and shear damage development in the tows. Metrics were developed for tracking the evolution of each of these types of

damage using a single parameter. By keeping track of the full effective compliance of the textile unit cell models as they underwent progressive failure, it was possible to characterize the effect each of these characteristic damage modes had on the effective in-plane moduli of the textile as they evolved.

A continuum damage mechanics model for a plain weave textile composite was developed using state variables based on the four identified characteristic damage mode from the textile unit cell analyses. This model includes a degradation law for the in-plane moduli based on the characterization that was performed for the effect of each characteristic damage mode on the effective textile unit-cell compliance. A comparison was made between the response predicted by this degradation law and the response obtained directly from progressive failure analysis of a textile unit cell for a wide variety of in-plane loads, and good agreement was found, indicating that the chosen damage state variables are good choices for a reduced-order representation of the damage state that exists in the textile. An approach for tracking the evolution of the damage parameters for arbitrary loadings using a table-lookup approach was developed, and was found to provide good predictions under proportional loading. Under non-proportional loading, it was found that the continuum damage mechanics model accurately predicted the effective response of the textile, but was unable to capture some of the more complex interactions that can occur between the different characteristic damage behaviors, leading to some inaccuracy in the prediction of critical failure in the textile.

REFERENCES

[1] Gates, D., "Boeing 787 wing flaw extends inside plane," *The Seattle Times*, July 30 2009.

[2] Sabbagh, K., "21st Century Jet: The Building of the 777," DVD Documentary, PBS, 2000.

[3] Kachanov, L., "Rupture time under creep conditions," *International Journal of Fracture*, Vol. 97, No. 1, 1999, pp. 11–18.

[4] Murakami, S. and Ohno, N., "A continuum theory of creep and creep damage," *Creep in Structures*, edited by A. R. S. Ponter and D. R. Hayhurst, Springer-Verlag, Berlin, 1981, pp. 422–444.

[5] Talreja, R., "A continuum mechanics characterization of damage in composite materials," *Proceedings of the Royal Society of London. Series A, Mathematical and Physical*, Vol. 399, No. 1817, 1985, pp. 195–216.

[6] Talreja, R., "Damage development in composites: mechanisms and modelling," *The Journal of Strain Analysis for Engineering Design*, Vol. 24, No. 4, 1989, pp. 215–222.

[7] Rybicki, E. F. and Kanninen, M. F., "A finite element calculation of stress intensity factors by a modified crack closure integral," *Engineering Fracture Mechanics*, Vol. 9, No. 4, 1977, pp. 931–938.

[8] Raju, I. S., "Calculation of strain-energy release rates with higher order and singular finite elements," *Engineering Fracture Mechanics*, Vol. 2, No. 3, 1987, pp. 251–274.

[9] Krueger, R., "The virtual approach crack closure technique: history, approach and applications," Tech. rep., NASA Langley Research Center ICASE, Hampton, Virginia, 2002.

[10] Varghese, J., Whitcomb, J. D., Goyal, D., and Tang, X., "Hierarchical analysis of woven composite DCB specimen," *Journal of Composite Materials*, Vol. 41, No. 8, April 2007, pp. 931–950.

[11] Hallett, S. R., Jiang, W.-G., Khan, B., and Wisnom, M. R., "Modelling the interaction between matrix cracks and delamination damage in scaled quasi-isotropic specimens," *Composites Science and Technology*, Vol. 68, No. 1, Jan. 2008, pp. 80–89.

[12] Wimmer, G., Schuecker, C., and Pettermann, H. E., "Numerical simulation of delamination in laminated composite components-A combination of a strength criterion and fracture mechanics," *Composites Part B: Engineering*, Vol. 40, No. 2, 2009, pp. 158–165.

[13] Dugdale, D., "Yielding of steel sheets containing slits," *Journal of the Mechanics and Physics of Solids*, Vol. 8, No. 2, May 1960, pp. 100–104.

[14] Barenblatt, G., "The mathematical theory of equilibrium cracks in brittle fracture," *Journal of Advanced Applied Mechanics*, Vol. 7, 1962, pp. 55–129.

[15] Hillerborg, A., Modeer, M., and Petersson, P., "Analysis of crack formation and crack growth in concrete by means of fracture mechanics and finite elements," *Cement and concrete research*, Vol. 6, No. 6, 1976, pp. 773–781.

[16] Needleman, A., "A continuum model for void nucleation by inclusion debonding," *Journal of Applied Mechanics*, Vol. 54, No. 3, 1987, pp. 525–531.

[17] Jin, Z.-H., Paulino, G. H., and Dodds, R. H., "Finite element investigation of quasi-static crack growth in functionally graded materials using a novel cohesive zone fracture model," *Journal of Applied Mechanics*, Vol. 69, No. 3, 2002, pp. 370.

[18] Park, K., Paulino, G. H., and Roesler, J. R., "A unified potential-based cohesive model of mixed-mode fracture," *Journal of the Mechanics and Physics of Solids*, Vol. 57, No. 6, June 2009, pp. 891–908.

[19] Roy, Y. and Dodds, R., "Simulation of ductile crack growth in thin aluminum panels using 3-D surface cohesive elements," *International Journal of Fracture*, Vol. 110, No. 1, 2001, pp. 21–45.

[20] Turon, A., Camanho, P. P., Costa, J., and Dávila, C. G., "A damage model for the simulation of delamination in advanced composites under variable-mode loading," *Mechanics of Materials*, Vol. 38, No. 11, Nov. 2006, pp. 1072–1089.

[21] Babuška, I. and Melenk, J. M., "The partition of unity method," *International Journal of Numerical Methods in Engineering*, Vol. 40, No. 4, 1997, pp. 727–758.

[22] Belytschko, T. and Black, T., "Elastic crack growth in finite elements with minimal remeshing," *International Journal for Numerical Methods in Engineering*, Vol. 45, No. 5, 1999, pp. 601–620.

[23] Belytschko, T., Zi, G., Xu, J., and Chessa, J., "The extended finite element method for arbitrary discontinuities," *Computational Mechanics-Theory And Practice*, edited by K. M. Mathisen, T. Kvamsdal, and K. M. Okstad, CIMNE, Barcelona, Spain, 2003.

[24] Hinton, M., Kaddour, A., and Soden, P., editors, *Failure Criteria in Fibre Reinforced Polymer Composites: The World-Wide Failure Exercise*, Elsevier Science Ltd., Kidlington, Oxford, UK, 2004.

[25] Christensen, R. M., "A comprehensive theory of yielding and failure for isotropic materials," *Journal of Engineering Materials and Technology*, Vol. 129, No. 2, 2007, pp. 173–181.

[26] Hill, R., *The Mathematical Theory of Plasticity*, Oxford University Press, London, 1950.

[27] Tsai, S. W., "Strength theories of filamentary structures," *Fundamental Aspects of Fiber Reinforced Plastic Composites*, edited by R. Schwartz and H. Schwartz, Wiley Interscience, Dayton, OH, 1968, pp. 3–11.

[28] Hoffman, O., "The brittle strength of orthotropic materials," *Journal of Composite Materials*, Vol. 1, No. 2, Jan. 1967, pp. 200–206.

[29] Tsai, S. W. and Wu, E. M., "A general theory of strength for anisotropic materials," *Journal of Composite Materials*, Vol. 5, No. 1, Jan. 1971, pp. 58–80.

[30] Narayanaswami, R. and Adelman, H. M., "Evaluation of the tensor polynomial and hoffman strength theories for composite materials," *Journal of Composite Materials*, Vol. 11, No. 4, Oct. 1977, pp. 366–377.

[31] Cowin, S., "On the strength anisotropy of bone and wood," *Journal of Applied Mechanics*, Vol. 46, No. 79, 1979, pp. 832–838.

[32] Wu, R.-Y. and Stachurski, Z., "Evaluation of the normal stress interaction parameter in the tensor polynomial strength theory for anisotropic materials," *Journal of Composite Materials*, Vol. 18, No. 5, Jan. 1984, pp. 456–463.

[33] Tsai, S. W. and Hahn, H., *Introduction to Composite Materials*, Technomic, Lancaster, PA, 1980.

[34] Liu, K.-S. and Tsai, S. W., "A progressive quadratic failure criterion for a laminate," *Composites Science and Technology*, Vol. 58, No. 7, July 1998, pp. 1023–1032.

[35] Kuraishi, A., Tsai, S. W., and Liu, K. K.-S., "A progressive quadratic failure criterion, part B," *Composites Science and Technology*, Vol. 62, No. 12-13, Sept. 2002, pp. 1683–1695.

[36] Sun, C., Quinn, B. J., Tao, J., and Oplinger, D. W., "Comparative evaluation of failure analysis methods for composite laminates," Tech. Rep. May, DOT/FAA/AR-95/109, Washington, D.C., 1996.

[37] Soden, P. D., Kaddour, A. S., and Hinton, M. J., "Recommendations for designers and researchers resulting from the world-wide failure exercise," *Composites Science and Technology*, Vol. 64, No. 3-4, March 2004, pp. 589–604.

[38] Zinoviev, P. A., Grigoriev, S. V., Lebedeva, O. V., and Tairova, L. P., "The strength of multilayered composites under a plane-stress state," *Composites Science and Technology*, Vol. 58, No. 7, 1998, pp. 1209–1223.

[39] Zinoviev, P. A., Lebedeva, O. V., and Tairova, L. P., "A coupled analysis of experimental and theoretical results on the deformation and failure of composite laminates under a state of plane stress," *Composites Science and Technology*, Vol. 62, No. 12-13, Sept. 2002, pp. 1711–1723.

[40] Bogetti, T. A., Hoppel, C. P. R., Harik, V. M., Newill, J. F., and Burns, B. P., "Predicting the nonlinear response and progressive failure of composite laminates," *Composites Science and Technology*, Vol. 64, No. 3-4, March 2004, pp. 329–342.

[41] Bogetti, T. A., Hoppel, C. P. R., Harik, V. M., Newill, J. F., and Burns, B. P., "Predicting the nonlinear response and failure of composite laminates: correlation with experimental results," *Composites Science and Technology*, Vol. 64, No. 3-4, March 2004, pp. 477–485.

[42] Hashin, Z., "Failure criteria for unidirectional fiber composites," *Journal of Applied Mechanics*, Vol. 47, No. 2, 1980, pp. 329.

[43] Paul, B., "A modification of the Coulomb-Mohr theory of fracture," *Journal of Applied Mechanics*, Vol. 28, No. 2, 1961, pp. 259–268.

[44] Christensen, R. M., "Stress based yield/failure criteria for fiber composites," *International Journal of Solids and Structures*, Vol. 34, No. 5, 1997, pp. 529–543.

[45] Puck, A. and Schurmann, H., "Failure analysis of FRP laminates by means of physically based phenomenological models," *Composites Science and Technology*, Vol. 58, No. 7, July 1998, pp. 1045–1067.

[46] Puck, A. and Schurmann, H., "Failure analysis of FRP laminates by means of physically based phenomenological models," *Composites Science and Technology*, Vol. 62, No. 12-13, Sept. 2002, pp. 1633–1662.

[47] Puck, A., Kopp, J., and Knops, M., "Guidelines for the determination of the parameters in Pucks action plane strength criterion," *Composites Science and Technology*, Vol. 62, No. 3, 2002, pp. 371–378.

[48] Cuntze, R. G. and Freund, A., "The predictive capability of failure mode concept-based strength criteria for multidirectional laminates," *Composites Science and Technology*, Vol. 64, No. 3-4, March 2004, pp. 343–377.

[49] Cuntze, R. G., "The predictive capability of failure mode concept-based strength criteria for multi-directional laminatespart B," *Composites Science and Technology*, Vol. 64, No. 3-4, March 2004, pp. 487–516.

[50] Davila, C. G., Camanho, P. P., and Rose, C. A., "Failure criteria for FRP laminates," *Journal of Composite Materials*, Vol. 39, No. 4, Feb. 2005, pp. 323–345.

[51] Mollenhauer, D. H., Iarve, E. V., Putthanarat, R., Hallett, S. R., and Li, X., "Application of discrete damage modeling to laminated composite overheight compact tension specimens," *51st AIAA/ASME/ASCE/AHS/ASC Structures, Structural Dynamics, and Materials Conference, Orlando, FL*, 2010, pp. 1–12.

[52] Iarve, E. V., Gurvich, M. R., Mollenhauer, D. H., Rose, C. A., and Dávila, C. G., "Mesh independent matrix cracking and delamination modeling in laminated composites," *International Journal for Numerical Methods in Engineering*, Vol. 88, No. 8, 2011, pp. 749–773.

[53] Swindeman, M. J., Iarve, E. V., Brockman, R. a., Mollenhauer, D. H., and Hallett, S. R., "Strength prediction in open hole composite laminates by using discrete damage modeling," *AIAA Journal*, Vol. 51, No. 4, April 2013, pp. 936–945.

[54] Hashin, Z. and Rosen, B. W., "The elastic moduli of fiber-reinforced materials," *Journal of Applied Mechanics*, Vol. 31, No. 2, 1964, pp. 223–232.

[55] Sun, C. and Vaidya, R., "Prediction of composite properties from a representative volume element," *Composites Science and Technology*, Vol. 56, No. 2, Jan. 1996, pp. 171–179.

[56] Asp, L. E., Berglund, L., and Talreja, R., "Prediction of matrix-initiated transverse failure in polymer composites," *Composites Science and Technology*, Vol. 56, No. 9, 1996, pp. 1089–1097.

[57] Asp, L. E., Berglund, L. A., and Talreja, R., "A criterion for crack initiation in glassy polymers subjected to a composite-like stress state," *Composites Science and Technology*, Vol. 56, No. 11, 1996, pp. 1291–1301.

[58] Mayes, J. and Hansen, A. C., "Multicontinuum failure analysis of composite structural laminates," *Mechanics of Composite Materials and Structures*, Vol. 8, No. 4, 2001, pp. 249–262.

[59] Ha, S. K., Huang, Y., Han, H. H., and Jin, K.-K., "Micromechanics of failure for ultimate strength predictions of composite laminates," *Journal of Composite Materials*, Vol. 44, No. 20, 2010, pp. 2347–2361.

[60] Raghava, R., Caddell, R. M., and Yeh, G. S. Y., "The macroscopic yield behaviour of polymers," *Journal of Materials Science*, Vol. 8, No. 2, Feb. 1973, pp. 225–232.

[61] Stamblewski, C., Sankar, B. V., and Zenkert, D., "Analysis of three-dimensional quadratic failure criteria for thick composites using the direct mi-

cromechanics method," *Journal of Composite Materials*, Vol. 42, No. 7, April 2008, pp. 635–654.

[62] Brennan, K. P. and Walrath, D. E., "Analysis of underlying organization in randomized fiber arrays," *Journal of Composite Materials*, Vol. 43, No. 21, Aug. 2009, pp. 2441–2453.

[63] Wilding, S. E. and Fullwood, D. T., "Clustering metrics for two-phase composites," *Computational Materials Science*, Vol. 50, No. 7, May 2011, pp. 2262–2272.

[64] Bhattacharyya, A. and Lagoudas, D. C., "Effective elastic moduli of two-phase transversely isotropic composites with aligned clustered fibers," *Acta Mechanica*, Vol. 145, No. 1-4, 2000, pp. 65–93.

[65] Adams, D. F. and Tsai, S. W., "The influence of random filament packing on the transverse stiffness of unidirectional composites," *Journal of Composite Materials*, Vol. 3, No. 3, Jan. 1969, pp. 368–381.

[66] Aghdam, M. M. and Dezhsetan, A., "Micromechanics based analysis of randomly distributed fiber reinforced composites using simplified unit cell model," *Composite Structures*, Vol. 71, No. 3-4, 2005, pp. 327–332.

[67] Teng, H., "Transverse stiffness properties of unidirectional fiber composites containing debonded fibers," *Composites Part A: Applied Science and Manufacturing*, Vol. 38, No. 3, March 2007, pp. 682–690.

[68] Ghosh, S., Nowak, Z., and Lee, K., "Quantitative characterization and modeling of composite microstructures by Voronoi cells," *Acta Materialia*, Vol. 45, No. 6, 1997, pp. 2215–2234.

[69] Bulsara, V. N., Talreja, R., and Qu, J., "Damage initiation under transverse loading of unidirectional composites with arbitrarily distributed fibers," *Composites Science and Technology*, Vol. 59, No. 5, 1999, pp. 673–682.

[70] Mollenhauer, D. H., Iarve, E. V., Hoos, K., Swindeman, M., and Zhou, E., "Simulation of mode I fracture at the micro-Level in polymer matrix composite laminate plies," *53nd AIAA/ASME/ASCE/AHS/ASC Structures, Structural Dynamics, and Materials Conference*, Honolulu, HI, 2012, pp. 1–8.

[71] Totry, E., González, C., and LLorca, J., "Failure locus of fiber-reinforced composites under transverse compression and out-of-plane shear," *Composites Science and Technology*, Vol. 68, No. 3-4, March 2008, pp. 829–839.

[72] Segurado, J. and Llorca, J., "A numerical approximation to the elastic properties of sphere-reinforced composites," *Journal of the Mechanics and Physics of Solids*, Vol. 50, No. 10, Oct. 2002, pp. 2107–2121.

[73] Rintoul, M. D. and Torquato, S., "Reconstruction of the structure of dispersions," *Journal of Colloid and Interface Science*, Vol. 186, No. 2, Feb. 1997, pp. 467–76.

[74] González, C. and LLorca, J., "Mechanical behavior of unidirectional fiber-reinforced polymers under transverse compression: Microscopic mechanisms

and modeling," *Composites Science and Technology*, Vol. 67, No. 13, Oct. 2007, pp. 2795–2806.

[75] O'Dwyer, D., O'Dowd, N., and McCarthy, C., "Numerical micromechanical investigation of interfacial strength parameters in a carbon fibre composite material," *Journal of Composite Materials*, Feb. 2013.

[76] Vaughan, T. and McCarthy, C., "A combined experimentalnumerical approach for generating statistically equivalent fibre distributions for high strength laminated composite materials," *Composites Science and Technology*, Vol. 70, No. 2, Feb. 2010, pp. 291–297.

[77] Garnich, M. R., Fertig III, R. S., Anderson, E. M., and Deng, S., "Micromechanics of fatigue damage in unidirectional polymer composites," *53nd AIAA/ASME/ASCE/AHS/ASC Structures, Structural Dynamics, and Materials Conference*, Honolulu, HI, 2012, pp. 1–9.

[78] Anderson, E. M., *An automated finite element program for micromechanics modeling of random-wavy fiber composites*, Masters, University of Wyoming, Laramie, 2010.

[79] Fiedler, B., Hojo, M., and Ochiai, S., "The influence of thermal residual stresses on the transverse strength of CFRP using FEM," *Composites Part A: Applied Science and Manufacturing*, Vol. 33, No. 10, Oct. 2002, pp. 1323–1326.

[80] Hobbiebrunken, T., Hojo, M., Fiedler, B., Tanaka, M., Ochiai, S., and Schulte, K., "Thermomechanical analysis of micromechanical formation of residual

stresses and initial matrix failure in CFRP," *JSME International Journal Series A*, Vol. 47, No. 3, 2004, pp. 349–356.

[81] Fiedler, B., Gagel, A., Hobbiebrunken, T., Schulte, K., Hojo, M., and Ochiai, S., "Modelling of the transverse strength of fibre reinforced epoxy composite at low and high temperature," *Composite Interfaces*, Vol. 12, No. 3-4, Jan. 2005, pp. 379–394.

[82] Maligno, A. R., Warrior, N. A., and Long, A. C., "Finite element investigations on the microstructure of fibre-reinforced composites," *eXPRESS Polymer Letters*, Vol. 2, No. 9, Aug. 2008, pp. 665–676.

[83] Leong, M. and Sankar, B. V., "Effect of thermal stresses on the failure criteria of fiber composites," *Mechanics of Advanced Materials and Structures*, Vol. 17, No. 7, Oct. 2010, pp. 553–560.

[84] Hojo, M., Mizuno, M., Hobbiebrunken, T., Adachi, T., Tanaka, M., and Ha, S. K., "Effect of fiber array irregularities on microscopic interfacial normal stress states of transversely loaded UD-CFRP from viewpoint of failure initiation," *Composites Science and Technology*, Vol. 69, No. 11-12, Sept. 2009, pp. 1726–1734.

[85] Vaughan, T. and McCarthy, C., "Micromechanical modelling of the transverse damage behaviour in fibre reinforced composites," *Composites Science and Technology*, Vol. 71, No. 3, Feb. 2011, pp. 388–396.

[86] Yang, L., Yan, Y., Ma, J., and Liu, B., "Effects of inter-fiber spacing and thermal residual stress on transverse failure of fiber-reinforced polymermatrix composites," *Computational Materials Science*, Vol. 68, Feb. 2013, pp. 255–262.

[87] Aveston, J., Cooper, G. A., and Kelly, A., "Single and multiple fracture," *Conf on the Properties of Fibre Composites, National Physical Laboratory*, IPC Science and Technology Press, Guildford, Surrey, UK, 1971, pp. 15–26.

[88] Aveston, J. and Kelly, a., "Theory of multiple fracture of fibrous composites," *Journal of Materials Science*, Vol. 8, No. 3, March 1973, pp. 352–362.

[89] Hashin, Z., "Analysis of cracked laminates: a variational approach," *Mechanics of Materials*, Vol. 4, No. 2, July 1985, pp. 121–136.

[90] Hashin, Z., "Analysis of stiffness reduction of cracked cross-ply laminates," *Engineering Fracture Mechanics*, Vol. 25, No. 5, 1986, pp. 771–778.

[91] Ladevéze, P. and Lubineau, G., "An enhanced mesomodel for laminates based on micromechanics," *Compites Science and Technology*, Vol. 62, No. 4, March 2002, pp. 533–541.

[92] Ivanov, D. S., Baudry, F., Van Den Broucke, B., Lomov, S. V., Xie, H., and Verpoest, I., "Failure analysis of triaxial braided composite," *Composites Science and Technology*, Vol. 69, No. 9, July 2009, pp. 1372–1380.

[93] Papadakis, N., Reynolds, N., Pharaoh, M. W., Wood, P. K. C., and Smith, G. F., "Strain rate dependency of the shear properties of a highly oriented

thermoplastic composite material using a contacting displacement measurement methodology - Part B: shear damage evolution," *Composites Sceince and Technology*, Vol. 64, No. 5, 2004, pp. 739–748.

[94] van der Meer, F. P. and Sluys, L. J., "Mesh-independent modeling of both distributed and discrete matrix cracking in interaction with delamination in composites," *Engineering Fracture Mechanics*, Vol. 77, No. 4, March 2010, pp. 719–735.

[95] Allix, O. and Blanchard, L., "Mesomodeling of delamination: towards industrial applications," *Composites Science and Technology*, Vol. 66, No. 6, May 2006, pp. 731–744.

[96] Maimí, P., Camanho, P. P., Mayugo, J., and Turon, A., "Matrix cracking and delamination in laminated composites. Part II: evolution of crack density and delamination," *Mechanics of Materials*, Vol. 43, No. 4, April 2011, pp. 194–211.

[97] Böhm, R., Gude, M., and Hufenbach, W., "A phenomenologically based damage model for 2D and 3D-textile composites with non-crimp reinforcement," *Materials & Design*, Vol. 32, No. 5, May 2011, pp. 2532–2544.

[98] Wisnom, M., "Modelling discrete failures in composites with interface elements," *Composites Part A: Applied Science and Manufacturing*, Vol. 41, No. 7, July 2010, pp. 795–805.

[99] Wisnom, M. R. and Chang, F.-K., "Modelling of splitting and delamination in notched cross-ply laminates," *Composites Science and Technology*, Vol. 60, No. 15, 2000, pp. 2849–2856.

[100] Hallett, S. R. and Wisnom, M. R., "Numerical investigation of progressive damage and the effect of layup in notched tensile tests," *Journal of Composite Materials*, Vol. 40, No. 14, Sept. 2005, pp. 1229–1245.

[101] Jiang, W.-G., Hallett, S. R., Green, B. G., and Wisnom, M. R., "A concise interface constitutive law for analysis of delamination and splitting in composite materials and its application to scaled notched tensile specimens," *International Journal for Numerical Methods in Engineering*, Vol. 69, No. 9, 2007, pp. 1982–1995.

[102] Jalalvand, M., Hosseini-Toudeshky, H., and Mohammadi, B., "Numerical modeling of diffuse transverse cracks and induced delamination using cohesive elements," *Proceedings of the Institution of Mechanical Engineers, Part C: Journal of Mechanical Engineering Science*, Vol. 227, No. 7, Sept. 2012, pp. 1392–1405.

[103] de Moura, M. F. S. F. and Gonçalves, J. P. M., "Modelling the interaction between matrix cracking and delamination in carbon-epoxy laminates under low velocity impact," *Composites Science and Technology*, Vol. 64, No. 7-8, June 2004, pp. 1021–1027.

[104] Moës, N., Dolbow, J., and Belytschko, T., "A finite element method for crack growth without remeshing," *International Journal for Numerical Methods in Engineering*, Vol. 46, No. 1, 1999, pp. 131–150.

[105] Iarve, E. V., "Mesh independent modelling of cracks by using higher order shape functions," *International Journal for Numerical Methods in Engineering*, Vol. 56, No. 6, Feb. 2003, pp. 869–882.

[106] van der Meer, F. P. and Sluys, L. J., "A phantom node formulation with mixed mode cohesive law for splitting in laminates," *International Journal of Fracture*, Vol. 158, No. 2, May 2009, pp. 107–124.

[107] Böhm, R., Gude, M., and Hufenbach, W., "A phenomenologically based damage model for textile composites with crimped reinforcement," *Composites Science and Technology*, Vol. 70, No. 1, Jan. 2010, pp. 81–87.

[108] Cuntze, R. G., "Strength failure conditions of the various structural materials: is there some common basis existing?" *SDHM: Structural Durability & Health Monitoring*, Vol. 3, No. 2, 2007, pp. 87–106.

[109] Chapman, C. D. and Whitcomb, J. D., "Thermally induced damage initiation and growth in plain and satin weave carbon-carbon composites," *Mechanics of Composite Materials and Structures*, Vol. 7, No. 2, 2000, pp. 177–194.

[110] Tang, X. and Whitcomb, J. D., "Progressive failure behaviors of 2D woven composites," *Journal of Composite Materials*, Vol. 37, No. 14, 2003, pp. 1239.

[111] Goyal, D. and Whitcomb, J. D., "Load flow in plain woven composites," *Journal of Composite Materials*, Vol. 42, No. 25, 2008, pp. 2761.

[112] Owens, B. C., Whitcomb, J. D., and Varghese, J., "Effect of finite thickness and free edges on stresses in plain weave composites," *Journal of Composite Materials*, Vol. 44, No. 6, Oct. 2009, pp. 675–692.

[113] Whitcomb, J. D., Chapman, C. D., and Tang, X., "Derivation of boundary conditions for micromechanics analyses of plain and satin weave composites," *Journal of Composite Materials*, Vol. 34, No. 9, Jan. 2000, pp. 724–747.

[114] Sherburn, M., *Geometric and mechanical modelling of textiles*, Ph.D. thesis, University of Nottingham, UK, 2007.

[115] Verpoest, I. and Lomov, S. V., "Virtual textile composites software WiseTex: Integration with micro-mechanical, permeability and structural analysis," *Composites Science and Technology*, Vol. 65, No. 15-16, Dec. 2005, pp. 2563–2574.

[116] Lomov, S. V., Ivanov, D. S., Verpoest, I., Zako, M., Kurashiki, T., Nakai, H., and Hirosawa, S., "Meso-FE modelling of textile composites: Road map, data flow and algorithms," *Composites Science and Technology*, Vol. 67, No. 9, 2007, pp. 1870–1891.

[117] Ivanov, D. S., Lomov, S. V., Ivanov, S. G., and Verpoest, I., "Stress distribution in outer and inner plies of textile laminates and novel boundary conditions for

unit cell analysis," *Composites Part A: Applied Science and Manufacturing*, Vol. 41, No. 4, April 2010, pp. 571–580.

[118] Ivanov, D. S., Ivanov, S. G., Lomov, S. V., and Verpoest, I., "Unit cell modelling of textile laminates with arbitrary inter-ply shifts," *Composites Science and Technology*, Vol. 72, No. 1, Sept. 2011, pp. 14–20.

[119] Wang, Y. and Sun, X., "Digital-element simulation of textile processes," *Composites Science and Technology*, Vol. 61, No. 2, 2001, pp. 311–319.

[120] Zhou, G., Sun, X., and Wang, Y., "Multi-chain digital element analysis in textile mechanics," *Composites Science and Technology*, Vol. 64, No. 2, Feb. 2004, pp. 239–244.

[121] Miao, Y., Zhou, E., Wang, Y., and Cheeseman, B. A., "Mechanics of textile composites: micro-geometry," *Composites Science and Technology*, Vol. 68, No. 7-8, 2008, pp. 1671–1678.

[122] Blackketter, D. M., Walrath, D. E., and Hansen, A. C., "Modeling damage in a plain weave fabric-reinforced composite material," *Journal of Composites Technology & Research*, Vol. 15, No. 2, 1993, pp. 136–142.

[123] Whitcomb, J. D. and Srirengan, K., "Effect of various approximations on predicted progressive failure in plain weave composites," *Composite Structures*, Vol. 34, No. 1, Jan. 1996, pp. 13–20.

[124] Choi, J. and Tamma, K., "Woven fabric composites part I: predictions of homogenized elastic properties and micromechanical damage analysis," *Inter-*

national Journal for Numerical Methods in Engineering, Vol. 50, No. 10, 2001, pp. 2285–2298.

[125] Guagliano, M. and Riva, E., "Mechanical behaviour prediction in plain weave composites," *Journal of Strain Analysis*, Vol. 36, No. 2, 2001, pp. 153–162.

[126] Srirengan, K. and Whitcomb, J. D., "Finite element based degradation model for composites with transverse matrix cracks," *Journal of Thermoplastic Composite Materials*, Vol. 11, No. 2, 1998, pp. 113.

[127] Zako, M., Uetsuji, Y., and Kurashiki, T., "Finite element analysis of damaged woven fabric composite materials," *Composites Science and Technology*, Vol. 63, No. 3-4, 2003, pp. 507–516.

[128] Murakami, S., "Mechanical modeling of material damage," *Journal of Applied Mechanics*, Vol. 55, No. 2, 1988, pp. 280–286.

[129] Lomov, S. V., Ivanov, D. S., Truong, T., Verpoest, I., Baudry, F., Vandenbosche, K., and Xie, H., "Experimental methodology of study of damage initiation and development in textile composites in uniaxial tensile test," *Composites Science and Technology*, Vol. 68, No. 12, Sept. 2008, pp. 2340–2349.

[130] Gorbatikh, L., Ivanov, D. S., Lomov, S. V., and Verpoest, I., "On modelling of damage evolution in textile composites on meso-level via property degradation approach," *Composites Part A: Applied Science and Manufacturing*, Vol. 38, No. 12, Dec. 2007, pp. 2433–2442.

[131] Karkkainen, R. L. and Sankar, B. V., "A direct micromechanics method for analysis of failure initiation of plain weave textile composites," *Composites Science and Technology*, Vol. 66, No. 1, Jan. 2006, pp. 137–150.

[132] Karkkainen, R. L., Sankar, B. V., and Tzeng, J. T., "A direct micromechanical approach toward the development of quadratic stress gradient failure criteria for textile composites," *Journal of Composite Materials*, Vol. 41, No. 16, Aug. 2007, pp. 1917–1937.

[133] Karkkainen, R. L., Sankar, B. V., and Tzeng, J. T., "Strength prediction of multi-layer plain weave textile composites using the direct micromechanics method," *Composites Part B: Engineering*, Vol. 38, No. 7-8, Oct. 2007, pp. 924–932.

[134] Hsu, S.-Y. and Cheng, R.-B., "Modeling geometry and progressive interfacial damage in textile composites," *Journal of Composite Materials*, Vol. 47, No. 11, June 2013, pp. 1343–1356.

[135] Turon, A., Dávila, C., Camanho, P., and Costa, J., "An engineering solution for mesh size effects in the simulation of delamination using cohesive zone models," *Engineering Fracture Mechanics*, Vol. 74, No. 10, July 2007, pp. 1665–1682.

[136] Czabaj, M. W. and Ratcliffe, J. G., "Comparison of intralaminar and interlaminar mode-I fracture toughness of unidirectional IM7/8552 graphite/epoxy composite," *American Society for Composites Twenty-Seventh Technical Conference*, Arlington, TX, 2012, pp. 1–18.

[137] Everett, R. and Chu, J., "Modeling of non-uniform composite microstructures," *Journal of Composite Materials*, Vol. 27, No. 11, Jan. 1993, pp. 1128–1144.

[138] Oh, J. H., Jin, K.-K., and Ha, S. K., "Interfacial strain distribution of a unidirectional composite with randomly distributed fibers under transverse loading," *Journal of Composite Materials*, Vol. 40, No. 9, July 2005, pp. 759–778.

[139] Du, X. and Ostoja-Starzewski, M., "On the size of representative volume element for Darcy law in random media," *Proceedings of the Royal Society A: Mathematical, Physical and Engineering Sciences*, Vol. 462, No. 2074, Oct. 2006, pp. 2949–2963.

[140] Huang, Y., Jin, K.-K., and Ha, S. K., "Effects of fiber arrangement on mechanical behavior of unidirectional composites," *Journal of Composite Materials*, Vol. 42, No. 18, 2008, pp. 1851.

[141] Widom, B., "Random sequential addition of hard spheres to a volume," *The Journal of Chemical Physics*, Vol. 44, No. 10, 1966, pp. 3888.

[142] Metropolis, N., Rosenbluth, A. W., Rosenbluth, M. N., Teller, A. H., and Teller, E., "Equation of state calculations by fast computing machines," *The Journal of Chemical Physics*, Vol. 21, No. 6, 1953, pp. 1087.

[143] Tomadakis, M. M. and Sotirchos, S. V., "Effective diffusivities and conductivities of random dispersions of nonoverlapping and partially overlapping unidirectional fibers," *The Journal of Chemical Physics*, Vol. 99, No. 12, 1993, pp. 9820.

[144] Berlyand, L. and Mityushev, V., "Generalized ClausiusMossotti formula for random composite with circular fibers," *Journal of Statistical Physics*, Vol. 102, No. 1/2, 2001, pp. 115–145.

[145] Wongsto, A. and Li, S., "Micromechanical FE analysis of UD fibre-reinforced composites with fibres distributed at random over the transverse cross-section," *Composites Part A: Applied Science and Manufacturing*, Vol. 36, No. 9, Sept. 2005, pp. 1246–1266.

[146] Gusev, A. A., Hine, P. J., and Ward, I. M., "Fiber packing and elastic properties of a transversely random unidirectional glass/epoxy composite," *Composites Science and Technology*, Vol. 60, No. 4, March 2000, pp. 535–541.

[147] Bentley, J. L., "Multidimensional binary search trees used for associative searching," *Communications of the ACM*, Vol. 18, No. 9, Sept. 1975, pp. 509–517.

[148] Shewchuck, J. R., "Triangle: engineering a 2D quality mesh generator and delaunay triangulator," *Applied Computational Geometry: Towards Geometric Engineering*, edited by M. C. Lin and D. Manocha, Vol. 1148, Springer-Verlag, Berlin, 1996, pp. 203–222.

[149] Pipes, R. B. and Pagano, N. J., "Interlaminar stresses in composite laminates under uniform axial extension," *Journal of Composite Materials*, Vol. 4, No. 4, 1970, pp. 538–548.

[150] Ballard, M. K., McLendon, W. R., and Whitcomb, J. D., "Influence of composite microstructure on apparent fiber properties," *American Society for Composites Twenty-Eighth Technical Conference*, University Park, PA, 2013, pp. 1–17.

[151] Huang, C.-Y., Trask, R. S., and Bond, I. P., "Characterization and analysis of carbon fibre-reinforced polymer composite laminates with embedded circular vasculature." *Journal of the Royal Society, Interface / the Royal Society*, Vol. 7, No. 49, Aug. 2010, pp. 1229–41.

[152] *HexTow IM7 Carbon Fiber Product Data*, Hexcel Corp, `http://www.hexcel.com/resources/datasheets/carbon-fiber-data-sheets/im7.pdf`, June 19, 2013.

[153] Rupnowski, P., Gentz, M., Sutter, J. K., and Kumosa, M., "An evaluation of elastic properties and coefficients of thermal expansion of graphite fibres from macroscopic composite input data," *Proceedings of the Royal Society A: Mathematical, Physical and Engineering Sciences*, Vol. 461, No. 2054, Feb. 2005, pp. 347–369.

[154] Rupnowski, P., Gentz, M., Sutter, J., and Kumosa, M., "An evaluation of the elastic properties and thermal expansion coefficients of medium and high modulus graphite fibers," *Composites Part A: Applied Science and Manufacturing*, Vol. 36, No. 3, March 2005, pp. 327–338.

[155] Rupnowski, P., *Multiscale stress and damage initiation analyses of graphite fiber/polyimide composites*, Ph.d., University of Denver, CO, 2005.

[156] Pagano, N. J., Schoeppner, G. A., Kim, R., and Abrams, F., "Steady-state cracking and edge effects in thermo-mechanical transverse cracking of cross-ply laminates," *Composites Science and Technology*, Vol. 58, No. 11, Nov. 1998, pp. 1811–1825.

[157] Pagano, N. J. and Tandon, G., "Thermo-elastic model for multidirectional coated-fiber composites: traction formulation," *Composites Science and Technology*, Vol. 38, No. 3, 1990, pp. 247–269.

[158] Kulkarni, R. and Ochoa, O. O., "Transverse and longitudinal CTE measurements of carbon fibers and their impact on interfacial residual stresses in composites," *Journal of Composite Materials*, Vol. 40, No. 8, July 2005, pp. 733–754.

[159] de Almeida, J. B., *Analytical and experimental study on the evolution of residual stresses in composite materials*, Master's thesis, University of Porto, Portugal, 2005.

[160] *HexPly 8552 epoxy matrix product data*, Hexcel Corp, `http://www.hexcel.com/Resources/DataSheets/Prepreg-Data-Sheets/8552\_us.pdf`, Sept. 27, 2011.

[161] Littell, J. D., Ruggeri, C. R., Goldberg, R. K., Roberts, G. D., Arnold, W. A., and Binienda, W. K., "Measurement of epoxy resin tension, compression, and shear stress-strain curves over a wide range of strain rates using small test specimens," *Journal of Aerospace Engineering*, Vol. 21, No. 3, 2008, pp. 162–173.

[162] Miyano, Y., Kanemitsu, M., Kunio, T., and Kuhn, H. a., "Role of matrix resin on fracture strengths of unidirectional CFRP," *Journal of Composite Materials*, Vol. 20, No. 6, Jan. 1986, pp. 520–538.

[163] Maxwell, K. S., Owens, B. C., McLendon, W. R., Whitcomb, J. D., and Varghese, J., "Evaluation of global/local strategies for detailed stress analysis of textile composites," *51st AIAA/ASME/ASCE/AHS/ASC Structures, Structural Dynamics, and Materials Conference*, Orlando, FL, 2010, pp. 1–15.

[164] McLendon, W. R. and Whitcomb, J. D., "Characteristic failure initiation sites in plain weave textile composites," *Journal of Composite Materials*, Vol. 47, No. 25, Nov. 2013, pp. 3143–3161.

[165] Jumbo, F., Ruiz, P. D., Yu, Y., Swallowe, G. M., Ashcroft, I. A., and Huntley, J. M., "Experimental and numerical investigation of mechanical and thermal residual strains in adhesively bonded joints," *Strain*, Vol. 43, No. 4, Nov. 2007, pp. 319–331.

[166] Araki, W., Nemoto, K., Adachi, T., and Yamaji, A., "Fracture toughness for mixed mode I/II of epoxy resin," *Acta Materialia*, Vol. 53, No. 3, Feb. 2005, pp. 869–875.

[167] Karahan, M., "Investigation of damage initiation and propagation in 2 x 2 twill woven carbon/epoxy multi-layer composites," *Textile Research Journal*, Vol. 81, No. 4, Feb. 2011, pp. 412–428.

APPENDIX A

PYTHON SCRIPT FOR FIBER-MATRIX RVE GENERATION

A.1 Fiber.py

```
#############
# Fiber.py #
#############
"""Fiber - Contains classes storing fiber data

Contained Classes:
Fiber - The basic class storing a fiber's center and radius
PeriodicMasterFiber - A specialization of Fiber for use in periodic RVEs
PeriodicGhostFiber - A Fiber represents a PeriodicMasterFiber's periodic
                     locations
"""

import matplotlib
import copy
import math

class Fiber:
    """The basic fiber class"""
    def __init__(self,center,radius):
        """Create a fiber with a given center coordinate and radius"""
        self.center = copy.deepcopy(center) # A list of form (x,y)
        self.radius = copy.deepcopy(radius) #radius of fiber

    def __str__(self):
        return "Fiber Center: " + str(self.center) + '\tr=' + str(self.radius)

    def overlaps_fiber(self,OtherFiber):
        """return true if this fiber overlaps OtherFiber, false otherwise"""
        return sqrt(  (OtherFiber.center[0]-self.center[0]) *
                      (OtherFiber.center[0]-self.center[0]) +
                      (OtherFiber.center[1]-self.center[1]) *
                      (OtherFiber.center[1]-self.center[1]) ) < \
               self.radius + otherFiber.radius

    def get_vector_to_other(self,OtherFiber):
        """Get a vector from this fiber's center to another fiber's center"""
        return [a-b for (a,b) in zip(OtherFiber.center,self.center)]

    def move(self,MoveVec):
        """Move the fiber by some vector"""
        self.center = [a+b for (a,b) in zip(self.center,MoveVec)]

    def draw(self,axes):
        """Draws the fiber on a matplotlib axes object"""
        axes.add_patch(matplotlib.patches.Circle(self.center,
                                                 self.radius,
                                                 linewidth=0.1))
```

```
class PeriodicMasterFiber(Fiber):
    """A class for storing a fiber that is in the RVE domain"""
    def __init__(self,center,radius,index,RVEDims,GhostBoundaryDistance):
        """Generate a PeriodicMasterFiber object"""
        Fiber.__init__(self,center,radius)
        # Dimensions of the RVE (Xdim, Ydim)
        self.RVEdims = RVEDims
        # If the fiber is within this distance from a boundary, make a periodic
        # ghost fiber
        self.GhostBoundaryDistance = GhostBoundaryDistance
        self.Index = copy.deepcopy(index)
        self.calc_ghost_fibers()
        # A list of nearby fibers to watch.  Will need to be updated
        # occasionally.
        self.NeighborFibers = []
        # How far this fiber has moved since the neighbors were last updated
        self.VecMovedSinceLastNeighborUpdate = [0.0,0.0]

    def __str__(self):
        return '\t'.join([str(self.Index),
                          str(self.center[0]),
                          str(self.center[1]),
                          str(self.radius)])

    def calc_ghost_fibers(self):
        """Make periodic ghost fibers as needed"""
        #First, get fiber in RVE bounds if it has moved out.
        self.fix_periodicity()
        self.GhostFibers = []
        for i in range(2):
            OtherIndex = 0
            if i == 0:
                OtherIndex = 1
            if self.center[i] < self.GhostBoundaryDistance:
                GhostCenter = [a for a in self.center]
                GhostCenter[i] += self.RVEdims[i]
                self.GhostFibers.append(
                    PeriodicGhostFiber(GhostCenter,self.radius,self))
                if self.center[OtherIndex] < self.GhostBoundaryDistance:
                    GhostCenter[OtherIndex] += self.RVEdims[OtherIndex]
                    self.GhostFibers.append(
                        PeriodicGhostFiber(GhostCenter,self.radius,self))
                elif self.center[OtherIndex] > \
                     self.RVEdims[OtherIndex] - self.GhostBoundaryDistance:
                    GhostCenter[OtherIndex] -= self.RVEdims[OtherIndex]
                    self.GhostFibers.append(
                        PeriodicGhostFiber(GhostCenter,self.radius,self))
            elif self.center[i] > self.RVEdims[i] - self.GhostBoundaryDistance:
                GhostCenter = [a for a in self.center]
                GhostCenter[i] -= self.RVEdims[i]
                self.GhostFibers.append(
                    PeriodicGhostFiber(GhostCenter,self.radius,self))
                if self.center[OtherIndex] < self.GhostBoundaryDistance:
                    GhostCenter[OtherIndex] += self.RVEdims[OtherIndex]
                    self.GhostFibers.append(
                        PeriodicGhostFiber(GhostCenter,self.radius,self))
```

```
            elif self.center[OtherIndex] > \
                 self.RVEdims[OtherIndex] - self.GhostBoundaryDistance:
                GhostCenter[OtherIndex] -= self.RVEdims[OtherIndex]
                self.GhostFibers.append(
                    PeriodicGhostFiber(GhostCenter,self.radius,self))


def move(self,MoveVec):
    """Move this fiber and all of its ghost fibers"""
    Fiber.move(self,MoveVec)
    self.VecMovedSinceLastNeighborUpdate = \
        [a+b for a,b in zip(MoveVec,
                            self.VecMovedSinceLastNeighborUpdate)]
    #since the ghost fiber's move method just calls the master's
    #move method, we need to actually move the ghosts, so we
    #use the base class's move method
    for ghost in self.GhostFibers:
        Fiber.move(ghost,MoveVec)

def get_distance_since_last_neighbor_update(self):
    """Returns total distance moved since neighbors were last updated"""
    return math.sqrt(sum(
        [a*a for a in self.VecMovedSinceLastNeighborUpdate] ) )

def fix_periodicity(self):
    """Return fiber to within RVE boundaries if it has moved out"""
    for i in range(2):
        if self.center[i] < 0:
            self.center[i] += self.RVEdims[i]
        elif self.center[i] > self.RVEdims[i]:
            self.center[i] -= self.RVEdims[i]

def get_index(self):
    """Retuns the index"""
    return self.Index

def update_neighbor_fibers(self,
                           FiberCentersKDTree,
                           AllFibers,
                           FiberDiamsToSearch):
    """Finds Neighbor Fibers

    Finds fibers within a certain distance of this one and adds to
    NeighborFibers

    Relies on a KD tree search to improve performance
    """
    # Note - this starts off as a set since we don't want to add a fiber
    # more than once.  It gets converted to a list sorted by index at the
    # end of the neighbor fiber update since we want consistent ordering
    self.NeighborFibers = set([])
    self.VecMovedSinceLastNeighborUpdate = [0.0,0.0]
    # Get the index numbers of the fibers within a certain distance of
    # this one
    NeighborFiberIndices = set(
        FiberCentersKDTree.query(self.center,
                                 k=len(AllFibers),
                                 p=2,
```

```
                                distance_upper_bound =
                                  self.radius*2.0*FiberDiamsToSearch)[1])
        # When you ask the KD tree for more nearest-neighbors than there
        # actaully are within the given tolerance, it pads the result with the
        # number of nearest neighbor values you asked for (in this case,
        # len(AllFibers)).  We don't want this value in NeighborFiberIndices.
        NeighborFiberIndices.remove(len(AllFibers))
        for i in NeighborFiberIndices:
            #print(i)
            if AllFibers[i].get_index() > self.Index:
                if AllFibers[i].__class__.__name__ == 'PeriodicMasterFiber':
                    self.NeighborFibers.add(AllFibers[i])
                elif AllFibers[i].__class__.__name__ == 'PeriodicGhostFiber':
                    self.NeighborFibers.add(AllFibers[i].MasterFiber)
        for gf in self.GhostFibers:
            gf.update_neighbor_fibers(FiberCentersKDTree,
                                      AllFibers,
                                      FiberDiamsToSearch)
        # We need to have consistent ordering.
        # This command changes NeighborFibers to a list sorted by fiber index.
        self.NeighborFibers = sorted(self.NeighborFibers,
                                     key=lambda x:x.get_index())

    def get_vector_to_other_periodic(self,OtherFiber,RVEDim):
        """
        Returns the shortest vector going from this fiber to the other fiber

        Accounts for periodicity
        """
        result = self.get_vector_to_other(OtherFiber)
        #Now modify result vector to account for periodicity
        for i in range(2):
            if result[i] > RVEDim[i]/2:
                result[i] -= RVEDim[i]
            elif result[i] < -RVEDim[i]/2:
                result[i] += RVEDim[i]
        return result

    def fix_overlap_with_neighbors(self,eps = 1.0e-3):
        """
        Fixes overlap

        Fixes any overlap with neighbors.
        Return true if any overlap was found.
        """
        OverlapFound = False
        for nf in self.NeighborFibers:
            #Only move fibers with higher indices
            #This _should_ be redundant since fibers only get added to
            #neighbor fibers if they have a higher index.
            if nf.Index < self.Index: continue
            vecToOther = self.get_vector_to_other_periodic(nf,self.RVEdims)
            dist = math.sqrt(sum([a*a for a in vecToOther]) )
            SumRadii = self.radius + nf.radius
            if dist < SumRadii:
                OverlapFound = True
                #Now move both fibers back from one another.
                NormVec = [a/dist for a in vecToOther]
```

```
                ProportionToMoveThisFiber = nf.radius/SumRadii;
                ProportionToMoveOtherFiber = 1.0-ProportionToMoveThisFiber
                TotalMoveBack = SumRadii - dist + SumRadii*eps
                NudgeVecThis = \
                  [-ProportionToMoveThisFiber*TotalMoveBack*a for a in NormVec]
                NudegVecOther = \
                  [ProportionToMoveOtherFiber*TotalMoveBack*a for a in NormVec]
                self.move(NudgeVecThis)
                nf.move(NudegVecOther)
        return OverlapFound

    def draw(self,axes):
        """
        Draws this fiber and all ghost fibers on the matplotlib axes object

        """
        Fiber.draw(self,axes)
        for ghost in self.GhostFibers:
            ghost.draw(axes)

class PeriodicGhostFiber(Fiber):
    """
    This class stores extra fibers that are periodic to a master fiber.
    When the master fiber moves, the periodic fibers should move as well.
    Similarly, moving this fiber will move the master fiber
    """
    def __init__(self,center,radius,MasterFiber):
        """Create PeriodicGhostFiber with a reference to the master fiber"""
        Fiber.__init__(self,center,radius)
        self.MasterFiber = MasterFiber

    def move(self,MoveVec):
        """
        Move the master fiber
        Note that this will move all the master's ghost fibers including this
        one
        """
        self.MasterFiber.move(MoveVec)

    def get_index(self):
        """Retuns the index of the master fiber"""
        return self.MasterFiber.get_index()

    def update_neighbor_fibers(self,
                               FiberCentersKDTree,
                               AllFibers,
                               FiberDiamsToSearch):
        """Finds Neighbor Fibers

        Finds fibers within a certain distance of this one and adds to
        NeighborFibers

        Relies on a KD tree search to improve performance
        """
        # Get the index numbers of the fibers within a certain distance of this
        # one
        NeighborFiberIndices = set(
            FiberCentersKDTree.query(self.center,
```

```
                                    k=len(AllFibers),
                                    p=2,
                                    distance_upper_bound =
                                      self.radius*2.0*FiberDiamsToSearch)[1])
        # When you ask the KD tree for more nearest-neighbors than there
        # actaully are within the given tolerance, it pads the result with
        # the number of nearest neighbor values you asked for (in this case,
        # len(AllFibers)).  We don't want this value in NeighborFiberIndices.
        NeighborFiberIndices.remove(len(AllFibers))
        for i in NeighborFiberIndices:
            if AllFibers[i].get_index() > self.get_index():
                if AllFibers[i].__class__.__name__ == 'PeriodicMasterFiber':
                    self.MasterFiber.NeighborFibers.add(AllFibers[i])
                elif AllFibers[i].__class__.__name__ == 'PeriodicGhostFiber':
                    self.MasterFiber.NeighborFibers.add(
                        AllFibers[i].MasterFiber)
```

A.2 RandomFMGeometry.py

```
########################
# RandomFMGeometry.py #
########################
"""RandomFMGeometry - Methods for making random periodic fiber-matrix geometry

Functions:
    make_RVE: Generates a random periodic RVE based on input parameters
    write_RVE: Writes RVE geometry data to a file
"""

from scipy import spatial
#from numpy import random #This is not threadsafe
import random #The native random number generator in python is threadsafe.
import matplotlib.pyplot as plt
import Fiber
import math
import time
import os
import shutil

def main():
    NumFibers = 1000
    Vf = 0.70
    AvDiam = 5.0e-6
    (FiberData,RVEDim) = make_RVE(NumFibers,Vf,AvDiam)
    write_RVE(FiberData,Vf,RVEDim,os.path.join('RVE_Data','RandomRVE.txt'))
    #plt.show()

def make_RVE( NumFibers,
              Vf,
              AvDiam,
              DiamStdDev = 0.0,
              RVEAspectRatio = 1.0,
              Visualize = False,
              ShowFinal = False,
              Epsilon = 1.0e-3):
    """Makes a random periodic fiber-matrix RVE
```

```
Inputs:
    NumFibers: Number of fibers in the RVE
    Vf:             Fiber volume fraction
    AvDiam:         Average fiber diameter
    DiamStdDev:     Standard deviation of fiber diameter (Defaults to zero)
    RVEAspectRatio: W/H of RVE (Defaults to 1, or square)
    Visualize:      If True, makes image of fibers for each iteration
                    (Defaults to False)
    ShowFinal:      If True, displays a matplotlib window showing final
                    fiber locations (Defaults to False)
    Epsilon:        Extra distance, as % of average fiber diameter, that
                    two overlapping fibers are moved away from each other
                    during iteration (Defualts to 1.0e-3)
Outputs: (MasterFibers,RVEDim)
    MasterFibers:   The fibers in the RVE domain.  Each fiber is only
                    output once even if it crosses an RVE boundary
    RVEDim:         The dimensions of the RVE in the form [w,h]
"""
start = time.time()
NumDiamsForNeighborSearch = 2
(RVEDim, MasterFibers) = make_fibers(NumFibers,
                                     Vf,
                                     AvDiam,
                                     NumDiamsForGhostFibers =
                                       NumDiamsForNeighborSearch+1)
#print(RVEDim)
recalculate_neighbors(MasterFibers,NumDiamsForNeighborSearch)
FoundOverlap = True
frame = None
fig = None
ax = None
if Visualize:
    if os.path.isdir('frames'):
        shutil.rmtree('frames')
    os.mkdir('frames')
    frame=0
    (fig,ax)=draw(MasterFibers,RVEDim,fig,ax,frame)

while(FoundOverlap):
    FoundOverlap = iterate_on_interference(MasterFibers,Epsilon)
    if Visualize:
        frame += 1
        draw(MasterFibers,RVEDim,fig,ax,frame)
    NeedToRecalcNeighbors = False
    for fiber in MasterFibers:
        # if any fiber has moved more than half the neighbor search
        # distance minus the radius, then we need to re-calculate the
        # neighbors
        if fiber.get_distance_since_last_neighbor_update() > \
           fiber.radius * (NumDiamsForNeighborSearch-1):
            NeedToRecalcNeighbors = True
            break
    if NeedToRecalcNeighbors:
        recalculate_neighbors(MasterFibers,NumDiamsForNeighborSearch)
elapsed = time.time() - start
print("Total Time to generate RVE Geometry: " + str(elapsed) + ' seconds')
if ShowFinal:
    draw(MasterFibers,RVEDim,fig,ax)
```

```
        plt.savefig('RandomFiberMatrix.eps',bbox_inches='tight')
        plt.show()
    return (MasterFibers,RVEDim)

def make_fibers(numFibers,
                Vf,
                AvDiam,
                DiamStDev=0.0,
                RVE_AR=1.0,
                NumDiamsForGhostFibers=4):
    """Generates Master Fibers
    Inputs:
        numFibers: Number of fibers
        Vf:        Fiber Volume Fraction
        AvDiam:    Average Fiber Diameter
        DiamStDev: Standard deviation of fiber diameters as a % of the average
                   diameter
        RVE_AR:    Aspect ratio of the RVE, w/h
    """
    #radii = [a/2 for a in DiamStDev*AvDiam * random.randn(numFibers) + AvDiam]
    radii = [random.gauss(AvDiam, DiamStDev)/2 for i in range(numFibers)]
    AreaFibers = sum([math.pi*a*a for a in radii])
    RVEArea = AreaFibers/Vf
    h = math.sqrt(RVEArea/RVE_AR)
    w = RVEArea/h
    RVEDim = [w,h]
    MasterFibers = []
    #randvals = random.rand(numFibers,2)
    randvals = [(random.random(), random.random()) for i in range(numFibers)]
    for i in range(numFibers):
        coord = [randvals[i][0]*w,randvals[i][1]*h]
        MasterFibers.append(
            Fiber.PeriodicMasterFiber(coord,
                                      radii[i],
                                      i,
                                      RVEDim,
                                      AvDiam*NumDiamsForGhostFibers))
    return (RVEDim,MasterFibers)


def recalculate_neighbors(MasterFibers,FiberDiamsToSearch):
    """Recalculates ghost fibers and neighbor fibers"""
    AllFibers = []
    for fiber in MasterFibers:
        fiber.calc_ghost_fibers()
        AllFibers.append(fiber)
        AllFibers.extend(fiber.GhostFibers)
    #print(len(AllFibers))
    AllFiberCenters = []
    for fiber in AllFibers:
        AllFiberCenters.append(fiber.center)
    FiberCentersKDTree = spatial.KDTree(AllFiberCenters)
    for fiber in MasterFibers:
        fiber.update_neighbor_fibers(FiberCentersKDTree,
                                     AllFibers,
                                     FiberDiamsToSearch)

def iterate_on_interference(MasterFibers,epsilon):
```

```
    """
    Loops through all fibers and resolves interference if it is found to exist
    """
    FoundOverlap = False
    for fiber in MasterFibers:
        FoundOverlap |= fiber.fix_overlap_with_neighbors(epsilon)
    return FoundOverlap

def write_RVE( FiberData,
               Vf,
               RVEDim,
               FileName):
    """Generates a file containing the RVE data, used by the mesh generator"""
    file = open(FileName,'w')
    file.write('\t'.join([str(len(FiberData)),
                          str(Vf),
                          str(RVEDim[0]),
                          str(RVEDim[1])])+'\n')
    for fiber in FiberData:
        fiber.fix_periodicity()
        file.write(str(fiber)+'\n')
    file.close()

def draw(Fibers,RVEDim,fig,ax,frame=None):
    """Draws the RVE in the input axes"""
    if not fig:
        fig = plt.figure()
    if not ax:
        ax = plt.axes()
    else:
        ax.clear()
    ax.get_xaxis().set_ticks([])
    ax.get_yaxis().set_ticks([])
    for fiber in Fibers:
        fiber.draw(ax)
    ax.set_aspect('equal')
    plt.xlim(0,RVEDim[0])
    plt.ylim(0,RVEDim[1])
    if frame:
        plt.savefig(os.path.join('frames',
                                 str(frame)+'_RVE.eps'),
                    transparent=True,
                    bbox_inches='tight')
    return (fig,ax)

if __name__=="__main__":
    main()
```